REASSESSMENT OF THE SEISMIC PARAMETERS FROM HISTORICAL SEISMOGRAMS OF 1912- MÜREFTE-ŞARKÖY, 1935-ERDEK-MARMARA ISLAND AND 1963-ÇINARCIK EARTHQUAKES

by

Nilay Başarır

B.S., Geophysical Engineering, Çanakkale Onsekiz Mart University , 2007

Submitted to the Kandilli Observatory and Earthquake Research Institute in partial fulfillment of the requirements for the degree of Master of Science

Graduate Program in Geophysics

Boğaziçi University

2011

REASSESSMENT OF THE SEISMIC PARAMETERS FROM HISTORICAL SEISMOGRAMS OF 1912- MÜREFTE-ŞARKÖY, 1935-ERDEK-MARMARA ISLAND AND 1963-ÇINARCIK EARTHQUAKES

APPROVED BY:

Assoc. Prof. Nurcan Meral Özel .....

(Thesis Supervisor)

Prof. Hayrullah Karabulut .....

Prof. Ali Pınar .....

(İstanbul University)

DATE OF APPROVAL: 13.06.2011

ACKNOWLEDGEMENTS

I owe my deepest gratitude to my advisor, Assoc. Prof. Nurcan Meral Özel, who was abundantly helpful and offered invaluable assistance, support and guidance from the beginning to the end of this thesis. This thesis would not have been possible without her great ideas, patient and encouragement.

It is a pleasure to thank to Prof. S. Balamir Üçer for his invaluable contributions during the preparation of this thesis. I am also greatful to Dr. Mehmet Yılmazer for his time and assist during the preparation of this thesis.

I would like to thank to all the faculty members in Geophysics Department for their support and help.

I have benefited from INGV, Istituto Nazionale di Geofisica e Vulcanalogia. I would like to thank to Marco Caciagli and other members of SISMOS Project of INGV.

Special thanks also to my dear friend, Pelin Pündük, for her support and valuable friendship from my college years to this day. I would like to express my deepeest gratitude to my friend Doğan Baştürk for his precious help and encouragment. I am greatful to my dear friend Özge Börek for her support. I also would like to thank to other friends; Melis Cevatoğlu, Yasemin Korkusuz and Res. Assist. Öcal Necmioğlu for their support and sharing the literature and invaluable assistance through my studies.

I would like to express my love and gratitude to my beloved parents; for their understanding and endless love throughout my life. I would like to thank my dad Ahmet Başarır, my mom Nebahat Başarır and my dear sister Çiğdem Başarır.

ABSTRACT

REASSESSMENT OF THE SEISMIC PARAMETERS FROM HISTORICAL SEISMOGRAMS OF 1912- MÜREFTE-ŞARKÖY, 1935- ERDEK-MARMARA ISLAND AND 1963-ÇINARCIK EARTHQUAKES

Marmara Region has witnessed many destructive earthquakes where some of them caused tsunami. Examination of these earthquakes through analyzing of analog records is crucial for the interpretation of seismotectonics and to assess the level of seismic hazard in this region. Many geological field surveys and geophysical studies to date indicated that 1912, Şarköy-Mürefte event, occurred on the Ganos Fault Zone, was one of the largest earthquake in the western Marmara Sea and caused tsunami. The same is also valid for 04.01.1935, 14:41, M=6.4 and 16:20 M=6.3 Erdek-Marmara Island, and 18.09.1963, 1963, M=6.3 Çınarcık Earthquakes. The purpose of this study is to contribute to the seismotectonics of this region by examining these earthquakes and revaluate source parameters of these shocks using seismic waveforms, which were previously not carried out by modern techniques.

In this study, the original seismograms from various countries for 1912 Şarköy-Mürefte, 1935, Erdek Marmara Island and 1963, Çınarcık Earthquakes were digitized. The magnitude Mw, seismic moment Mo, the radius of circular source zone R and stress drop $\Delta\sigma$ values were redetermined using digitized original seismic waveforms from displacement spectra for these historical events. For this purpose, a large number of seismic station bulletins have been consulted for the instrumental information to remove the instrument response. In addition, the epicentral locations have been calculated using available readings from original records and also ISS bulletins for 04.01.1935-14:41 and 16:20 Marmara Island-Erdek Earthquake and 18.09.1963-16:58 Çınarcık Earthquake. For the 1912 event, the magnitude Mw=7.13 and radius of the fault area R=41 km were

determined. Also, 04.01.1935- 14:41 and 16:20 Earthquakes showed a fault radius of about 15 km with magnitudes Mw=6.0 and Mw=5.9, respectively. The epicenter determinations showed that the first event in 04.01.1935 was located at 40.72 N- 27.72 E while the second one occurred at 40.61 N-27.43 E. The epicenter estimation for the first event in 04.01.1935 indicated a difference about 19 km from the macroseismic epicenter result of Ambraseys (1988), while the second event was located 27 km away from the result of Ambraseys and Jackson (2000). Another finding is of the 1963 event, which gave a fault radius of approximately 13 km with a magnitude Mw=5.9. It was found that the 1963 event was located at 40.80 N-29.18 E. Furthermore; in this study moment tensor inversion method was applied on these earthquakes by using original seismograms collected from various observatories. The fault mechanisms for 04.01.1935-14:41 and 16:20 Earthquakes were determined using moment tensor inversion from the original seismic waveforms for the first time. Likewise, fault mechanism for the 1963 Çınarcık Earthquake was also obtained. The results showed that these earthquakes have normal fault mechanism. Considering its epicenter and fault mechanism, the 1963 event may be related to the pull-apart structure of the Çınarcık Basin. The application of moment tensor inversion method to the historical earthquakes records will give an opportunity to understand the geometry of the known faults possibly shed light some unknown structures and illuminate the seismotectonic features of Marmara Region based on the retrieved fault mechanism solution.

ÖZET

1912- MÜREFTE-ŞARKÖY, 1935-ERDEK-MARMARA ISLAND VE 1963-ÇINARCIK DEPREMLERİNİN SİSMİK PARAMETRELERİNİN TARİHSEL SİSMOGRAMLAR KULLANILARAK YENİDEN DEĞERLENDİRİLMESİ

Marmara Bölgesi, yıllarca bir çok yıkıcı depreme tanık olmuştur. Bu depremlerin analog kayıtlarının analiz edilerek araştırılması, bu bölgenin sismotektonik yorumu ve sismik tehlikesinin değerlendirilmesi için oldukça önemlidir. Bu güne kadar gerçekleştirilmiş olan jeofizik ve jeolojik çalışmaların bir çoğunda, Ganos Fay Zonu'nun üzerinde meydana gelen 1912, Şarköy-Mürefte Depremi'nin, Batı Marmara Denizi'nde meydana gelmiş en büyük depremlerden biri olduğu ve tsunamiye de neden olduğu iddia edilmektedir. Aynı şekilde, 04.01.1935, 14:41 M=6.4 ve 16:20 M=6.3 Erdek-Marmara Adası, ve 18.09.1963 Çınarcık M=6.3 depremlerinin de araştırılması sismik risk çalışmalarına katkı sağlayacaktır. Bu çalışmanın amacı, bu depremlerin orjinal kayıtlarını sayısallaştırarak, bu depremleri gözden geçirmek ve kaynak parametrelerini yeniden değerlendirmektir.

Bu çalışmada, çeşitli ülkelerden Şarköy-Mürefte, 1935, Erdek Marmara Adası ve 1963, Çınarcık depremleri için çeşitli ülkelerden elde edilmiş olan orjinal sismogramlar sayısallaştırılmıştır. Sayısallaştırılmış olan orjinal sismik dalga formlarını kullanarak elde edilen yer değiştirme spektrumlarından bu tarihsel depremlerin büyüklüğü Mw, sismik moment Mo, depreme neden olan fayın kaynak yarıçapı R ve gerilim düşümü $\Delta\sigma$ değerleri hesaplanmıştır. Bir çok sismik istasyon bültenine ulaşılarak, alet etkisini gidermek için bu depremleri kaydeden aletlerin bilgileri elde edilmiştir. Ayrıca, 04.01.1935-14:41 and 16:20 Erdek-Marmara Adası, 18.09.1963 Çınarcık depremleri için, ISS bültenlerinden elde edilen P ve S dalgası varış zamanlarının yanısıra elde bulunan orjinal sismogramlardaki okumalarda kullanılarak dışmerkez tayini yapılmıştır. 1912 Depremi için, büyüklük Mw=7.13 ve fayın kaynak yarıçapı 41 km olarak bulunmuştur. Ayrıca, 04.01.1935, 14:41

ve 16:20 depremlerinin fayın kaynak yarıçapı 15 km bulunurken, büyüklükleri sırasıyla Mw=6.0 ve Mw=5.9 olarak hesaplanmıştır. Dışmerkez hesaplamaları ise ilk depremin 40.72 N- 27.72 E , ikinci depremin ise 40.61 N-27.43 E koordinatlarında olduğunu göstermiştir. 04.01.1935 yılında meydana gelen bu depremlerden birincisinin, Ambraseys (1988)'in makrosismik dışmerkez çözümünden yaklaşık 19 km uzaklıkta olduğu görülürken, ikinci deprem ise Ambraseys and Jackson (2000)'in tespit ettiği dışmerkez çözümünden 27 km kadar uzakta tespit edilmiştir. 1963 Depremi için ise fay kaynak yarıçapı 13 km, büyüklüğü Mw=5.9 olarak bulunmuştur. Bu depremin dışmerkezi 40.80 N-29.18 E olarak bulunmuştur. Bunun yanısıra, bu çalışmada, bu depremlere çeşitli istasyonlardan elde edilmiş olan orjinal sismogramlar kullanılarak, moment tensor ters çözüm işlemi uygulanmıştır. 04.01.1935-14:41 ve 16:20 depremlerinin fay mekanizması çözümleri ilk defa bu çalışmada elde edilmiştir. Yine aynı şekilde, 1963 depremi için de fay mekanizması elde edilmiştir. Sonuçlar; bu depremlerin fay çözümlerinin normal faylanma mekanizmasına sahip oldukları yönündedir. Dışmerkezi ve fay mekanizması göz önünde bulundurulursa, 1963 Depremi'nin, Çınarcık çukurundaki pull-apart yapıyla alakalı olduğu söylenebilir. Tarihsel depremlere moment tensor ters çözüm işlemi uygulaması, bilinen fayların geometrisinin anlaşılmasını, bazı bilinmeyen yapıları ortaya çıkarılmasını ve yeniden gözden geçirilen fay mekanizma çözümlerine dayanarak Marmara Bölgesi'nin sismotektonik özelliklerinin aydınlatılmasını sağlayacaktır.

TABLE OF CONTENTS

LIST OF FIGURES

LIST OF TABLES

LIST OF SYMBOLS / ABBREVIATIONS

A	Distance between the recording paper and galvanometer
T	Period of pendulum
H	Damping constant
V	Magnification
k	Transfer factor
I	Reduced pendulum length and the galvanometer
Є	Damping ratio
M_0	Seismic Moment (Nm)
Ms	Surface wave Magnitude
R	Radius of the circular source zone
$\Delta\sigma$	Stress drop (bar)
I_O	Intensity
Ωo	Low frequency level
f_c	Corner frequency
Mw	Moment Magnitude
G (r)	Geometrical spreading
AF	Anafartalar Fault
ASCII	American Standard Code for Information Interchange
BCIS	Bureau central international de séismologie

CLVD	Compensated linear vector dipole
Dpi	Dots per inch
EMSC	European Mediterranean Seismological Centre
EUROSEISMOS	Saving and Studying the Seismograms of the Strongest EuroMediterranean Earthquakes
GMT	Greenwich Mean Time
GIMP	The GNU Image Manipulation Program
GF	Gelibolu Fault
IASPEI	International Association of Seismology and Physics of the Earth's Interior
IDA	International Deployment of Accelerographs
IDC	International Data Centre
ISS	International Seismological Summary
INGV	Istituto Nazionale di Geofisica e Vulcanalogia
Lat	Latitude
Lon	Longitude
LP	Long Period
MB	Megabayt
MSK	Medvedev-Sponheuer-Karnik
SAC	Seismic Analysis Code
SISMOS	Sismogrammi Storici
SG	Sigindere Fault
WWSSN	Worldwide Standardized Seismograph Network

TESEO	Turn the Eldest Seismograms into the Electronic Original Ones
NAF	North Anatolian Fault
TIFF	Tagged Image File Format
SEMOC	Strong Earthquake Motion Observation Center
RMS	Root Mean Square
TDMT-INV	Time Domain Moment Tensor Inversion
VR	Variance Reduction
xcf	Experimental Computing Facility

1. INTRODUCTION

Earlier seismograms, which date from the end of the XIX century to the day of the birth of modern seismic stations and tools, represent a big part of instrumental seismology. These historical seismograms are analog records which are not in digital form and it has no suspect that they are the unique documents for the seismology (Battllo, 2008). Until now, collection, copying and distribution of these early records necessitated too much effort as a result of deficiencies in technology. Many initiatives around the world have been indented to create digital forms of the early seismograms and their related material to preserve seismological heritage of the world such as IDC, WWSSN, and IASPEI. More recently, SISMOS and the EUROSEISMOS projects undertake the storing the copies of old seismograms as images in digital format (Michelini, 2005).

Given the fact that the earthquake cycle is long-time, it is inevitable to realize the importance of early seismograms that contain valuable information enabling seismologists to gain an understanding of the mechanisms of past earthquakes (Kanamori, 1988). Kanamori (1988), suggested a comprehensive list including different seismological research fields such as global seismicity, seismotectonics of subduction zones, rupture process of large earthquakes, study of seismic gaps, regional seismotectonics, seismic moment release, strong motion seismology, tsunami earthquakes and other unusual events.

But analyzing old seismograms is not a straightforward process and requires too much effort. Above all, it should be keep in mind that these old seismograms have been recorded with narrow-band range frequency instruments, which creates a big discretion from the technology of today. At a first glance, studying with old seismograms seems just the digitization of a certain section of the seismic traces on the records. However, the process is more complicated than it is thought. Usually the information necessary for the all process of the analyzing of these records such as instrument constants and time accuracy is missing or doubtful (Battllo, 2008). Moreover, the original papers containing the seismic traces are exposed to chemical, physical and biological factors, which decreasing the quality of the records (Ferrari and Monaco, 2005). In brief, there is no

specific method to make historical seismograms useful; each seismogram may require different approximation to be solved.

The importance of studying historical earthquakes by analysing original records through the modern techniques have been realized by many researchers over the world, which stimulated to carry out more comprehensive investigations about old earthquakes. Costa *et al*., (1999) studied 23 April 1909 Benavente (Portugal) earthquake using historical seismograms. The study indicated that the magnitude of this earthquake was overestimated. The selection of relatively good seismograms from Sweden, Strasbourg and several stations in Germany and their analyzing with modern techniques presented a better interpretation for seismic hazard of the region. Another study carried out by Dineva *et al*., (2002) redetermined the origin time, location, seismic moment and magnitudes (Mw-Ms) for four earthquakes in the beginning of the 20th century. They used ISS bulletins for the epicenter and origin estimations based on iterative procedures. Digitized seismograms were used for displacement spectra after necessary corrections. Stich *et al*., (2003) examined analogue recordings from 6 early mechanical seismographs for the 1910 Adra earthquake. They applied time-domain analysis techniques to historical data to estimate source parameters of the event. The seismic moment tensor was inverted based on available recordings at mechanical horizontal seismographs. Baskoutas *et al*., (2000) presented an operation to convert the seismograms from mechanical seismograms in Greece in the time period of 1910-1960 time periods, into digital format. All of these studies indicate the difficulties of studying with old seismograms and that there is no just one method while dealing with them.

This study aimed at gaining a more comprehensive knowledge about the historical earthquakes, 1912, Mürefte M=7.3, 1935 Erdek-Marmara Islands M=6.4, 1963 Çınarcık M=6.3 Earthquakes, which play an important role in understanding of the seismotectonics of the Marmara Region by using the analog seismograms through the modern techniques that were not applied previously.

One of the most important earthquakes is the 1912 Mürefte Earthquake in Marmara Region, which was investigated by various researchers. Ambraseys and Finkel *et al*., (1987) calculated the surface wave magnitude of this event Ms 7.4 ± 0.3 from Milne

pendulum seismographs. Based on the observations of surface wave ruptures and ground displacements on field surveys, they reported that the length of the fault responsible for the 1912 Earthquake was reported as 50 km. Fault systems, where dextral strike-slip displacements reaching up to 3 m with a significant normal component, have been observed. The epicenter of this earthquake was assigned as 40.7 N, 27.2 E coordinates using well-defined macroseismic data. Seismic moment was determined as 1.230×10^{20} Nm using global average scaling log (M_0)–(Ms) laws of Ekström and Dziewonski relation (1988). It has been reported that seismic sea waves were observed in the area (Ambraseys, 2002b). Recently, seismic reflection data and the multibeam bathymetry indicated that the total length of the surface rupture is approximately 56 km (Altınok *et al.*, 2003). The focal mechanism of this earthquake has been proposed as 68/55/-145 (strike/dip/rake) while modelling this earthquake for investigating Coloumb stress interactions of earthquakes that have occurred in the Region of northwest Turkey and North Aegean Sea since the 1912 Earthquake in the study of Nalbant *et al*., (1998). This proposal was based on the previous geological and macroseismic knowledge about the fault responsible for the 1912 Earthquake. Vannucci and Gasperini (2003) collected the fault characteristics of earthquakes between time intervals of 1905-2003 to create a catalog for EMSC (European Mediterranean Seismological Centre). The parameters were collected from different articles and catalogues and these collected solutions for an event were tested to establish preferred solutions. The seismic moment of this earthquake was reported as 1.549×10^{20} Nm in this catalog. However, there is no information about where this information comes from. In a more recent study carried out by Aksoy *et al*., (2010) determined the strike slip fault mechanism for the 1912 Earthquake by using the P wave first motion polarities of some analog records.

Likewise, 1935 Erdek-Marmara Island Earthquake is an important event that occurred in the Marmara Region. Actually, there have been two earthquakes of nearly equal magnitude, spaced two hours apart, one at 14:41(GMT) and the other at 16:20(GMT) in 4 January 1935. The maximum intensity of the first shock was assigned as IX on the isoseismal map drawn by Ambraseys (1988). He determined the epicenter of this earthquake as 40.64 N, 27.51 E from the macroseismic observations and the magnitude as Ms=6.4. The depths of these two earthquakes were reported as 20 km for the first shock and 30 km for the second shock by Ayhan *et al*., (1986). Although a seismological research

based on original seismic waveforms was not carried out for these earthquakes, the focal mechanism for the fault concerned has been proposed as 100/40/-90 (strike/dip/rake) by Nalbant *et al*., (1998) who investigated the Coloumb stress change after these shocks. This fault mechanism solution together with seismic moment Mo=3.467×10^{18} Nm and magnitude Mw=6.3 are also reported in the catalog EMSC.

Another earthquake, occurred in Marmara Region, interest of this study is the 1963 Çınarcık M=6.3 event. The maximum intensity was assigned as VII (Özçiçek, 1996). The epicenter of this earthquake was assigned as 40.6 N, 29.1 E. Lately, the seismic moment and fault characteristics of the event were determined as Mo=$9,6\times10^{17}$ Nm, 304/56/-82, respectively ,using P and SH waveforms and first motion polarities by Taymaz *et al*., (1991). The depth of source was found as about 15 km and proposed the epicenter as 40.9 N, 29.2 E by the study of Taymaz *et al*., (1991).

In this study, the historical 1912, Mürefte M=7.3, 1935 Erdek-Marmara Islands M=6.4, 1963 Çınarcık M=6.3 Earthquakes were investigated using modern approaches. For this purpose, the seismic traces recorded on the analog seismograms were obtained in digital form through the vectorization method using TESEO plug in of an image manipulation software named GIMP. The seismic traces acquired in the digital form were corrected geometrically to avoid the distortions related to old-time instruments. In addition, the instrumental responses were removed to obtain the true ground motion using the collected instrument constants from various sources. From the displacement spectra, the dynamic parameters such as magnitude Mw, seismic moment Mo, fault area R, stress drop σ, were recalculated. In addition, the epicenters of the 1935 Erdek-Marmara Islands M=6.4, the 1963 Çınarcık M=6.3 Earthquakes were redetermined using the arrival times obtained from ISS bulletins as well as the P and S readings based on original seismograms through the HYPOCENTRE 3.2. by Lienert (1994). Fault plane solutions were also obtained for the 1935 Erdek-Marmara Islands M=6.4, 1963 Çınarcık M=6.3 Earthquakes using the moment tensor inversion TDMT-INV (time domain moment tensor inversion) algorithm produced by Dreger (2002). For this process, the Green's functions or synthetic waveforms were obtained from (FKRPROG) algorithm produced by Saikia (1994). In this study, the Green's functions were calculated from 4 km depth to 40 km depth in 2 km increments and from 10 km distance to 5000 km distance in 5 km increments.

During this study, the methods and the processes followed step by step for the reassessment of these earthquakes enabled us to gain a valuable understanding for the approaches to historical seismogram analysis.

2. TECTONIC SETTINGS AND HISTORICAL SEISMICITY OF THE MARMARA REGION

The active tectonics of the Marmara Sea Region is controlled by the right-lateral North Anatolian Fault system which extends from the Karlıova in the east to the Gulf of İzmit in the north. It is a well-known fact that this seismic activity is the result of the westward motion of the Anatolian block to the Europe on the NAF fault system. The NAF system is a complex structure since it branches into three strands. One of them passes by Sapanca and enters the Gulf of İzmit, and a southern strand runs toward Lake Iznik and Bursa. The southern strand splits up again into a middle and southern branch, the former passing south of Iznik and the latter south of Bursa, by the Lakes of Apolyont and Manyas into the North Aegean extensional province (Ambraseys, 2002a). The north Marmara Basin is stituated by 70 km-wide step-over between two strike-slip faults. One of them is the 1912 Ganos Earthquake that ruptured in Dardanelles Region to the west of the Marmara Sea. The second one is the 1999 İzmit Earthquake, which caused a rupture to the east of the Marmara Sea (Armijo *et al.*, 2005). The Marmara Sea Basin is about 230 km long and 70 km wide with a shallow shelf to the south and a series of subbasins to the north, namely, the Tekirdağ, Central, Çınarcık, Karamürsel, and İzmit Basins (Ambraseys, 2002).

Firstly, the Marmara Sea Basin was considered to be a graben or a structure of right-lateral faults exhibiting an overall normal motion (Barka and Kadinsky-Cade, 1988). In a more recent study of Le Pichon *et al*., (2000) proposed that the Marmara Sea Basin was controlled by a strike-slip fault that extended between the Gulf of Izmit and the Galipoli Peninsula. However, it was found that the bathymetry and faults identified by seismic reflection surveys and focal mechanisms of a few earthquakes (Ambraseys and Jackson, 2000), presents a series of pull-apart basins which are bounded by a system of mostly short strike-slip and normal faults, implying significant regional extension responsible for the formation of the Marmara Sea Basin. The depths and steep bathymetric gradients of Tekirdağ and Çınarcık Subbasins in the west and east part of the Marmara Sea Basin demonstrate high seismicity (Ambraseys, 2002a). Using multibeam bathymetry and high resolution multichannel seismic reflection data, Armijo *et al*., (2005) indicated that the

geometry of submarine scraps in the Marmara Region is controlled by a segmentation of the pull-apart fault system. Also, they described a large component of normal slip along the southern margin of Tekirdağ Basin. One of the most important models for the tectonic and morphological structure of Marmara Region, the "pull-apart" model by Armijo *et al*., (2005) is shown in Figure 2.1 that shows clearly inner pull- apart in the Central Basin. The trace of active faults with colour outlines and dates indicating the earthquake breaks with pull-apart in the Marmara Sea Basin are shown in Figure 2.1. Recent earthquake breaks of large earthquakes are also shown.

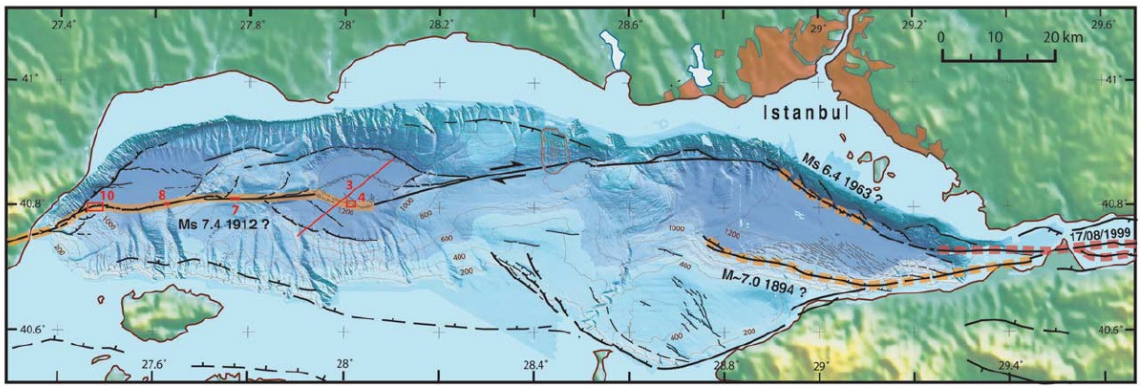

Figure 2.1. Bathymetry and active faults in the North Marmara Basin (Armijo *et al*., 2005)

Marmara Region has been exposed to many destructive earthquakes for years. It is certain that the NAF zone, which is a major right-lateral transform fault controlling the westward motion of the Anatolian Plate, has played a significant role in this seismicity. The NAF system which has a branch in the Marmara Sea Region spreading into two major fault branches about 100 km apart, which results in a active seismic behaviour. Figure 2.2 demonstrates the historical earthquakes occurred in the Marmara Region from 360 B.C. to present (Altınok and Alpar, 2003).

Ambraseys and Jackson (2000), Ambraseys (2002a) investigated the long-term seismicity of the Marmara Region over the last 500 and 2000 yr for both instrumental and historical data. The reported damage showed that the 1999 Izmit Earthquake appears to be similar to the 1719 Earthquake. There were also two earthquakes in 1766 and one in 1754 that probably resulted from fault ruptures closer to Istanbul. These earthquakes were likely similar in size to the major events of the 20th century. The robust measurement of

earthquake parameters especially for the magnitude is very important issue still for Marmara Region (Ambraseys, 2002a).

Ambraseys (2002a) identified 581 earthquakes during the last 20 centuries in the Marmara Sea Region. 408 of 581 earthquakes occured in the preinstrumental period. The magnitudes of 107 earthquakes in the preinstrumental period were assessed as values ranging between 5.0 and 7.4. The magnitudes of 173 earthquakes occurred in the instrumental period were calculated as values ranging 4.0 and 7.4.

The seismicity of the last 2000 years may be responsible for the right-lateral slip 2.2±3 cm/yr. No macroseismic evidence has been observed for a major earthquake that could be related to the rupture of the offshore NAF all along the north coast of the Marmara Basin from the Gelibolu Peninsula to the Gulf of İzmit. The historical earthquakes in the Basin close to the İstanbul have been observed smaller than those occurred east and west in the Ganos Aegean Region (Ambraseys, 2002a). Figure 2.2 shows the map of the historical earthquakes in the Marmara Region 360 B.C. to present.

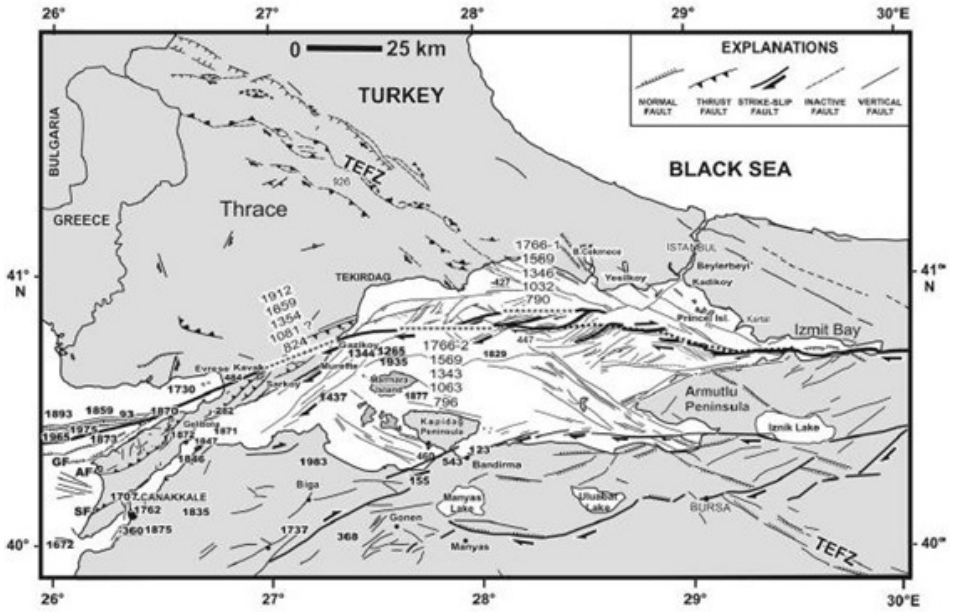

Figure 2.2. The map of historical earthquakes from of the Western Marmara Sea Region GF=Gelibolu fault, AF: Anafartalar thrust fault SG: Sigindere Fault (Altınok *et al*., 2003)

2.1. 9 August 1912, Mürefte-Şarköy Earthquake

Throughout history, Gelibolu Peninsula has witnessed the damaging earthquakes. One of the biggest earthquakes in the Marmara Region was 09.08.1912-01:29:00(GMT), Şarköy-Mürefte Earthquake which occurred on a western segment of the northern strand of the NAF zone, the Ganos Fault Zone, bounded by the Tekirdağ Trough to the east (Figure 2.2) (Altınok *et al*., 2003).

The NAF in the Sea of Marmara Region underwent the 1912 Mürefte Earthquake and the 1999 Izmit Earthquake (Mw 7.4; Barka *et al*., 2002) at the western and eastern ends of the Sea of Marmara, respectively. It is thought that at least 250 km of the NAF might have ruptured during these 2 events, leaving a 70–150-km-long seismic gap in the Sea of Marmara. This uncertainty is probably the result of the poorly known eastern extension of the 1912 Earthquake rupture in the Sea of Marmara (Aksoy *et al*., 2010).

One of the most comprehensive investigations by Ambraseys and Finkel (1987) stated that the 1912 Earthquake which was one of the most devastating disasters in The Balkans, caused approximately 2000 dead and more than 300 damaged villages. The 1912 Şarköy-Mürefte Earthquake is also known Saros-Marmara Earthquake since it was felt in a large area. Due to the fact that the seismic networks were primitive at that time, determining an accurate instrumental location for this event is not possible. However, Ambraseys and Finkel (1987) determined a reliable surface wave magnitude Ms=7.4 by using teleseismic amplitudes from Milne seismographs. The epicenter of this earthquake was reported as 40.7 N-27.2 E by Ambraseys (2000). The earthquake lasted 40-50 seconds with three successive distinct events. The aftershocks after this earthquakes lasted two months, the largest one was 13 September 1912 (Mw 6.7) earthquake. This earthquake may have been triggered in a secondary segment (Papadimitriou *et al*., 2001). Figure 2.4 demonstrates the destruction caused by the 1912 Earthquake. Among isoseismal maps drawn by various researches, probably the most reliable one indicated that the maximum intensity of X (MSK) was in the NE trending area between Tekirdağ and Gökçeada. Figure shows the isoseismal map drawn by Ambresesys and Finkel (1987).

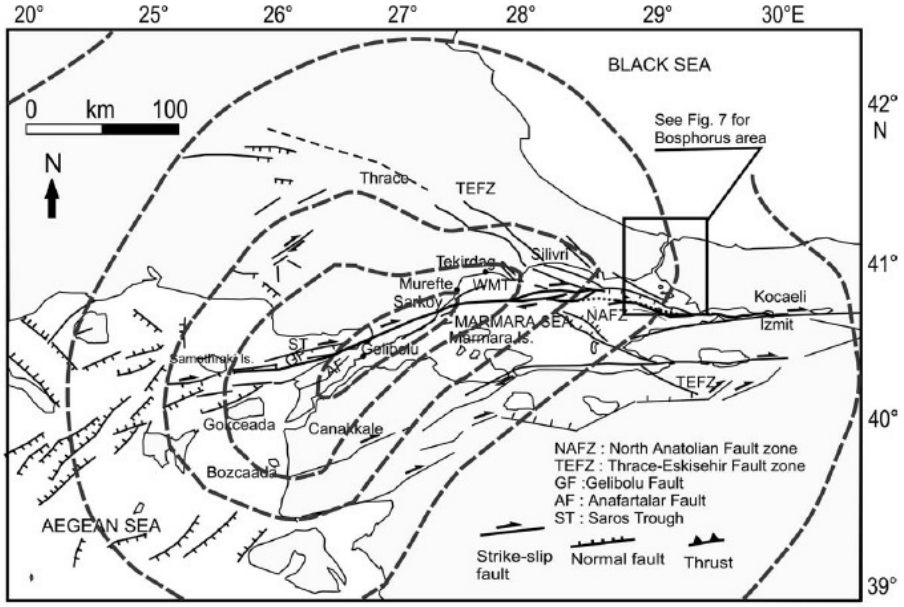

Figure 2.3. Isoseismal map of 1912 Ganos Earthquake NAF: North Anatolian fault, TEF: Thrace-Eskişehir fault, WMT: West Marmara (Tekirdağ) Trough, ST: Saros Trough (Altınok *et al*., 2003)

Because of the coincidence between the 1912 Earthquake and political conflicts which resulted in Balkan Wars (8 October 1912) at that time, the obtaining of the specific documents related to this event is difficult. However, a large number of studies based on both geological field surveys and geophysical researches together with the macroseismic studies have let light on the knowledge of this earthquake and indicated that 1912 earthquake produced a tsunami (Altınok *et al.*, 2003).

Ergin *et al*., (1967) stated that the Ganos Earthquake caused to a split in 5m width and 10 m in depth, extending in an area between Yenice and Kestanbol. Epicenter of the earthquake was related to faults in the Sea of Marmara. The earthquake resulted in 183 dead, 324 injured, 2650 demolished houses in Mürefte and Şarköy and 33 dead, 142 injured, 2890 demolished houses.

Another research carried by Mihailoviç (1927, 1933) indicated that 73.6 per cent of the buildings in Thrace, 42.7 per cent of buildings in Anatolia were destroyed as a result of this earthquake. The fire after this earthquake played a significant role in the damage rate.

42.1 per cent of public in the Thrace and 12.8 per cent of the public living in Anatolia lost their houses.

Öztin (1987) reported that the 1912 Earthquake affected mostly Şarköy-Mürefte Region and all the houses were destructed as a result of this event. The damage is also large in the Gelibolu and Çanakkale Regions. According to this study, the earthquake led to 1115 dead. In Tekirdağ, Gümrük Mosque was demolished and Paşa Mosque and a clock tower close to landing were damaged. Gelibolu was also affected badly by this earthquake. The buildings close to the seaside was damaged.

Ateş and Tabban (1976) reported that the buildings of court-house, the police station was highly damaged and a mosque was demolished. In addition, seven mosques in the region were damaged. The earthquake also caused damage in Istanbul. Some cracks were observed on the walls of Ortaköy Mosque.

This devastating earthquake occurred on Şarköy and Mürefte which caused damages on Gelibolu Peninsula. Mürefte and Şarköy was the epicenter of the earthquake. 80 per cent of the buildings demolished and rest of the buildings became unstable in Şarköy and Mürefte. There had been lots of fissures in walleyes which have 0.3-0.5m width. One of the biggest fissures was between Yenice and Kestanbol which had 5 m width, 10 m depth and 1-2 km length. Water sources near Mürefte dried and hot spring on Dedeağaç decreased water. In Mürefte and Şarköy, 2650 buildings destroyed, 183 people died and 324 people wounded, in Gelibolu 2890 buildings ruined, 33 people died and 142 people wounded because of the happening. The earthquake epicenter is related to Marmara Sea. The earthquake was one of the most intensive earthquake for last fifty years which has intensity of X and magnitude of 8(Pınar and Lahn, 1952). Masonry structures in the vicinity of surface ruptures were totally demolishe and timber-frame houses were severely damaged (Ambraseys and Finkel, 1987). Figure 2.4 indicates the damage caused by the 1912 Earthquake around Ganos.

Figure 2.4. Historical photographs around Ganos (A). Hoşköy (Hora). (B) Gaziköy (Ganos) (Altınok *et al*., 2003)

The direct observations of the ruptures on land of the 1912 Ganos Earthquake were reported by Mihailovich (1927). Later studies carried out by Ambraseys and Finkel (1987) and Altunel *et al*., (2004) based on the observations on the field investigations and damage distribution revealed that the rupture propagated into the Sea of Marmara, with an unknown extent. Despite the fact that the field investigations defined well surface ruptures on the land, the total length of the main segment remains controversial (Armijo, 2005). It was considered about 50 km by Ambraseys and Finkel (1987). Lately, Ambraseys and Jackson (2000) estimated, assuming the thickness of seismogenic layer (W) about 15 km, the rupture length as about 84 km, which is consistent with the damage distribution caused by the 1912 Earthquake. Figure 2.5 shows the estimated rupture lengths with their locations for the 1912 Earthquake as well as the 1509 Earthquake by Ambraseys and Jakson (2000). The black bars represent the rupture if the W is assumed 15 km. The shaded bars show the estimated rupture lengths if W is assumed about 10 km.

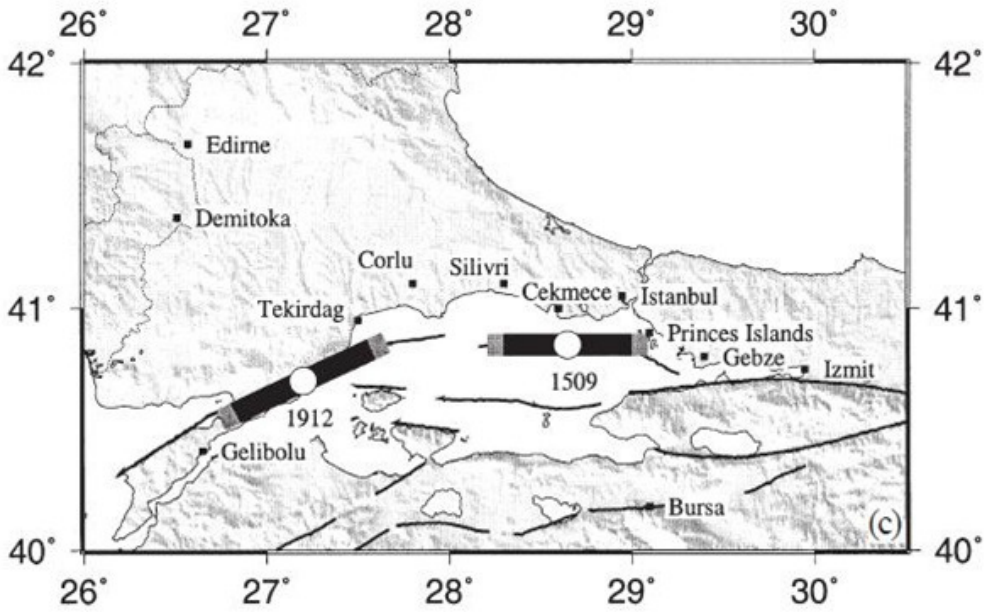

Figure 2.5. Location map for discussion of the 10 September 1509 and 9 August 1912 Earthquakes (Ambraseys and Jakson, 2000)

Recently, Altınok *et al*., (2003) estimated the length of the surface rupture is about 56 km based on a detailed field surveys as well as the multibeam bathymetry and seismic reflection data. It was also observed right-lateral strike-slip motion along the Ganos Fault, with displacements varying 3.5 to 4.5 m. Relating the surface rupture to seismic moment formula based on the field observation, they calculated moment magnitude of the event Mw=7.3.

Ambraseys and Jackson (2002) determined the seismic moment of this event as 1.230×10^{20} Nm and 2.19×10^{20} Nm of the aftershock 13.09.1912 event using global average scaling log (M_0) − (Ms) laws of Ekström and Dziewonski(1988). Nalbant *et al*., (1998) proposed an appropriate fault plane solution, considering the structure of this region from previous knowledge, with 68/55/-145(Strike/Dip/Rake) when determining Coulomb stress change for the fault concerned the 1912 Earthquake. They thought that branch of the NAF steps from the Sea of Marmara to the Aegean Sea such that it should locally have a reverse component.

Vannucci and Gasperini (2003) collected the fault characteristics of earthquakes between time intervals of 1905-2003 to create a catalog for EMSC. These collected fault

solutions were checked to verify the consistency among nodal planes or axes. The parameters collected from different articles and catalogues were used as input files. They also developed new fields to correct the possible or obvious errors. In addition, collected solutions for the same events from different sources were tested to established preferred solutions. The fault mechanism of this event and the seismic moment were reported as 68/55/-145 and 1.549×10^{20} Nm. In this study, the fault mechanism of this event is given as 68/55/-145(Strike/Dip/Rake). However, there is no information about its reference.

The documents about the tsunami of the 1912 Earthquake are scarce because of the politic conflicts. Reached sources are generally in Ottoman and French language. It was reported that during the earthquake hot water strung up in Abdimi, which was an old seashore village. Sulphur smell came from the sea, which may also be interpreted as the gas created by decomposition of organic matter. In Çanakkale, most of the coastal area of Strait of Çanakkale was inundated by sea waves. In Yeşilköy, an eyewitness reported that the sea receded and anchored ships were aground with the recede of the sea after the earthquake. A rowing-boat and a fishery boat displaced as a result of the return of the sea and caused the rowing-boat to lift up to a height of 2.7 m. A high water occurred as the result of the earthquake and destroyed the Hidiv Pasha's yatch named 'Mahrussa' anchored off Paşabahçe (Altınok *et al.*, 2003). Ambraseys and Finkel (1987, 1991) and Mihailovich (1927) reported small sea waves that suggest a possible submarine extension of the rupture along the shores of the Sea of Marmara at the time of the 1912 event.

According to Armijo (2005), who used multibeam bathymetric and high resolution seismic reflection data, the 1912 Ganos Earthquake has probably ruptured from the Gulf of Saros to the Central Basin in Marmara and the rupture had total length of about 140 km, not 50 km as previously thought by Ambraseys and Finkel (1987).

A recent study of Aksoy *et al*., (2010) based on field investigations and analyzing of original seismograms indicated that recent field investigations of the 1912 a maximum 5.5 of right lateral-slip on land. According to this study, the focal mechanism from P wave arrivals from original seismograms and a field-based N68°E fault strike indicate a strike-slip mechanism provided a strike-slip fault mechanism. The study showed a significant

portion of the earthquake rupture is offshore and 30 km rupture length for the second shock, the total earthquake fault rupture length sums to 150 ± 30 km.

The damage and size of the aftershock the 13 September 1912 Earthquake suggest that this event is most likely the southwest continuation of the 9 August ruptures rather than a large aftershock (Aksoy *et al*., 2010). The epicenter 40.7 N-27.E and the magnitude Ms=6.8 were reported for this shock by Ambraseys and Jackson (2000) estimated. They estimated the seismic moment as 2.19×10^{19} Nm and suggested a 37-km-long coseismic rupture.

2.2. 4 January 1935, Erdek-Marmara Island Earthquake

This earthquake occurred at 14:41:29, 40.64 N, 27.51 E, h=0–60 km (SEAP), Ms=6.4, Io=IX (MSK) (Ambraseys, 1988). The earthquake was followed by 15:18:57 (Ms=4.6), 15:19:24 (Ms=4.5) and 16:20:05 (Ms=6.3) earthquakes and continued until 7 March 1935. Three earthquakes hit Marmara Islands and Erdek. On the Marmara Island Gündoğdu, Çınarlı and Asmalı villages were totaly destroyed and the centre of the Island was partialy destroyed by the event. Yiğitler Village was destroyed completely and 128 houses demolished in Türkeli Village on Avşar Island. On Paşalimanı Island, the earthquake also destroyed Poyraz and Harmanlı villages and also demolished the main Island and Balıklı Villages partialy. Some buildings in the Villages of Narlı, Ocaklar and İlhan ruined on Kapıdağ Peninsula. Fountains on Avşar and Marmara Island dried. The earthquake was also come with a loud sound. Causalities were low thanks to the day time occurance. 5 people died and 30 people hurt according to the records. The epicenter of the earthquake should be on a crack between the Kapıdağ Peninsula, Paşalimanı Island, Avşar Island and Marmara Island. Intense could be IX and the magnitude is between 6 and 9 (Pınar and Lahn, 1952). The maximum intensity of IX (MSK) was assigned by Ambraseys (1988).

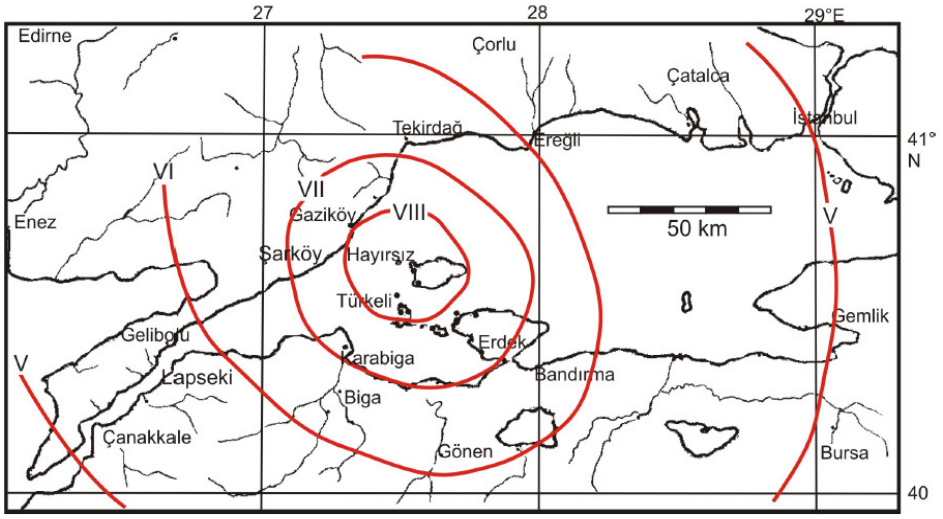

Figure 2.6. The isoseismal map of the 4 January 1935 Earthquake (Ambraseys, 1988)

Mr. Kevork reported to Kurun newspaper publised in 10 January 1935. During this earthquake, he was able to see from 100 m above the sea level the rising sea waves which were normally invisible. His words may indicate that a tsunami occured after this event. Mr Kevork stated that;

"We were constructing a big foghorn for the lifeboat service at Hayırsız Island, right across Marmara Island. We had already placed the concrete foundations on top of the marble grounding and had almost completed the building up to its roof. We were to finish it up in a day or two. On Friday 14:45 (local time), the first tremors came. We were in the building then. The tremors lasted for 2 minutes. 15 minutes later a second, half an hour later, a third set of tremors followed. When the third came, I was outside, trying to gauge the damage done to the building. Suddenly I saw the ground move to and fro. I immediately sat down. Although from where I was sitting, normally the sea is not visible, somehow, I don't know how, I was able to see the sea. It was during this last tremor, when the whole building just collapsed" (Altınok and Alpar, 2006).

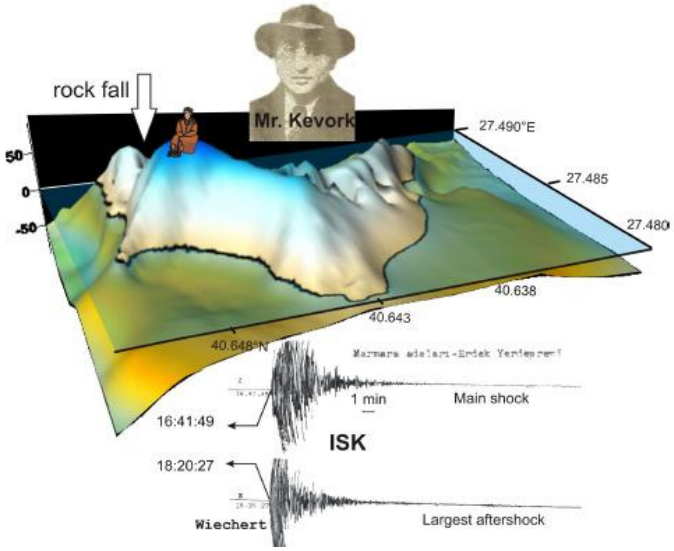

Figure 2.7. Morphological and bathymetric demonstration of position of eyewitness Mr. Kevork during the 1935 Earthquake (Altınok and Alpar, 2003). The data based upon the ISK (Istanbul, Kandilli) Wiechert seismograms are also seen

The epicentral locations from various historical earthquake studies are available for the 4 January 1935 Earthquake. Most of these studies were based on the macroseismic investigations. Table 2.1 shows the epicentral locations from some articles related to the 4 January 1935 Earthquake.

Table 2.1. Epicenter locations for 4 January 1935 14:41 (GMT) Earthquake from different sources

No	**Date**	**Time**	**Latitude**	**Longitude**	**Depth**	**Ms**	**Reference**
1	1935.01.04	14:41	40.64 N	27.51 E		6.4	Ambraseys (1988)
2	1935.01.04	14:41	40.50 N	27.60 E		6.4	Ambraseys and Jackson (2000)
3	1935.01.04	14:41	40.0 N	27.5 E			ISS Bulletin
4	1935.01.04	14:41	40.40 N	27.49E	30	6.4	Kalafat *et al.*, (2007)

5	1935.01.04	16:20	40.55 N	27.75 E		6.3	Ambraseys and Jackson (2000)
6	1935.01.04	1620	40.0 N	27.5 E			ISS Bulletin
7	1935.01.04	1620	40.30N	27.45E	20	6.3	Kalafat *et al*., (2007)

Nalbant *et al*., (1998) modelled these two earthquakes as resulted from one rupture to determine Coloumb stress change after this shock. They chose an appropriate focal mechanism value for these shocks related isoseismal map of Ambraseys (1988), which indicates the location of this event near to the east-west, north dipping, normal fault system forming the southern edge of the Sea of Marmara. From this point of wiev, they considered the focal mechanism for this shocks as 100/40/-90, normal faulting. They modeled proposed a dip of 45° fault length of 20 km, slip 0.85 m considering the near active faults in morphology. The magnitude and seismic moment were also reported as Mw=6.3 and Mo=3.467×10^{18} Nm, respectively, in EMSC catalog moment tensor catalog prepared by Vanucci and Gasperini (2003). In this catalog, the fault solution for this event is also given as 100/40/-90, as Nalbant *et al*., (1988). However, in this catalog, the source of this information could not be found.

2.3. 18 September 1963, Çınarcık Earthquake

The earthquake, M=6.3, occured in the sea and was felt in Çınarcık and Yalova Area. It was observed that the earthquake caused boiling in the sea. In addition, the seashells were noticed on the coastline of the Mudanya Bay in the east-west direction (Özçiçek, 1996). Kuran ve Yalçıner (1993) stated that the sea waves reached about 1m height along the shore in some region, which was the result of tsunami. Figure 2.10 shows the isoseismal map drawn by Özçiçek (1996-1967) for the 1963 Earthquake. Intensity evaluations are according to the MS Scale. It is also seen a focal mechanism solution for this earthquake by McKenzie (1972).

Ergin *et al*., (1967) reported that 4 buildings were destroyed and 2 buildings were damaged. The damage was observed in Çınarcık mostly. However, there were also

damages in Yalova. In total, 7 buildings were demolished in Yalova and Çınarcık Regions. This earthquake caused 1 dead.

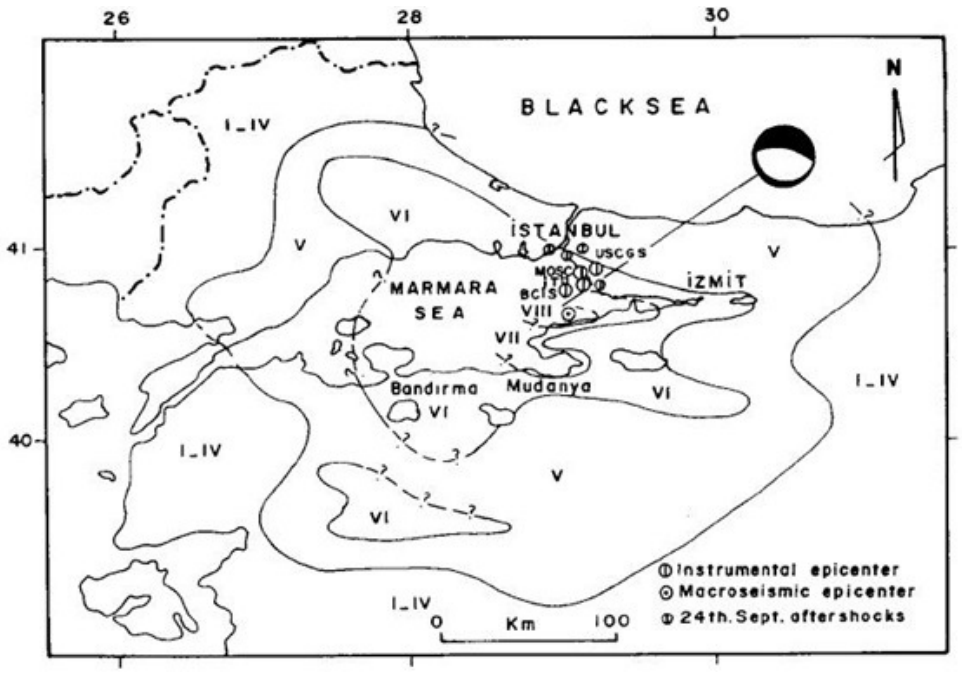

Figure 2.8. The isoseismal map of the 18 September 1963 Earthquake (Altınok and Ersoy, 1999)

There are some epicenter locations reported for the 1963 Earthquake. However, many of these are based on the macroseismic observations. Bulut and Aktar (2007) investigated the epicenter location of the 1963 event using ISC bulletin data that includes only the stations within a 12 ^{0} distance. They concluded that this event occurred on the Peninsula and not off-shore. In addition, two waveforms pairs including mainshocks and aftershocks, one was recorded at ISK (1999) and the other recorded at IST (1963) stations were also compared. Although two waveforms were recorded different type of recording systems, the similarities are observed in terms of the various crustal phase arrivals and also the overall shape of the envelope. In both examples, the first motion polarities shows similarity, which may be interpreted as the same fault mechanism.

Table 2.2. Epicenter locations for 18 September 1963 16:58 (GMT) Earthquake from different sources

No	Date	Time	Latitude	Longitude	Depth	Ms	Reference
1	1963.09.18	16:58	40.83 N	29.01 E			Özçiçek (1996)
2	1963.09.18	16:58	40.80 N	29.13 E			ISS Bulletin
3	1963.09.18	16:58	40.77N	29.12E	40	6.3	Kalafat *et al*., (2007)
4	1963.09.18	16:58	40.90 N	29.20 E			Taymaz *et al*., (1991)

Taymaz *et al*., (1991) determined fault characteristics of the 1963 event using P and SH waveforms and first motion polarities of P waves. The shapes of and amplitudes of long period P and SH waveforms with synthetic waveforms were compared. The algorithm they used is based on an inversion procedure minimizing the misfit between observed and synthetic waveforms. As a result of this study, they found almost pure normal slip on south and north dipping nodal planes with 304/56/-82 (Strike/Dip/Rake). The seismic moment was found as $Mo=9.6\times10^{17}$ Nm. The fault mechanism was also reported in another source prepared by Kalafat *et al*., (2009) that this earthquake had a fault mechanism solution of 152/40/-32 (Strike/Dip/Rake).

3. HISTORICAL RECORDING SYSTEMS

Over the last century, the seismological investigations have witnessed the evaluation of the ideas, principles and design of instrumentation, from seismoscops to broadband instruments. In spite of the fact that the concept behind the earthquake physics was not well understood at that time, the basic theory of the seismometer was known as a suspended mass (a pendulum) oscillates with the earthquakes. This basic idea inspired seismologists to develope the mechanical instruments. In 1875, an instrument was built by Flippo Cecchi. His invention, which can be considered as the first modern seismograph, had two horizontal pendulums, one vibrating in a north-south plane and the other vibrating in an east-west plane. The British scientists, Milne, Ewing and others, carried out their investigations and they were already recording earthquakes in Japan in 1888. Omori designed a seismograph with magnification of 10 and natural period 20 seconds, which was the inspiration for the invention of Bosh-Omori seismograph in 1889. At the beginning of 1900s, many observatories were established and all these developments, encouragements led several seismologists to invent more improved mechanical instruments such as Bosh-Omori and Wiechert seismographs. These seismographs were the most widespread and installed in many seismological observatories (Battllo, 2008). In order to measure ground motion more sensitively, electromagnetic instruments based on ideas on pendulum with a galvonemeter recorded ground motion on a photographic paper. These electromagnetic instruments were also widely used; however its introduction to many observatories over the world came true in the late of 1950's. Their highly sensitive electromagnetic sensors and the recording systems let behind the almost all mechanical instruments available up to that time (Battllo, 2000). To comprehend the old seismic instruments, it is important to learn basic properties and the mechanism of these recording systems. Here, the historical seismometers mostly used are presented.

3.1. Milne Horizontal Seismograph

John Milne designed an extensive use of a horizontal-pendulum seismograph in 1894. The schematic representation of his invention is shown in the Figure 3.1. The design

includes two crossed slits, one is fastened to the pier and the other is pivoted to the pendulum. The light L is reflected onto the photographic paper by mirror M through the intersection of two slits. When the pendulum moves with the oscillations by ground motion, the spots of light moves on the paper. The instrument of Milne had a period of about 15 seconds and a static magnification of 6. Figure 3.1 shows a schematic representation for the Milne Horizontal seismograph systems. T is a flexible wire holding up the boom. The weight W is pivoted on the boom. The lower illustration is a top view of the instrument. Figure 3.2 shows a seismogram recorded on 5 April 1901 by Milne Horizontal seismograph system (Dewey and Byerly, 1969).

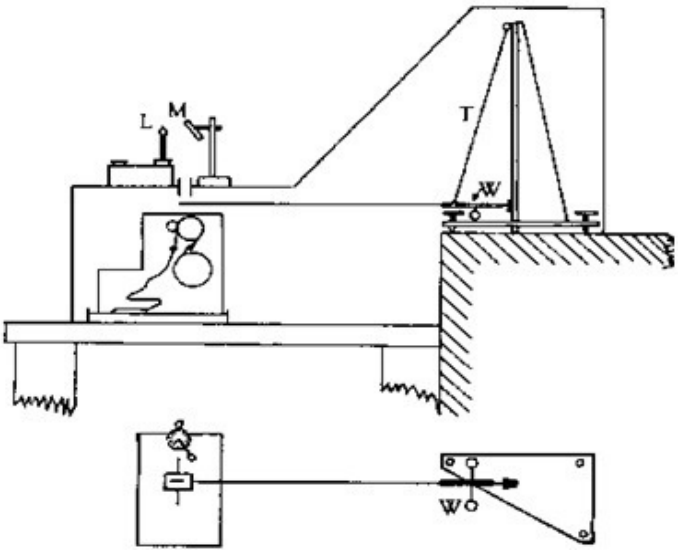

Figure 3.1. The schematic representation of the Milne seismograph, the upper illustration shows instrument from its side while the bottom shows from the top (Dewey and Byerly, 1969)

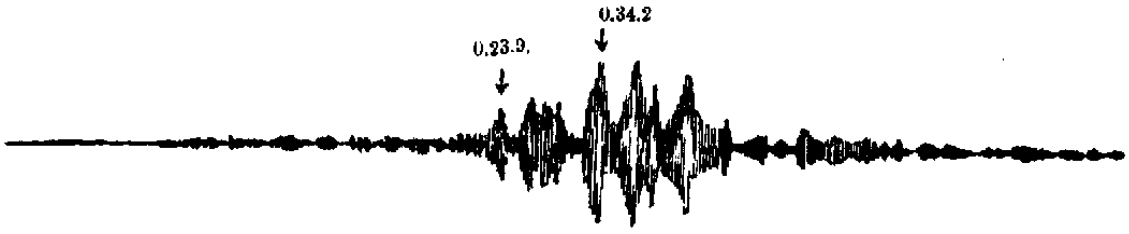

Figure 3.2. A record obtained from a Milne horizontal seismograph on April 5 1901 (Dewey and Byerly, 1969)

3.2. Wiechert Horizontal Seismograph

In 1898, E. Wiechert introduced a seismometer with a viscous damping pendulum and a photographic record. The first seismograph invented by Wiechert was a horizontal-pendulum instrument, decreasing the effects of pendulum oscillations with its damping. However, the mechanically-recording instrument was built in 1900 and the first description with improved version of his invention to the world was published in 1904. The Wiechert horizontal seismograph with the mass of 1000 kg had an inverted pendulum in stable equilibrium with the springs, free to oscillate horizontally. The horizontal motion of the mass with respect to the ground is resolved into its two perpendicular components. The mechanical lever system magnified the relative motion 200 times on the smoked paper used for registration. The Wiechert seismograms contained time marks made by lifting the two recording styluses in every minute. The damping for the pendulum was caused by this resistance of the air to the motion of the piston in a cylinder. A valve was used for adjusting this resistance of the air and provided the amount of air space between the piston and cylinder. Figure 3.3 shows the schematic drawing of the Wiechert pendulum. P denotes the plate attached to the frame of the instrument. A is the point where the motion of the mass relative to the frame is resolved. C, C' are the springs from where the restoring force applied to the mass M through rods *B, B′*.. H, H' are the damping cylinders. The inverted pendulum is pivoted at K point and the rotation of the pendulum at this point occurred in springs of a Cardan enabling the pendulum to move in any horizontal direction (Dewey and Byerly, 1969).

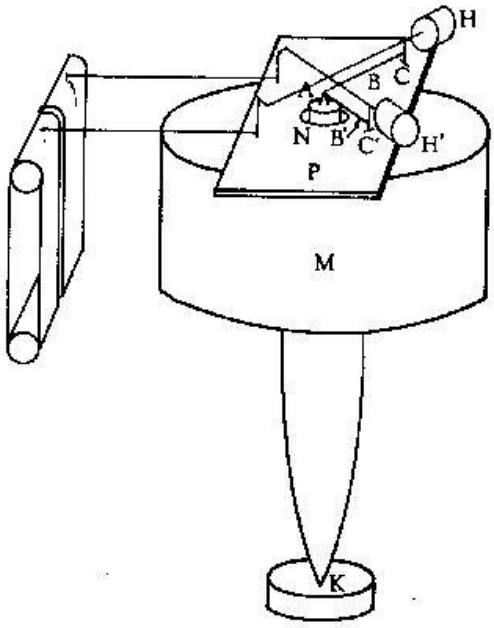

Figure 3.3. Schematic drawing of the Wiechert inverted pendulum seismograph of 1000 kg mass (Dewey and Byerly, 1969)

3.3. Mainka Seismograph

Another mechanical seismograph that found extended use was developed by Mainka, with a mass in the range 200-500 kg and a magnification of about 300. These seismographs were purely mechanical instruments with viscous damping, in which the amplification was produced by a system of levers and recorded on a drum with smoked paper together with time marks from a clock (Udias, 2000).

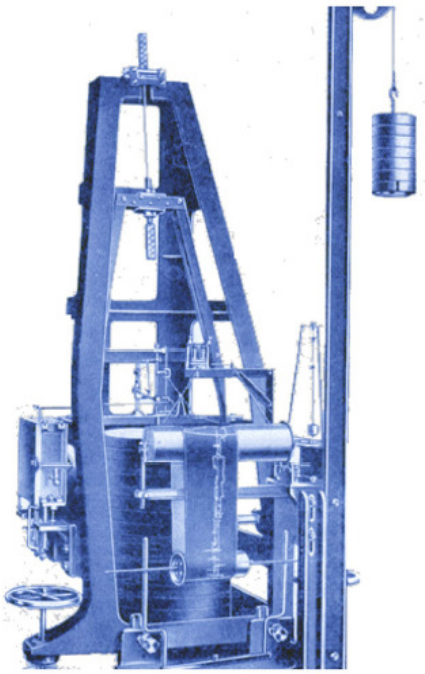

Figure 3.4. Mainka Seismograph System (http://eost.u-strasbg.fr)

3.4. Galitzin Seismograph

Galitzin developed the first electromagnetic seismograph in 1914. The seismometer that he invented consisted of a hinged horizontal or vertical pendulum that carried a moving coil in the field of a pair of permanent magnets. The coil was linked to a galvanometer depending on the circuit resistance for its damping. A copper vane oscillating in the field of a second pair of magnets provided the damping of the pendulum. Damping of both seismometer and the galvanometer were critically damped. The deflection of the galvanometer provided additional magnification. The period of the galvanometer and the seismometer had the same period about 12 seconds (Eaton, 1957). Figure 3.4 shows the photos of Galitzin seismograph systems from different museum. Left one is a Galitzin-Willip vertical seismograph from Saint Louis University. The right one is Vertical Galitzin Seismograph (10 kg mass and 24 sec. period) at Strasburg Seismological Museum.

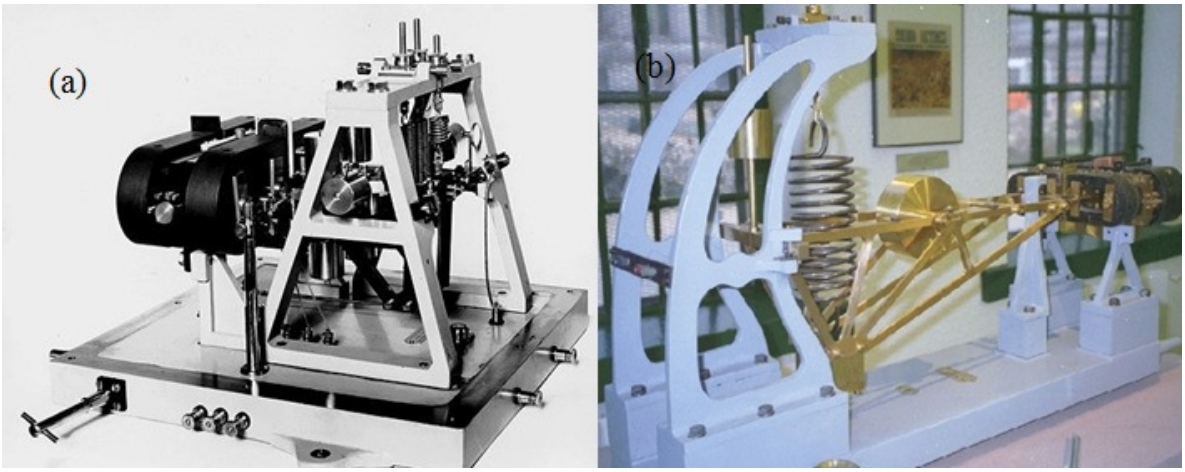

Figure 3.5. Galitzin seismograph system (a) is from the Saint Louis University (www.eas.slu.edu) (b) is from Strasburg Seismological Museum

4. DATA

4.1. Scanning Process of the Analog Records

The original records for the 9 August 1912, Şarköy-Mürefte (Ms=7.4), 04.01.1935 Erdek-Marmara Islands (Ms=6.4), 18.09.1963 Çınarcık (Ms=6.3) Earthquakes were mostly obtained from the archives of the European countries and also Kandilli Observatory within the scope of the SISMOS project. In addition to European observatories, original records from Japan were obtained for the 9 August 1912 earthquake. These analog records were scanned at a resolution of 1016 dpi with 256 grey levels for the raster images using very high-quality A0 scanners at Istituto Nazionale di Geofisica e Vulcanalogia (INGV) labaratories. As historical seismograms were recorded on black and white papers, they were obtained as grayscale images which are enough to protect all properties of the trace without any loss of resolution (Battllo, 2008). The raster image files with TIFF extension requires approximate 400-500 MB for a 120 cm× 40 cm sheet of paper of seismogram. This rigorous scanning process guarantees acquiring paper seismograms with their all information on digital media.

During the analysis of the analog records, I realized that earthquakes of my interest were not registered some paper records. In addition, it was not possible for some records to be digitized due to the poor quality of paper. Therefore, I selected suitable seismograms for the data-processing. Consequently, I have used 10 seismograms from 5 stations for 09.08.1912 (01:29:00) Şarköy-Mürefte Earthquake, 35 seismograms from 16 stations for 1935.01.04 14:41:29, 33 seismograms from 11 stations for 1935.01.04 16:20:05 Erdek Earthquake, 29 seismograms from 10 stations for 1963.09.18 16:58:08 Çınarcık Earthquake, Şarköy-Mürefte Earthquake. Table 4.1, Table 4.2 and Table 4.3 show the list of the records that analyzed earthquakes for the 1912, 1935 and 1963.

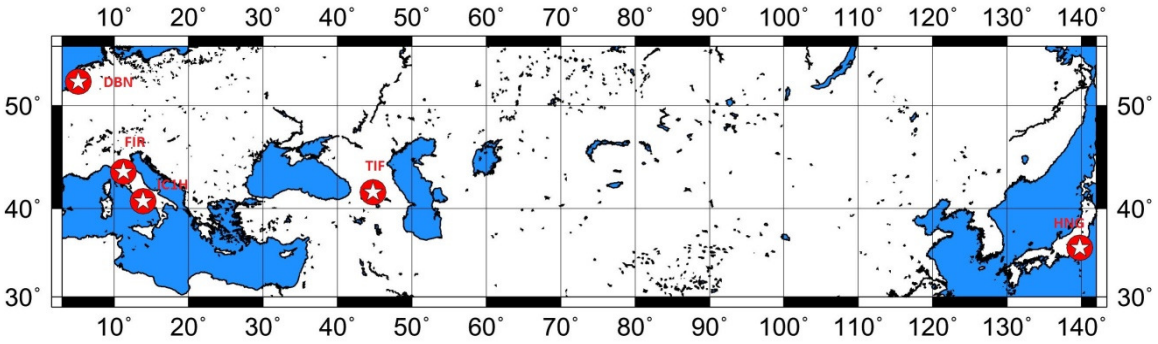

Figure 4.1. The station locations of obtained seismograms for 09.08.1912, Şarköy-Mürefte Earthquake

Table 4.1.The list of station, country, city and seismograph of available seismograms for 09.08.1912 -01:29:00, Şarköy-Mürefte Earthquake

No	Country	City	Station Code	Component	Seismograph
1	The Netherlands	De Bilt	DBN	NS	Wiechert
2	The Netherlands	De Bilt	DBN	EW	Wiechert
3	Italy	Firenze	FIR	NE	Omori
4	Italy	Firenze	FIR	NW	Omori
5	Italy	Isola D'ischia	IC1H	EW	Omori
6	Georgia	Tiblisi	TIF	EW	Reuber_Ehlert
7	Japan	Hongo	HNG	EW	Omori
8	Japan	Hongo	HNG	NS	Omori
9	Japan	Hongo	HNG	EW	Omori
10	Japan	Hongo	HNG	NS	Omori

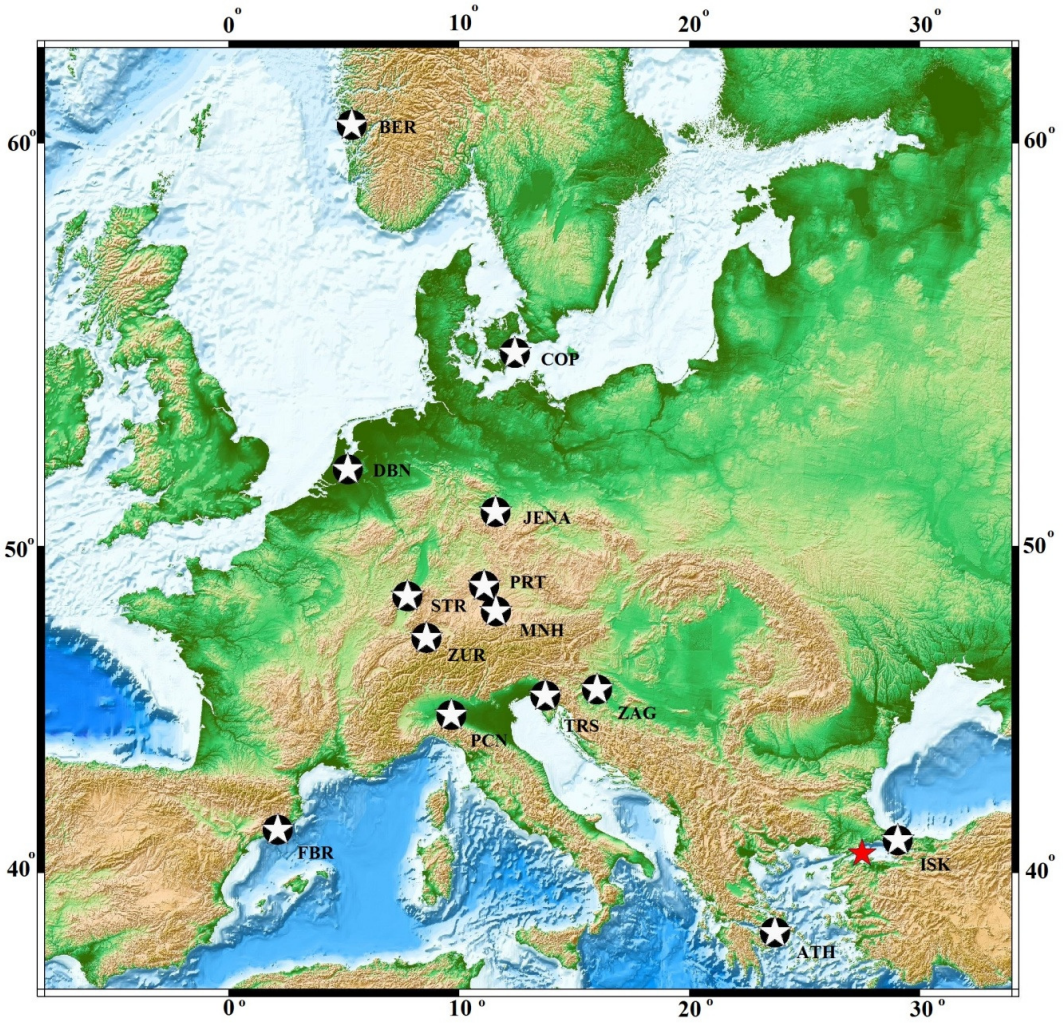

Figure 4.2. The station locations of obtained seismograms for 04.01.1935 14:41 and 16:20 Marmara Island-Erdek Earthquakes

Table 4.2. The list of station, country, city and seismograph of available seismograms for 1935.01.04 -14:41 and 16:20 Marmara Island-Erdek Earthquakes

No	Country	City	Station	Component	Seismograph
1	Greece	Athens	ATH	NS	Wiechert
2	Greece	Athens	ATH	EW	Wiechert
3	Norvey	Bergen	BER	EW	Wiechert
4	Portugal	Coimbra	COI	NS	Wiechert
5	Denmark	Copenhagenen	COP	EW	Wiechert

6	Denmark	Copenhagenen	COP	EW	Wood-Anderson
7	Denmark	Copenhagenen	COP	NS	Wiechert
8	Denmark	Copenhagenen	COP	EW	Milne Shawn
9	Denmark	Copenhagenen	COP	Z	Wiechert
10	The Netherlands	De Bilt	DBN	EW	Galitzin
11	The Netherlands	De Bilt	DBN	NS	Galitzin
12	The Netherlands	De Bilt	DBN	Z	Galitzin
13	Spain	Barcelona	FBR	EW	Mainka
14	Spain	Barcelona	FBR	NS	Mainka
15	Turkey	İstanbul	ISK	EW	Mainka
16	Germany	Jena	JEN	NS	Wiechert
17	Germany	Jena	JEN	EW	Wiechert
18	Germany	Jena	JEN	NS	Wiechert
19	Germany	Jena	JEN	EW	Wiechert
20	Germany	Jena	JEN	Z	Wiechert
21	Germany	Munich	MNH	EW	Wiechert
22	Germany	Munich	MNH	NS	Wiechert
23	Italy	Piacenza	PCN	EW	Wiechert
24	Italy	Piacenza	PCN	NS	Wiechert
25	Czech Republic	Prague	PRA	NS	Wiechert
26	Italy	Trieste	TRS	Z	Wiechert
27	Italy	Trieste	TRS	NE	Wiechert
28	Belgium	Uccle	UCC	EW	Galitzin
29	Switzerland	Zurich	ZUR	EW	Mainka
30	Switzerland	Zurich	ZUR	NS	Mainka
31	Croatia	Zagreb	ZAG	NE	Wiechert
32	Croatia	Zagreb	ZAG	NW	Wiechert
33	Croatia	Zagreb	ZAG	Z	Wiechert
34	France	Strasbourg	STR	E	Galitzin
35	Italy	Prato	PRT	N	T. Omori
36	France	Strasbourg	STR	Z	Galitzin

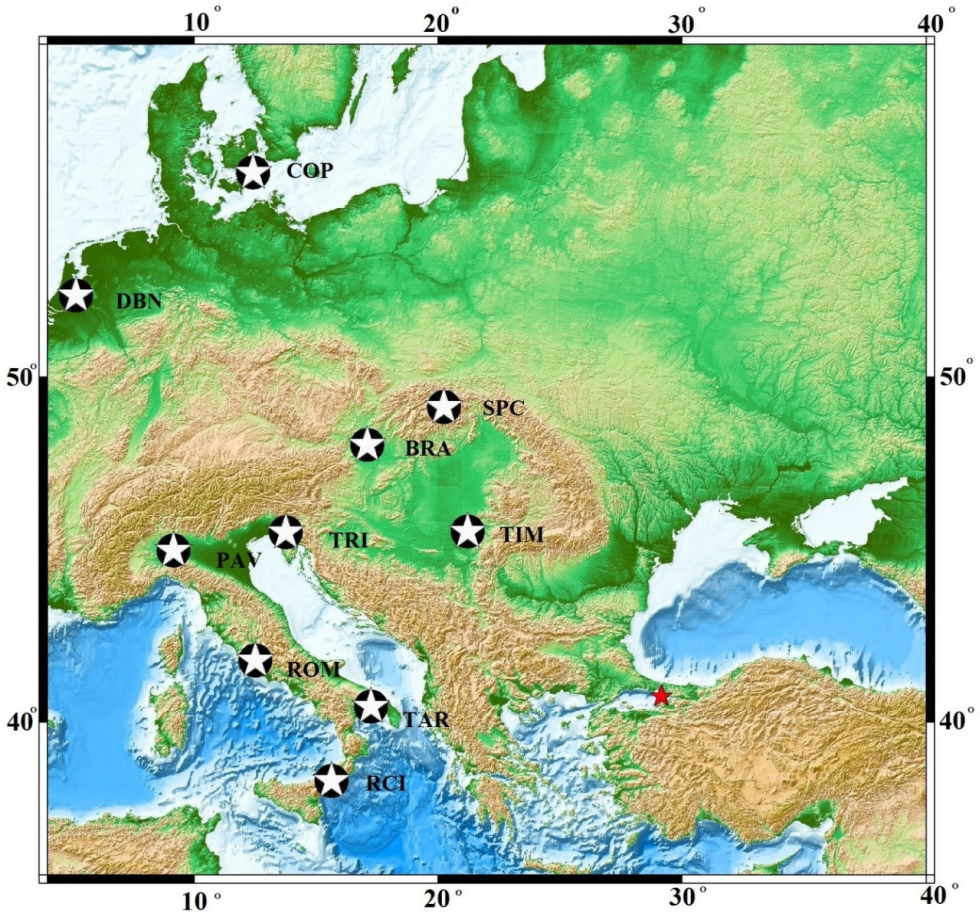

Figure 4.3. The station locations of obtained seismograms for 1963.09.18 -16:58, Çınarcık-Yalova Earthquake

Table 4.3. The list of station, country, city and seismograph of available seismograms for 1963.09.18 -16:58, Çınarcık-Yalova Earthquake

No	Country	City	Station	Component	Seismograph
1	Denmark	Copenhagenen	COP	EW	Wiechert
2	Denmark	Copenhagenen	COP	NS	Wiechert
3	Denmark	Copenhagenen	COP	NS	Galitzin
4	Denmark	Copenhagenen	COP	Z	Galitzin
5	Denmark	Copenhagenen	COP	Z	Benioff
6	Netherlands	De Bilt	DBN	EW	Galitzin
7	Netherlands	De Bilt	DBN	NS	Galitzin

8	Netherlands	De Bilt	DBN	Z	Galitzin
9	Italy	Pavia	PAV	EW	Wiechert
10	Italy	Pavia	PAV	NS	Wiechert
11	Italy	Pavia	PAV	Z	Wiechert
12	Italy	Pavia	PAV	Z	Galitzin_Pannoichia
13	Italy	Reggio	RCI	EW	Wiechert
14	Italy	Reggio	RCI	NS	Wiechert
15	Italy	Rome	ROM	EW	Wiechert
16	Italy	Rome	ROM	NS	Wiechert
17	Italy	Rome	ROM	Z	Wiechert
18	Italy	Rome	ROM	EW	Wiechert
19	Italy	Rome	ROM	NS	Wiechert
20	Italy	Taranto	TAR	NS	Horizontal
21	Romania	Timisoara	TIM	EW	Mainka
22	Romania	Timisoara	TIM	NS	Mainka
23	Italy	Trieste	TRI	EW	Ewing
24	Italy	Trieste	TRI	Z	Benioff
25	Slovakia	Bratislava	BRA	EW	Wiechert
26	Slovakia	Bratislava	BRA	NS	Wiechert
27	Slovakia	Bratislava	BRA	Z	Wiechert
28	Slovakia	Skalnete_Pleso	SPC	NS	Wiechert
29	Slovakia	Skalnete_Pleso	SPC	Z	Wiechert

5. DIGITIZATION OF THE ANALOG RECORDS

After obtaining scanned records with high resolution on digital media, the main objective is to convert seismic traces recorded on paper to a digital time series of seismic ground motion for the usage of present waveform analysis tool (Battllo, 2008). The seismic waveform recorded on the paper seismogram must be transformed in a format to use further modern seismic analysis (Batlló, 2008). This necessitates the digitization process, namely, obtaining the seismic traces a series of points. Earlier studies, in which advance technological tools are not available, digitized analog seismograms in the form of film or paper by enlarging the copies obtained with photographic techniques.

Today, many free types of software are available to perform this process. Using these programs, it is possible to pick the points that represent the seismic waveform. Many studies have carried out digitization process using these modern softwares. Most of them involve the manual picking of points. Among them, one of the most comprehensive one is TESEO produced by Pintore (2005). TESEO is the plug-in of powerful graphics software named GIMP which supports very high-resolution images as scanned historical seismograms. GIMP gives the opportunity to create piecewise cubic B´ezier curves to represent the seismic traces on historical records and save the image in xcf format which enables TESEO program to convert old seismograms with their all information to the format of modern seismic wave tool softwares. In addition, the original seismic records can be enhanced for a better vectorization process.

The softwares produced to perform vectorization, as TESEO, offer several methods to perform the process of vectorization; manual, automatic and semiauotomatic digitization.

The automatic digitization is problematic due to the interruptions on the trace lines, the variations of the contrast of the image (Batlló, 2008). The manual vectorization method is based on redrawing seismic traces on old record by using the mouse pointer. Although the process is simple, creating curves and splines on seismic traces point by point is highly time-consuming (Pintore *et al*., 2005). However, when the image quality is not good, this

method provides a more reliable and faster vectorization process than any semiautomatic vectorization procedures (Battllo, 2008).

5.1. The Most Common Problems During the Process of Digitising Historical Seismograms

Vectorization process is of considerable effort due to many problems that arise from quality of trace on the paper and the mechanism of traditional seismometers. Examples are pen slipping on the paper and little oscillations that are interpreted as noise on the trace because of instrumentation. Correct identification of the earthquake to be studied can also be troublesome, which necessitates to count very carefully time marks available on records. Yet, some of the historical records do not have well-marked time marks, therefore it is essential to obtain some bulletins for stations and regard delay times of the first motion polarities in relation to station distances (Batlló, 2008). Besides, the needle mechanism leads to curvatures of the traces. Inadequate contrast between recorded waveform and the background poses a serious problem during the digitization of the historical seismograms, which may be seen in the case of smoked paper is insufficiently burned (Batlló *et al*., 1997). It is also a problem to encounter with the seismograms with unknown components and station in the case of old records. These seismograms make impossible to carry out the analysis for the old earthquakes. In addition, the absence of the necessary information of these seismograms, they were the best examples for the difficulty of studying of old earthquakes since their data quality is very poor.

Another difficulty during digitization process is that some records have thick traces that make difficult to vectorize correctly the frequency path on record. This situation may cause missing of the true trace since it is difficult to distinguish the frequency paths. Figure 5.1 shows the seismic traces that include thick traces. As it can be seen from Figure 5.1, it is difficult to deal with this kind of seismogram.

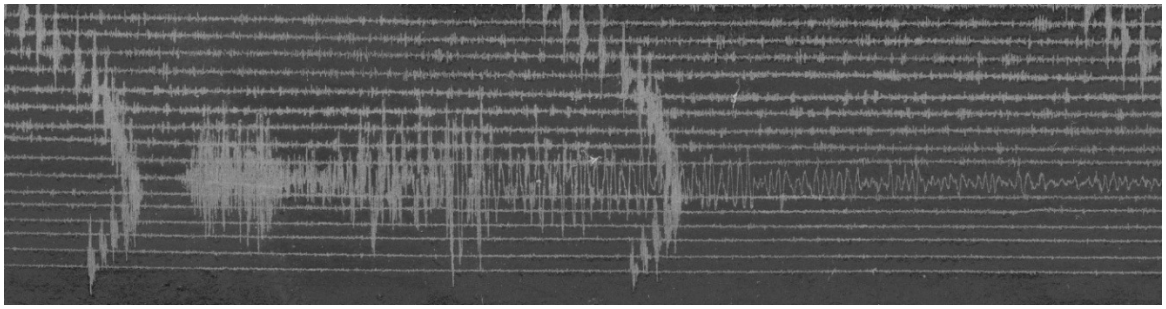

Figure 5.1. Example of a seismogram that includes thick traces, recorded at ISCH1 (Italy) station for the 1912 Earthquake

Since the historical records were exposed to many external factors, it is possible to encounter records includes erased parts of traces. It is also difficult to vectorize old seismograms when a part of trace is erased on the paper. If the missing part is small, interpolation methods can be utilized, however, they do not provide a reliable basis when large parts are missing from the records.

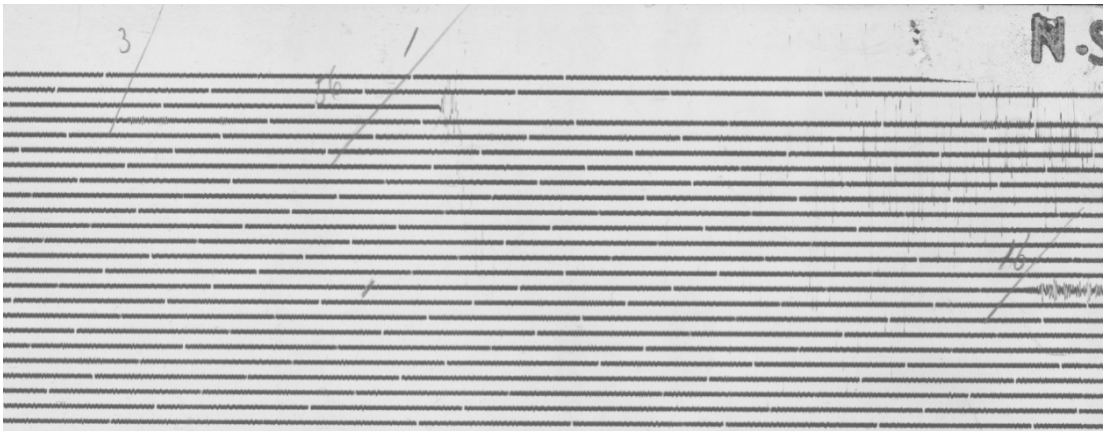

Figure 5.2. Example of a seismogram with a big erases part, recorded at KAS (Kastamonu, Turkey) station for the 1963 Earthquake

Baseline changes on the records may lead us to disrupt the waveform that is so important for vectorization. Figure 5.3 shows baseline changes on a historical record.

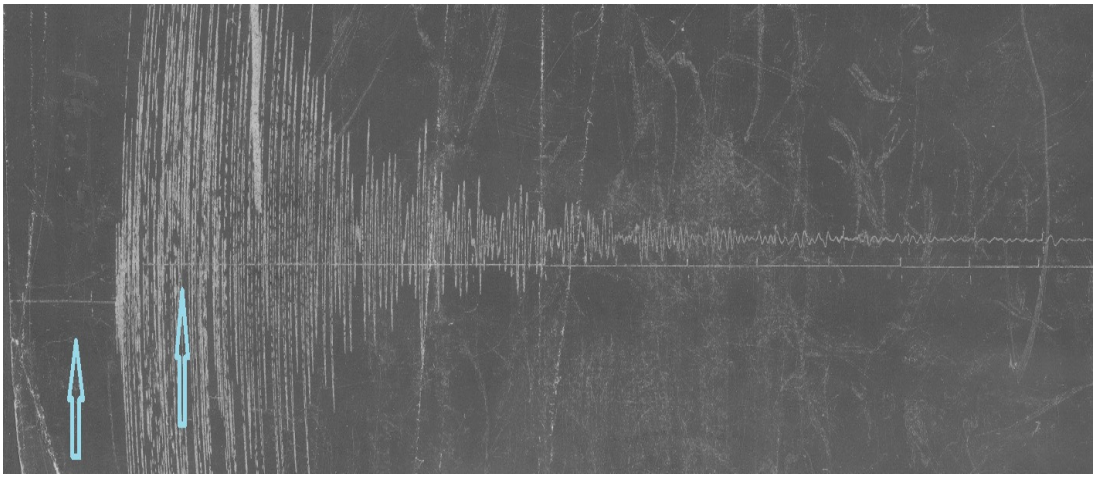

Figure 5.3. Example of a seismogram with baseline slip, recorded at ISK (Kandilli, Turkey) station for the 1935 Earthquake

Another problem with the historical records is the traces in mesh on the records, which is an outcome of drum recording mechanism. Digitization of these kinds of records entails considerable effort and too much time.

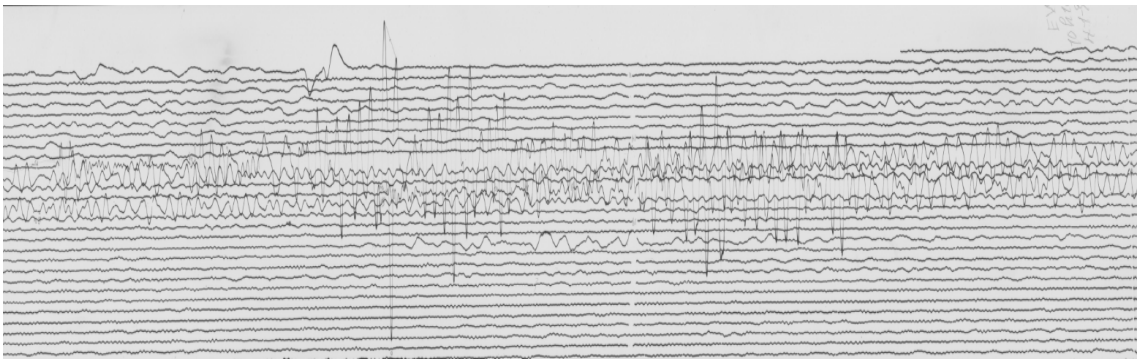

Figure 5.4. Example of a seismogram with traces in mesh, recorded at UCC (Uccle, Belgium) station for the 1935 Earthquake

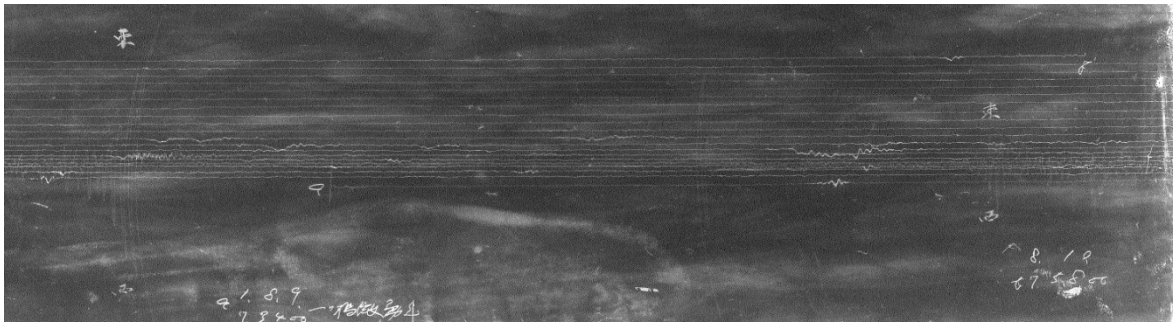

Figure 5.5. Example of a troublesome seismogram for vectorization, recorded at HNG (Hongo, Japan) station for the 1935 Earthquake

Although dealing with the troubles related to the paper quality seems difficult and time-consuming, further problems arise after vectorization when trying to analyze obtained digital data with available seismic wave tools. For this reason, some procedures must be followed.

5.2. Analysis After Trace Vectorization

After obtaining a series of points of seismic ground motion, the problems arise as a result of the geometrical, timing and instrument factors of the old historical records. Therefore, it is essential to perform correction processes dealing with these kinds of problems (Batlló, 2008).

5.2.1. Curvature and Skew Corrections of Seismic Traces

In an early mechanical instrument system, the pen records the seismic traces while the drum moves around on the rotating axis at a constant speed (Cadek, 1987). This mechanism of needle mounted on a finite-length pivoting arm of mechanical seismometer results in the curvatures of seismic traces on the record. In such a case, the abscissa of the seismogram cannot be obtained as linear function of time (Grabrovec and Alegretti, 1994). This results in obtaining a seismic data with wrong amplitude and time. Such a problem requires user to perform a curvature correction process (Pintore and Quintiliani, 2007).

Cadek (1987) gave a procedure for the correction of the geometrically distorted seismic traces and transforming the coordinates into time and amplitude. The solution that he found is given in the Equation 5.1.

$$t = \frac{60}{d}.\left(x - arcsin\frac{2r^2+y^2-2by}{2ar} + r.arcsin\frac{r}{a}\right) \quad (5.1)$$

In order to use this equation, it is necessary to know the radius of the cylinder, the length of the recording arm, and the distance from the axis of the rotating arm to the axis of the cylinder. The origin of the distortion is shown in Figure 5.6(a). Figure 5.6 shows a schematic representation of mechanism of the old recording system and important parameters for the process of curvature correction. R indicates the length of the writing arm from its rotating axis to the tip of the needle, r is the radius of the drive cylinder bearing the smoked paper, a is the distance from the rotating arm axis to the driving cylinder axis, b is the shift of the arm axis, d is minute length (paper speed) on the original record in millimetres (Pintore and Quintiliani, 2007).

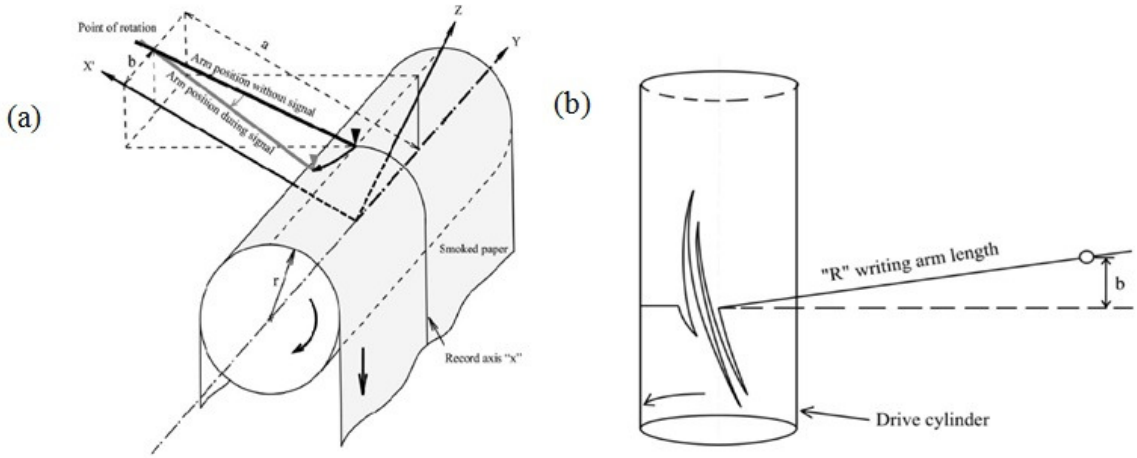

Figure 5.6. Schematic representation of mechanism of the old recording system (a) shows the important parameters for the process of curvature correction (b) shows the arm length and shift on a paper caused by mechanical instrument (Pintore and Quintiliani, 2007)

Crouse and Matuschka (1983), who investigated the SEMOC methodology (Strong Earthquake Motion Centre, Japan) applied to SMAC accelerograms, stated that in addition to curvature appearance, the mechanism of early recording systems leads to a slanted appearance in the seismograms. The problem of record skew arises if the rest position of the pen arm is initially offset such that it is not parallel to the direction of movement of the recording paper. Record skew correction, also known detrending of the zero-line, is necessary. The amount of pen offset can be found directly on the seismogram as long as recording paper is still in the seismometer. However, determination of skew is highly complicated once the paper has been removed. The correction procedure applied by them was a trial and error method. Crouse and Matuschka (1983) derived criteria that specify the upward motion of the needle is equal to the downward one. Namely, the uptime and down time for each record can be defined as the total times of the negative and positive movements of the pen.

According to Samardjieva *et al*., (1998), the mechanism of traditional seismograph leads to circular arcs instead of deflections perpendicular to the time axis. As it can be seen from Figure 5.7, both the shape and the size of the distortions depend on the length (R) of the pen arm and on the value of the deflection angle (β) formed with the time axis (X axis). In the figure, Xdig and Ydig indicate the coordinates of the digitized distorted seismic signal. In order to overcome the erroneous results of this distorted signal, it is necessary to rotate the digitized coordinates (Xdig, Ydig) to a series of points of seismic waveform with Xcor and Ycor coordinates of corrected seismic signal. Here, record is needed to be obtained with the coordinates (Xrig, Yrig) which are perpendicular to horizontal axis. In order to acquire a record with coordinates (Xrig, Yrig), the Equations 5.2 and 5.3 can be applied;

$$X_{rig} = X_{dig} + Y_{dig} \tan \beta \tag{5.2}$$

$$Y_{rig} = \frac{Y_{dig}}{\cos \beta} \tag{5.3}$$

In the Equation 5.3, β, is the deflection angle and can be measured from the geometry of the seismogram. The next step is to calculate the correct positions of each point A^1 (X_{cor}, Y_{cor}) from the corresponding digitized point A (X_{rig}, Y_{rig}).

$$X_{cor} = X_{rig} - R(1 - \cos\alpha) \tag{5.4}$$

$$Y_{cor} = R\alpha \tag{5.5}$$

$$\alpha = arc\sin\frac{Y_{rig}}{R} \tag{5.6}$$

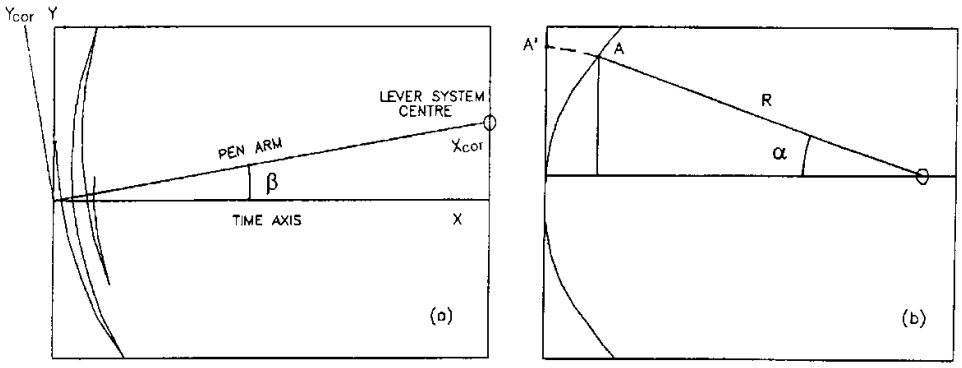

Figure 5.7. Simple demonstration of mechanical recording system (a) shows the geometry to correct small deviations in the position of the lever centre of the seismograph system (b) shows the geometry to remove distortion of circular arcs from seismic traces (Samardjieva *et al*., 1998)

As mentioned, it is possible to fix the curvature and skew problem on seismic traces, if the length of the arm and its angle from the vector of angular velocity on the drum are known (Battllo, 2008). Determining the skew value is one of the most difficult processes that necessitated measuring directly on the original seismogram (Schlupp, 1996). It is uncommon to obtain skew in photographic records because of the misalignments between the recording drum and the light projection system. Another difficulty is that removing the curvature from traces is a highly time-consuming process due to the fact that arm length

values of the early seismometers are not known. In the case of the old seismograms, arm length of the mechanical old type seismographs may not be found in the available documents related to recording instruments (Battllo, 2008).

Inoue and Matsumoto (1988) estimated the arm length from the original record of strong ground motion. Figure 5.8 shows a method for measuring arm length from the original seismogram. R is the arm length, C is the position of the pivot of the arm. They chose a portion where the amplitude of time history is very large. They put three points, *P1, P2* and *P3* on the iso-time circle which passes through the peak or through of the large amplitude. The perpendicular bisectors of the line $\overline{P_1.P_2}$ and the line $\overline{P_2.P_3}$ were drawn, and the coordinates of the point C which is the intersection of the two bisectors was calculated. That point indicates the position of the pivot arm. The length of the line segment $\overline{P_1.C}(\overline{P_2.C} = \overline{P_3.C})$ was measured. That is the arm length of the seismograph.

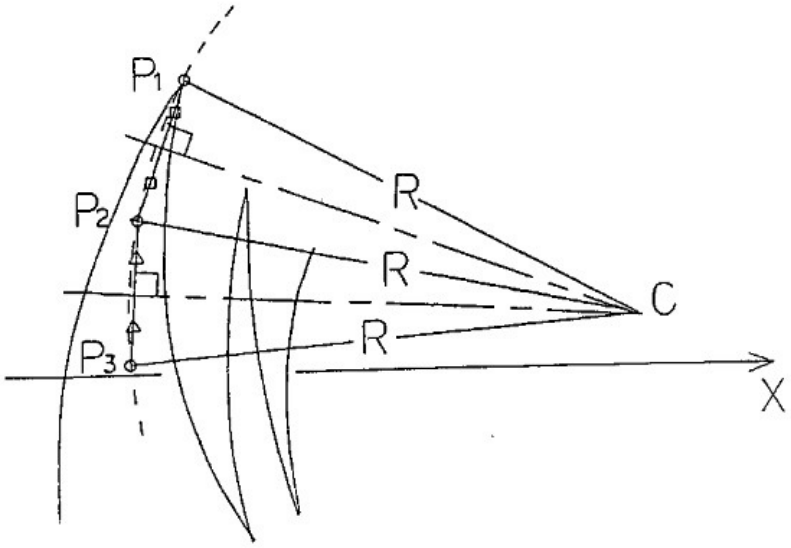

Figure 5.8. Method for estimating arm length from the original seismogram (Inoue and Matsumoto, 1988)

Schulup and Cisternas (2007) evaulated the procedures for trace correction given by Cadek (1987) and Crouse and Matuschka (1983). Based on their criterion, they deduced different ‘b’ values for each record with an uncertainty going from ±1 to±3 mm. Since the shift ‘b’ of the axis of the arm with respect to the base line must be determined directly

from records and the distortions due to the shift ‘b’ are combined with those due to the geometry of the recording system they corrected the seismograms for all the distortions for different trial values of ‘b’, and chose the best ‘b’ value with lowest error.

Batlló *et al*., (2010) also used the method as described by Samardjieva *et al*., (1998). It was observed that problems appeared during the curvature correction of the seismic traces were not the result of the mistakes of the manual digitization but low resolution of the image due to the absolute dimension of the whole seismograms. Batlló *et al*., (2010) compared the original seismograms with the digital images; traces of 0.1 mm width in images digitized at 1016 dpi have a minimum width of 4 pixels, each pixel being 0.025 mmx0.025 mm in real size. They realized that taking a look at the real dimension of the recorded signal an oscillation with frequency of 1 is just 0.25 mm in the seismogram image. In this case, the smallest oscillation of the axis of the recording arm introduces lateral perturbations of the recorded traces that are greater than its resolution, which leads a serious problem for maintaining the order of acquired points once corrected. They observed that moving the position of two consecutive digitized points within the width of a pixel alters its final order after corrections have been applied.

5.2.2. Timing Corrections

Time marks are the key to control paper speed and transform distance (mm) to time (sec) on seismic record. The correction of time marks is a considerable problem that necessitates special effort while studying old seismogram. Almost all historical records have time marks. Batlló (2008) observed time marks in the record in three ways.

1. Time marks that do not introduced as distortion on the records in the mechanism of with an additional stylus, external to the recording stylus. Absolute timing problem arise from the parallax.

2. Time marks can be seen directly on the records. The records are interrupted with the shaking of electromagnet.

3. The record line is displaced by the electromagnet. The displaced fragment should be integrated to the unaltered trace.

Between time marks, fluctuation of the recording drum angular velocity may distort the apparent frequency of the frequency contents of the record. Since the real instantaneous velocity of the drum is not known, interpolation linearly between time mark is essential (Batlló, 2008).

It is a big challenge to measure the accurate time marks on the original seismogram since most of the old records usually do not include equal time intervals. For this reason, it is needed to find some solutions depending on the seismogram of interest. In order to avoid this problem, there is not a direct solution and each record requires different kinds of approximations (Batlló, 2008).

5.2.3. Instrument Response Correction

After dealing with troubles arising from the geometry of old-time seismic instruments, it is essential to figure out the behaviour of true ground motion. This requires deconvolution of seismic instrument response to the real ground displacement response. The transfer function of an old seismometer is specified by the free period of pendulum (To), damping constant (h) and the magnification (V) of the instrument for mechanical sensors. In case of the electromagnetic sensors, the free period of galvanometer is needed to calculate transfer function. The magnification drops rapidly, following a ω^{-2} slope for purely mechanical sensors, and a ω^{-3} slope for electromagnetic sensors above the free period of the instruments. Below the free period, nominal sensor sensitivity is nearly flat for purely mechanical sensors and drops proportional to ω for electromagnetic sensors. Near the free period, the response curve is conditioned by the damping of the pendulum motion. Some of the earliest instruments are essentially undamped except of friction effects, making a stable restitution of ground motion problematic (Batlló, 2008). The amplitude of the calculated transfer function in the frequency domain allows obtainment of the amplitude response curves of the seismogram (Batlló, 2000).

The ratio of trace amplitude to the displacement amplitude of the ground is called "magnification of a seismograph". Actual magnification of a seismograph is the product of dynamic magnification and the static magnification. The total magnification of the system is given by the product of both factors. The total response of the seismograph is given by the magnification curve in the frequency domain. The ground motion x(t) is obtained from the recorded signal z'(t), dividing its transform by the response of the instrument(Udias, 2000)

$$X_{(\omega)} = \frac{Z'_{(\omega)}}{V_{(\omega)}} \tag{5.7}$$

For the mechanical Wiechert seismograph the dynamic magnification as a function of period (T) can be estimated by three constants, To, h and Vo (Herak, 1998).

$$V_T = \frac{V_0}{\sqrt{\left(1-\frac{T^2}{T_0^2}\right)^2 + 4h^2\frac{T^2}{T_0^2}}} \tag{5.8}$$

where T is free period of pendulum, h is the damping constant and Vo is the magnification.

As for Galitzin electromagnetic seismometer, the system consists of an electro-magnetic seismograph which is combined with galvanometer. Considering the response of the galvanometer the response of the system in terms of poles and zeros can be given as below;

The response of the seismograph:

$$T_{s(S)} = s^3 \frac{S}{(s^2+2h_s\omega_s S+\omega_s^2)} \tag{5.9}$$

The response of the galvanometer:

$$T_{g(S)} = \frac{\gamma \omega g^2}{S^2 + 2h_g \omega_g S + \omega_g^2} \quad (5.10)$$

Total response:

$$T_{tot(S)} = T_{s(S)}.T_{g(S)} \quad (5.11)$$

The gain of a Galitzin seismograph system can be found using the Equation 5.12 derived by Galitzin,

$$V_m = \frac{0{,}56.k.A.T_m}{\pi.I} \quad (5.12)$$

where k, the transfer factor, A, the distance between the recording paper and the galvanometer, I, reduced pendulum length.

T_m is the period where the response of the seismograph is maximum can be found using the Equation 5.13,

$$T_m = \frac{1}{\sqrt{3}} T_s \quad (5.13)$$

Ts and Tg values are periods of the pendulum and the galvanometer, respectively. They are equal to each other due to fact that damping constant of an electromagnetic seismograph is close to zero (Dost, Haak, 2002).

Kanomori (1988) evaluated the amplitude response curves of eight representative seismographs. The response curves of the mechanical seismographs were founded by using 3 constants pendulum period, T, damping ratio Є, (or damping constant ,h) and the static magnification ,Vo while the response of the Galitzin seismograph were found by using 4 constants. In Kanamori's study, damping constant of the seismometer and the galvanometer were assumed as 1.0 and the coupling constant was assumed as 0.02.

The peak magnification for Galitzin seismograph was calculated using the Equation 5.14;

$$V_m = \frac{0{,}32.k.A_1T}{\pi.I} \tag{5.14}$$

which is an agreement with the Equation 5.12 derived by Galitzin.

Table 5.1. Instrument constants used by Kanamori (1988) for mechanical instruments

Instrument	**Pendulum period, Ts(sec)**	**Damping ratio, Є**	**Damping constant, h**	**Static magnification, V**
Wiechert	5	4	0,404	80
Bosh-Omori 1	12	4	0,404	40
Bosh-Omori 2	30	5,3	0,469	10
Mainka	10	2	0,215	120
Wiechert 2	12,6	3,4	0,363	180
Milne Shawn	12	20	0,69	250

If the value damping ratio Є is known, damping constant can be calculated using the Equation 5.15

$$\ln(\varepsilon) = \frac{\pi h}{\sqrt{1-h^2}} \tag{5.15}$$

Table 5.2. Instrument constants used by Kanamori (1988) for electromagnetic instruments

Instrument	**Pendulum period (sec)**	**Galvanometer period (sec)**	**Maximum Gain, Vm**
Galitzin 1	12	12	580
Galitzin 2	25	25	310
WWSSN LP	15	100	1500

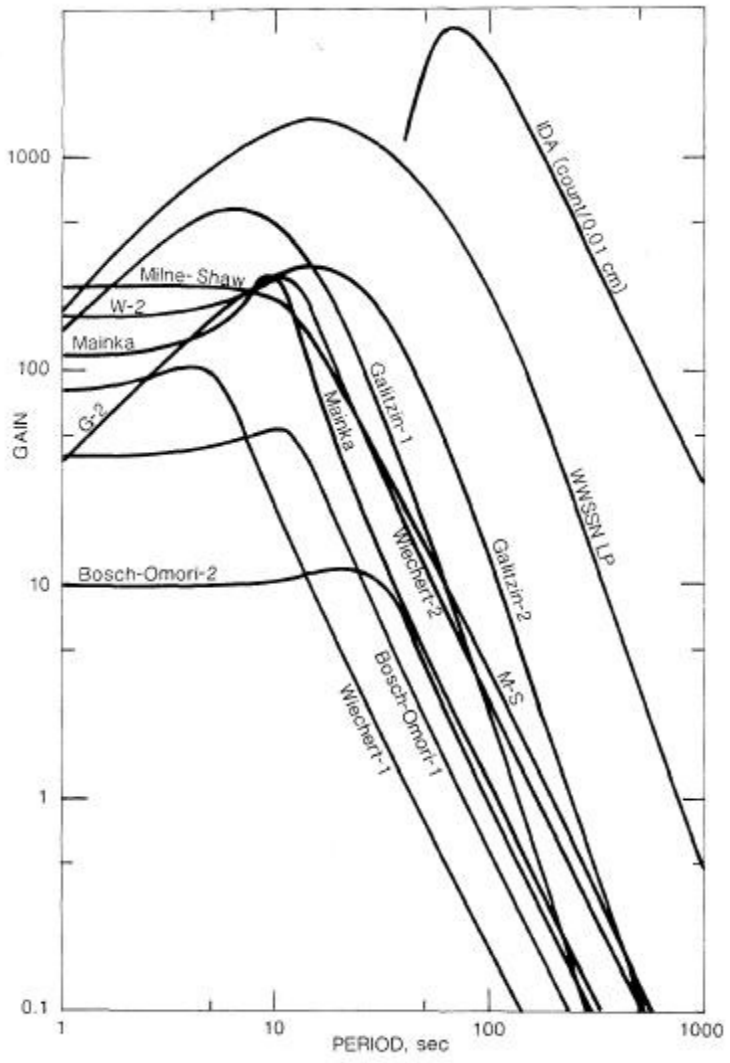

Figure 5.9. Amplitude response curves for eight representative traditional seismograph systems (Kanomori, 1988)

Figure 5.9 shows the calculated amplitudes curves for eight different seismometers. For comparison IDA (International Deployment of Accelerographs) and WWSSN (LP) seismographs response curves were also shown. The gain for IDA seismogram refers to the number of counts for ground displacement with the amplitude of 0.01 cm.

Mechanical seismographs are very limited by friction between their parts, and the dimensions of the pendulum and amplification and recording systems. To increase their magnification, their mass was increased in order to overcome friction, reaching several tons in some cases.

The Wiechert seismograph of 1000 kg had a maximum magnification of nearly 1000. Mainka device of 350 kg had magnification of about 400. Wood-Anderson device attained a magnification of 2800 (Udias, 2000). For mechanical seismograph, the inscription system presents a non negligible amount of dry friction, which is dissipative force and introduces a loss of signal energy (Batlló, 2008). In addition, sometimes transfer functions may not be exactly linear for some mechanical instruments since they are influenced by the interaction between their mass and frame especially for high frequencies (Herak *et al*., 1997).

5.3. Spectral Analysis

5.3.1. Seismic Source Model

The most common seismic source model used for the earthquake is the Brune's model which usually gives good agreement with observation from many different tectonic regions and for a large number of magnitudes. The source model of the log-log displacement spectra is shaped as in figure. At low frequencies, the spectrum is flat with a level of proportional to seismic moment (Mo) while at high frequencies, the spectral level decays linearly with a slope of -2. At the corner frequency (f=fo), the spectral amplitude is half of the amplitude of the flat level (Havskov and Ottemöller, 2008).

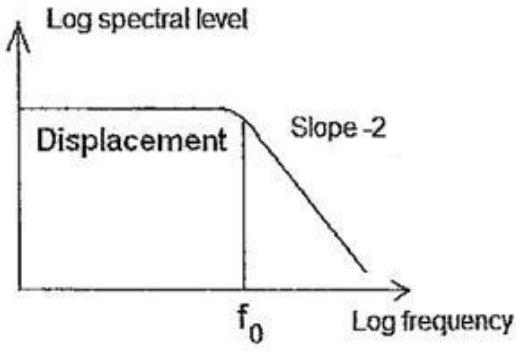

Figure 5.10. The source model of the log-log displacement spectra (Havskov, Ottemöller, 2008)

5.4. Applications for Estimating of Seismic Parameters from Displacement Spectra

In this section, the process followed step by step from digitization of the scanned seismograms to the obtainment of displacement spectra and estimations for seismic moment Mo, magnitude Mw, fault area R and stress drop Δσ, can be found in details. Figure 5.11 shows a flow diagram that summarizes the procedure from digitization to acquiring displacement spectra.

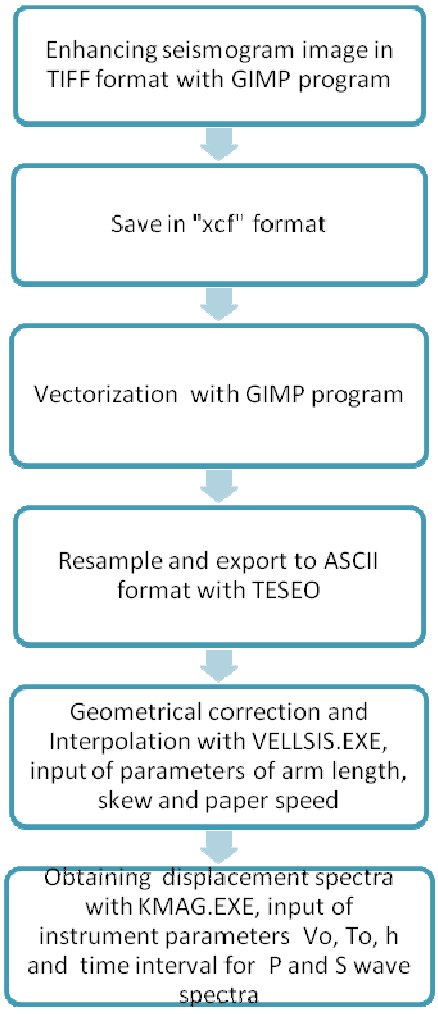

Figure 5.11. A simple flow diagram for the process of obtaining displacement spectra for the thesis

5.4.1. Applications for Vectorization of Scanned Images

The seismic waveforms on the images of the scanned seismograms were digitized using GIMP program. All seismic traces were vectorized point by point, which takes too much time.

In order to perform more accurate and faster vectorization process, some remarks are needed to take into consideration before vectorization. This enhancing process includes;

1. Cutting the image of the old seismogram to make its dimension smaller
2. Increasing the contrast or brightness to improve the image
3. Rotating or flipping the direction of the seismic traces on seismogram if necessary,
4. Measuring time marks visible on paper in mm.

After these enhancement operations, the image is saved with “xcf” extension.

Using “paths” tool in GIMP tool box, I performed vectorization process by drawing the seismic traces through the points. Once the desired shapes were achieved, the curves containing points of seismic waveform were resampled at 0.5 using TESEO and exported to ASCII format for further analysis.

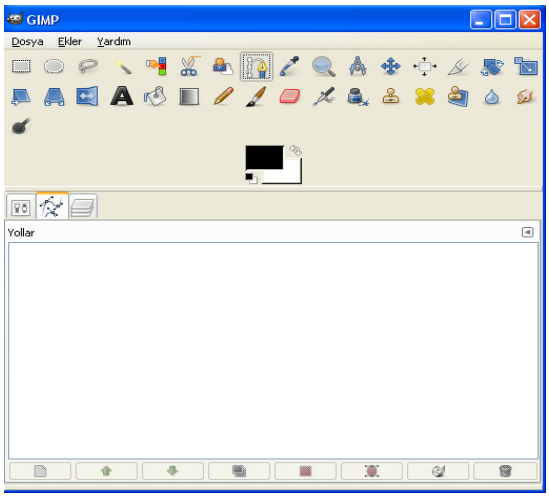

Figure 5.12. GIMP tool box

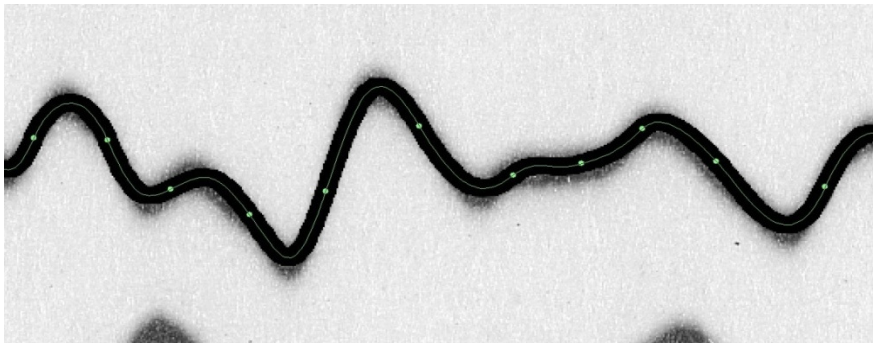

Figure 5.13. An example of seismic traces that are vectorized using manual vectorization process

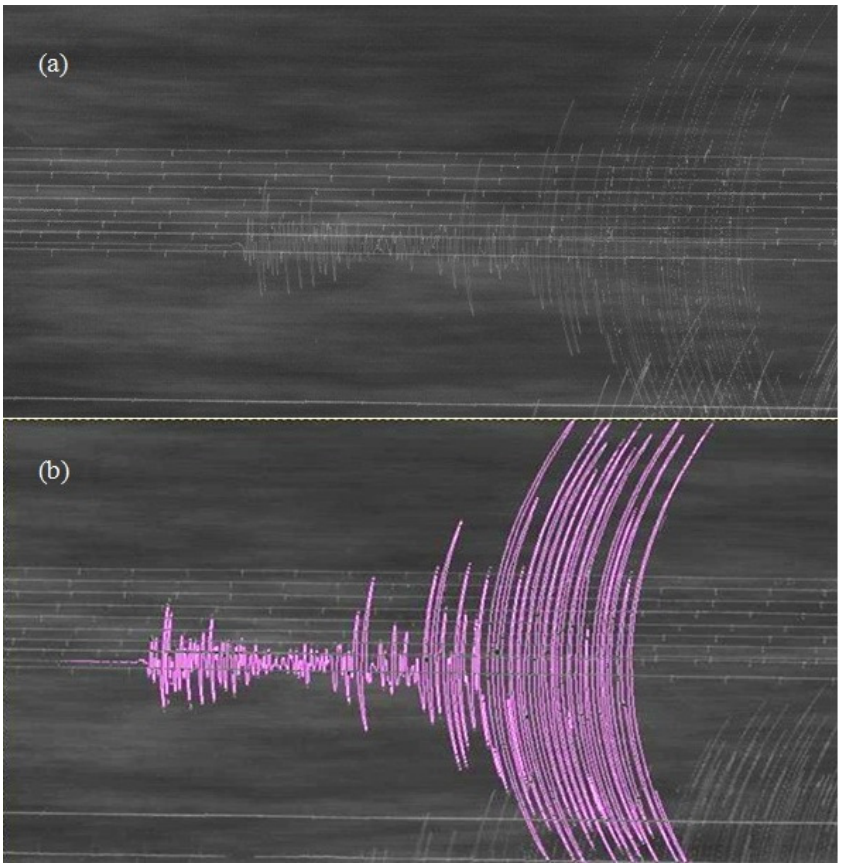

Figure 5.14. The original and vectorized waveforms on the record of DBN (The Netherlands) station for 09.08.1912-01:29 Ganos Earthquake (a) shows the original seismic traces on the original record (b) shows the vectorized seismic traces

5.4.2. Application of Curvature, Skew and Timing Corrections of Digitized Seismograms

The digitized seismograms which contain a series of points were obtained in ASCII using TESEO program. An input file is needed to carry out the process. This input file necessitates some parameters related to the arm length (mm), skew and the paper speed (mm/min) of the seismograph. Using VELLSIS3.EXE (Josep Batlló and Ramon Macia, 1999-2003) program the seismic traces were geometrically corrected and scaled to time and amplitude axis at constant intervals. In this study, 450 mm for arm length and -3.1 for skew values were used for the correction in the algorithm obtained. However, for some seismograms I could not obtain the proper waveforms with these values. Therefore, I found different values by producing new solutions. The distortions such as skew (arm inclination), pen curvature, and uneven paper speed on the old seismograms recorded by mechanical seismogram can be avoided using some corrections. The program applies the formula found in Grabrovec and Allegretti (1994) and Samardjieva *et al*., (1998) to implement the curvature correction. In addition, it performs smoothing of data by using linear interpolation to obtain an equal sampling interval of 0.1 second. The corrected and interpolated seismic traces were plotted using GNUPLOT software.

As arm length values are not reported for most instruments, this application takes too much time by trying different values to reach the best solutions.

In cases where the proper seismic traces could not be obtained after correction process, I tried different solutions to find especially for the arm length value of the recording systems of the seismograms. For example, I observed a big problem for the records of ISK (Kandilli) station. Since it has been possible for us to obtain the arm length values by measuring directly from instruments available at ISK (Kandilli) station, I used these values to remove circular arcs on original seismograms for the 1935 Earthquake. This effort considerably changed the seismic traces on the records from its first solutions with wrong arm length value. The arm length value of the Wiechert ISK (Kandilli) station seismometer was measured as 150 mm, while the value of the arm length of Mainka seismometer was measured as 450 mm. In spite of the fact that I obtained a more proper seismogram, there were still problems with the records of ISK station. Probably, this

situation arises from the traces that are very close to each other, which is also a considerable effort during vectorization process. Figure 5.15(a) shows the original seismogram recorded by Wiechert seismometer at ISK (Kandilli) station for 04.01.1934-14:41 Erdek-Marmara Island Earthquake. Figure 5.15 (b) shows digitized seismic traces before curvature correction, Figure 5.15 (c) shows digitized seismic traces after curvature correction.

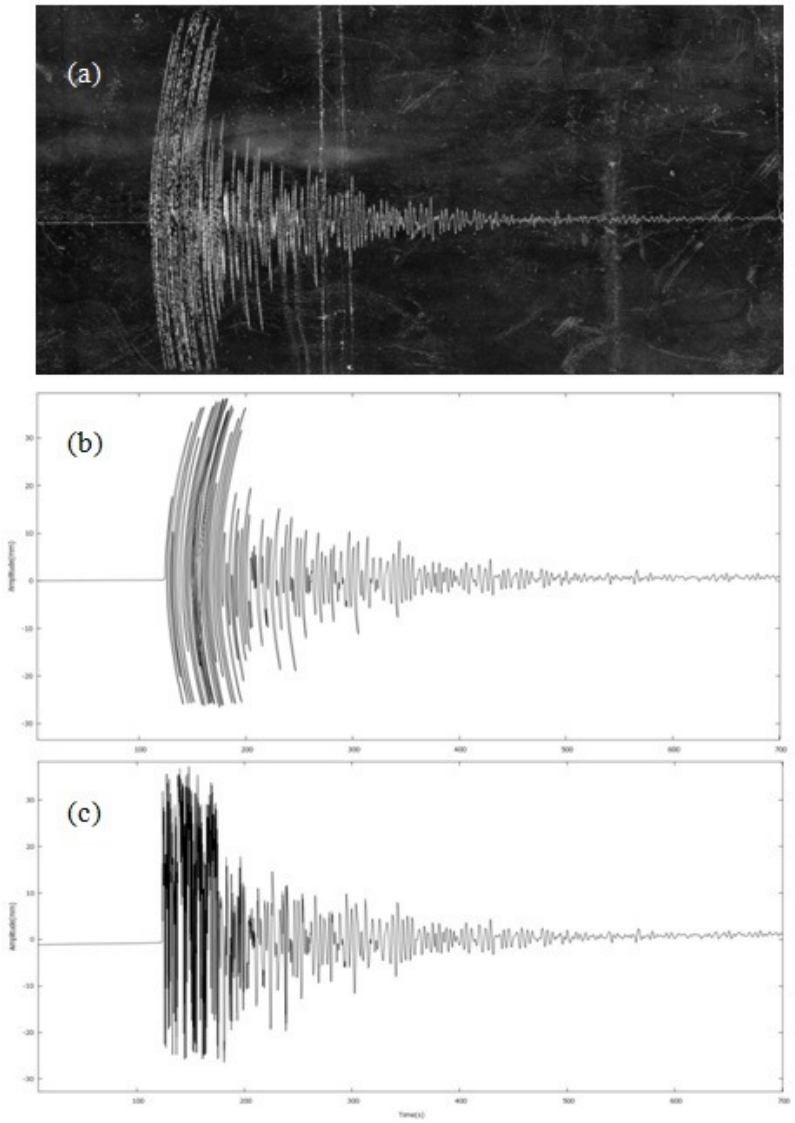

Figure 5.15. The comparison between the uncorrected and corrected seismic traces recorded at ISK (Kandilli, İstanbul) station (a) shows the original record from ISK (Turkey) station for the 1935 Earthquake, (b) shows seismic traces before curvature correction, (c) shows seismic traces after curvature correction

In cases where the arm length and skew values for the mechanical instruments are unknown, the correction was performed by trying different values for arm length and skew, which takes too much time. In fact, it is possible to determine arm length value from the original seismograms since the curvature of the seismic traces is related to the arm length of the mechanical instrument. For this purpose, method is followed by the selection of a portion where the amplitude is maximum on the seismogram and curvature shaped amplitude can be drawn as a circle. If the seismic trace is considered as a portion of a circle, the radius of this circle can give us the arm length of the seismometer of our interest. In this study, I used this method to estimate arm length value for some records. In the case of the seismogram recorded by Tromometrograph Omori instrument at PRT (Italy) station for the 1935 Earthquake, I had trouble to correct the arcs on the seismic traces. Therefore, I tried to measure the arm length values on the original seismogram. For this purpose, I draw two lines which are perpendicular to the circle of the amplitude trace. Where these two lines intersect gave us an approximate arm length value. The radius of the circle was measured as about 200 mm. In fact, after trying this value to remove the arcs on seismic traces, the best solution was obtained for this seismogram. Figure 5.16 shows curvature on the seismic traces caused by the arm of the seismograph for the record from PRT(Italy) station and the successfully corrected seismic traces overlapping with uncorrected seismic traces. Figure 5.17 shows the original seismogram from MNH(Germany), and its seismic traces before and after applying curvature corection. The red traces indicate the uncorrected traces while green traces show the corrected seismic traces.

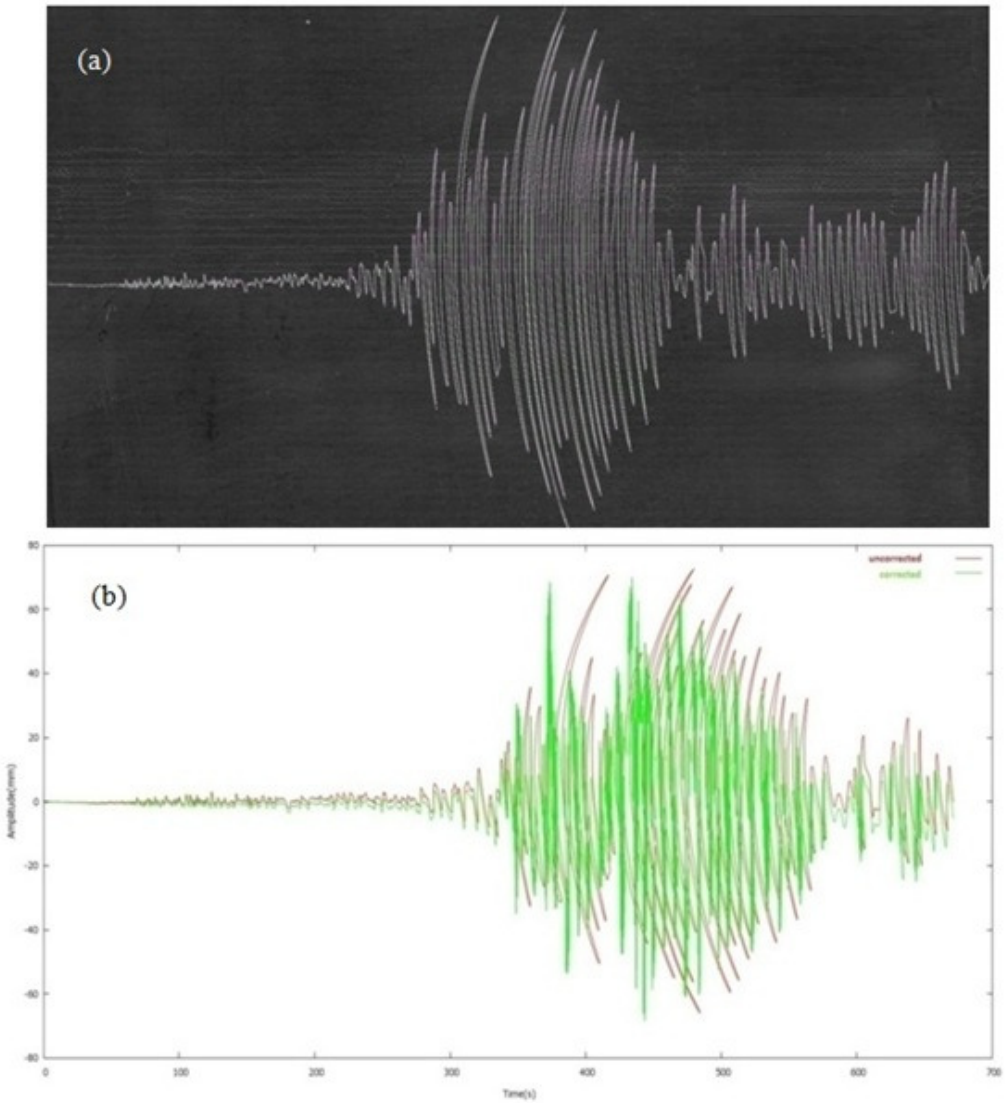

Figure 5.16. The comparison between the uncorrected and corrected seismic traces recorded at PRT (Prato, Italy) station (a) shows the original record for 04.01.1935-16:20 Earthquake (b) shows the overlap of the uncorrected and corrected seismic traces

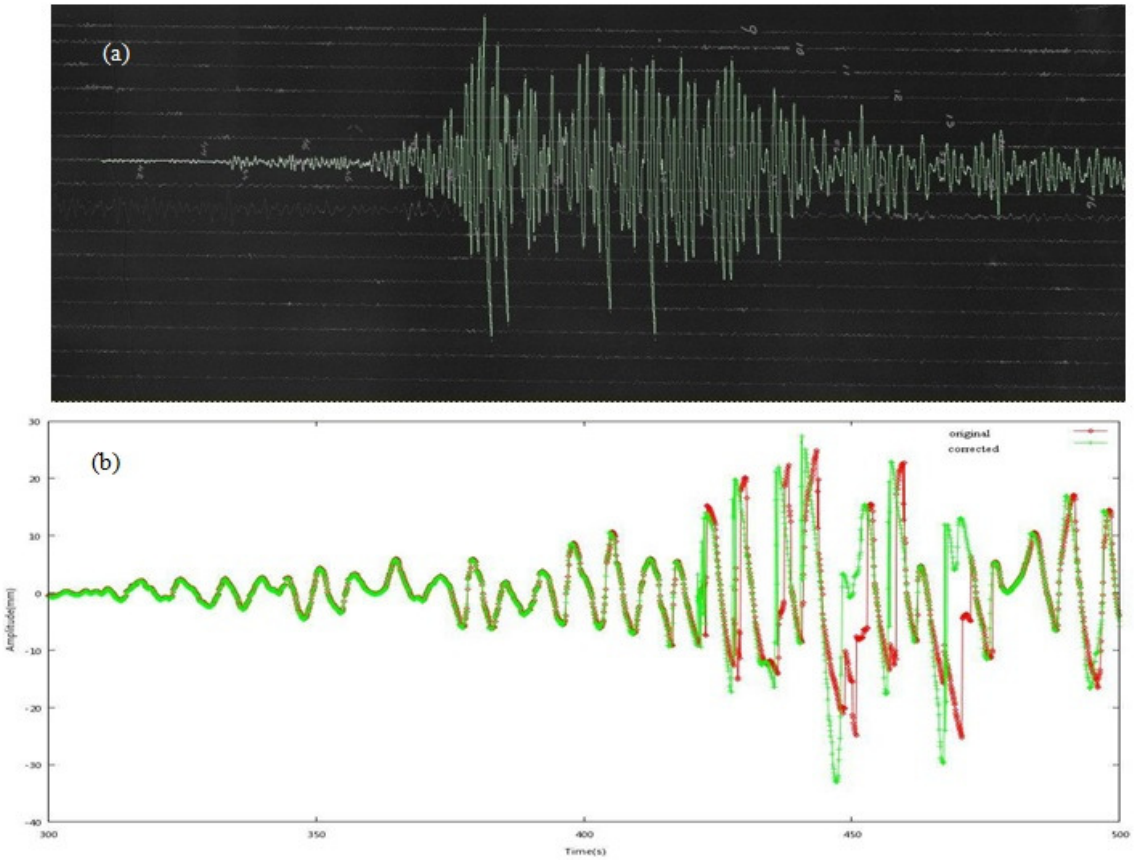

Figure 5.17. The comparison between the uncorrected and corrected seismic traces recorded at MNH (Munich, Germany) station (a) shows sismogram with curvature produced by the mechanical instrument (b) shows overlap of the uncorrected and corrected seismic traces

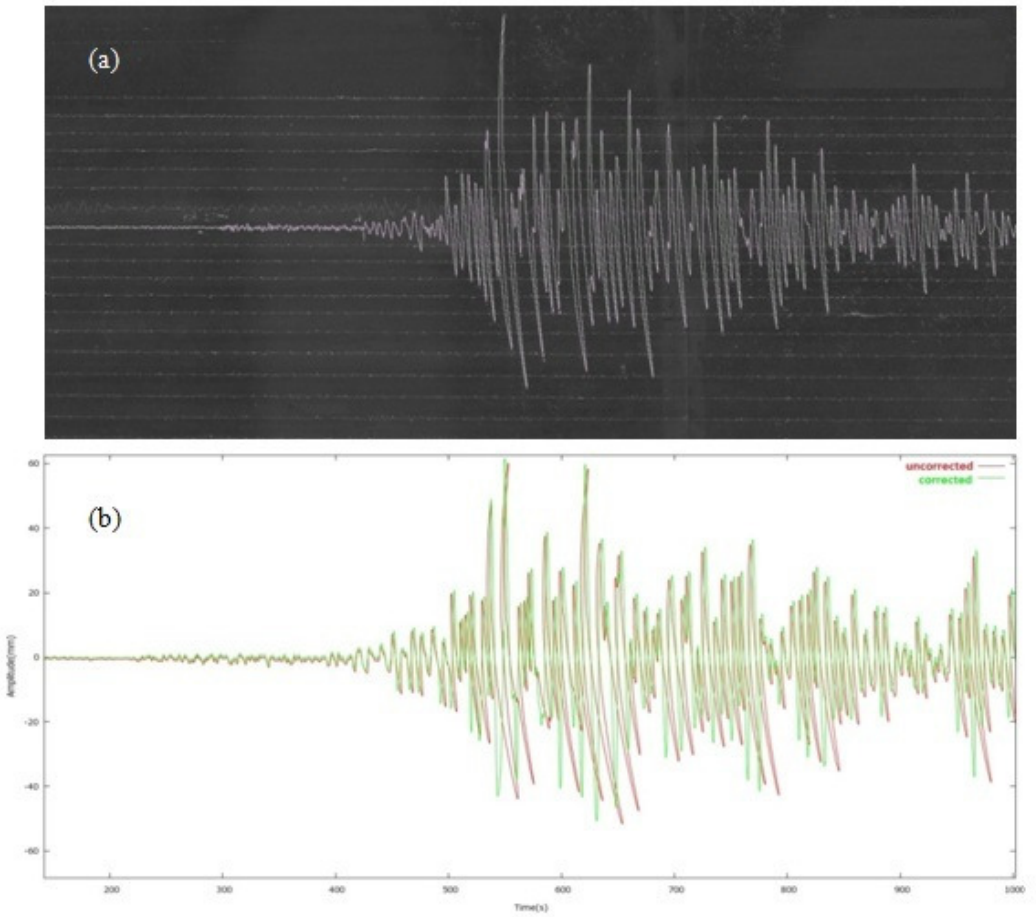

Figure 5.18. The comparison between the uncorrected and corrected seismic traces recorded at PCN (Piacenza, Italy) station (a) shows seismogram with curvature produced by the mechanical instrument (b) shows overlap of the uncorrected and corrected seismic traces

The digitized points of seismic signal recorded on original seismogram were scaled to time(X) and amplitude(Y) axis considering the length of between two time marks on the original records to obtain equal time intervals on time (X) axis. In order to acquire equally spaced points on the time axis, a polynomial interpolation method has been used. Interpolated data have been sampled using 0.1 sampling rate.

Although different approaches can be made, dealing with curvature and skew problems related to mechanism of arm and needle requires too much effort and time, and sometimes these problems cannot be overcame. It has no doubt that this indicates how challenging making old seismograms useful is. Although we have alternatives to obtain

useful seismic waveforms, the procedure to reach the best solutions is slow, based on iterative processes and each seismogram requires a special effort.

5.4.3. Application for Obtaining Displacement Spectra

In this study, displacement spectra dynamic parameters were estimated from P and S wave ground displacement spectra obtained digitized seismograms using the KMAG program produced by Josep Batlló and Ramon Macia (1999-2003). Digital seismograms which are sequences of numbers must be processed by using some basic operations such as baseline correction, trend-removing, tapering and butterworth filter to the records in digital form. These processes together with instrumental response correction were applied to the digitized seismograms using this program.

The geometrically corrected seismic traces are obtained in ASCII files after executing VELLSIS3 program produced. This ASCII files which contain the points of corrected seismic traces were processed by KMAG2 .EXE program. It is needed to put some parameters such as the magnification (V), damping constant (h), natural period of the seismogram and the time interval for P and S wave spectra are written in the input file. KMAG2 program applies the baseline correction, trend removing, cosine windowing, Gaussian filter, Butterworth filter which are necessary for the processing of seismic signals. Then, it calculates the amplitude response functions of the instruments, defined by the magnification (V), damping constant (h), and natural period. Finally, the displacement spectra are obtained by dividing the response functions of the instruments to the seismic signal.

In this study, the instrumental parameters such as Vo, T and h were collected from various documents, such as seismic station bulletins. In fact, it is sometimes possible to find these values on the original seismograms even though it is a low possibility. Usually, collection of the true instrument constants for the old seismic recording systems is highly difficult since the necessary documents are not available. For this reason, a special effort has been made to obtain the instrumental constants of the seismometers used for the historical seismograms analyzed in this work.

For this process, a large number of sources such as seismic bulletins, papers were investigated. However, it is a really big effort to obtain these sources. Uccle(UCC), Prague(PRA), Fabra(FBR), DeBilt(DBN), Copenhagen(COP) seismic station bulletins for the 1935 year and Timisoara(TIM) seismic station bulletin for the year 1963 have been obtained. In addition, countries of the seismograms with unknown components have been consulted. During this process, I have also benefited the Bulletin of the National Research Council and INGV website. In most cases, obtaining displacement spectra was highly time-consuming since acquired instrument parameters are doubtful. Table 5.3 summarizes the instrument constants collected from different sources and used to remove the instrument response correction in this study.

Table 5.3. The list of the instrument constants for the recording systems used for instrument response correction

Sta.	Com.	Instrument	M kg	To	Tg	Vo	Vm	h	k	A	l	d. mm
ATH	EW	Wiechert	1000	9.2		175		0.4				12.8
ATH	NS	Wiechert	1000	9.2		175		0.4				12.8
BER	EW	Wiechert	1000	9		100		0.33				18.5
COI	NS	Wiechert	1000	13		130		0.5				13.6
FBR	EW	Mainka	141.2	8.6		65		0.43				16.1
FBR	NS	Mainka	144.1	9.6		64		0.33				16.2
MNH	NS	Wiechert	1000	5		190		0.46				15
MNH	EW	Wiechert	1000	5		190		0.46				14.9
TRS	NE	Wiechert	1000	5		202		0.45				19
TRS	Z	Wiechert	80	4.3		81		0.36				21
PRA	N	Wiechert	1000	10.5		179		0.46				12.1
ZUR	EW	Mainka	450	7		140		0.33				23.2
ZUR	NS	Mainka	450	7		140		0.33				15.3
COP	Z	Wiechert	1300	7		165		0.4				9.9
COP	EW	Wiechert	1000	9.3		195		0.4				12.8
COP	NS	Wiechert	1000	9.5		215		0.4				12.6
COP	EW	Milne Shaw	2.2	12		300		0.69				8.1
COP	EW	Wood Anderson		0.8		2800		0.8				44

COP	N	Galitzin Willip		12	12.6	1007		6.9	103	100	12	30
COP	Z	Benioff		1	0.75	12500		0.58				30.1
COP	Z	Galitzin Willip		11	10.2	1098		8.9	100	100	14	30.1
DBN	EW	Galitzin		25	24.4	315.3	310	0.5	11	1380	123	29.2
DBN	NS	Galitzin		25	24.4	313		14	11	1380	123	29.2
DBN	Z	Galitzin		12	12	727.2	727		175	1380	406	30.5
DBN	N	Wiechert	200	5		170		0.4				9.9
DBN	E	Wiechert	200	5		170		0.4				10
ZAG	Z	Wiechert	1300	5		200		0.5				60.6
ZAG	NE	Wiechert	1000	7		200		0.5				36.2
ZAG	NW	Wiechert	1000	7		200		0.54				36.2
STR	EW	Galitzin	7	22.2	22.2	594.5	660	12.8	33	1000	124	31.5
STR	Z	Galitzin	10	11	11	66.64	710	6.7	24	1000	433	26.2
PCN	EW	Wiechert	1000	10		173		0.38				15.2
PCN	NS	Wiechert	1000	11		170		0.4				15.2
UCC	EW	Galitzin		24	24.2	808.9		13.9	39	1037	124	30
JENA	EW	Wiechert	1200	8.8		230		0.36				54.8
JENA	NS	Wiechert	1200	9.6		200		0.58				74.2
JENA	EW	Wiechert	15000	2.05		2200		0.48				14.8
JENA	NS	Wiechert	15000	2.1		2200		0.43				15
JENA	Z	Wiechert	1300	3.3		155		0.4				15
BRA	EW	Wiechert Krumbach	4	1.7		1900		0.41				29.6
BRA	NS	Wiechert Krumbach	4	2		2000		0.4				20.3
BRA	Z	Wiechert Krumbach	4	1.9		1850		0.33				20.2
PAV	EW	Wiechert	200	3.3		140.4		0.27				30.2
PAV	NS	Wiechert	200	3.5		112		0.32				29.4
PAV	Z	Galitzin Pannoichia		20	21		545	11.4	333			30
PAV	Z	Wiechert	80	3.4			124.6	0.27				29.9
RCI	EW	Wiechert	200	3.4		90		0.32				25
RCI	NS	Wiechert	200	3.5		99		0.31				29.6
ROM	EW	Wiechert	1000	8.8		148		0.27				29.3

ROM	NS	Wiechert	1000	8.9		160		0.33				29.3
ROM	Z	Wiechert	1300	3.3		400		0.29				30
ROM	EW	Wiechert	200	4.3		248		0.32				30.1
ROM	NS	Wiechert	200	4.5		245		0.27				29.8
SPC	NS	Wiechert		2		2000		0.4				20.6
SPC	Z	Wiechert Krumbach	4	1.9		1850		0.33				20.6
TAR	NS	Horizontal Pendulum	600	13		125		0.4				10.5
TIM	EW	Mainka	540	8.1		162		0.8				30.3
TIM	N	Mainka	540	8		161		0.81				30
TRI	EW	Benioff		1	0.75		50000	0.57		1030		58.8
TRI	Z	Benioff		1	0.75		12500	0.57		1030		59.3
PRT	NS	Omori	450	9		100		0.33				17.2
FIR	NE	Omori	250	20		20		0.33				17.3
FIR	NW	Omori	250	20		20		0.33				17
IC1H	NS	Pendulum Horizontal		12		40		0.40				4.9
TIF	EW	Reuber Euhlert		12		120		0.28				14.4
ISK	EW	Mainka	450	10		80		0.36				8
ISK	NS	Wiechert	200	5.6		50						8
HNG	NS	Omori-1		210		1.5		0.12				27.3
HNG	EW	Omori-2		60		15		0.34				20.1
HNG	EW	Omori-3		60		15		0.35				20.1
HNG	NS	Omori-4		60		30		0.22				21.3

Obtained displacement spectra were viewed using GNUPLOT software. From obtained spectra, (*Ωo),* the low-frequency level and fc ($\omega c = 2\pi fc$) the corner frequency values were chosen considering the seismic source model. In addition, these spectra can be modeled by fitting Equation 5.16 of Brune's model.

$$u_\omega = \frac{\Omega_0}{\left(1+\left(\frac{\omega}{\omega_c}\right)^\gamma\right)} \tag{5.16}$$

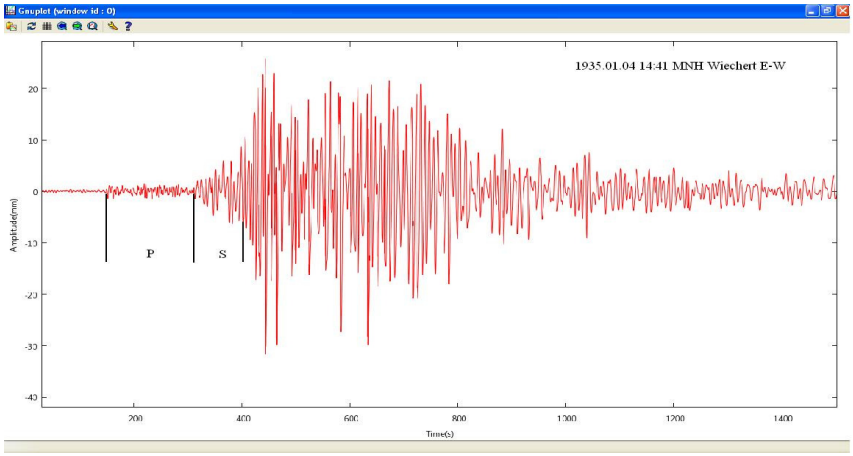

Figure 5.19. P and S wave time interval chosen for the E-W component seismogram of MNH (Munich, Germany) station

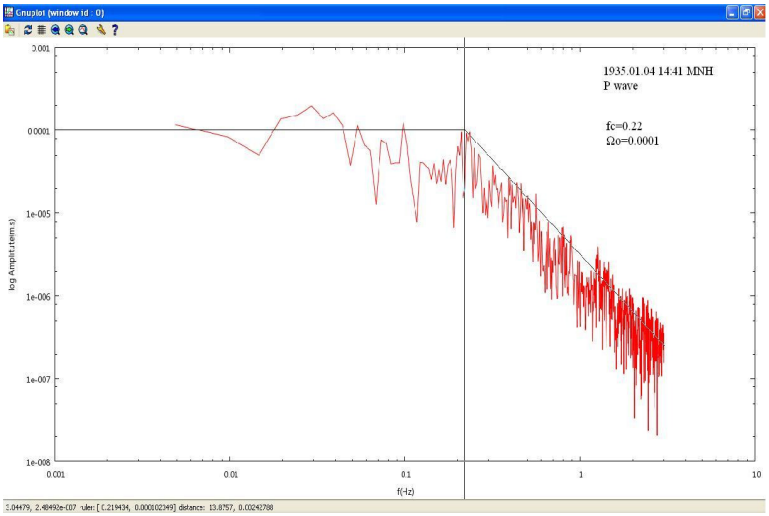

Figure 5.20. Obtained P wave spectrum and fc, Ωo values for the E-W component seismogram of MNH (Munich, Germany) station

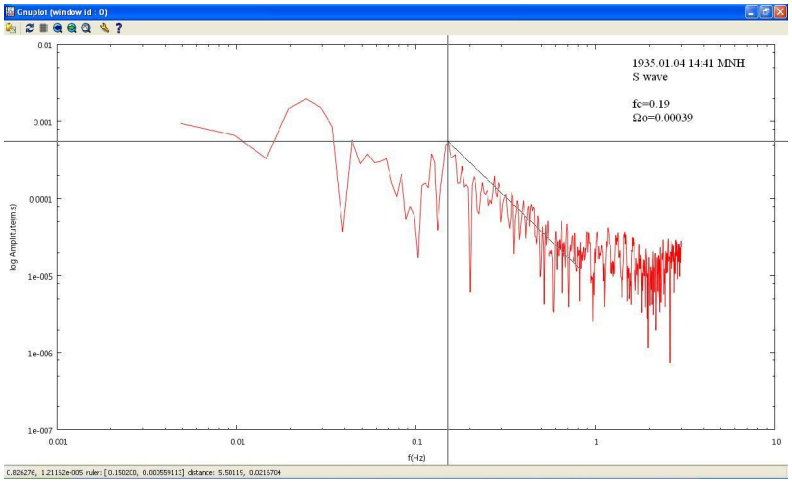

Figure 5.21. Obtained S wave spectrum and fc, Ωo values for the E-W component seismogram of MNH station

Two important parameters, low frequency level amplitude and corner frequency determined from the displacement spectra used for the estimation of seismic moment, source radius and stress drop values.

5.4.4. Seismic Moment, Mw, Fault Area and Stress Drop Estimations

The seismic moment is calculated from the Equation 5.17 of Keilis-Borok(1960).

$$M_0 = \frac{4\pi\rho v^3 \Omega_0}{G(r)\, R_{\theta\varphi} C} \tag{5.17}$$

where ρ is the density in the source , v is the wave velocity , Ωo is the low frequency level, G (r) is the geometrical spreading, $R_{\theta\varphi}$ is the correction for the radiation pattern, C is the free surface correction.

Geometrical spreading is related to the distance from the station to the epicenter r and can be described with the function G (Δ,h). At local distances, body wave spreading can be expressed by simple Equation 5.18;

$$G(\Delta, h) = \frac{1}{\sqrt{\Delta^2 + h^2}} = \frac{1}{r} \tag{5.18}$$

Equation 5.18 assumes a constant type of geometrical spreading independent of hypocentral distance (Havskov, Ottemöller, 2008).

In the Equation 5.17, the density in the source region was assumed 2,7 g/cm^3. Geometrical spreading values were calculated by the simple body wave spreading 1/r.

$R_{\theta\varphi}$ value changes for the P and S wave. Wyss and Brune (1968) accepted the value of the correction for the radiation pattern 0, 4 for P waves and Boore and Boatwright (1984) assumed this value as 0.63 for S waves. C, the correction for the free surface is equal to 2.

Seismic moment, Mo is expressed in Nm, which is equal to kg.(m^2/sn^2), if the Ωo is given in meter.sec, v is given in m/sec; ρ is given in kg/m^3.

The Moment magnitude, Mw, was calculated by relation (Hanks and Kanamori, 1979);

$$Mw = \frac{2}{3} log\, M_0 - 6 \qquad (5.19)$$

with Mo given in Nm.

Fault radius, the source dimension for a circular source is determined using:

$$R = \frac{k v_s}{f_c} \qquad (5.20)$$

where R is the radius of the circular source zone, vs is (the average) S-wave velocity at the source region.

k = 0.37 for P-waves (Brune 1970; 1971) and k = 0.64 for S-waves (Hanks and Wyss, 1972) can be accepted for an instantaneous rupture, k = 0.32 for P-waves and k = 0.21 for Swaves (Madariaga, 1976) for a circular fault rupturing from the center with rupture velocity of 0.9 for vs.

Static stress drop in terms of bar (1 bar=10^6 dyn/cm^2) for a circular fault can be estimated using the Equation 5.21.

$$\Delta\sigma = \frac{7}{16} M_0 R^{-3} \tag{5.21}$$

Equation 5.20 is expressed in dyn/cm^2; therefore, Mo must be in dyn.cm and the radius of the fault R is in cm. Since we obtain Mo is in Nm=kg.(m^2/s^2), a multiplication factor 10 ^{7} (1 newton=10^5 dyn, 1m=100 cm) is needed to obtain the Mo in terms of dyn.cm and fault radius needs to be converted into cm.

6. EPICENTRAL LOCATION

It is usually believed that instrumental epicenters are more accurate than the macroseismic ones which were especially used until the establishment of the seismological observatories with the mechanical instruments. In regions where the modern seismographic systems are available, this is true. However, before the 1960s seismological observatories in many places including Mediterrian countries, the distribution of the seismic stations and the quality of input data containing the arrival times are not sufficient for an accurate epicentral location procedure. The biggest problem is the accuracy of the pre-1960 ISS epicenters, especially in terms of their actual locations. It was found that in Middle East large shocks reported in ISS bulletins, were located many tens to hundreds of kilometres away from their true location. The problems of instrumental location were common to all earlier epicenters calculated by ISS, BCIS, USGS, and Gutenberg and Richter (1965) and others (Ambraseys and Melville, 1982).

A very early study carried out by Reid (1910) determined foreshock hypocentre by using combination of least-squares calculations with and without trial values for the hypocentral depth. He tested various positions for the hypocentral along the San Andreas fault and in depth and by solving by least squares for the origin time and wave velocity. He carried out a coarse but systematic search over velocity, position along the fault, and depth to find the best solutions and their formal errors. However, his preferred result has relatively large residuals and it invokes a *P*-wave velocity of 7.2 km/sec, which is now known to be unreasonable at local distances. On the other hand, Bolt (1963) calculated the epicenter location of the great 1906 California Earthquake using theoratical arrival times from emprical tables based on the epicentral distances to the four observing points. Lomax (2005) revaluated probabilistic hypocentral locations for the foreshock and mainshock of the 1906 California earthquake through reanalysis of arrival-time observations in conjunction with modern wave-speed models and event location techniques. The mainshock location determined by the Lomax (2005) has a large uncertainty but it is consistent with the assosciation of initial rupture of the 1906 earthquake.

Recently, many studies re-determined the epicentral locations of historical earthquakes. Many of these studies used the bulletin arrival times by using modern location algorithms. Dineva *et al*., (2002) relocated the epicenters of historical earthquakes using the bulletin data that contain the P and S wave arrival times. The large errors were eliminated by following a few step procedures to obtain the best results. Batlló *et al.,* (2008) relocated the mainshocks and 20 aftershocks based on their revised compilation of phase readings using the at least-squares method (HYPO71) with a regional velocity model. They used the stations out to 800 km distances. Just like in other studies reassessing the epicentral locations of historical earthquakes, the inaccuracy of the picking and timing indicated uncertainties in the epicenters. Detection of several misinterpretations in the original bulletins permitted better constrained hypocenter relocations, about 10 km apart from the previous one.

In the scope of this study, we re-determined the epicenter locations of 4 January 1935 (14:41 (GMT), 16:20 (GMT)) and 18 September 1963 earthquakes. Unfortunately, we could not reassess epicenter for the 9 August 1912 event since the data necessary for the estimation epicentral location is insufficient.

6.1. Application for Locating Epicenter

In order to re-determine the epicenters of 1935 and 1963 events, I used the P and S arrival times from International Seismological Summary (ISS) bulletins. In addition to the P and S time arrivals from the ISS bulletins, I included readings based on original seismograms. Epicentral location was performed using the program HYPOCENTRE 3.2. (Lienert, 1994) and the velocity model of Kalafat *et al*., (1987). The data obtained from the ISS Bulletin for this earthquake indicated large errors during the process of epicentral location. For this reason, I followed the process of removing the arrival time readings that show time residuals above 100 seconds. However, the total rms value was still too large after the first run. Then, the readings with time residuals larger than 10 seconds were removed to obtain smaller total rms value.

6.1.1. Estimation for 04.01.1935, 14:41 Erdek-Marmara Island Earthquake

In addition to data from ISS Bulletin, the readings from obtained original records which are not on the list of ISS bulletin are seismogram of ISK, ATH, MNH, FBR, COI stations were included. The readings of P and S arrival times from the seismograms of ZUR, STR, PRA, JENA, DBN, COP, BER, ZAG, VIE, PCN stations were also available in the ISS Bulletin. The data used for epicenter estimation for this earthquake is shown in Table C 1.

During the process of epicenter location of this event, P and S arrival times in original seismograms were also checked and the large residuels were reduced. In most cases, my readings for P and S wave agree with the readings of ISS Bulletins. However, I identified a problem with S-phase reading for TRS station for 4 January, 14:41 (GMT) Erdek Earthquake. I realized that the Sn arrival of this event is mismathed about 1 minute. Figure 6.1 shows the phases as they appear on the original seismogram for TRS station record.

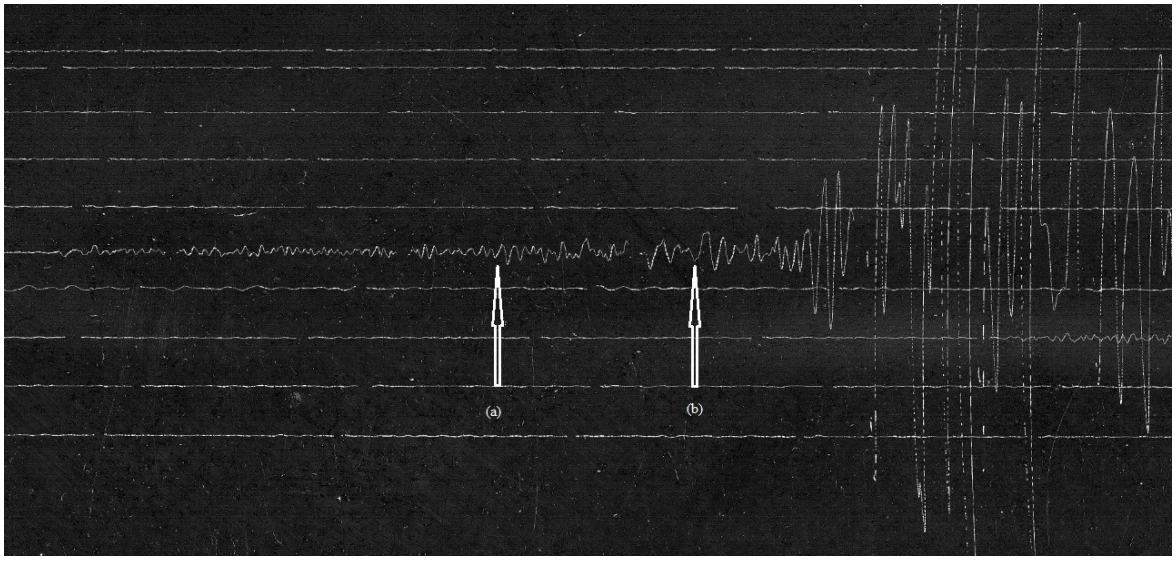

Figure 6.1. A section of the north-east seismogram at TRS (Trieste, Italy) observatory for the 1935.01.04, 14:41 Erdek-Marmara Island Earthquake, The arrow (a) indicates the choice of the thesis for the S-wave arrival and The arrow (b) indicates S-wave arrival reported on ISS bulletin

6.1.2. Estimation for 04.01.1935, 16:20 Erdek-Marmara Island Earthquake

For 1935.01.04, 16:20 Erdek-Marmara Island Earthquake , the readings of P and S arrival times obtained from ISS Bulletins indicated large errors for 1935.01.04, 14:41 as in the case of first event. The readings based on available original records enabled to compare P and S arrival times with ISS bulletin and reduce large rms values. I followed same procedure and removed residuals larger than 10 seconds. The data used for epicenter estimation for this earthquake is shown in Table C 2.

6.1.3. Estimation for 18.09.1963, 16:58, Çınarcık Earthquake

For 1963.09.18, 16:58, Çınarcık Earthquake the readings based on original seismograms were also available in the list of ISS Bulletins, except the S wave readings of PAV and TAR stations. Therefore, I included these readings in my epicenter solution. Most of the readings for P and S wave based on original records agree with the readings of ISS Bulletins. The data used for epicenter estimation for this earthquake is shown in Table C 3.

7. MOMENT TENSOR COMPONENTS

Equivalent forces of general seismic point sources, which produce displacement at the earth surface, form the double couple. A seismic moment tensor is the general concept that describes a double couple source among a variety of seismic source models. The analysis of the eigenvalues and eigenvectors of moment tensor determines the equivalent forces. The volume change in the source is described by the sum of the eigen vectors (Jost and Herrman 1989). In an isotropic medium for a double couple of equivalent forces, the moment tensor components are given by;

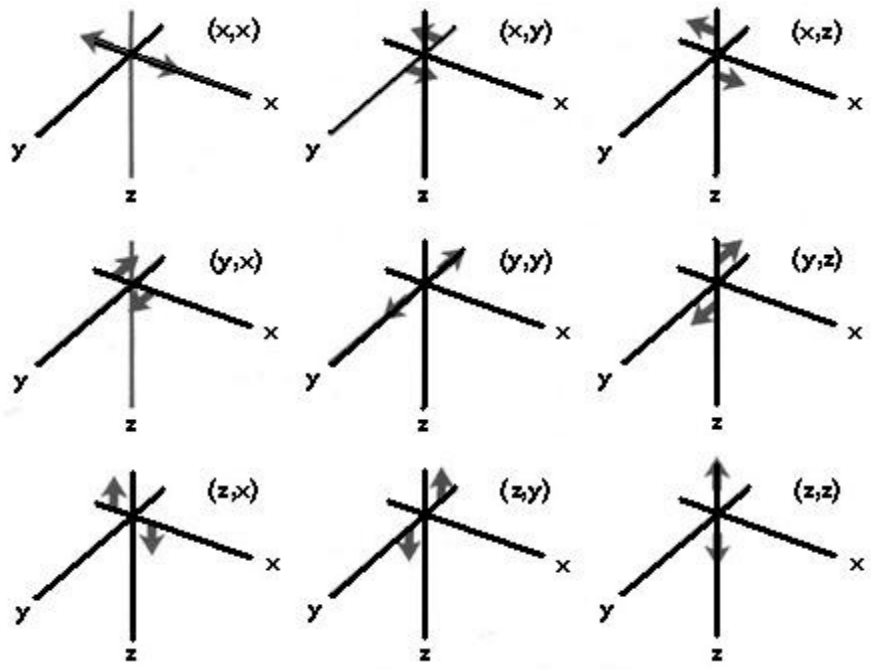

Figure 7.1. The nine generalized couples of the seismic moment tensor (Jost and Herrman 1989)

If these double couple sources are written in the matrix format, the Equation 7.1 can be obtained.

$$M = \begin{bmatrix} M_{xx} & M_{xy} & M_{xz} \\ M_{yx} & M_{yy} & M_{yz} \\ M_{zx} & M_{zy} & M_{zz} \end{bmatrix} \quad (7.1)$$

If the Equation 7.1 is written in terms of Mo, strike, dip and rake, Equation 7.2 can be obtained.

$$m_1 = M_{11} = M_{xx} = -M_0 [\sin(\delta) \cos(\lambda) \sin(2\Phi) + \sin(2\delta) \sin(\lambda) \sin^2(\Phi)]$$

$$m_2 = M_{12} = M_{xy} = M_0 [\sin(\delta) \cos(\lambda) \cos(2\Phi) + 0.5 \sin(2\delta) \sin(\lambda) \sin(2\Phi)]$$

$$m_3 = M_{13} = M_{xz} = -M_0[\cos(\delta) \cos(\lambda) \cos(\Phi) + \cos(2\delta) \sin(\lambda) \sin(\Phi)]$$

$$m_4 = M_{22} = M_{yy} = M_0 [\sin(\delta) \cos(\lambda) \sin(2\Phi) - \sin(2\delta) \sin(\lambda) \cos^2(\Phi)]$$

$$m_5 = M_{23} = M_{yx} = -M_0[\cos(\delta) \cos(\lambda) \sin(\Phi) - \cos(2\delta) \sin(\lambda) \cos(\Phi)]$$

$$m_6 = M_{33} = M_{zz} = M_0 [\sin(2\delta) \sin(\lambda)] = -(M_{11} + M_{22}) \quad (7.2)$$

where;

δ : The angle between the fault and a horizontal plane, 0^0 to 90^0,

Φ : Strike is measured clockwise from north,

λ : The angle between the slip vector and the fault direction.

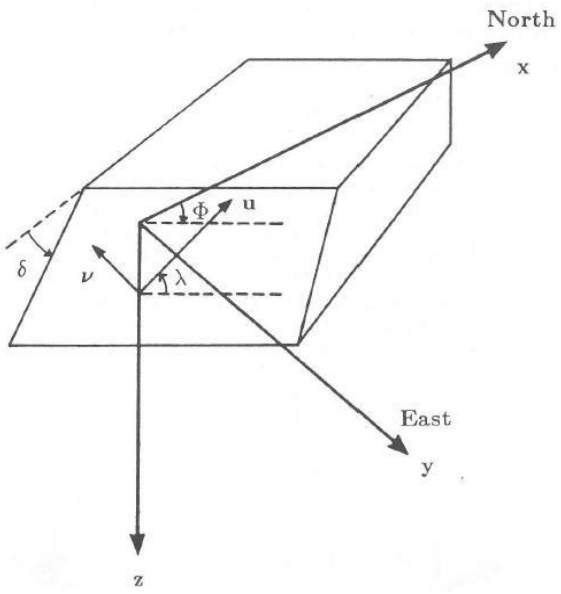

Figure 7.2. The definition of the Cartesian coordinates (x, y, z) Strike, dip and rake are denoted with δ, Φ, λ respectively. u and ν are the slip vector and fault normal, respectively(Jost and Herrman 1989)

In the Equation 7.2, the first five equations define the dislocations of P, SV, and SH, while the last equation describes the source radiating the enery equally in every direction, such as explosion. Moment tensor for the earthquake waves is given by the sum of the first five components (Bergman, 1997).

$$M = \sum_{i=1}^{5} m_i \tag{7.3}$$

Seismic source can be represented by considering both a spatial and temporal point-source.

$$U_n(x,t)=M_{ij}\,(z,t) \cdot G_{ni,j}(x,z,t) \tag{7.4}$$

Ui is the observed n^{th} component of displacement, $Gn_{i,j}$ is the n^{th} component Green's function for specific force-couple orientations, and Mij is the scalar seismic moment tensor, which describes the strength of the force-couples. i an j refer to geographical directions. For a given depth, Equation 7.4 is solved using linear least squares. The

Green's functions $G_{ni,j}(x,z,t)$ are produced as synthetic data for an assumed velocity model. What we are looking for is the correlation between the observed and synthetic waveforms for a given depth and distance from the source. Using these synthetic data, the seismic moment tensor components can be found and, the strike, dip and rake angles can be determined. The method assumes that the media is layered. For this reason, the synthetic seismograms are valid in the local and regional scale and the misfit will increase depending on the distance from the source (Dreger, 2002).

The procedure above is assessed with variance reduction (VR). Here, it is expected that the largest variance reduction is the solution produced iteratively that finds the source depth. In the Equation 7.5, $data_i$ represents the observed waveforms whereas the $synth_i$ indicates the synthetic waveforms (Dreger, 2002).

$$VR = \left[1 - \sum_i \frac{\sqrt{(data_i - synth_i)^2}}{\sqrt{data_i^2}}\right].100 \qquad (7.5)$$

7.1. Moment Tensor Inversion Studies for Historical Earthquakes

Moment tensor inversion of mechanical seismographs provides estimations of source parameters for a number of important earthquakes. However, even though moment tensor inversion gives many advantages for the modern seismic data, it may not work well for early seismograms. It is highly difficult and sometimes impossible to accomplish this process for historical records (Stich *et al.*, 2005). Stich *et al*., (2005) underlined the problems of using moment tensor inversion for historical earthquakes based on their study;

One of the problems with the moment tensor inversion for the historical seismograms is the absence of the three components. Early seismograph systems which usually consisted of mechanical sensors, recorded only horizontal components. Although, there were few vertical sensors, their bandwidth was insufficient for regional waveform modelling. Also, the knowledge for the instrumental parameters such as polarity, gain, damping and free period, remains unknown (Stich *et al*., 2005).

It is commonly observed, in the case of early seismograms, that time marks at constant intervals may not be well synchroned when two horizontal seismograms superposed to each other. This leads to an incoherency among them. In this situation, it is difficult to align traces coherently. In addition, single horizontal components were lost during nearly 1 century of data storage, which makes rotation impossible. Even though two horizontal seismograms are available, one of them may have wrong polarity. In this situation, both radial and transverse components cannot be obtained (Stich *et al.*, 2005).

Stich *et al.,* (2005) used a method that uses directly single unrotated horizontal components seismograms instead of the usual radial (P–SV) and transverse (SH) waveforms, which avoids distortions encountered after rotation horizontal seismograms with incorrect alignment, uneven drum speed and imprecise instrumental correction. This method was used to carry out the moment tensor inversion for the 1909 Benavente (Portugal) and Lambesc (France) Earthquakes. An advantage of this method is that it increases the data set and improves azimuthal coverage since one component seismograms are also used. In the study, original single-component horizontal traces were used without rotation. Instead, theoretical Green's functions were produced and rotated. Displacement defined by the moment tensor element elements is connected to standard cylindrical moment tensor inversion depend the station azimuth, sensor orientation related to the old-time instrumentation. The instrument responses were expressed as poles and zero type transfer functions to obtain displacement seismograms.

This modified moment tensor inversion scheme of Stich *et al*., (2005) enabled to use single seismograms. Considering the inadequate seismogram problem of historical earthquake studies, this method is useful. However, despite the rigorous study, there may be doubts about a moment tensor inversion process carried out by using individual waveforms. It is certain that the analysis, of the old seismograms including moment tensor inversion processes, must be achieved with a wide datasets of any information such as sensor orientation, instrument constants.

Batlló *et al*., (2008) also followed the method of Stich *et al*., (2005) to include single components to the solution for 1951, Mw=5.2 and Mw=5.3 Jaen Southern Spain earthquake. Another study for the historical earthquakes carried out by Stich *et al*., (2003)

also performed the moment tensor inversion by minimizing the least-squares misfit between observed displacement seismograms within a long period passband and their synthetic predictions corresponding to the moment tensor.

7.2. Application of Moment Tensor Inversion

In order to perform moment tensor inversion, the data must be prepared before starting this process. This includes; cutting three components from the starting time of the traces. The instrumental response must be removed. Radial and transversal components must be obtained by rotating the N-S and E-W components. The waveforms must be integrated. At the same sampling interval observational and synthetic data must be filtered (Yılmazer, 2009).

For this process, three component seismograms of DBN, ZAG, JENA, COP stations for the 1935 Earthquakes and BRA, COP, DBN, PAV, ROM for the 1963 Earthquake selected. Digitized and geometrically corrected seismic traces in ASCII format were converted to SAC format in order to perform the essential operations such as filtering, rotating and integration. TDMT-INV algorithm produced by Dreger (2002) was used to moment tensor inversion. The synthetic data were generated using an algorithm named FKRPROG (Saikia 1994), which calculates the Green's functions in the frequency domain. The Green's functions were modeled using the velocity model estimated by Kalafat *et al.,* (1987). Here, the objective is the correlation between these synthetic waveforms and the waveforms produced with the earthquake source. The synthetic waveforms were calculated from 4 km depth to 40 km depth in 2 km increments and form 10 km distance to 5000 km distance in 5 km increments.

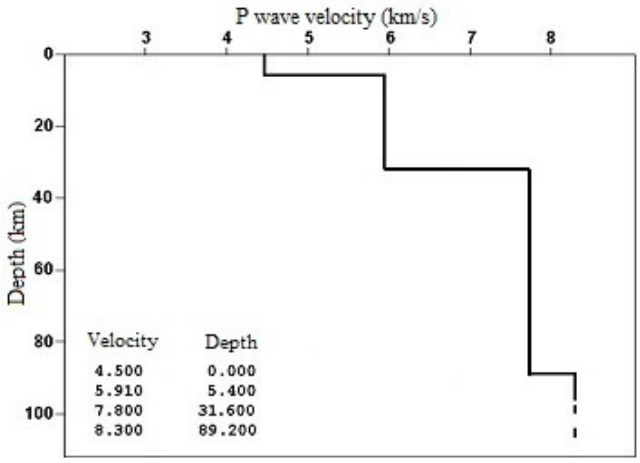

Figure 7.3. The velocity model used for the calculating of synthetic waveforms (Kalafat *et al.*, 1987)

I used 0.025-0.075 filter for the 1935 14:41:30 and 16:20:05 events and 0.035-0.075 filter for the 1963 event. The instrumental correction was performed by multiplying the amplitudes with a coefficient to approximate to synthetic waveforms. These coefficients were determined by trying different values and approximate these values to the previously calculated magnitudes of these events. For the 1935, 14:41:30 and 16:20:05 events, the amplitudes were multiplied by 1/50000 for all stations, except east component from COP station. I used 1/20000 coefficient for the east component of COP station with Wood-Anderson recording system. For the 1963, 16:58:08 event I used 1/5000 for the east and north components, 1/10000 for the vertical component of BRA, 1/2000 for all components of ROM station, 1/500 for all components of PAV station, 1/1000 for east and north components of and 1/10000 of COP and 1/1000 for all components of DBN stations.

In the application of moment tensor inversion, I encountered the common problems also cited by Stich *et al*., (2005). For two earthquakes, the seismograms were obtained from the eastern part of the epicenter, which is a trouble for estimating earthquake fault mechanism. The process of cutting three components from the starting time is troublesome due to the fact that the starting times of the waveforms are usually doubtful on the original seismograms. Radial and transversal components must be obtained by rotating the NS-EW components.

Other problems can be summarized as the unknown starting time of the traces and also imprecise instrument constants, which are also main difficulties for the other analysis of the historical earthquakes.

8. RESULTS

8.1. Results for 09.08.1912-01:29, Ganos Earthquake

8.1.1. Seismic Moment, Mw, Radius of the Source, Stress Drop Results for 09.08.1912-01:29 Earthquake

Table 8.1. Mo, Mw, R and Δσ values obtained for 09 August 1912, 01:29 Earthquake

Sta.	Count.	Comp	Inst.	Mo(Nm)	Mw	R(km)	Δσ
DBN	The Netherlands	NS	Wiechert	1.6×10^{20}	7.4	38.5	13.08
DBN	The Netherlands	EW	Wiechert	1.4×10^{20}	7.4	41.7	9.01
FIR	Italy	NE	Omori	3.4×10^{19}	6.9	12.1	85.69
FIR	Italy	NW	Omori	3.4×10^{19}	6.9	15.5	47.5
IC1H	Italy	EW	Pendulumhorizontal	9.6×10^{19}	7.1	63.3	1.17
TIF	Georgia	EW	Reuber-Ehlert	1.0×10^{19}	6.8	78.6	0.1
HNG	Japan	NS	Omori-1	1.5×10^{20}	7.3	11.1	400.35
HNG	Japan	EW	Omori-1	1.5×10^{20}	7.3	12.8	405.54
HNG	Japan	EW	Omori-2	2.1×10^{19}	6.8	25.6	6.37
HNG	Japan	N	Omori-2	2.1×10^{19}	6.8	33.84	4.125

Table 8.1 shows the seismic parameter values that obtained for all station. The magnitude results for 9 August 1912 Earthquake are consistent with results that previously reported.The records of HNG station were very low quality in terms of their paper. An average of the results from DBN, FIR, IC1H, TIF can be obtained as shown in Table 8.2.

Table 8.2. Average values of Mo, Mw, R and Δσ for 09 August 1912, 01:29 Earthquake

Result	Average	P	S
Mo [Nm]	8.3×10^{19}	1.05×10^{20}	6.02×10^{19}
Mw	7.13	7.24	7.01
R [km]	41.6	45.02	38.31
Δσ [bar]	26.09	39.45	12.73

8.2. Results For 04.01.1935-14:41, Erdek Earthquake

8.2.1. Seismic Moment, Mw, Radius of the Source, Stress Drop Results for 04.01.1935-14:41 Earthquake

Table 8.3. Mo, Mw, R and Δσ values obtained for 04 January 1935, 14:41 Earthquake

Sta.	Count.	Comp	Inst.	Mo(Nm)	Mw	R(km)	Δσ
BER	Bergen	EW	Wiechert	4.72×10^{18}	6.39	12.5	11
COI	Portugal	NS	Wiechert	2.5×10^{17}	5.59	12.7	0.8
FBR	Spain	EW	Mainka	2.6×10^{18}	6.08	45	0.9
FBR	Spain	NS	Mainka	4.2×10^{18}	6.42	82.6	0.03
MNH	Germany	NS	Wiechert	3.2×10^{18}	6.34	10.7	11
MNH	Germany	EW	Wiechert	3.2×10^{18}	6.34	10.5	12.2
TRS	Italy	NE	Wiechert	6.0×10^{18}	5.84	5.6	14
TRS	Italy	Z	Wiechert	8.4×10^{18}	5.94	7.36	9.1
PRA	Czech Republic	N	Wiechert	1.3×10^{18}	6.02	11.8	3
ZUR	Switzerland	EW	Bosh_Mainka	2.3×10^{18}	6.12	9.8	11.5
ZUR	Switzerland	NS	Bosh_Mainka	2.3×10^{18}	6.12	11.3	7.7
COP	Denmark	Z	Wiechert	4.0×10^{18}	5.62	9.5	6.6
COP	Denmark	EW	Wiechert	8.8×10^{18}	5.95	12.9	5.4
COP	Denmark	NS	Wiechert	9.9×10^{18}	5.99	8.8	7.1
COP	Denmark	EW	Milne_Shaw	5.8×10^{18}	5.82	13.8	1.5
COP	Denmark	EW	Wood Anderson	1.1×10^{18}	5.99	7.4	12.3
DBN	The Netherlands	EW	Galitzin	2.2×10^{18}	6.15	11	8.2
DBN	The Netherlands	NS	Galitzin	1.9×10^{18}	6.12	10	8.3
DBN	The Netherlands	Z	Galitzin	1.2×10^{18}	5.98	11.7	6.6
ZAG	Croatia	Z	Wiechert	1.3×10^{18}	6.08	7.5	14
ZAG	Croatia	NE	Wiechert	2.6×10^{18}	6.28	8.4	20
ZAG	Croatia	NW	Wiechert	2.6×10^{18}	6.28	8.1	21
STR	France	EW	Galitzin	8.8×10^{17}	5.91	9.0	12
STR	France	Z	Galitzin	2.5×10^{18}	6.08	12.2	7.1
PCN	Italy	EW	Wiechert	2.1×10^{18}	6.2	9.4	10.8
PCN	Italy	NS	Wiechert	2.1×10^{18}	6.2	9.8	9.5
UCC	Belgium	EW	Galitzin	4.1×10^{17}	5.74	11.6	5.7
JENA	Germany	EW	Wiechert-1200kg	8.1×10^{18}	5.9	11.8	34
JENA	Germany	NS	Wiechert-1200kg	7.4×10^{18}	5.87	10.3	18
JENA	Germany	EW	Wiechert-15000kg	1.7×10^{18}	6.14	34.3	0.18
JENA	Germany	NS	Wiechert-15000kg	1.8×10^{18}	6.15	30.9	0.49

Table 8.4. Average values of Mo, Mw, R and Δσ for 4 January 1935, 14:41 Earthquake

Result	Average	P	S
Mo [Nm]	2,15 x10^{18}	2,41 x10^{18}	1,13E x10^{18}
Mw	6,1	6,17	5,94
R [km]	14	12,65	17,69
Sress drop [bar]	9	14,67	4,27

If we take an average of all values to interpret the earthquake parameters, we can say that 4 January 1935 Earthquake was a magnitude of Mw=6.05±0.4. The seismic moment was about 1.76x10^{18} Nm., the radius of the source that ruptured was calculated as 15.17 km. Although the values are variable, the consistency of the results expected from such an earthquake considering its intensity, is provided as a result of this study.

The magnitude estimation from S wave spectrum gave small values for some stations. This may arises from several reasons. One of the reasons may be the mechanism of old seismometers. After all, these instruments recorded at large sampling intervals compared to the seismometers of today. In this case, it is expected to loss of frequency. The other reason may be the frequency range of the old recording systems may not be sensitive for S-wave since their frequencies are lower than the P waves. Taking into consideration the difficulty of studying with historical seismograms which were recorded with a very low magnification and loss of frequency, the results of this study are reasonable for such an earthquake.

8.2.2. Epicenter Location Results for 04.01.1935-14:41, Erdek Earthquake

After the final run of the program, I located of 4 January, 14:41 (UTC) Erdek Earthquake at 40°43.28 N- 27°43.25 E (40.72 N- 27.72 E), (rms=2.47) h=6.5 km for the epicentral location. The obtained results do not show large deviations from the previously reported epicenter locations at recent studies. However, the location result of this study (40.0 N, 27.5 E) indicated a difference about 60 km from ISS bulletin. The Figure 8.1

shows the epicentral location of the thesis, Ambraseys (1988) and ISS bulletin for 04.01.1935-14:41, Erdek Earthquake.

Figure 8.1. Demonstration of epicenter locations for 04.01.1935-14:41, Erdek Earthquake (1) is the result of thesis (2) is the result of Ambraseys (1988) (3) is the result of ISS Bulletin

8.2.3. Moment Tensor Inversion Results for 04.01.1935-14:41 Erdek Earthquake

The moment tensor solution for 04.01.1935-14:41 Earthquake gave the mechanism of the normal faulting with nodal plane orientations of 140/56/-98 (strike/dip/rake). The depth of this earthquake has been calculated 4 km.

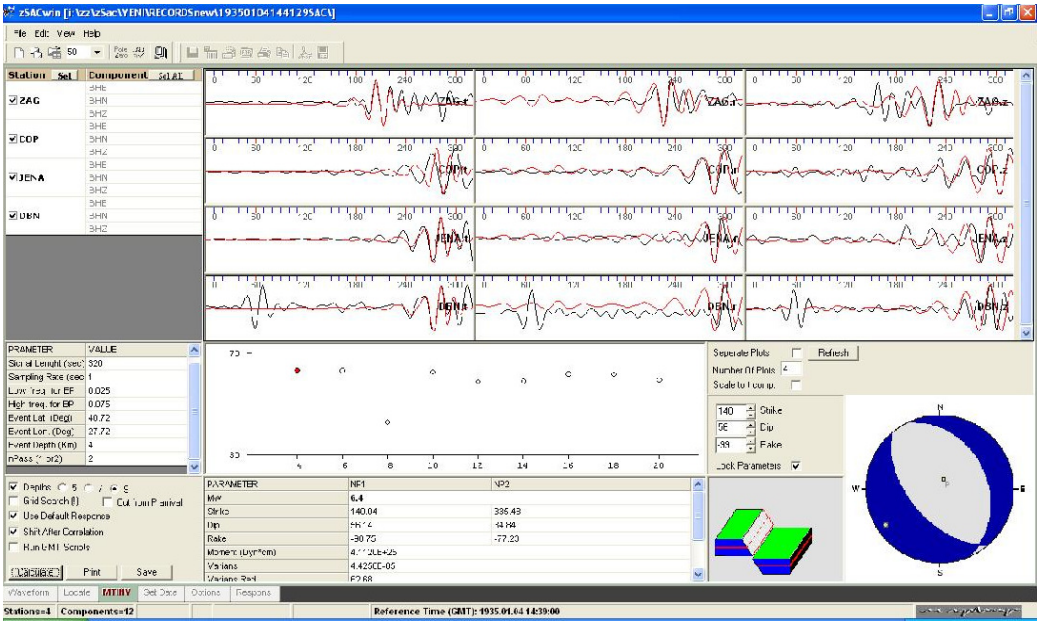

Figure 8.2. The fault plane solution for 04.01.1935- 14:41 Erdek Earthquake on Zsac software screen

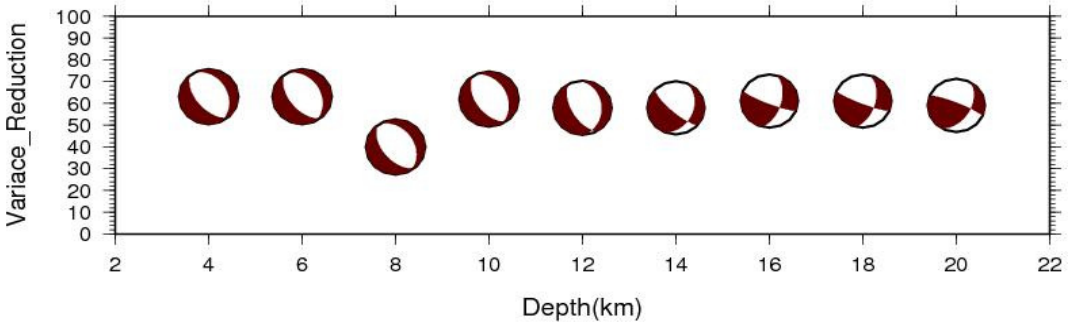

Figure 8.3. Fault plane solutions and the variance reduction with corresponding depth for 04.01.1935- 14:41 Erdek Earthquake

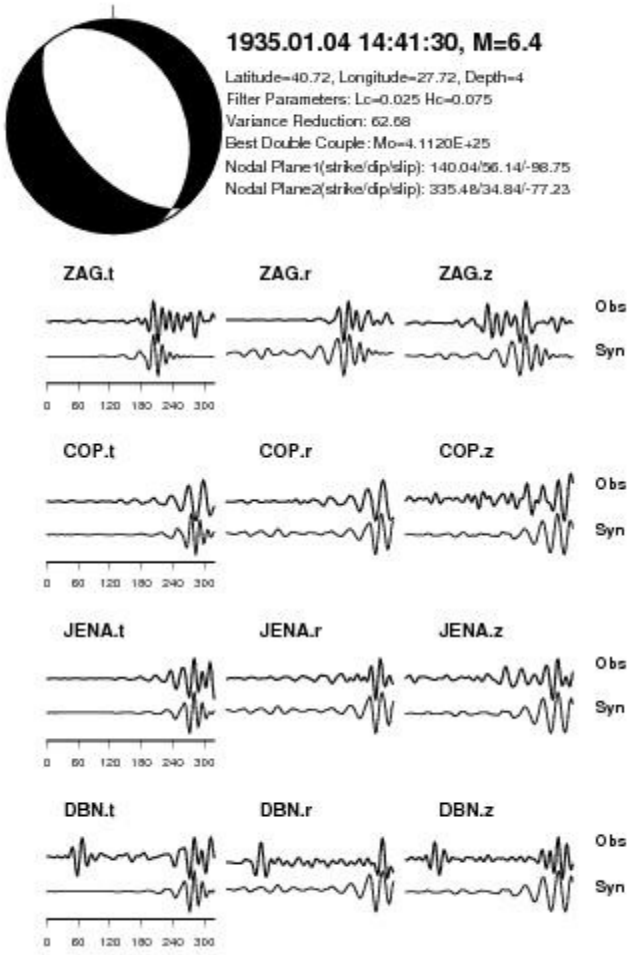

Figure 8.4. Fault plane solution and the coherency of the waveforms obtained for 04.01.1935- 14:41 Erdek Earthquake

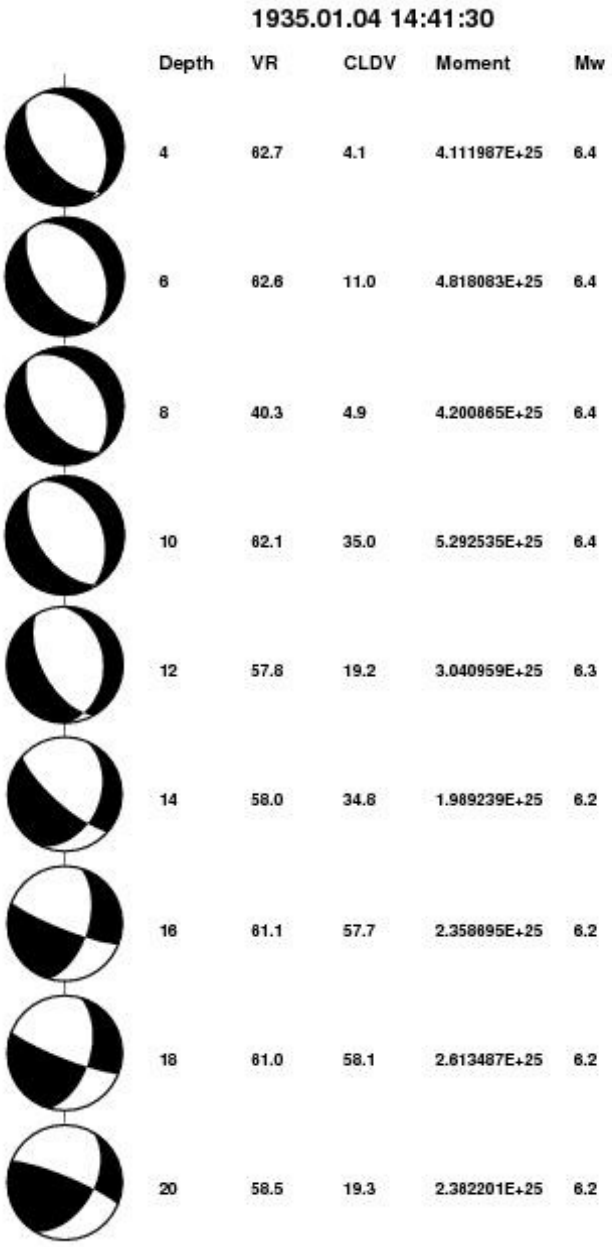

Figure 8.5. The coherency of waveforms and VR, CLVD, seismic moment, Mw and fault mechanism with corresponding depth for 04.01.1935- 14:41 Erdek Earthquake

8.3. Results for 04.01.1935-16:20, Erdek Earthquake

8.3.1. Seismic Moment, Mw, Radius of the Source, Stress Drop Results for 04.01.1935-16:20 Earthquake

Table 8.5. Mo, Mw, R and Δσ values obtained for 4 January 1935,16:20 Earthquake

Sta.	Count.	Comp	Inst.	Mo(Nm)	Mw	R(km)	Δσ
BER	Bergen	EW	Wiechert	2.6×10^{18}	6.26	10	12.4
COI	Portugal	NS	Mainka	1.9×10^{17}	5.52	11	1.1
FBR	Spain	EW	Mainka	4.5×10^{18}	6.44	45	0.9
FBR	Spain	NS	Wiechert	4.8×10^{18}	6.46	82	0.04
MNH	Germany	NS	Wiechert	1.9×10^{18}	6.2	8.1	16
MNH	Germany	EW	Wiechert	1.9×10^{18}	6.2	8.0	16
TRS	Italy	NE	Wiechert	4.9×10^{17}	5.8	8.1	4
TRS	Italy	Z	Wiechert	9.9×10^{17}	5.93	8.3	11
PRA	Czech Republic	N	Bosh_Mainka	6.7×10^{17}	5.87	8.3	4.9
ZUR	Switzerland	EW	Bosh_Mainka	6.8×10^{17}	5.84	7.7	7
ZUR	Switzerland	NS	Wiechert	1.3×10^{18}	6.09	15	7.1
COP	Denmark	Z	Wiechert	6.9×10^{17}	5.89	7.3	11.5
COP	Denmark	EW	Wiechert	8.6×10^{17}	5.95	8	8.4
COP	Denmark	NS	Milne_Shaw	8.6×10^{17}	5.95	7.8	9.7
COP	Denmark	EW	Wood Anderson	9.9×10^{17}	5.98	13	2.8
COP	Denmark	EW	Galitzin	2.1×10^{18}	6.08	9	13.7
DBN	The Netherlands	EW	Galitzin	2.8×10^{18}	6.17	10	15.2
DBN	The Netherlands	NS	Galitzin	2.7×10^{18}	6.08	10	11.7
DBN	The Netherlands	Z	Wiechert	6.7×10^{17}	5.87	12	9.2
ZAG	Croatia	Z	Wiechert	6.1×10^{17}	5.84	6.3	10.8
ZAG	Croatia	NE	Wiechert	1.0×10^{18}	6	6.8	15.3
ZAG	Croatia	NW	Galitzin	1.0×10^{18}	6	7.9	10.3

PCN	France	EW	Galitzin	1.5×10^{18}	6.13	7.6	20
PCN	France	NS	Wiechert	1.5×10^{18}	6.13	7.9	18
UCC	Italy	EW	Wiechert	1.1×10^{18}	5.98	10.9	14
JENA	Italy	EW	Galitzin	2.6×10^{18}	6.27	7.2	32
JENA	Belgium	NS	Wiechert-1200 kg	2.6×10^{18}	6.27	12.5	10
JENA	Germany	EW	Wiechert-1200 kg	1.2×10^{18}	6.06	30	0.3
JENA	Germany	NS	Wiechert-15000 kg	2.4×10^{18}	6.25	59	0.09
JENA	Germany	Z	Wiechert-15000 kg	9.3×10^{17}	5.91	44	0.04
PRT	Italy	E	Wiechert	2.6×10^{18}	6.26	12	16.3

Table 8.6. Average values of Mo, Mw, R and Δσ for 4 January 1935, 16:20 Earthquake

Result	**Average**	**P**	**S**
Mo [Nm]	1.46×10^{18}	2.04×10^{18}	8.83×10^{18}
Mw	5.99	6.12	5.87
R [km]	15.19	13.94	16.44
Sress drop [bar]	10.12	15.32	4.92

8.3.2. Epicenter Location Results for 04.01.1935-16:20 Earthquake

The readings of P and S arrival times obtained from ISS Bulletins indicated large errors as in the case of 1935.01.04, 14:41 event. I followed same procedure and removed residuals larger than 10 seconds. Finally, I obtained 40°36.66 N- 27°26.03 E (40.61 N-27.43 E), (rms=3.44) h=0 km result.

Figure 8.6. Demonstration of epicenter locations for 04.01.1935-16:20, Erdek Earthquake (1) is the result of thesis (2) is the result of Ambraseys (2000) (3) is the result of ISS Bulletin

8.3.3. Moment Tensor Inversion Results for 04.01.1935-16:20 Earthquake

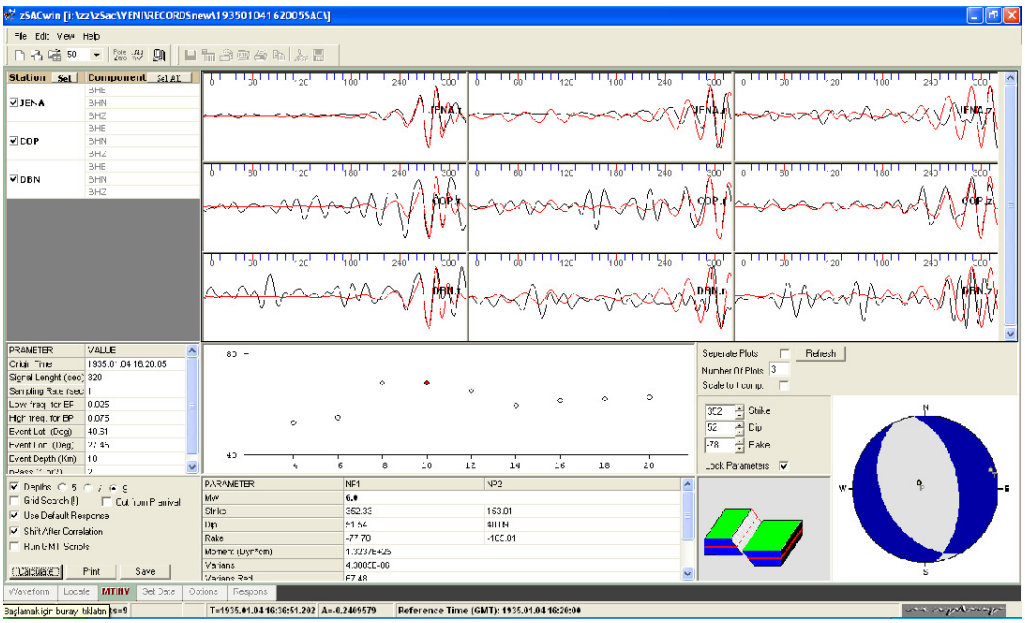

Figure 8.7. The fault plane solution for 04.01.1935- 16:20 Erdek Earthquake on Zsac software screen

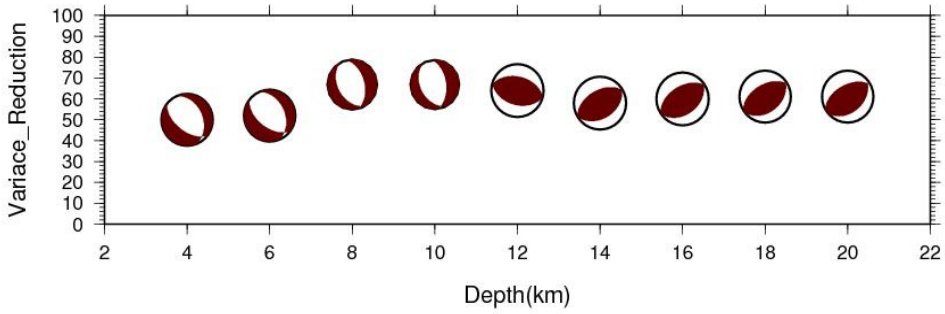

Figure 8.8. Fault plane solutions and the variance reduction with corresponding depth for 04.01.1935- 16:20 Erdek Earthquake

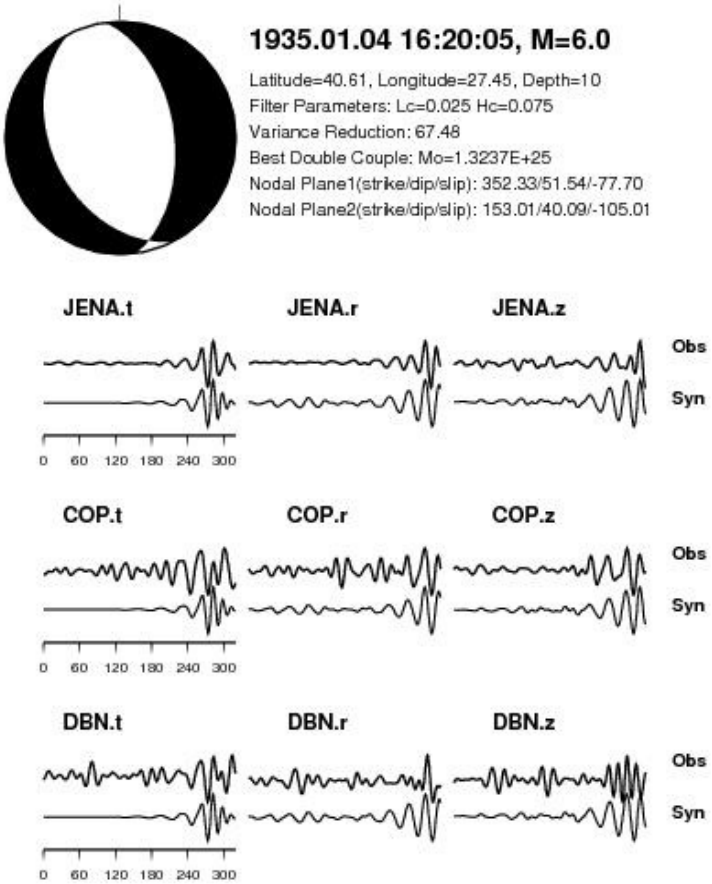

Figure 8.9. Fault Plane solution and the coherency of the waveforms obtained for 04.01.1935- 16:20 Erdek Earthquake

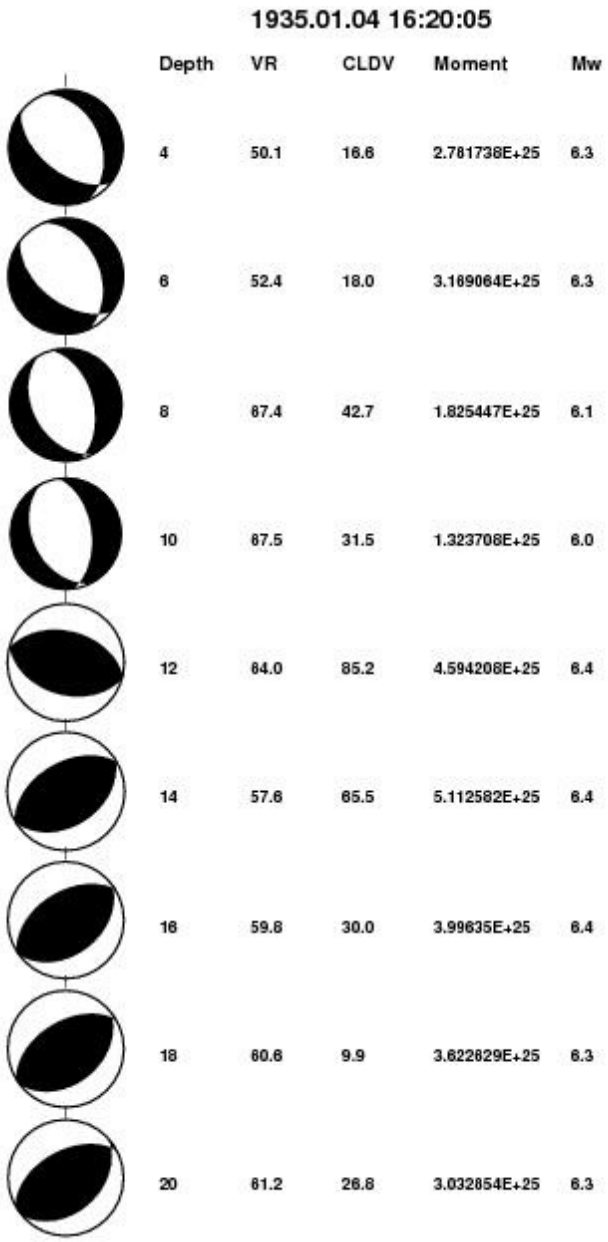

Figure 8.10. The coherency of waveforms and VR, CLVD, seismic moment, Mw and fault mechanism with corresponding depth for 04.01.1935- 16:20 Erdek Earthquake.

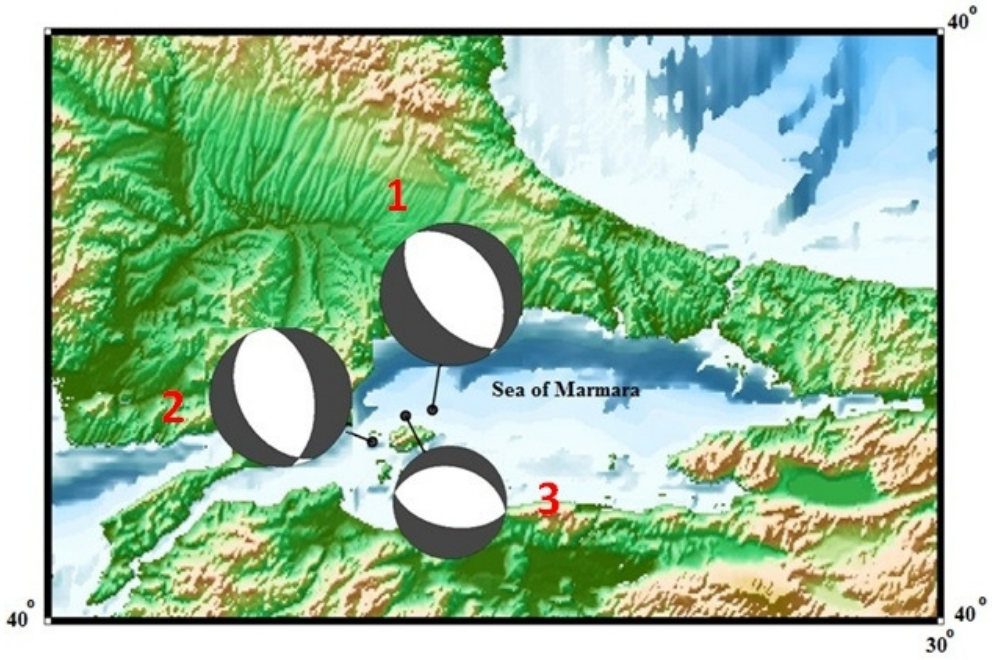

Figure 8.11. Fault plane solutions for 04.01.1935- 14:41 and 16:20 Erdek Earthquakes

Figure 8.11 shows the comparison of the moment tensor solutions for 04.01.1935- 14:41 and 16:20 Erdek Earthquakes (1) indicates the thesis result for the 14:41 Earthquake (2) indicates the thesis result for the 16:20 Earthquake (3) shows the fault mechanism given by EMSC moment tensor catalog. The fault mechanism for the fault responsible of 14:41 event is given by 100/40/-90 (strike/dip/rake). As it can be understood from the method and the coherency of the observed and synthetic waveforms, the thesis solutions of fault mechanisms of these two events are reliable since no study was carried out using original seismograms. In addition, this rigorous effort contains valuable importance as it clarifies the fault charactersitics for the first time.

8.4. Results For 18.09.1963-16:58, Çınarcık Earthquake

8.4.1. Seismic Moment, Mw, Radius of the Source, Stress Drop Results for 18.09.1963-16:58 Earthquake

Table 8.7. Mo, Mw, R and Δσ values obtained for, 18 September 1963, 16:58, Çınarcık Earthquake

Sta.	Count.	Comp	Inst.	Mo(Nm)	Mw	R(km)	Δσ
COP	Denmark	EW	Instrument	$5.3x10^{17}$	5.82	13	2.2
COP	Denmark	NS	Wiechert	$5.3\ x10^{17}$	5.82	9.6	2.6
COP	Denmark	NS	Wiechert	$4.3\ x10^{17}$	5.76	11	1.5
COP	Denmark	Z	Galitzin	$4.8\ x10^{17}$	5.79	14	0.7
DBN	The Netherlands	EW	Galitzin	$2.4\ x10^{18}$	6.20	12	6.6
DBN	The Netherlands	Z	Galitzin	$5.1\ x10^{17}$	5.73	12	1
DBN	The Netherlands	NS	Galitzin	$2.4\ x10^{18}$	6.20	11	6.8
BRA	Slovakia	EW	Galitzin	$1.1\ x10^{18}$	5.95	17	2.3
BRA	Slovakia	NS	Wiechert	$1.1\ x10^{18}$	5.94	22	0.4
BRA	Slovakia	Z	Wiechert	$1.2\ x10^{17}$	5.31	22	0.1
TAR	Italy	NS	Wiechert	$1.4\ x10^{18}$	5.88	7.7	9.6
PAV	Italy	EW	HorizontalPendulum	$2.7\ x10^{18}$	6.29	9.1	16
ROM	Italy	NS	Wiechert	$5.1\ x10^{17}$	5.72	8.4	2.9
PAV	Italy	NS	Wiechert-200kg	$2.5\ x10^{18}$	6.27	10.7	30
PAV	Italy	Z	Wiechert	$1.6\ x10^{18}$	6.14	10.1	9.3
PAV	Italy	Z	Galitzin	$6.3\ x10^{18}$	6.44	12.2	11
RCI	Italy	EW	Wiechert	$1.5\ x10^{18}$	6.11	7.1	18
RCI	Italy	NS	Wiechert	$6.9\ x10^{17}$	5.84	14	7.2
ROM	Italy	EW	Wiechert	$5.7\ x10^{18}$	5.80	13	5.6
ROM	Italy	Z	Wiechert-1000kg	$2.0\ x10^{17}$	5.41	8.5	1.3
ROM	Italy	EW	Wiechert	$9.1\ x10^{17}$	5.93	7.3	12
SPC	Slovakia	NS	Wiechert-200kg	$1.1\ x10^{18}$	6.05	7.5	16
SPC	Slovakia	Z	Wiechert	$3.0\ x10^{17}$	5.85	8	11

TIM	Romania	EW	Wiechert	9.9×10^{17}	6.00	4	165
TIM	Romania	NS	Mainka	9.9×10^{17}	6.00	4.1	103
TRI	Romania	EW	Mainka	8.8×10^{18}	6.48	66	0.1

Table 8.8. Average values of Mo, Mw, R and Δσ for 18 September 1963, 16:58 Earthquake

Result	**Average**	**P**	**S**
Mo [Nm]	1.579×10^{18}	2.13×10^{18}	1.02×10^{18}
Mw	5.95	6.02	5.88
R [km]	13.32	11.33	15.32
Sress drop [bar]	17.28	28.07	6.50

8.4.2. Epicenter Location Results for 18.09.1963-16:58 Earthquake

I obtained 40°46.97 N- 29°11.09 E (40.78 N, 29.11 E), (rms=3.74) h=10.1 km epicentral location for the 1963.09.18, 16:58 event.

Figure 8.12. Demonstration of epicenter locations for 18.09.1963-16:58, Erdek Earthquake (1) is the result of thesis (2) is the result of ISS Bulletin (3) is the result of Taymaz *et al*., (1991)

8.4.3. Moment Tensor Inversion Results for 18.09.1963-16:58 Earthquake

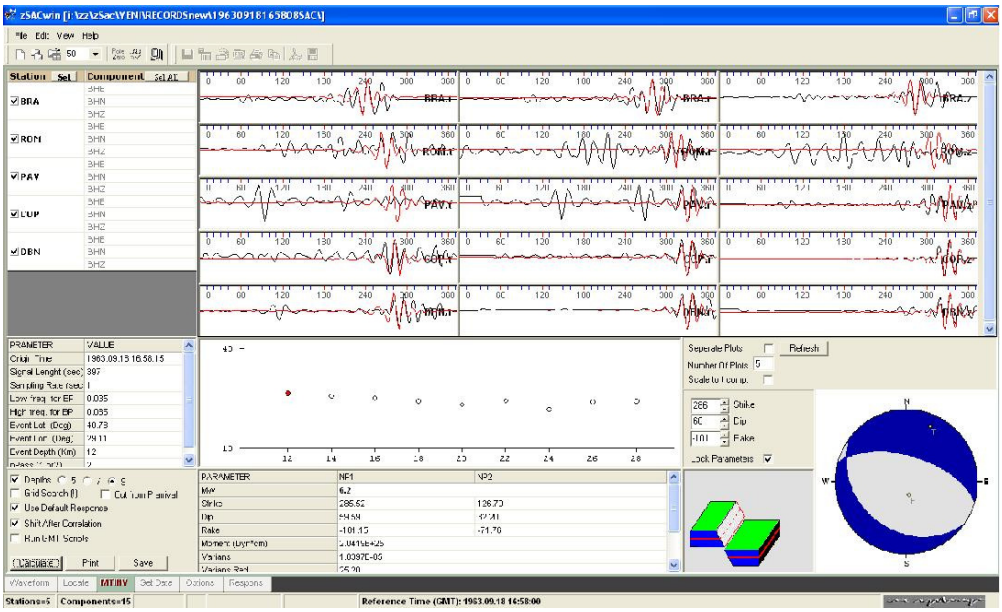

Figure 8.13. The fault plane solution for 18.09.1963-16:58 Çınarcık Earthquake on Zsac software screen

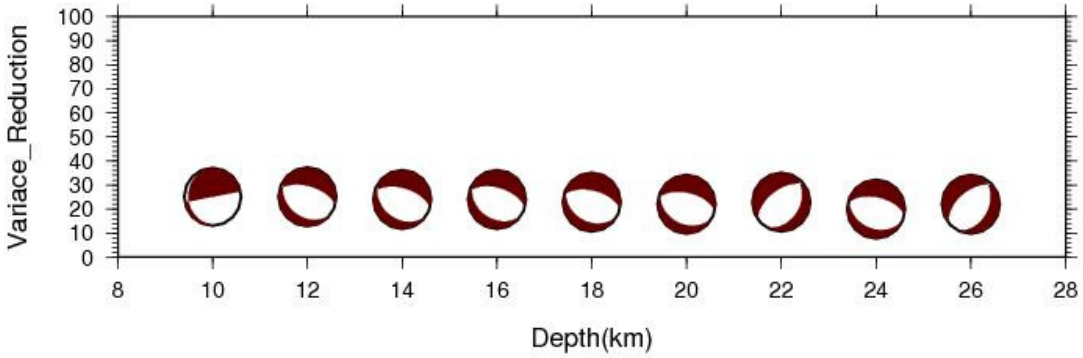

Figure 8.14. Fault plane solutions and the variance reduction with corresponding depth for 18.09.1963-16:58 Çınarcık Earthquake

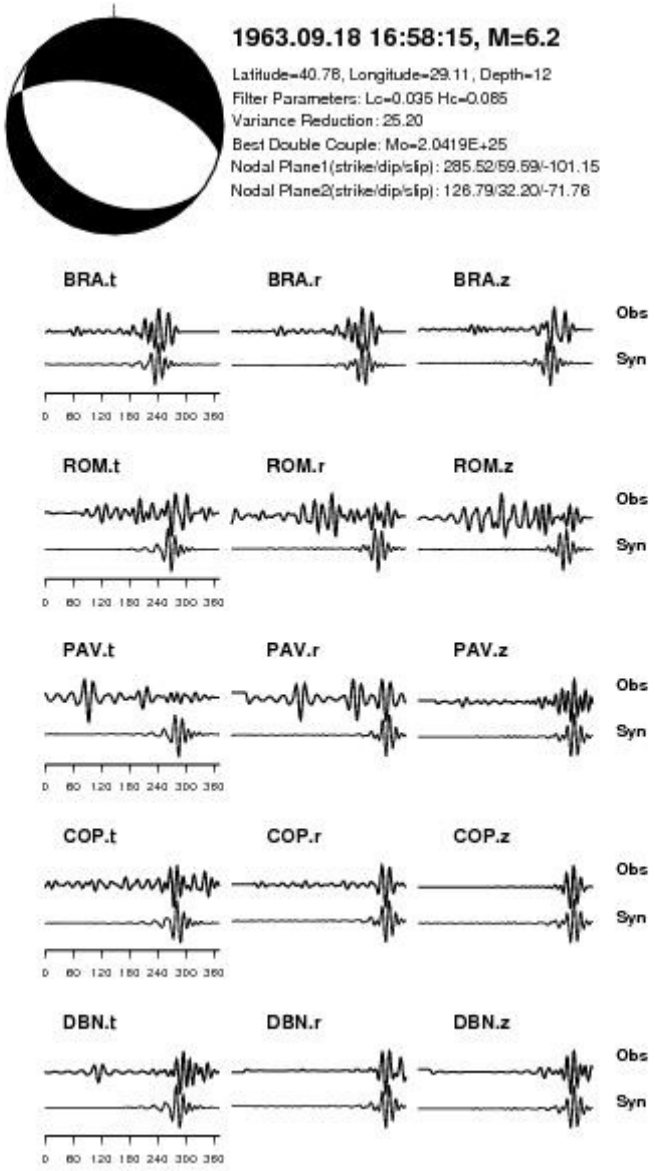

Figure 8.15. Fault plane solution and the coherency of the waveforms obtained for 18.09.1963 16:58 Çınarcık Earthquake

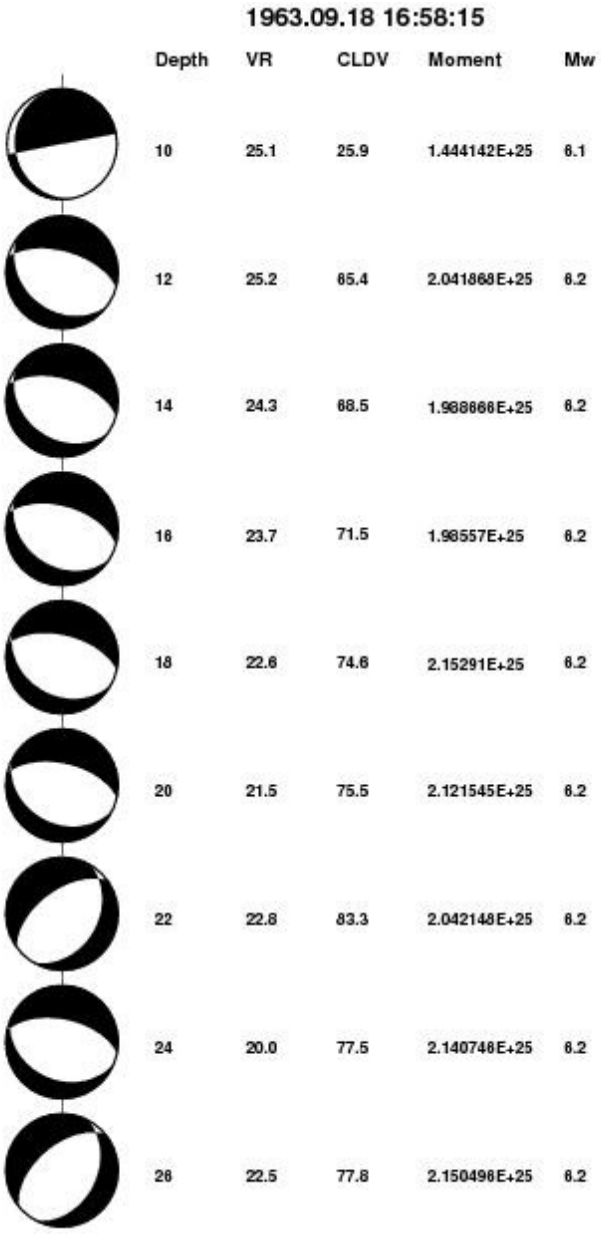

Figure 8.16. The coherency of waveforms and VR, CLVD, seismic moment, Mw and fault mechanism with corresponding depth for 18.09.1963 16:58 Çınarcık Earthquake

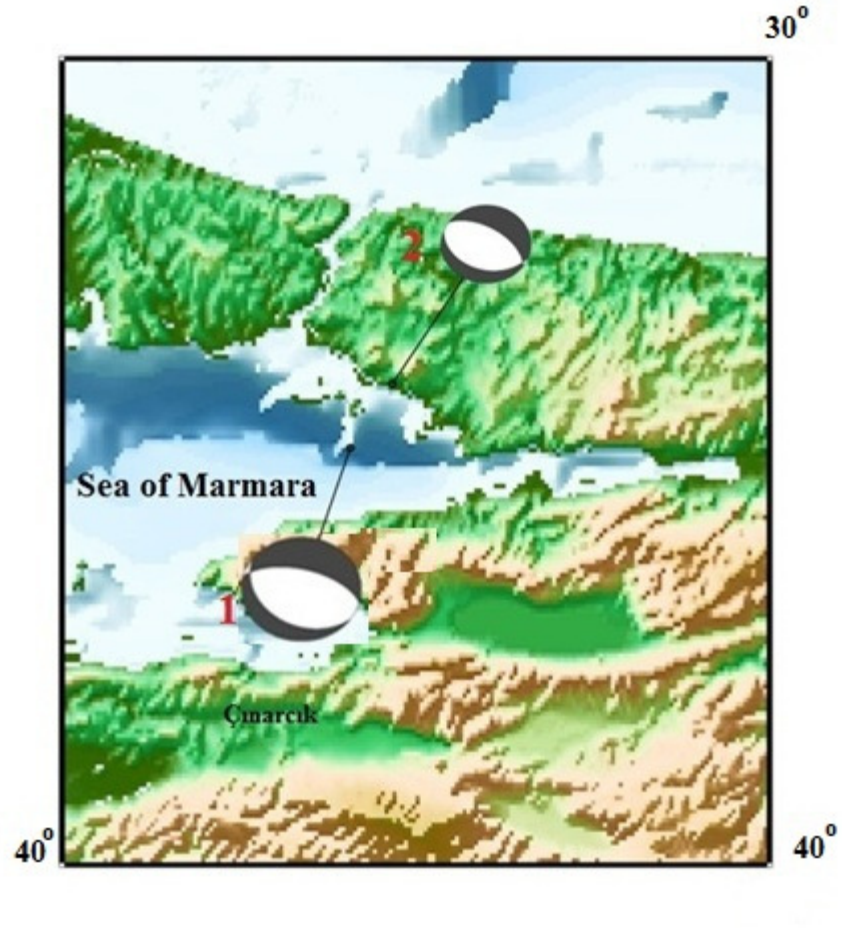

Figure 8.17. Fault plane solutions for 18.09.1963 16:58 Çınarcık Earthquake

Figure 8.17 shows the fault plane solutions for the 1963 Çınarcık Earthquake with their epicenter locations. (1) indicates the thesis result, which gave the normal fault mechanism with 285/59/-101(Strike/Dip/Rake). (2) indicates the fault solution 304/56/ 82(Strike/Dip/Rake) of Taymaz *et al*., (1991).

The fault solution for the 1963 Earthquake gives normal fault mechanism. The result is close to the solution, NE dipping, pure normal fault which was thought to have ruptured to NE margin of the Çınarcık Basin, found by Taymaz *et al*., (1991). The thesis solution has a strike more easterly than of the Taymaz *et al*., (1991). As already mentioned, the pull apart mechanism in the Marmara Sea is thought to have formed the basin structures in this region. Also, the normal faults dipping both north and south bound the deep basins in the Sea of Marmara and may be responsible for the uplifted Islands as stated by Taymaz *et al*.,

(1991). Considering the epicenter location result which was found offshore, the rupture of this earthquake may be related to the margin of Çınarcık Basin.

9. CONCLUSIONS

In this study, the seismic parameters of three large historical earthquakes, 1912 (Mürefte), 1935, Marmara Island-Erdek, 1963, Çınarcık-Yalova Earthquakes, which occured in the Marmara Region, have been reassessed using original records from mechanical seismographs. Previously, there have been studies about these earthquakes but they were based on geological studies and macroseismic observations. In this study, I studied these important earthquakes by digitizing original seismograms and analysing them through the modern techniques that were applied before, which indicates the importance of this thesis.

The Mw magnitude of 09.08.1912-01:29 Ganos Earthquake was estimated as Mw=7.13 by displacement spectra from vectorized seismic traces. Previously the magnitude of this earthquake was calculated as Ms=7.3 from Milne seismograms and a fault length was proposed about 50 km based on the surface rupture observations, by Ambrasesys (1988), which were not based on seismological analyzes. By examining original seismograms, I found the seismic moment, the radius of source rupture and stress drop values as $8.26.10^{19}$ Nm, 41.6 km and 26 bar, respectively.

In this study, the seismic parameters and fault mechanism solutions were obtained for 04.01.1935-14:41 and 16:20 Earthquakes through the modern seismological techniques based on original seismograms. This is so important because there are no previous studies that investigate the seismological properties of these earthquakes. Many of the studies were based on macroseismic observations and field surveys. There are reports about epicenter locations by Ambraseys (1988) and some catalogs but these are not beyond the macroseismic observations. Also, it is certain that ISS epicenter results for both earthquakes of 04.01.1935 are not accurate estimations. In fact, epicentral results of this study are more reliable than others since the time arrivals of the waveforms from the original seismograms are revised, which gave an opportunity to check the difference in arrival times between ISS and readings based on original records and reduce the large rms values during this process. Although there was not much, additional readings based on original seismograms enabled us to obtain a more accurate epicentral location. I obtained

40.72 N- 27.72 E for the 04.01.1935-14:41 Earthquake, which is located about 19 km NE of the epicentral location determined by Ambraseys (1988). The second large shock occurred at 16:20 was located 40.61N-27.43E, which is situated at about 27 km NW of the epicentral location (40.55N-27.43E) determined by Ambraseys (2000). I estimated magnitude Mw=6.06, seismic moment Mo=1,77.10^{18} Nm, the radius of source rupture R=15,17 km and stress drop $\Delta\sigma$ =9,47 bar for the first shock occurred at 04.01.1935. For the second shock which occurred at 16:20, I obtained a magnitude Mw=5.99, seismic moment Mo=1,46.10^{18} Nm, the radius of the circular source zone R=15.19 km and stress drop $\Delta\sigma$ =10.12 bar. A thorough re-assessment of the fault mechanism of these earthquakes was one of the object of the thesis since the information of fault characteristics are not available. I investigated the fault characteristics of these two earthquakes, which were not determined previously by analysing of original seismograms. Nalbant *et al*., (1998) modelled these two earthquakes as resulted from one rupture for investigating Coloumb stress changes. The appropriate focal mechanisms assumption when modelling these earthquakes were chosen as 100/40/-90(Strike/Dip/Rake). In this study, the fault characteristics of these two earthquakes have been determined for the first time, which demonstrates the importance of this study. I found fault characteristics for these two shocks by appliying moment tensor inversion of the waveforms obtained by vectorizing on the original records. Comparing the observed and synthetic waveforms, the coherency between them presents reliable solutions. According to my results, the first large shock occurred at 14:41 gave 140/56/-90(Strike/Dip/Rake) at a 4 km depth. This indicates that the focus of this earthquake was closer to the surface than previously reported as 20 km by Ayhan *et al*., (1986). Moment tensor inversion solutions for the second large shock, occurred at 16:20, gave the results for fault characacteristics of 352/51/-77 at a depth of 10 km, not previously reported as 40 km by Ayhan *et al*., (1986). Other finding related to these two earthquakes that they are two separate events, not related to each other. I realized the waveforms are not similar to each other in terms of their shape by comparing available original seismograms. This can be seen dominantly especially in the original seismograms of ISK station. Their nearly equal magnitude and the proximity of occurring time are also indications that the second shock at 16:22 is not the aftershock of the first shock at 14:41.

In this study, the moment magnitude of Mw=5.95, seismic moment Mo=1,57.10^{18} Nm, the radius of the circular source zone R=13.32 km and stress drop $\Delta\sigma$ =17.98 bar were

determined from the displacement spectra obtained from the analysing of original seismograms for 18.09.1963-16:58 Çınarcık Earthquake. I have located this earthquake at 40.80N-29.13N, in the Sea of Marmara not located in the off-shore (40.90N-29.20E) proposed by Taymaz *et al*., (1991). My result is closer to the epicenter location (40.80N-29.13E) of ISS. The best result obtained for 18 September 1963 16:58, Çınarcık Earthquake from moment tensor inversion applications, is a fault mechanism with 285/59/-101 (Strike/Dip/Rake) at 12 km. Previously, the fault characteristics 304/56/-82 (Strike/Dip/Rake) of this earthquake determined by Taymaz *et al*., (1991) through the modelling P- and SH- body wave. The solution of the fault mechanism for the 1963 event of this thesis has a more easterly strike than of the study of Taymaz *et al*., (1991). The finding ,as a result of this study, about the fault mechanism of the 1963 Earthquake may indicate that the fault is related to the Çınarcık Basin considering its normal fault mechanism.

In conclusion, I have investigated three important earthquakes, 09.08.1912-01:29, Ganos, 04.01.1935-14:41 and 16:20, Erdek and 18.09.1963-18:58 Çınarcık Earthquakes, that occured in the Marmara Region by analyzing original seismograms. Undoubtedly, the importance of this rigorous study is the approaching these earthquakes through the modern seismological techniques, which resulted in new findings about these earthquakes. These findings may be developed by analyzing also other historical earthquakes in the Marmara Region and attribute to understanding of its complicated seismotectonic structure and seismic hazard analysis.

REFERENCES

Aksoy, M.E., M. Meghraoui, M. Vallée, Z. Çakır, 2010, "Rupture Characateristics of the A.D. 1912 Mürefte(Ganos) Earthquake Segment of the North Anatolian Fault (western Turkey)", *Geological Society of America*, Vol.38, pp.37-57.

Ambraseys, N.N. and J.A. Jackson, 2000, "Seismicity of Sea of Marmara (Turkey) since 1500", *Geophysical Journal International,* 141, F1-F6.

Ambraseys, N.N., and C.F. Finkel, 1987, "The Saros-Marmara Earthquake of 9 August 1912", *Earthquake Eng. and Struct. Dyn.* 15, 189–211.

Ambraseys, N.N., 2002a, "The Seismic Activity of the Marmara Sea Region Over the Last 2000 years, *Bull. Seism. Soc. Am.* 92, 1–18.

Ambraseys, N.N., 2002b, "Seismic Sea-Waves in the Marmara Sea Region During the Last 20 Centuries", *J. Seismology,* 6,571-578.

Ambraseys, N. N., and & C. P. Melville, 1982, *A History of Persian Earthquakes*, Cambridge University Press, Cambridge, London, New York, New Rochelle, Melbourne, Sydney.

Altınok. Y., B. Alpar and C. Yaltırak, 2003, " Sarköy-Mürefte 1912 Earthquake's Tsunami, Extension of the Associated Faulting in the Marmara Sea, Turkey", *Journal of Seismology*, 7, 329-346.

Altınok, Y., and B. Alpar, 2006, "Marmara Island Earthquakes, of 1265 and 1935; Turkey", *Natural Hazards and Earth Systems Sciences*, 6, 999-1006.

Armijo, R., N. Pondard.,B. Meyer, G. Uçarkuş, B.M.d. Lepinay, J. Malavieille, S. Dominguez, M. A. Gustcher, S. Schmidt, C. Beck, N. Çağatay, Z. Çakır, C. İmren, K. Eriş, B. Natalin, S. Özalaybey, L. Tolun, I. Lefevre, L. Seeber, L. Gasperini, C.

Rangin, O. Emre and K. Sarıkavak, 2005 " Submarine Fault Scarps in the Sea of Marmara Pull-Apart (North Anatolian Fault): Implications for Seismic Hazard in İstanbul", *Geochemistry Geophysics Geosystems*, V.6, Q06009.

Ates, R., and A. Tabban, 1976, "9 Agustos 1912 Şarköy-Mürefte Depremi Çalışmaları Ön Raporu" , T.C. İmar ve İskan Bakanlığı, Deprem Araştırma Enstitüsü Başkanlığı, Ankara.

Ayhan, A., E. Alsan., N.Sancaklı,S.B. Üçer, 1980, "Türkiye ve Dolayları Deprem Kataloğu 1881-1980" , Boğaziçi Üniversitesi.

Batlló, J., D. Stich, B. Palombo, R. Macià and J. Morales, 2008, "The 1951, Mw 5.2 and 5.3, Jaén (Spain) Earthquake Doublet Revisited", *Bulletin of the Seismological Society of America*, 98, 1535–1545.

Batlló, J., D. Stich, R. Macià and J. Morales, 2010, Moment Tensor Inversion for the 5 July 1930 Montilla Earthquake (Southern Spain), *Seismological Research Letters*, Vol.82, No.5,

Batlló, J., T. Susagna and A. Roca, 1997, "A Processing System for Old Records of Regional Earthquakes: Analysis of the 19th November 1923 Earthquake in the Pyrenees", *Cahiers du Centre Européen de Géodynamique et de Séismologie,* 13, 149–157.

Baskoutas, I.G., I.S. Kalogeras, M. Kourouzidis and G. Panopoulou, 2000, "A Modern Technique for the Retrieval and Processing of Historical Seismograms in Greece", *Natural Hazards,* 21, 55–64.

Bergman, E., 1997, MSOP: *Manuel of Seismological Observatory Practice*, http://www.seismo.com/msop/msop_intro.html

Brune, J.N., 1970, "Tectonic Stress and the Spectra of Seismic Shear Waves from Earthquakes", *Journal of Geophysical Research* , 75, 4997–5009.

Bolt, A.B., 1968, "The Focus of the 1906 California Earthquake" , , Vol.50, pp. 457-471 February.

Bulut, F., and M. Aktar, 2007, "Accurate Relocation of İzmit Earthquake (Mw = 7.4, 1999) Aftershocks in Çınarcık Basin Using Double Difference Method", *Geophysical Research Letters, V.34,* L10307

Cadek, O., 1987, "Studying Earthquake Ground Motion in Prague from Wiechert Seismograph Records". *Gerl. Beitr. Geoph.,* 96, 438–447.

Crouse, C.B., and T. Matuschka, 1983, "Digitialization Noise and Accelerograph Pen Offset Associated with Japanese Accelerograms", *Bulletin of the Seismological Society of America*, 73, 1187–1196.

Dewey, J. and P. Byerly, 1969, "The Early History of Seismometry (to 1900)", *Bulletin of the Seismological Society of America,* 59, 183–227.

Dineva, S., J. Batlló , D. Mihailov and T. van Eek, 2002, "Source Parameters of Four Strong Earthquakes in Bulgaria and Portugal at the Beginning of the 20th Century", *Journal of Seismology,* 6, 99–123.

Dost, B. and H. Haak., 2002, *A Comprehensive Description of the KNMI Seismological Instrumentation*, Technical Report, KNMI, No: TR-245.

Dreger, D.S., 2002, *Time-Domain Moment Tensor Inverse Code (TDMT_INVC) Version 1.1*, ftp://www.orfeus-eu.org/pub/software/iaspei2003/8511_tutorial.pdf

Eaton, J.P., 1957, "Theory of the Electromagnetic Seismograph", *Bulletin of the Seismological Society of America,* Vol.47, pp.37-55.

Ekström, G., and A. Dziewonski, 1988, "Evidence of Bias in Estimation of Earthquake Size", *Nature,* 332, 319–323.

European Mediterranean Seismological Centre (*EMSC), 2010, http://www.emsc-csem.org/Earthquake/index_tensors.php*

Ergin,K., U. Guclu and Z. Uz, 1967, "A Catalog of Earthquakes for Turkey and Surrounding Area (11 A.D. to 1964 A.D.)" , Istanbul Technical University, Faculty of Mining Engineering, Istanbul, Turkey.

Ferrari, G., and C. Roversi Monaco, 2005, "Restoration and Conservation of the Scientific Documentation of Seismology". http:// storing.ingv.it/ es_web/ Data/ restoration/ restoration.html, INGV.

Gianfranco V., Gasperini P., 2003, "A Database of Revised Fault Plane Solutions for Italy and Surrounding Regions", *Computers & Geosciences*, 29, 903–909

Grabrovec, D. and I. Allegretti, 1994, "On the Digitizing of Historical Seismograms", *Geofizika,* 11, 27–31.

Hanks, T.C. and M. Wyss, 1972, "The Use of Body-Wave Spectra in the Determination of Seismic-source Parameters", *Bulletin of the Seismological Society of America*, 62, 561–589.

Hanks, T., H. Kanamori, 1979, " A Moment Magnitude Scale" , *Journal of Geophysical Research*, 84, 2348–2350.

Havskov, J., L. Ottemöller, 2008, "Processing Earthquake Data", Book in Preparation, Preliminary Version at SEISAN web site, September.

Herak, M., I. Allegretti, D. Herak, and S.J. Duda, 1998, "Numerical Modeling of the Observed Wiechert Seismograph Magnification, *Pure and Applied Geophysics* 152, 539-550.

Istituto Nazionale di Geosifica e Vulcanologia (INGV), 2006, http://storing.ingv.it/es_web/Data/events/60302tab.htm

Inoue, R. and T. Matsumoto, 1988, "Digitization and Processing of the J.M.A. Strong Motion Records in the Period of 2 to 20 sec. from Nine Great Earthquakes", in WHK. Lee, H. Meyers, and K. Shimazaki (eds.), *Historical Seismograms and Earthquakes of the World*, Academic Press, San Diego.

Jost , M. L. and R.B. Herrmann, 1989, "A Student's Guide to and Review of Moment Tensors", *Seismological Research Letters*, Vol.60, pp.37-57.

Kanamori, H. ,1988, "Importance of Historical Seismograms for Geophysical Research", in WHK. Lee, H. Meyers, and K. Shimazaki (eds.), *Historical Seismograms and Earthquakes of the World*. Academic Press, San Diego.

Keilis-Borok, V.I., 1960, "Investigation of the Mechanism of Earthquakes", *Sov. Res. Geophys*., 4, 29.

Kalafat, D., Gürbüz, C., Üçer, S.B., 1987, Batı Türkiye'de Kabuk ve Üst Manto Yapısının Araştırılması. *Deprem Araştırma Bülteni, 59 43-64*.

Kalafat, D., Y. Güneş, M. Yılmazer, M. Kara, P. Deniz, K. Kekovalı, H.S. Kuleli, L. Gülen, M. Yılmazer, N.M. Özel. ,2007, "A Revised and Extended Earthquake Catalogue for Turkey since 1900(M ≥4.0) Boğaziçi University.

Kalafat, D., K. Kekovalı, Y. Güneş, M. Kara, P. Deniz, M. Berberoğlu, ,2009, "A Catalog of Source Parameters of Moderate and Strong Earthquakes for Turkey and is Surronding Area(1938-2008)", Boğaziçi University.

Lienert, B. R. E, 1994, HYPOCENTER 3.2: A Computer Program for Locating Earthquakes Locally, Regionally and Globally, Technical report, Hawaii Institute of Geophysics & Planetology.

Lomax, A., 2005, ″ A Reanalysis of the Hypocentral Location and Related Observations for the Great 1906 California Earthquake", *Bulletin of the Seismological Society of America*, Vol.95, pp. 861-877.

Maggi, A., Sunday Seismometer, http:// eost.u-strasbg.fr/ alessia/ papers/ SundaySeismometer.pdf.

Madariaga. R, 1976, Dynamics of an Expanding Circular Fault, *Bulletin of the Seismological Society of America,* 60, 639–666.

Michelini, A., B. De Simoni, A. Amato, and E. Boschi ,2005, "Collecting, Digitizing and Distributing Historical Seismological Data". *EOS Trans. AGU* 12 July 2005, 28/86

Mihailoviç, J., 1927 , Grandes Le catastrophes Seismiques la me de Marmara, Institut Seismologiue de I'Universite de Belgrad.

Nalbant. S., A. Hubert and G.C.P. King, 1991, "Stress Coupling Between Earthquakes in Northwest Turkey and the North Aegean Sea ", *Journal of Geophysical Research"*, 103, 24469-24486.

Öztin, F., 1987, "9 Agustos 1912 Şarköy-Mürefte Depremi", *Deprem Araştırma Bülteni*, 56, 91-127.

Özçiçek, B., 1966-1967, "18 Eylül 1963 Doğu Marmara Depremi Etüdü", *Jeofizik* 1(2), 49–69.

Papadimitriou, E.E., V.G. Karakostas and B.C. Papazachos, 2001, "Rupture Zones in the Area of the 17.08.99 Izmit (NW Turkey) Large Earthquake (Mw 7.7) and Stress Changes Caused by Its Generation", *Journal of Seismology,* 5, 269–276.

Pınar, N. and Lahn, E., 1952, *Türkiye Depremleri İzahlı Kataloğu*, Bayındırlık ve İskan Bakanlığı, İmar Reisliği Yayınları, Vol. 6, No. 36.

Pintore, S., M. Quintiliani and D.Franceschi, 2005, "Teseo: A Vectorizer of Historical Seismograms", *Computers & Geosciences,* 31, 1277–1285.

Reid, H. F., 1910, "*The California Earthquake of April 18, 1906*", Report of the State Earthquake Investigation Commission, Vol.2, The Mechanics of the Earthquake, 192 pp., Carnegie Inst. of Wash., Washington, D. C.

Samardjieva, E., G. Payo and C. Lopez, 1988, "Creation of Digital Database for XXth Century Historical Earthquakes Occured in the Iberian Area", *Pure and Applied Geophysics*, 152, 139-163.

Schlupp, A., and A. Cisternas, 2007, "Source History of the 1905 Great Mongolian Earthquakes (Tsetserleg, Bolnay)", *Geophysical Journal International*, 169, 1115–1131.

Saint Louis University Earthquake Center http:// www.eas.slu.edu/ Earthquake_Center/ Instruments/ galitzinz.html

Stich. D., J. Batlló, J. Morales, R. Macià and S. Dineva, 2003, "Source Parameters of the 1910 Mw=6.1 Adra Earthquake (Southern Spain)", *Geophysical Journal International,* 155,539-546.

Stich D., J. Batlló, R. Macià, P. Teves-Costa, and J. Morales, 2005, "Moment Tensor Inversion with Single-Component Historical Seismograms: The 1909 Benavente (Portugal) and Lambesc (France) Earthquakes", *Geophysical Journal International,* 162, 850-858.

Taymaz. T., J. Jackson and D. McKenzie, 1991, " Active Tectonics of the North and Central Aegean Sea", *Geophysical Journal International*, 106, 433-490.

Teves-Costa, P., J.F. Borges, I. Rio, R. Ribeiro and C. Marreiros, 1999 "Source Parameters of Old Earthquakes: Semi-Automatic Digitization of Analog Records and Seismic Moment Assessment", *Natural Hazards,* 19, 205-220.

Udías. A, 2000, *Principles of Seismology*, Cambridge University Press, Madrid.

Vannucci, G., and P. Gasperini, 2003, "A Database of Revised Fault Plane Solutions for Italy and Surrounding Regions", *Computers & Geosciences* , 29, 903-909.

Yılmazer,. M., 2009*, Türkiye'de 3-Bileşenli Kuvvetli Yer Hareketi ve Geniş Bantlı Deprem Kayıtlarından Faylanma Mekanizmalarının Belirlenmesi ve Sismotektonik Yorumları,* phD Dissertation, İstanbul University.

REFERENCES NOT CITED

Bulletin of the seismological station, Copenhagenen, No.33, 1935.

Bulletin Seismique, Praha,1935.

Estacion sismica del Observatorio, Fabra, de la Real Academia de Ciencias y Artes, Barcelona, No. 169, 1935.

Krumbach G., *Seismische Registrierungen in Jena*, 1935.

Mc Comb H. E., *List of Seismological Stations of the World*, Bulletin of the National Research Council, No.15, 1935.

Stroobant P., *Bulletin Seismique*, Uccle, 1935.

Wood.O.H., *A list of Seismological Stations of the World*, Bulletin of the National Research Council, Vol.2, No.15, 1935.

APPENDIX A. EXAMPLES OF DIGITIZED SEISMIC TRACES ON ORIGINAL RECORDS

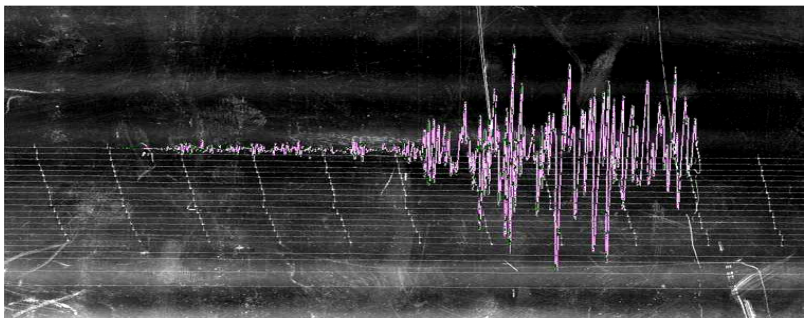

Figure A 1. Digitized seismic traces on original N-E seismogram of 08.09.1912, 01:29 Earthquake from FIR station , recorded by Omori seismometer

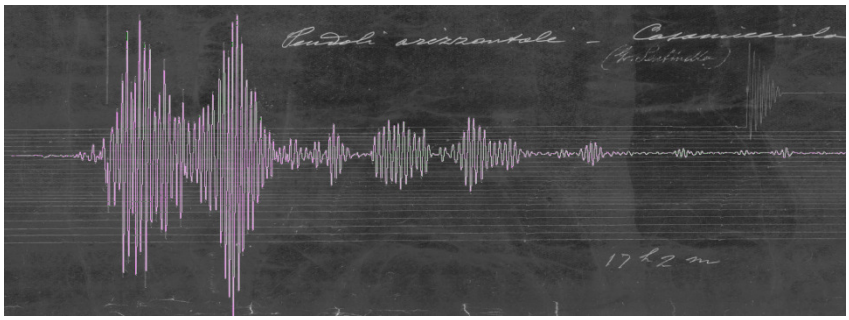

Figure A 2. Digitized seismic traces on original E-W seismogram of 08.09.1912, 01:29 Earthquake from IC1H station, recorded by Horizontal Pendulum

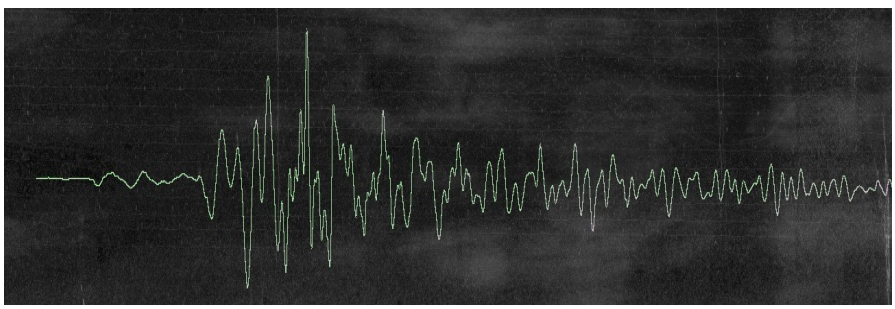

Figure A 3. Digitized seismic traces on original E-W seismogram of 08.09.1912, 01:29 Earthquake from TIF station, recorded by Reuber-Ehlert seismometer

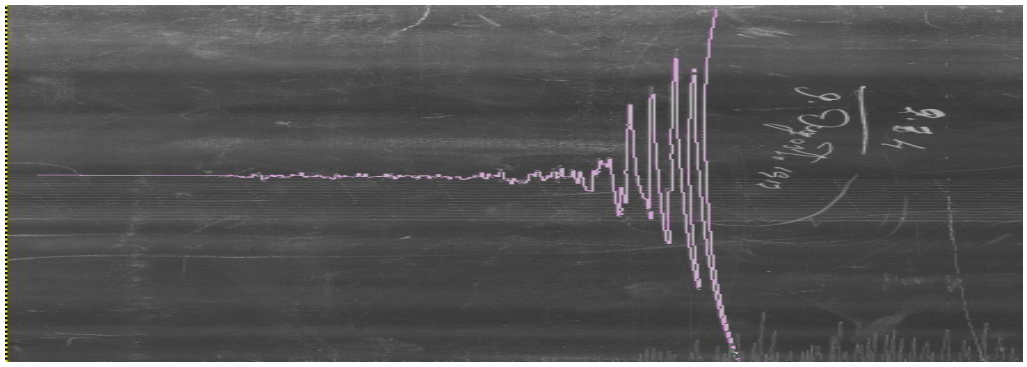

Figure A 4. Digitized seismic traces on original N-W seismogram of 08.09.1912, 01:29 Earthquake from FIR station, recorded by Horizontal pendulum

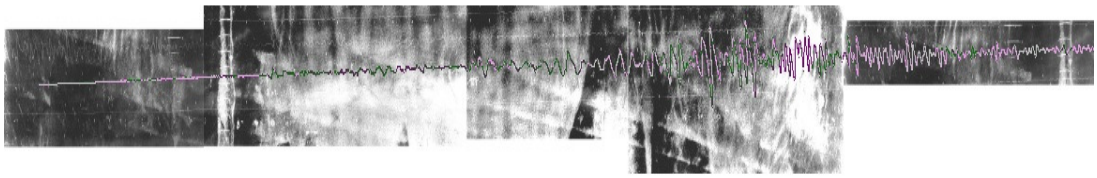

Figure A 5. Digitized seismic traces on original N-s seismogram of 08.09.1912, 01:29 Earthquake from HNG station, recorded by Omori-1 seismometer

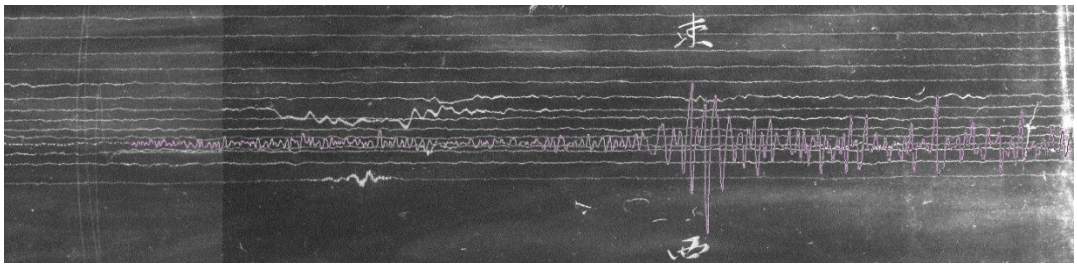

Figure A 6. Digitized seismic traces on original E-W seismogram of 08.09.1912, 01:29 Earthquake from HNG station, recorded by Omori-2 seismometer

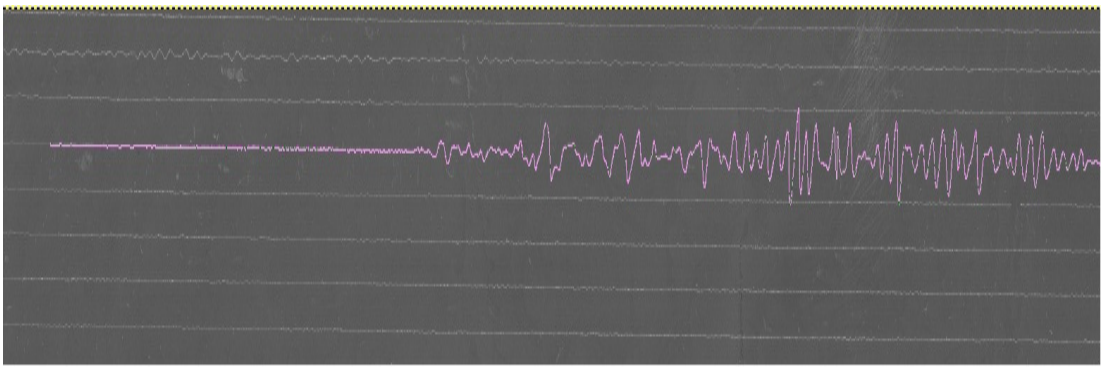

Figure A 7. Digitized seismic traces on original N-S seismogram of 04.01.1935, 14:41 Earthquake from COI station, recorded by Wiechert seismometer

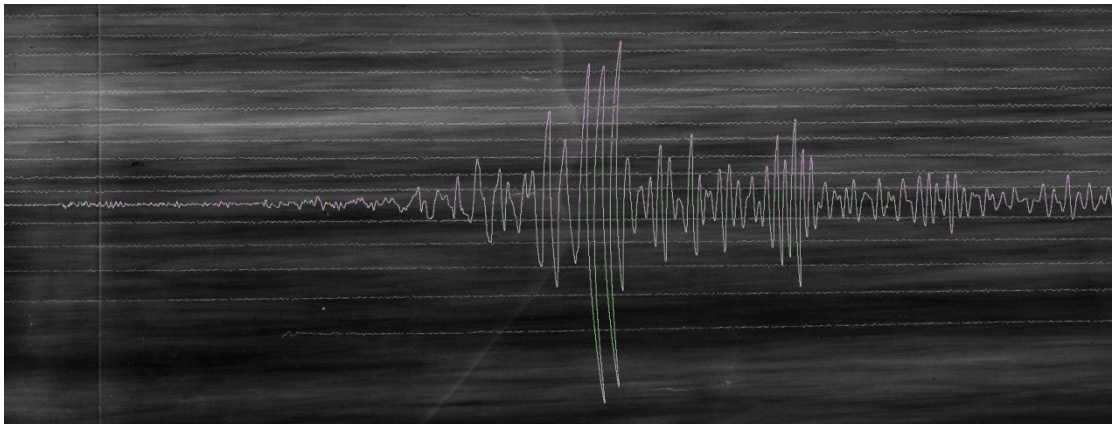

Figure A 8. Digitized seismic traces on original E-W seismogram of 04.01.1935, 14:41 Earthquake from COP station, recorded by Wiechert seismometer

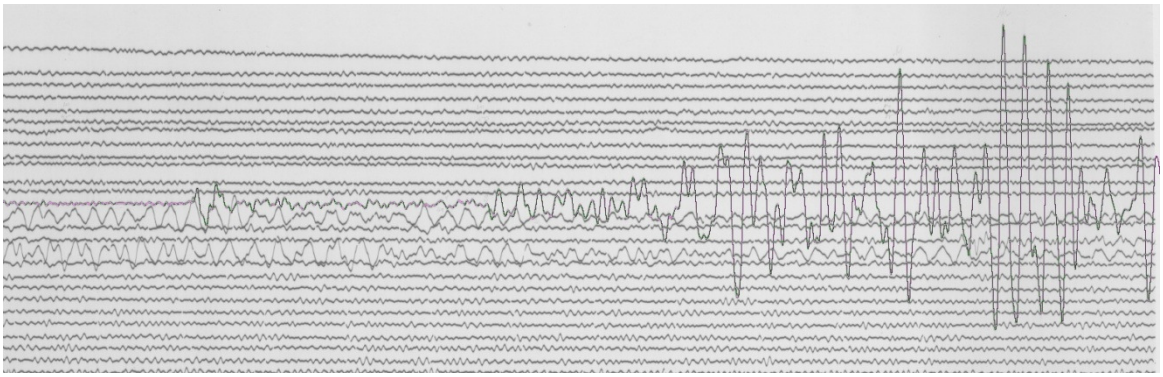

Figure A 9. Digitized seismic traces on original E-W seismogram of 04.01.1935, 14:41 Earthquake from DBN station, recorded by Galitzin seismometer

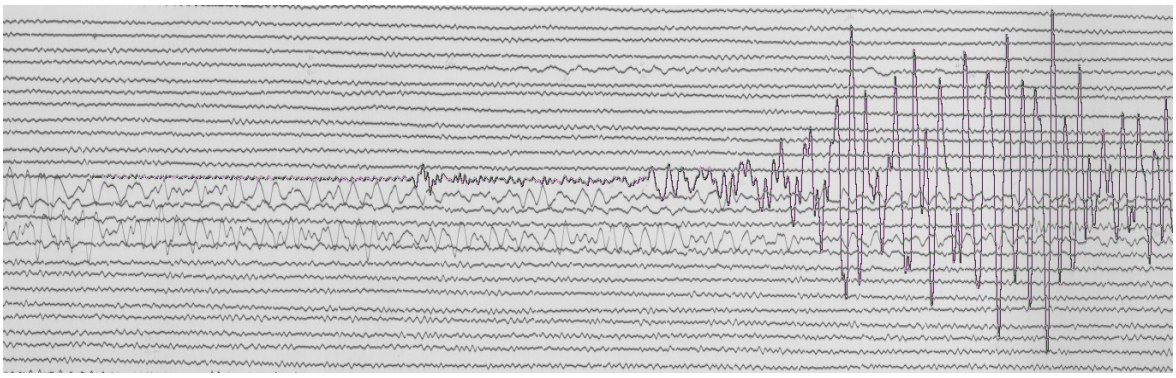

Figure A 10. Digitized seismic traces on original N-S seismogram of 04.01.1935, 14:41 Earthquake from DBN station, recorded by Galitzin seismometer

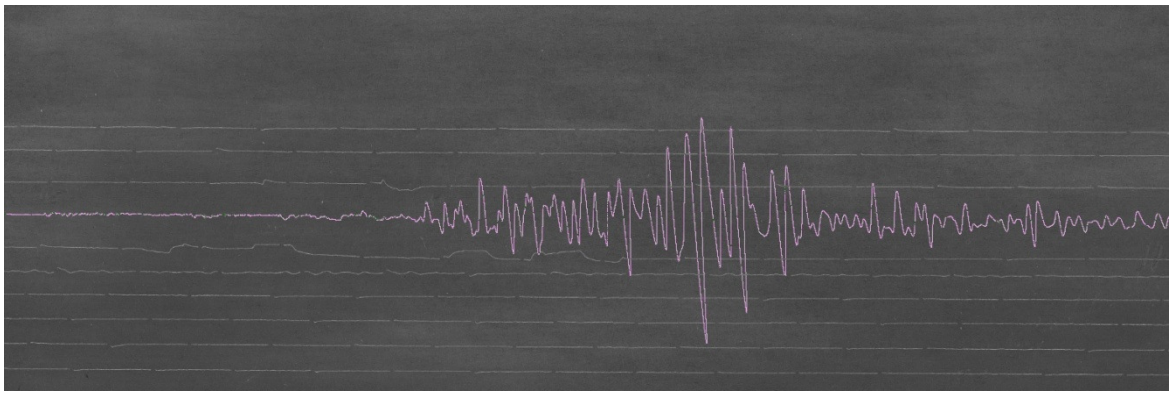

Figure A 11. Digitized seismic traces on original E-W seismogram of 04.01.1935, 14:41 Earthquake from JENA station, recorded by Wiechert(15000kg) seismometer

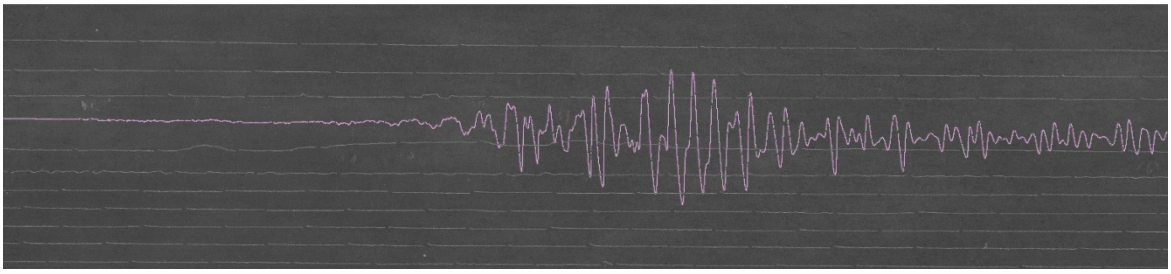

Figure A 12. Digitized seismic traces on original N-S seismogram of 04.01.1935, 14:41 Earthquake from JENA station, recorded by Wiechert(15000kg) seismometer

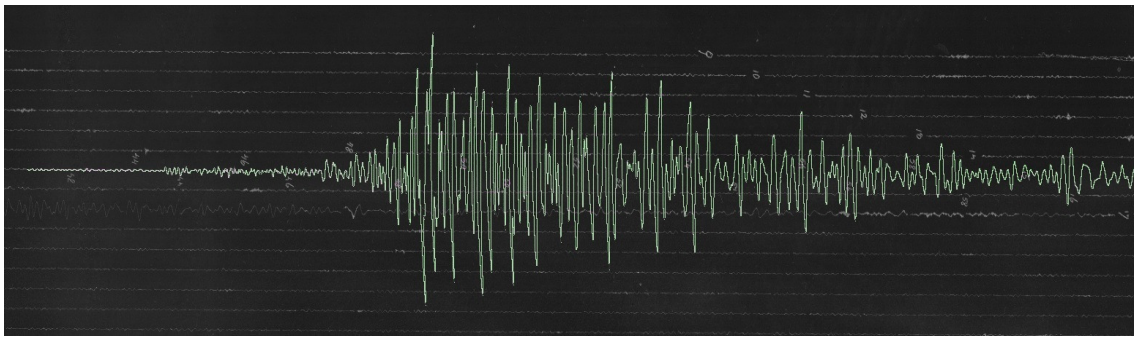

Figure A 13. Digitized seismic traces on original N-S seismogram of 04.01.1935, 14:41 Earthquake from MNH station, recorded by Wiechert seismometer

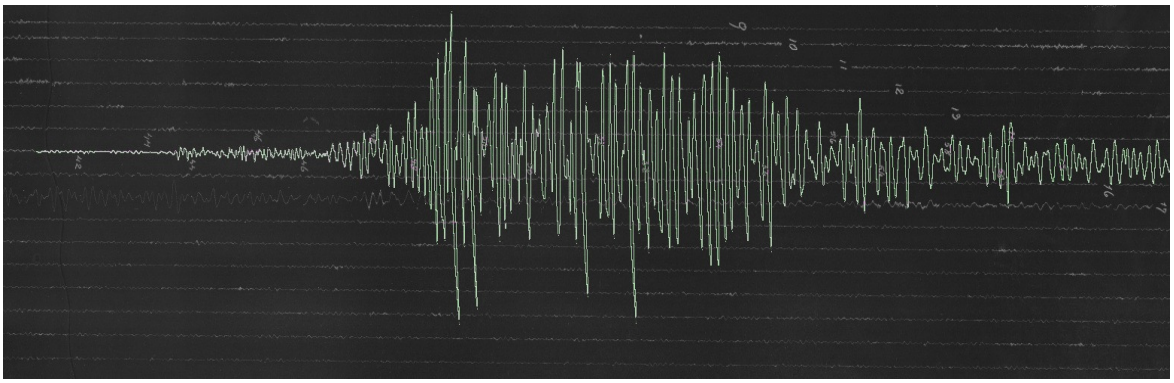

Figure A 14. Digitized seismic traces on original E-W seismogram of 04.01.1935, 14:41 Earthquake from MNH station, recorded by Wiechert seismometer

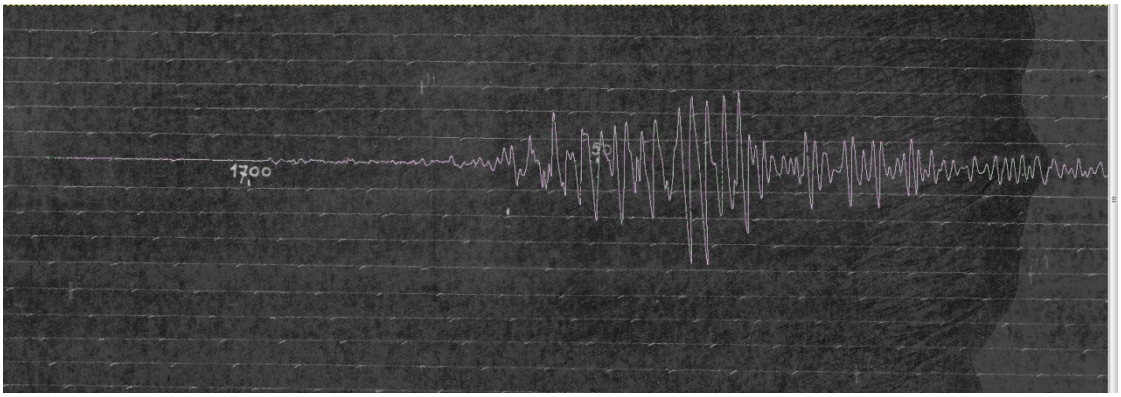

Figure A 15. Digitized seismic traces on original N-S seismogram of 04.01.1935, 14:41 Earthquake from PRA station, recorded by Wiechert seismometer

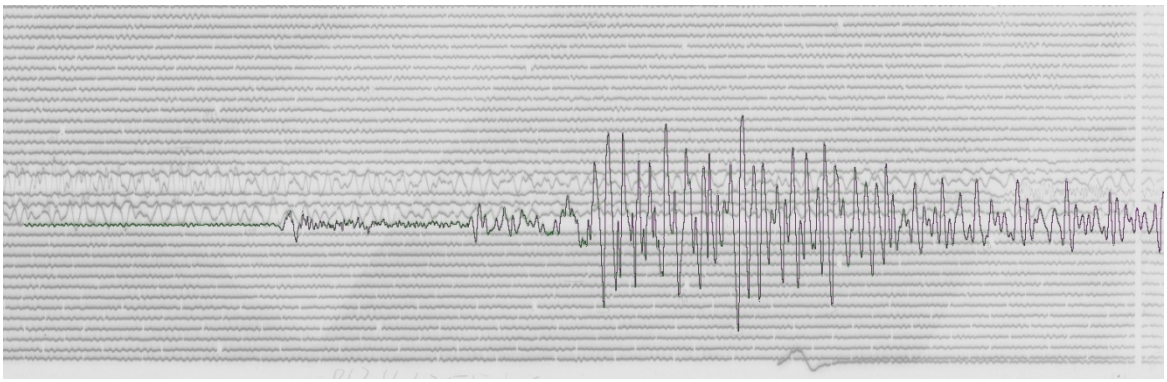

Figure A 16. Digitized seismic traces on original E-W seismogram of 04.01.1935, 14:41 Earthquake from STR station, recorded by Galitzin seismometer

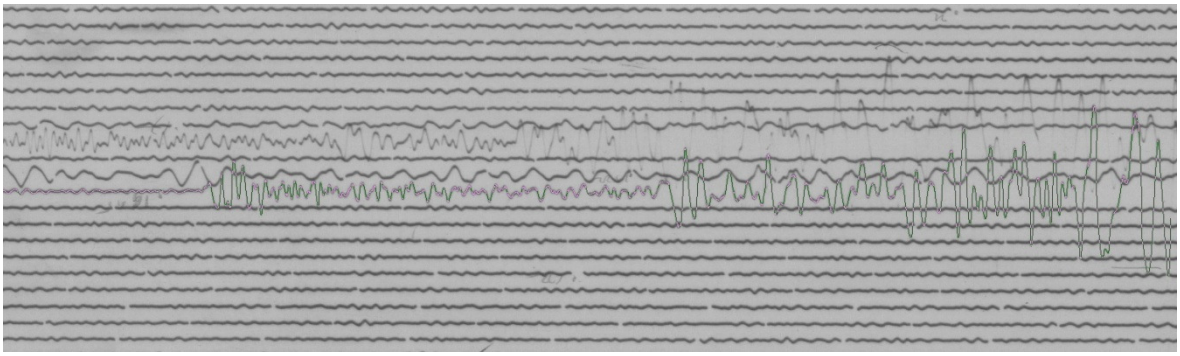

Figure A 17. Digitized seismic traces on original E-W seismogram of 04.01.1935, 14:41 Earthquake from STR station, recorded by Galtizin seismometer

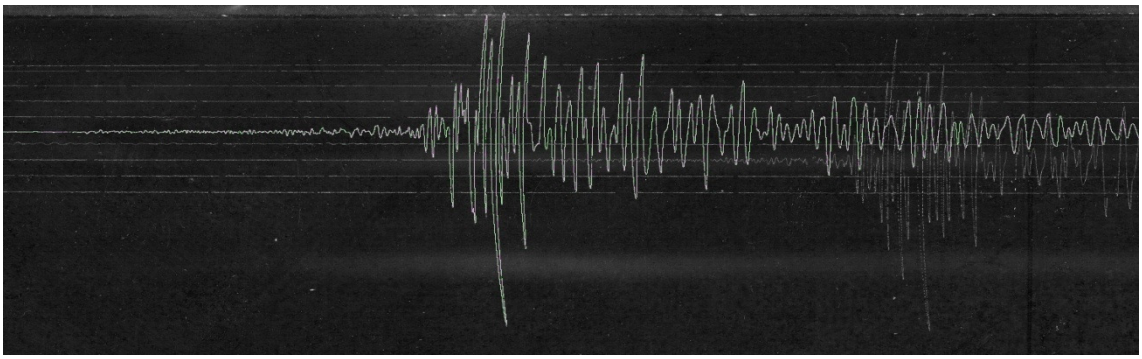

Figure A 18. Digitized seismic traces on original N-E seismogram of 04.01.1935, 14:41 Earthquake from TRS station, recorded by Wiechert seismometer

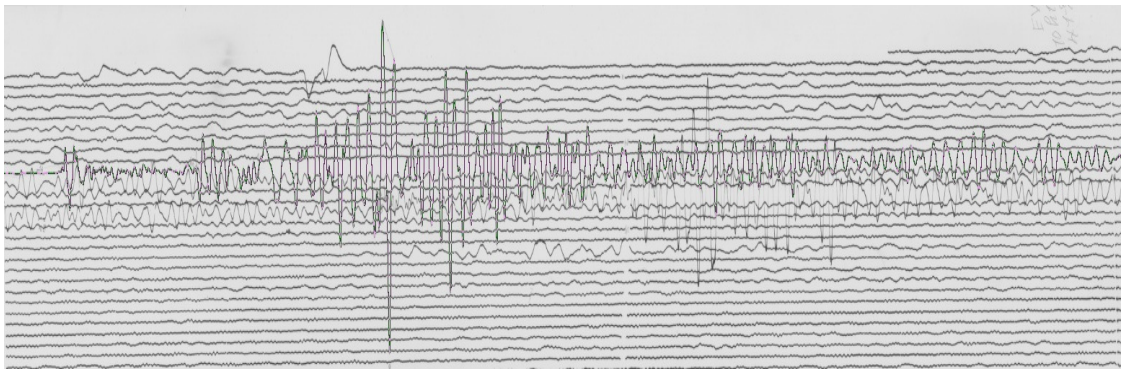

Figure A19. Digitized seismic traces on original E-W seismogram of 04.01.1935, 14:41 Earthquake from TRS station, recorded by Wiechert seismometer

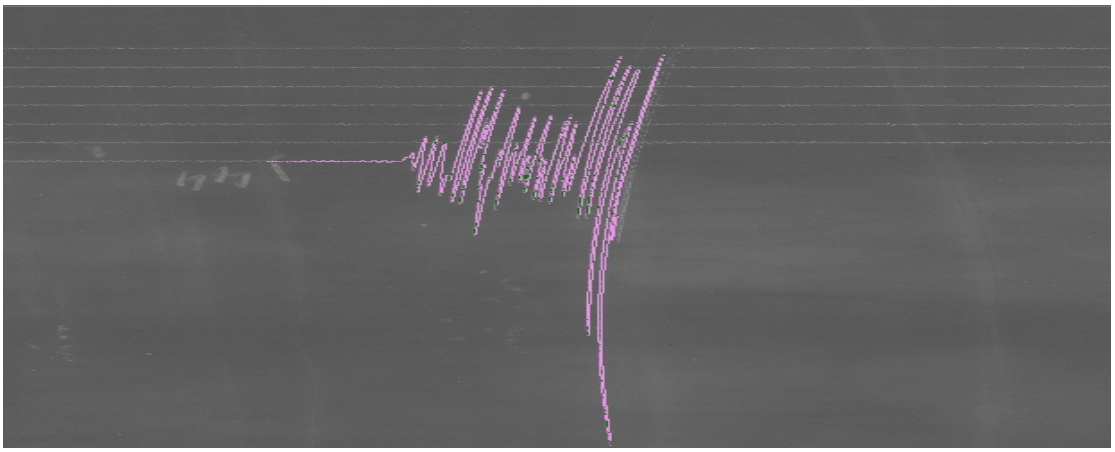

Figure A 20. Digitized seismic traces on original E-W seismogram of 04.01.1935, 14:41 Earthquake from ATH station, recorded by Wiechert seismometer

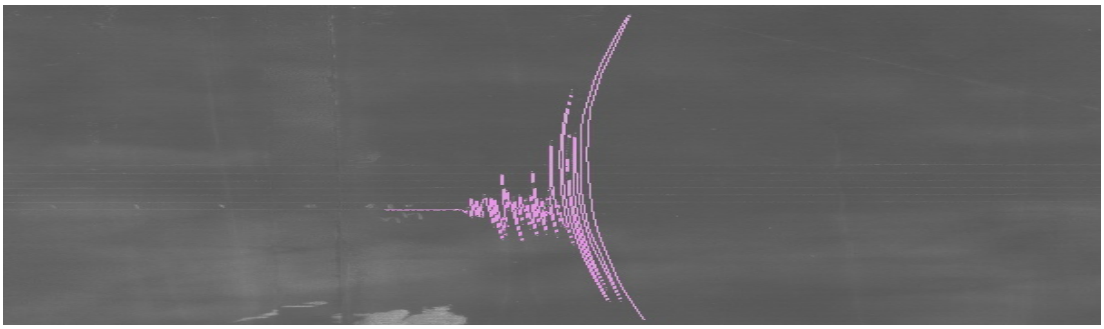

Figure A 21. Digitized seismic traces on original N-S seismogram of 04.01.1935, 14:41 Earthquake from ATH station, recorded by Wiechert seismometer

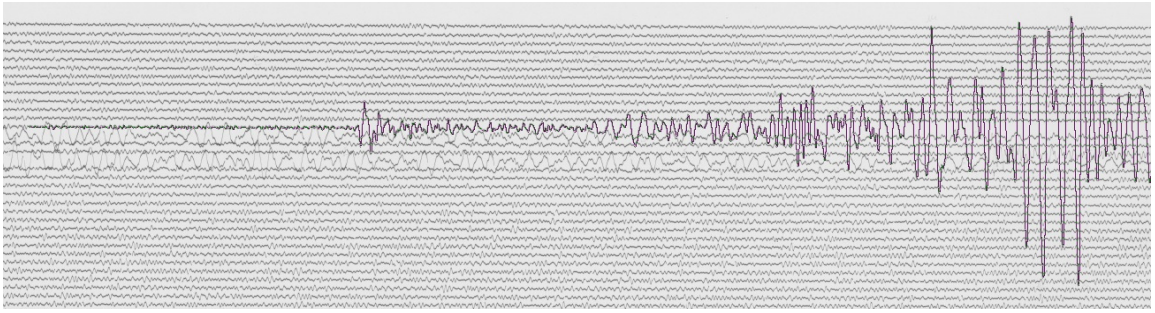

Figure A 22. Digitized seismic traces on original E-W seismogram of 04.01.1935, 14:41 Earthquake from DBN station, recorded by Galitzin seismometer

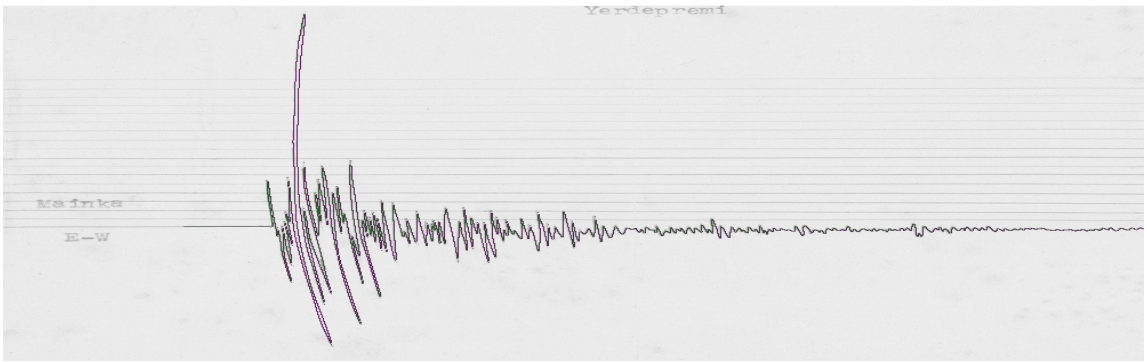

Figure A 23. Digitized seismic traces on original E-W seismogram of 04.01.1935, 14:41 Earthquake from ISK station, recorded by Mainka seismometer

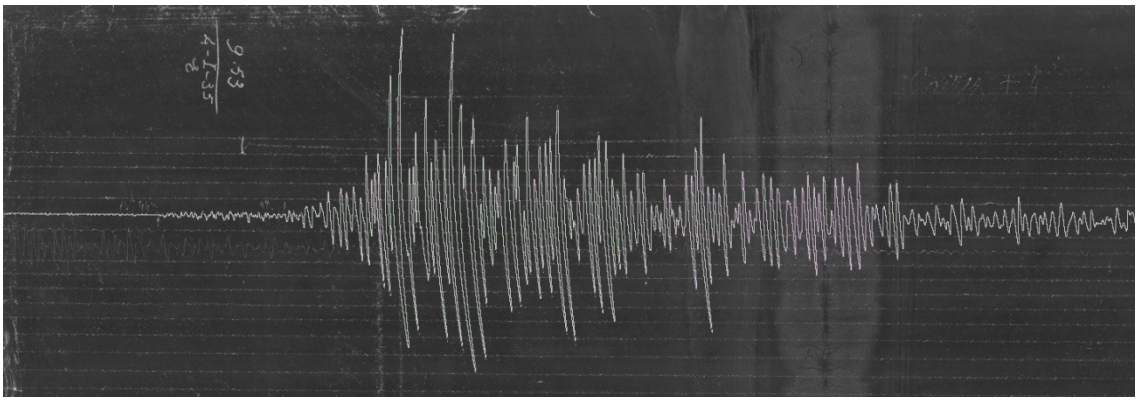

Figure A 24. Digitized seismic traces on original E-W seismogram of 04.01.1935, 14:41 Earthquake from PCN station, recorded by Wiechert seismometer

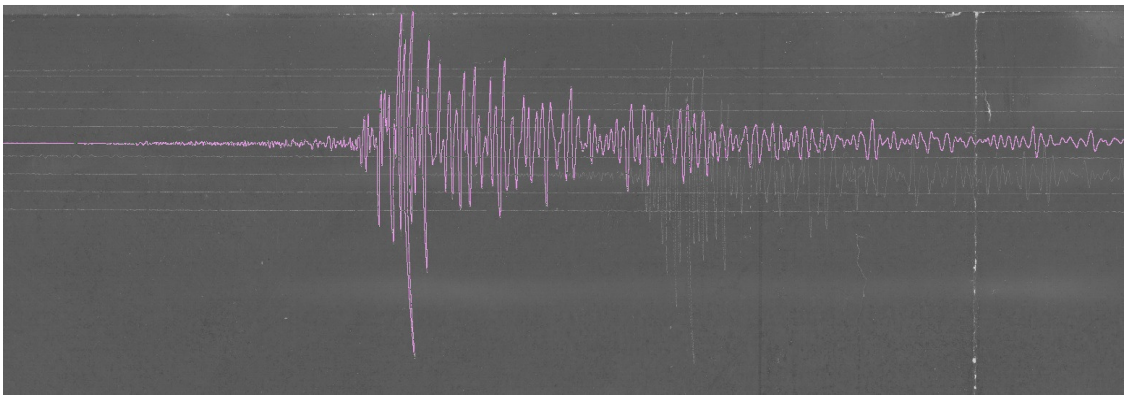

Figure A 25. Digitized seismic traces on original N-E seismogram of 04.01.1935, 14:41 Earthquake from TRS station, recorded by Wiechert seismometer

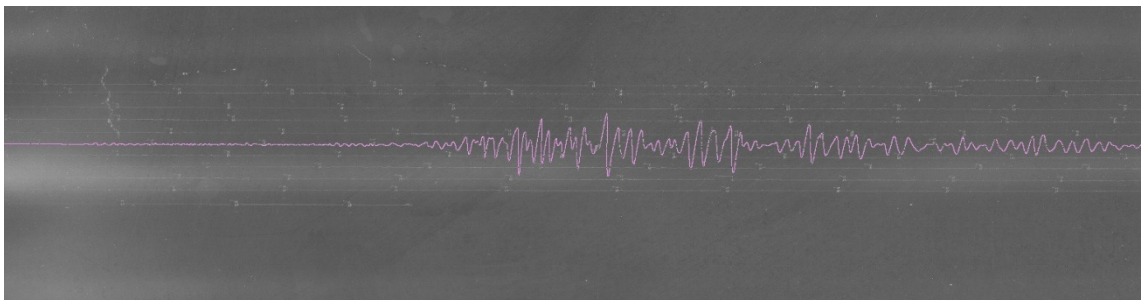

Figure A 26. Digitized seismic traces on original Z seismogram of 04.01.1935, 14:41 Earthquake from TRS station, recorded by Wiechert seismometer

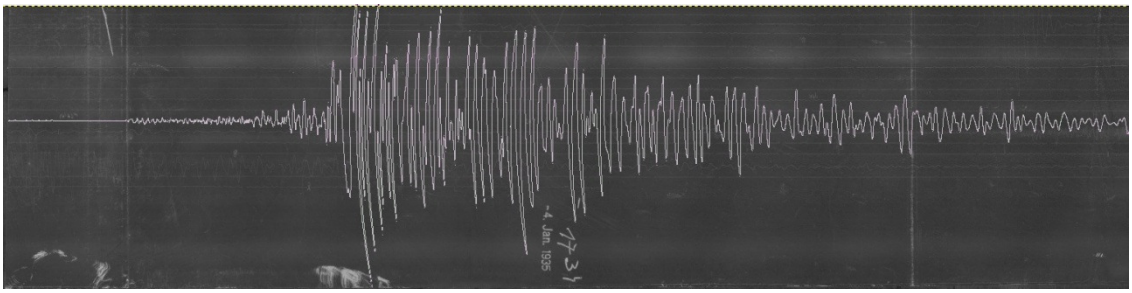

Figure A 27. Digitized seismic traces on original N-E seismogram of 04.01.1935, 14:41 Earthquake from ZAG station, recorded by Wiechert seismometer

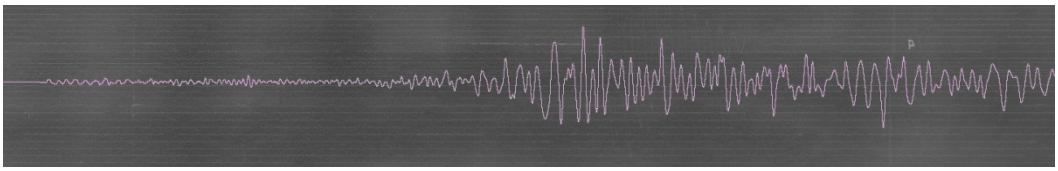

Figure A 28. Digitized seismic traces on original Z seismogram of 04.01.1935, 14:41 Earthquake from ZAG station, recorded by Wiechert seismometer

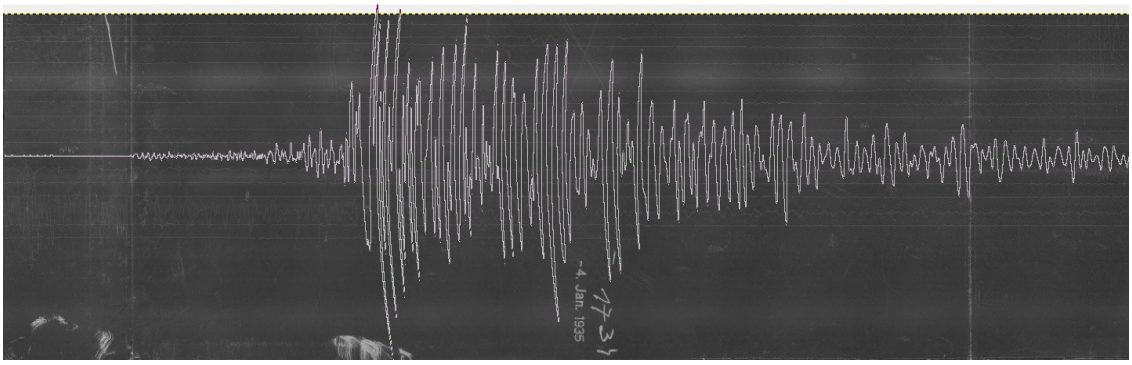

Figure A 29. Digitized seismic traces on original N-W seismogram of 04.01.1935, 14:41 Earthquake from ZAG station, recorded by Wiechert seismometer

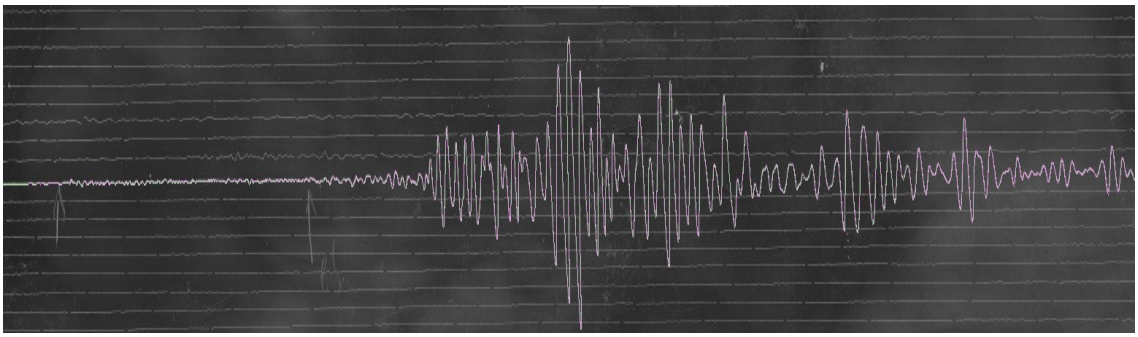

Figure A 30. Digitized seismic traces on original E-W seismogram of 04.01.1935, 14:41 Earthquake from ZUR station, recorded by Wiechert seismometer

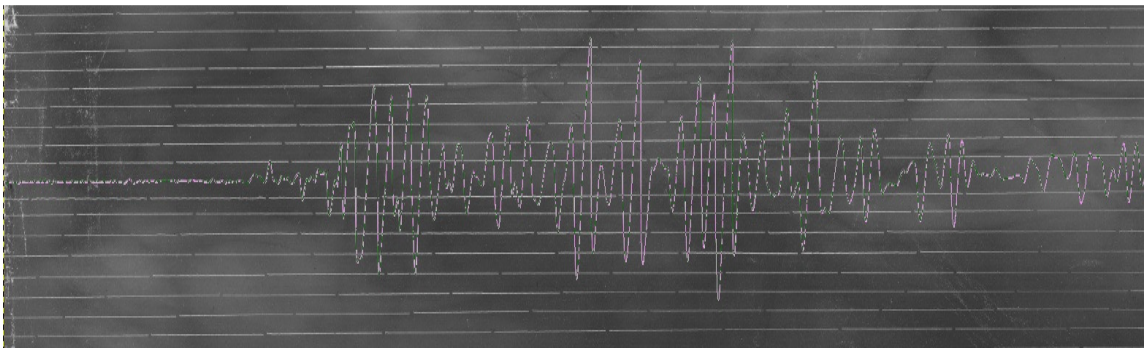

Figure A 31. Digitized seismic traces on original N-S seismogram of 04.01.1935, 14:41 Earthquake from ZUR station, recorded by Wiechert seismometer

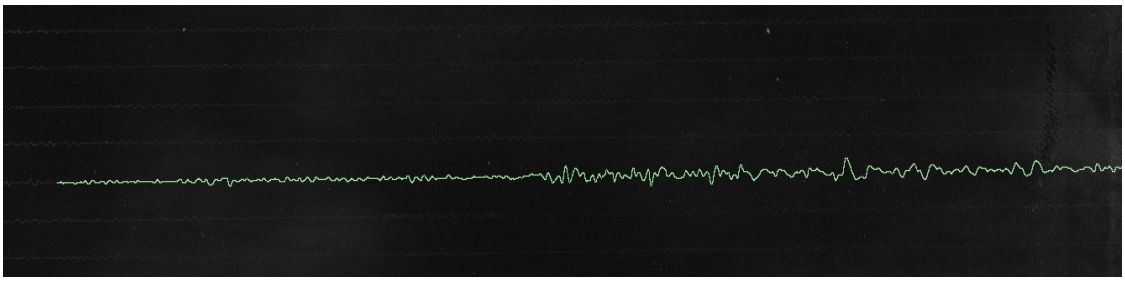

Figure A 32. Digitized seismic traces on original E-W seismogram of 04.01.1935, 16:20 Earthquake from BER station, recorded by Wiechert seismometer

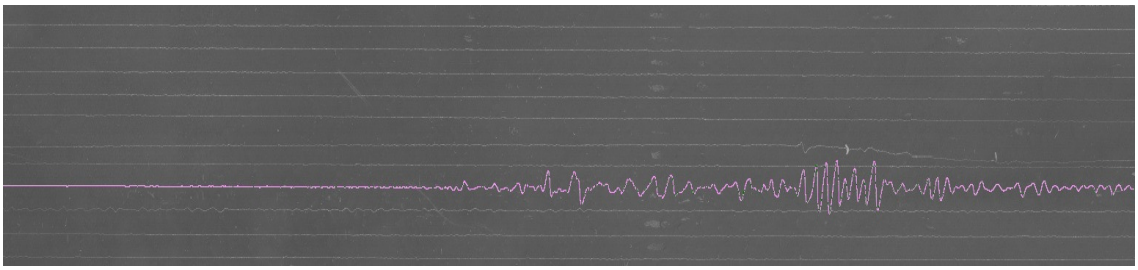

Figure A 33. Digitized seismic traces on original N-S seismogram of 04.01.1935, 16:20 Earthquake from COI station , recorded by Wiechert seismometer

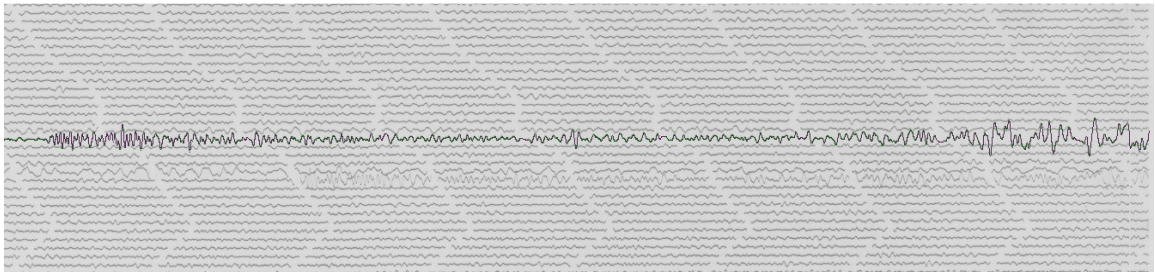

Figure A 34. Digitized seismic traces on original E-W seismogram of 04.01.1935, 16:20 Earthquake from COI station , recorded by Wood-Anderson seismometer

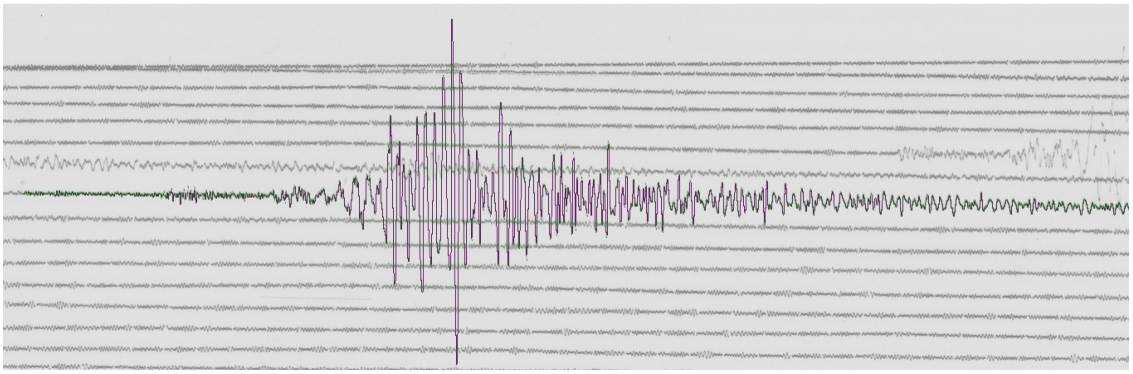

Figure A 35. Digitized seismic traces on original E-W seismogram of 04.01.1935, 16:20 Earthquake from COP station , recorded by Milne-Shawn seismometer

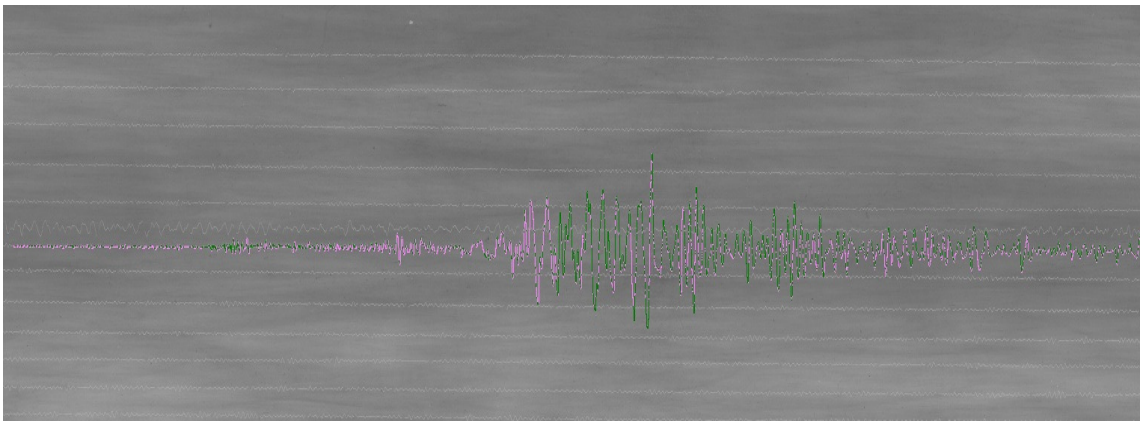

Figure A 36. Digitized seismic traces on original N-S seismogram of 04.01.1935, 16:20 Earthquake from COP station , recorded by Wiechert seismometer

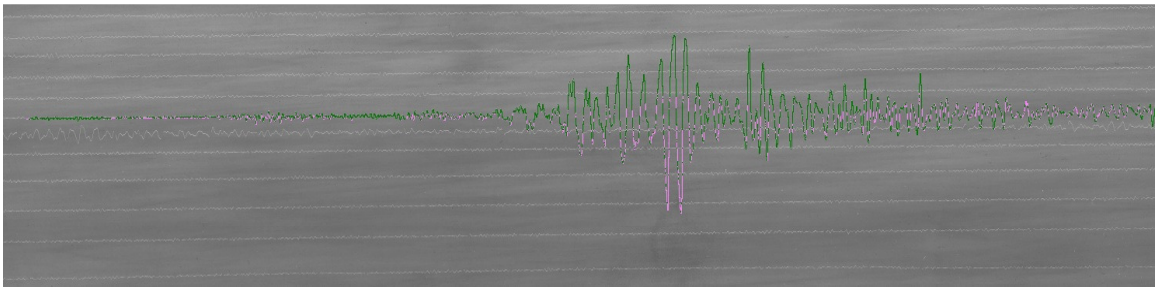

Figure A 37. Digitized seismic traces on original E-W seismogram of 04.01.1935, 16:20 Earthquake from COP station , recorded by Wiechert seismometer

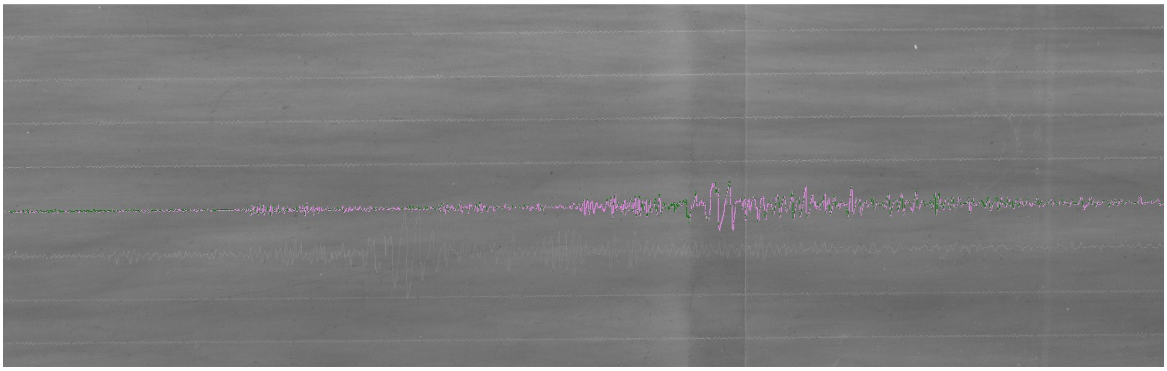

Figure A 38. Digitized seismic traces on original Z seismogram of 04.01.1935, 16:20 Earthquake from COP station , recorded by Wiechert seismometer

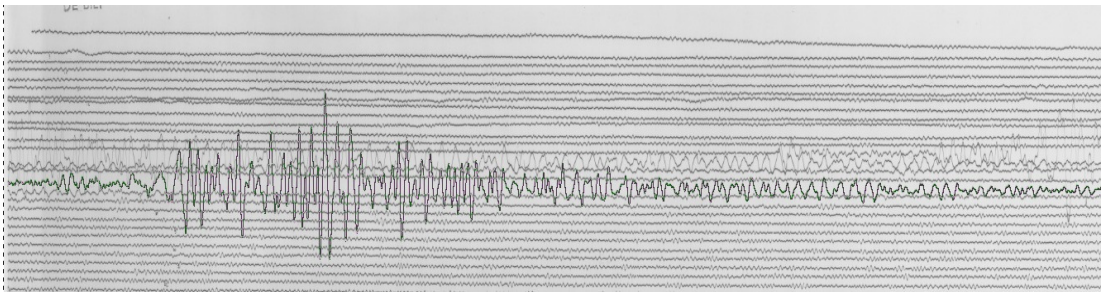

Figure A 39. Digitized seismic traces on original E-W seismogram of 04.01.1935, 16:20 Earthquake from DBN station , recorded by Galitzin seismometer

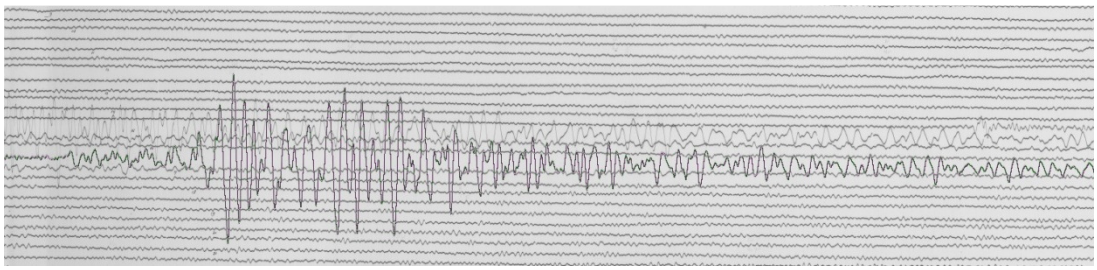

Figure A 40. Digitized seismic traces on original N-S seismogram of 04.01.1935, 16:20 Earthquake from DBN station , recorded by Galitzin seismometer

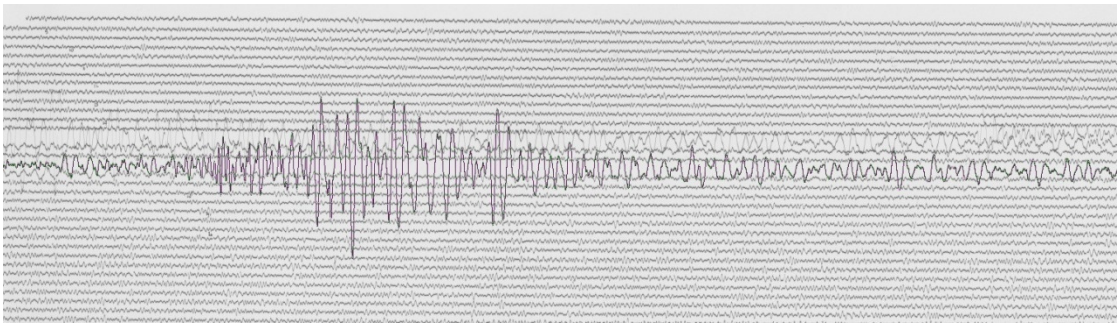

Figure A 41. Digitized seismic traces on original Z seismogram of 04.01.1935, 16:20 Earthquake from DBN station , recorded by Galitzin seismometer

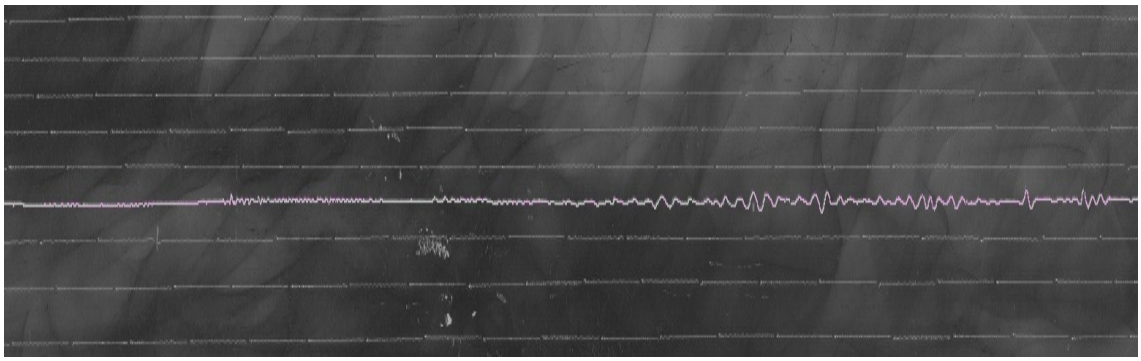

Figure A 42. Digitized seismic traces on original E-W seismogram of 04.01.1935, 16:20 Earthquake from FBR station , recorded by Mainka seismometer

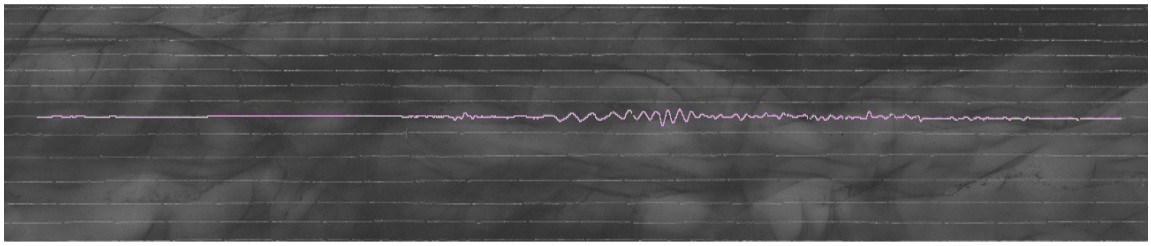

Figure A 43. Digitized seismic traces on original N-S seismogram of 04.01.1935, 16:20 Earthquake from FBR station , recorded by Mainka seismometer

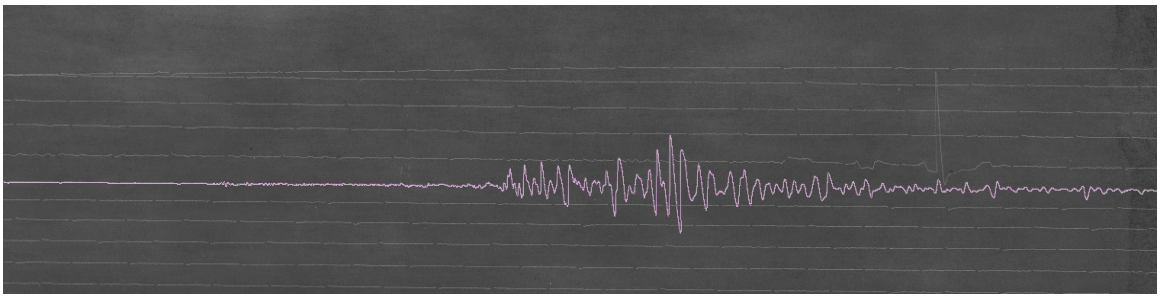

Figure A 44. Digitized seismic traces on original E-W seismogram of 04.01.1935, 16:20 Earthquake from DBN station , recorded by Wiechert(15000kg) seismometer

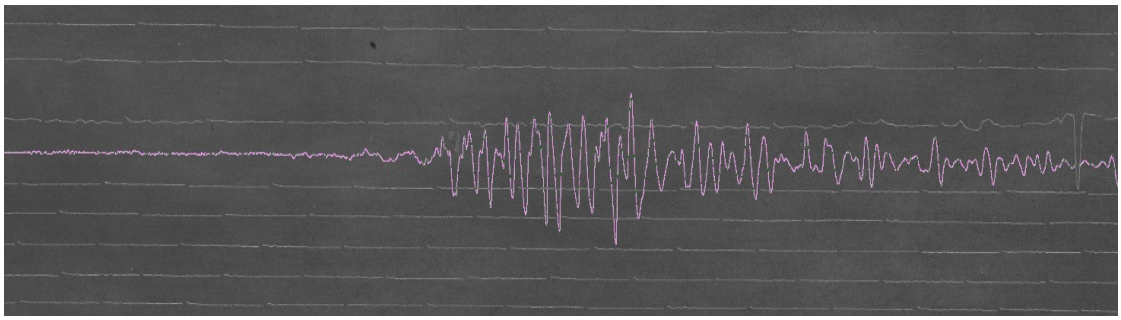

Figure A 45. Digitized seismic traces on original N-S seismogram of 04.01.1935, 16:20 Earthquake from DBN station , recorded by Wiechert(15000kg) seismometer

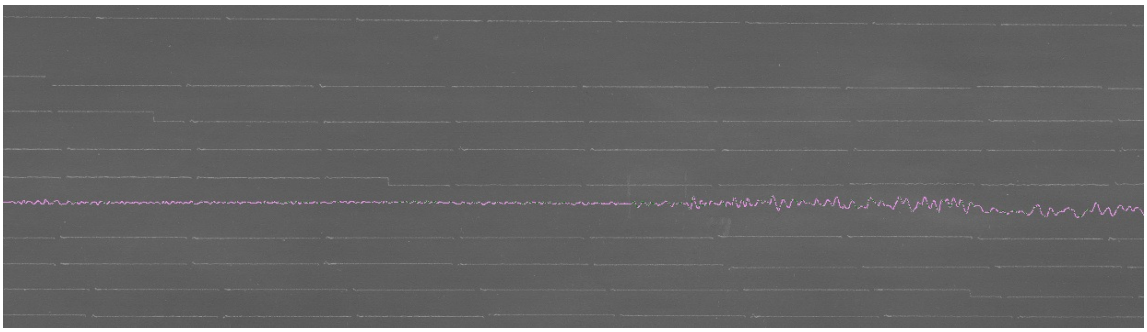

Figure A 46. Digitized seismic traces on original Z seismogram of 04.01.1935, 16:20 Earthquake from DBN station , recorded by Wiechert(15000kg) seismometer

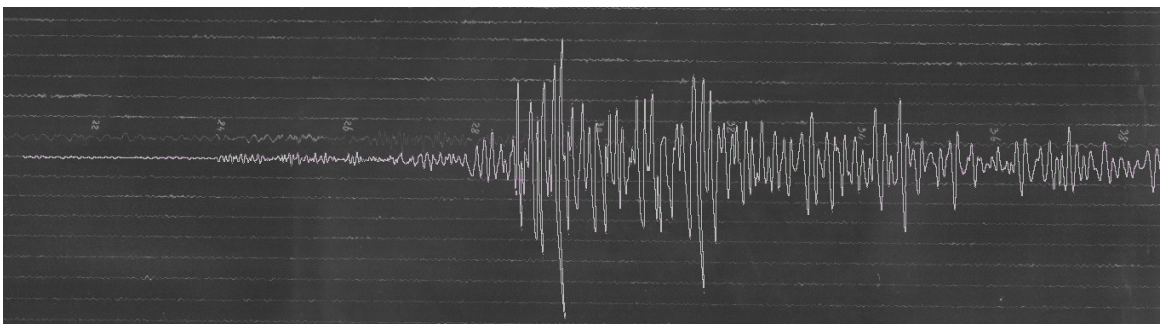

Figure A 47. Digitized seismic traces on original E-W seismogram of 04.01.1935, 16:20 Earthquake from MNH station , recorded by Wiechert seismometer

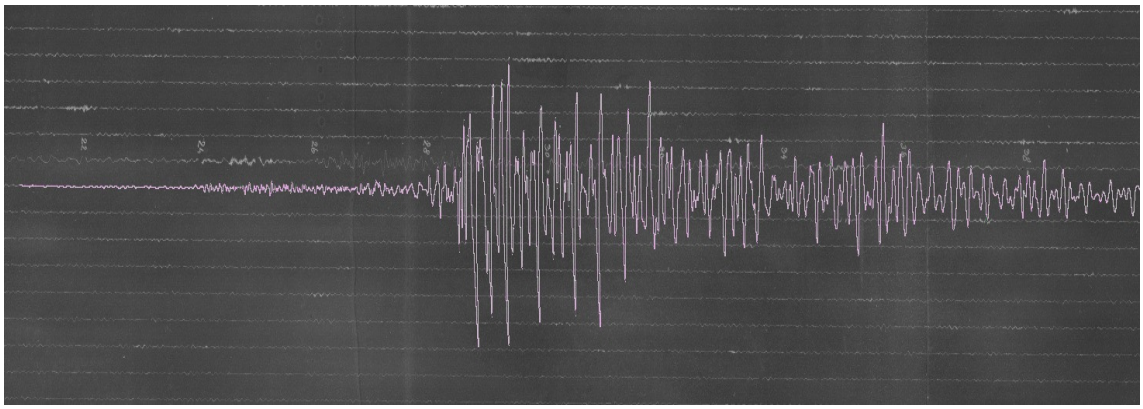

Figure A 48. Digitized seismic traces on original N-S seismogram of 04.01.1935, 16:20 Earthquake from MNH station , recorded by Wiechert seismometer

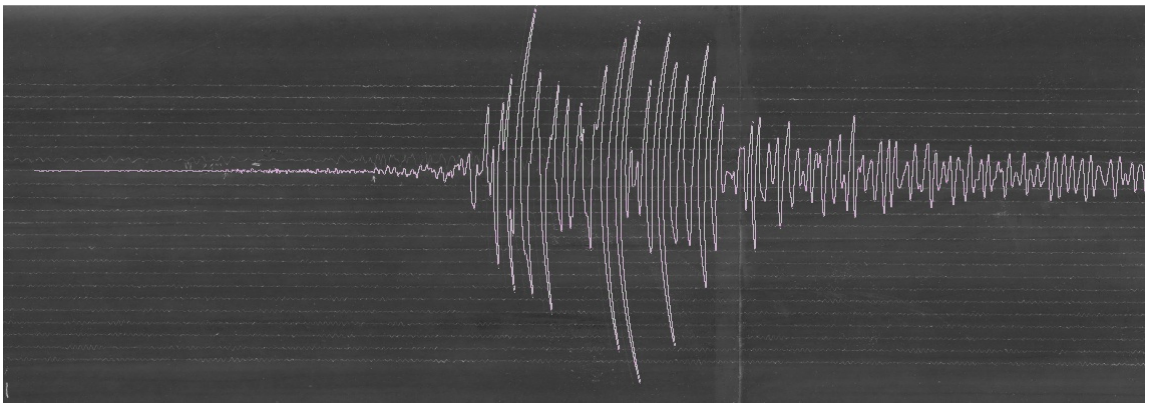

Figure A 49. Digitized seismic traces on original N-S seismogram of 04.01.1935, 16:20 Earthquake from PCN station , recorded by Wiechert seismometer

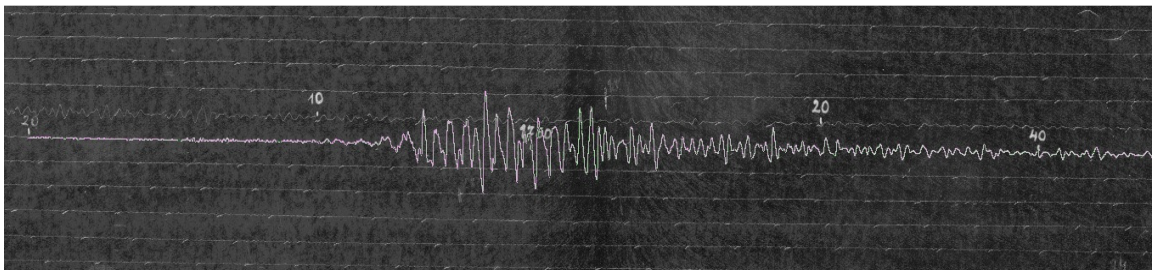

Figure A 50. Digitized seismic traces on original N-S seismogram of 04.01.1935, 16:20 Earthquake from PRA station , recorded by Wiechert seismometer

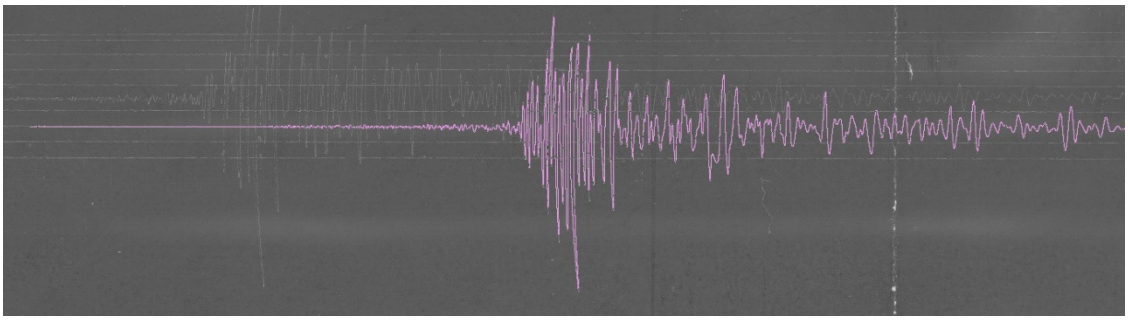

Figure A51. Digitized seismic traces on original N-S seismogram of 04.01.1935, 16:20 Earthquake from TRS station , recorded by Wiechert seismometer

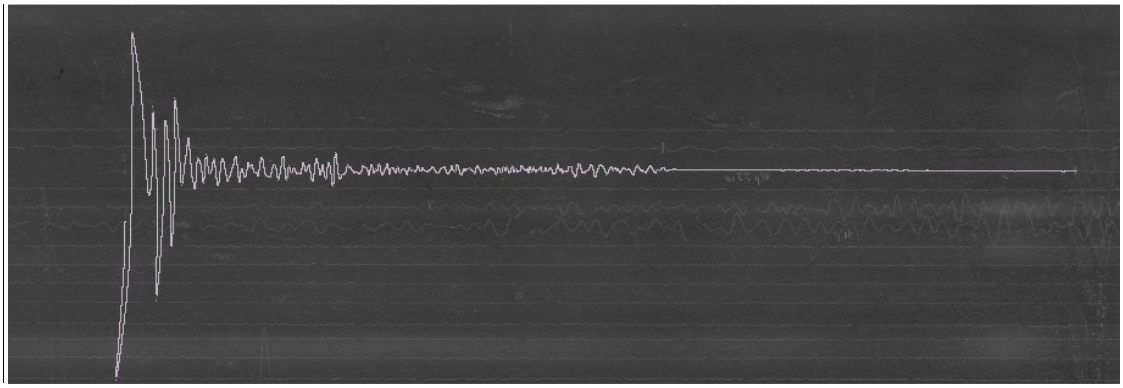

Figure A 52. Digitized seismic traces on original N-E seismogram of 04.01.1935, 16:20 Earthquake from ZAG station , recorded by Wiechert seismometer

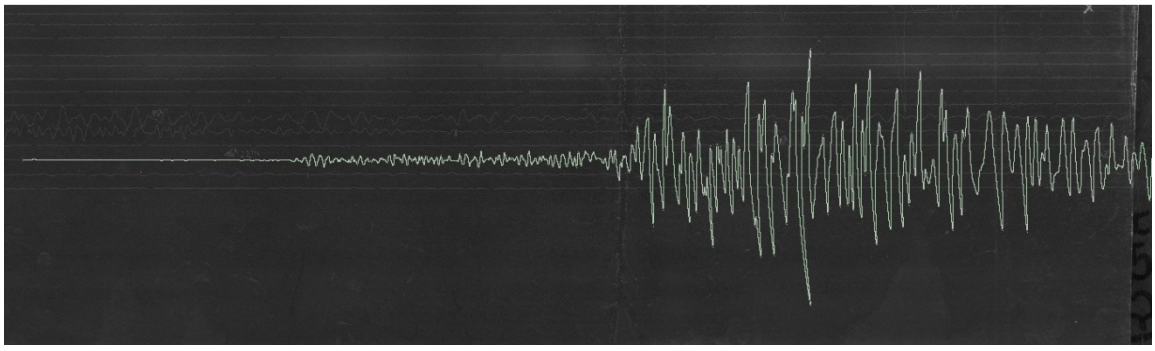

Figure A 53. Digitized seismic traces on original N-W seismogram of 04.01.1935, 16:20 Earthquake from ZAG station , recorded by Wiechert seismometer

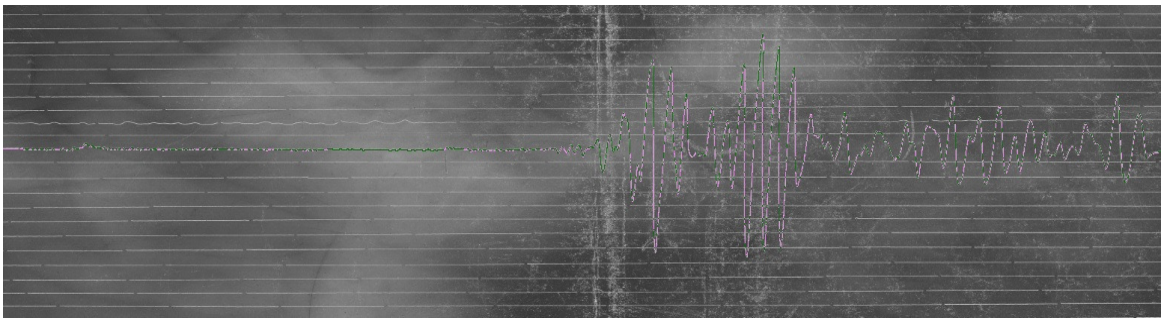

Figure A 54. Digitized seismic traces on original N-S seismogram of 04.01.1935, 16:20 Earthquake from ZUR station , recorded by Mainka seismometer

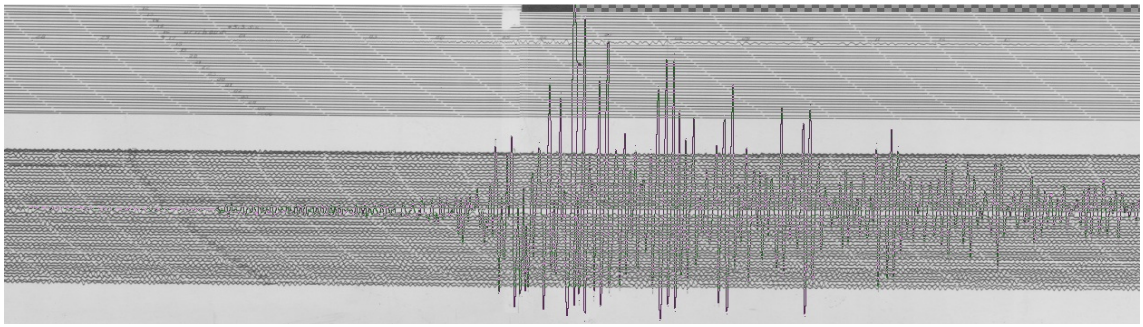

Figure A 55. Digitized seismic traces on original E-W seismogram of 18.09.1963, 18:58 Earthquake from BRA station , recorded by Wiechert seismometer

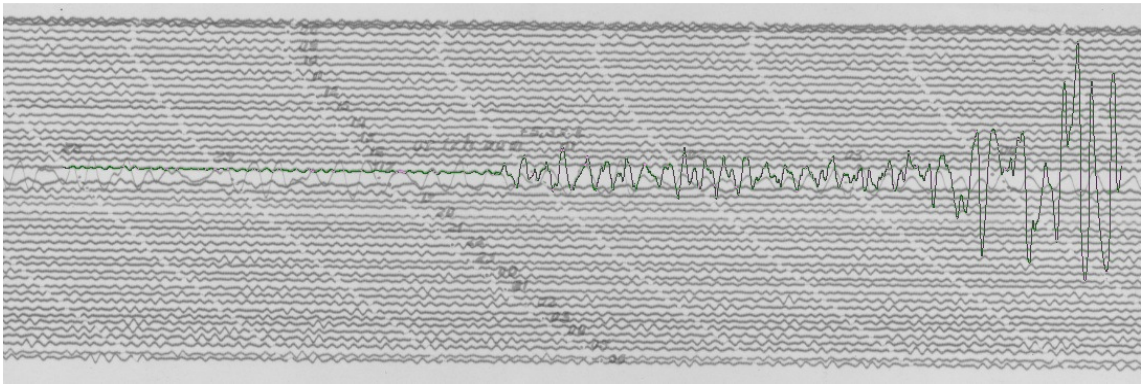

Figure A 56. Digitized seismic traces on original Z seismogram of 18.09.1963, 18:58 Earthquake from BRA station , recorded by Wiechert seismometer

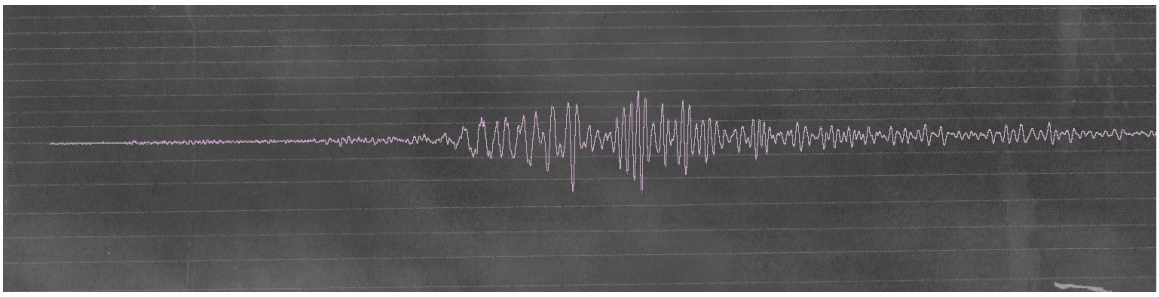

Figure A 57. Digitized seismic traces on original E-W seismogram of 18.09.1963, 18:58 Earthquake from COP station , recorded by Wiechert seismometer

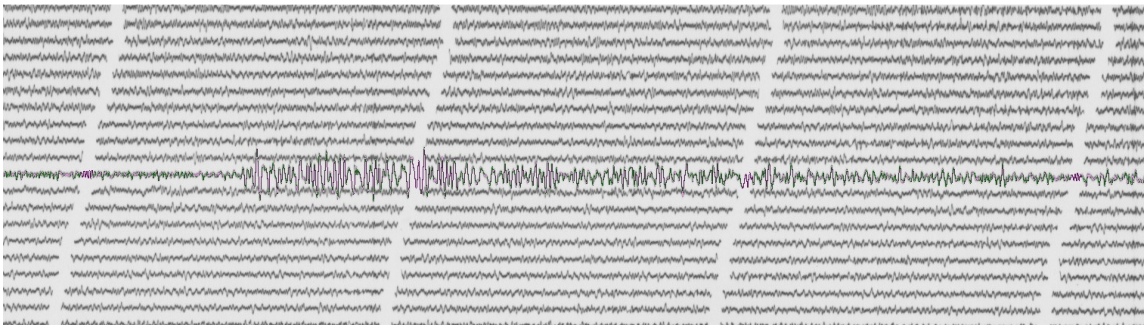

Figure A58. Digitized seismic traces on original Z seismogram of 18.09.1963, 18:58 Earthquake from COP station , recorded by Benioff seismometer

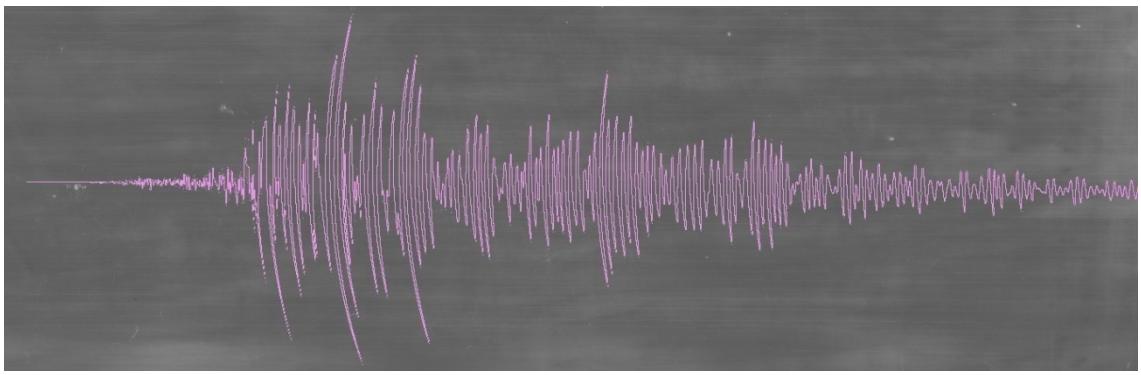

Figure A 59. Digitized seismic traces on original Z seismogram of 18.09.1963, 18:58 Earthquake from TIM station , recorded by Mainka seismometer

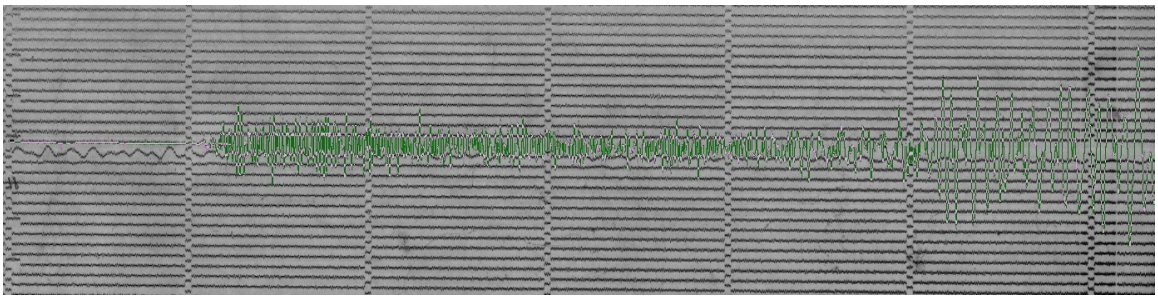

Figure A60. Digitized seismic traces on original E-W seismogram of 18.09.1963, 18:58 Earthquake from TRI station , recorded by Benioff seismometer

APPENDIX B: P AND S WAVE DISPLACEMENT SPECTRA FOR 1912, 1935 AND 1963 EARTHQUAKES

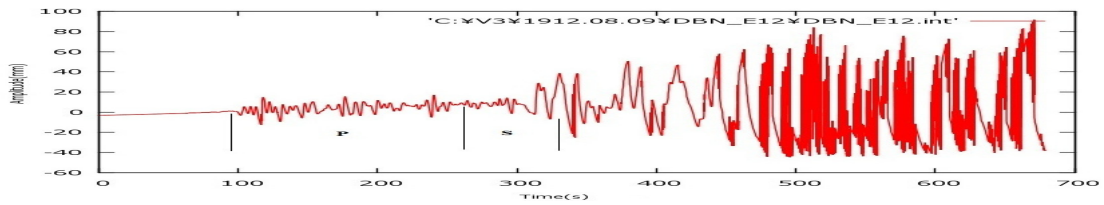

Figure B 1. P and S wave time interval chosen for the E-W component seismogram from DBN (Debilt, The Netherlands) station for 09.08.1912, 01:29 Earthquake, recorded by Wiechert seismometer

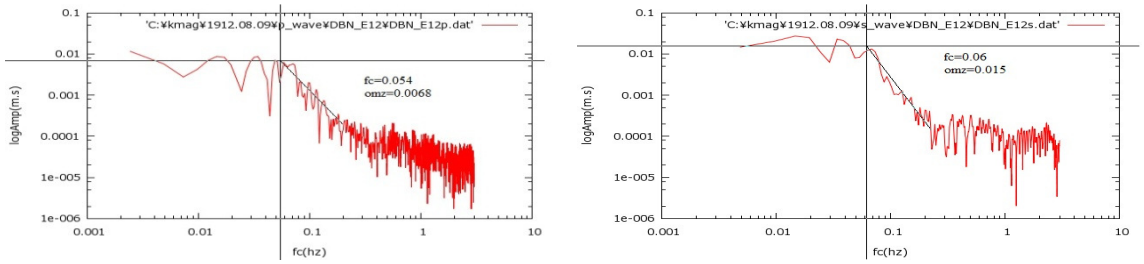

Figure B 2. P and S wave displacement spectra of E-W component seismogram of DBN station for 09.08.1912, 01:29 Earthquake. Left figure shows P wave spectra (fc=0.054, Ω_o=0.0068). Right figure shows S wave spectra(fc=0.06, Ω_o=0.015)

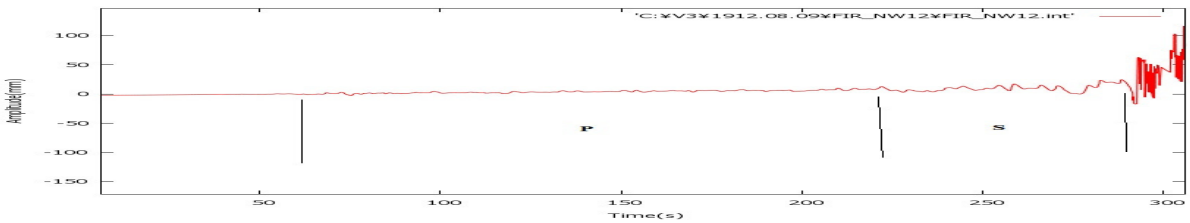

Figure B 3. P and S wave time interval chosen for the N-W component seismogram from FIR (Firenze, Italy) station for 09.08.1912, 01:29 Earthquake, recorded by Omori seismometer

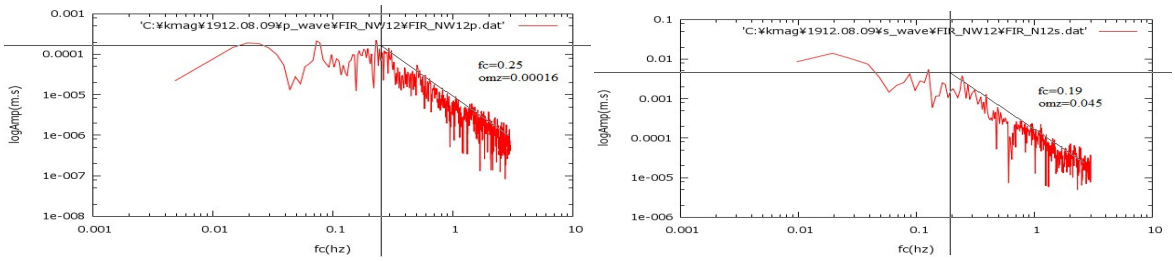

Figure B 4. P and S wave displacement spectra of N-W component seismogram of FIR station for 09.08.1912, 01:29 Earthquake. Left figure shows P wave spectra (fc=0.25, Ω_o=0.00016). Right figure shows S wave spectra(fc=0.19, Ω_o=0.045)

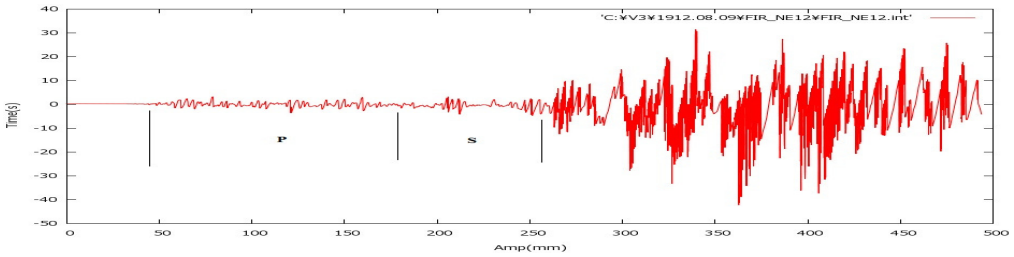

Figure B 5. P and S wave time interval chosen for the N-E component seismogram from FIR (Firenze, Italy) station for 09.08.1912, 01:29 Earthquake, recorded by Omori seismometer

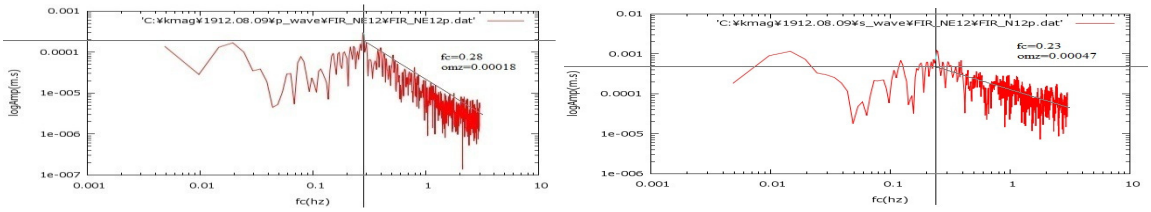

Figure B 6. P and S wave displacement spectra of N-W component seismogram of FIR station for 09.08.1912, 01:29 Earthquake. Left figure shows P wave spectra (fc=0.25, Ω_o=0.00016). Right figure shows S wave spectra(fc=0.19, Ω_o=0.045)

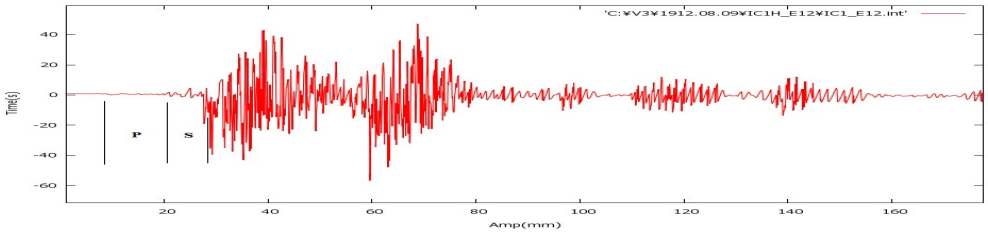

Figure B 7. P and S wave time interval chosen for the E-W component seismogram from IC1H (Isola D'ischia, Italy) station for 09.08.1912, 01:29 Earthquake, recorded by horizontal pendulum

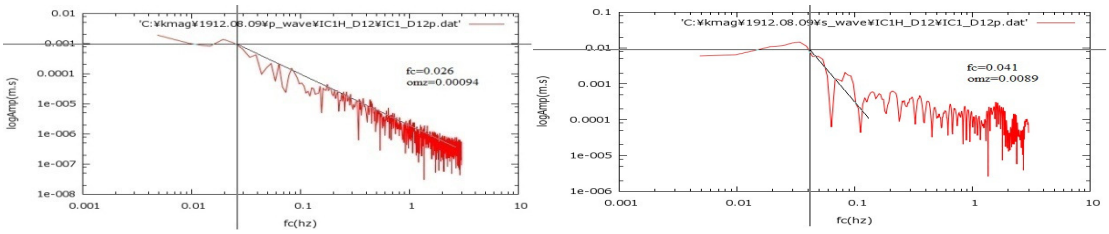

Figure B 8. P and S wave displacement spectra of E-W component seismogram of IC1H station for 09.08.1912, 01:29 Earthquake. Left figure shows P wave spectra (fc=0.26, Ω_o=0.00094). Right figure shows S wave spectra(fc=0.041, Ω_o=0.089)

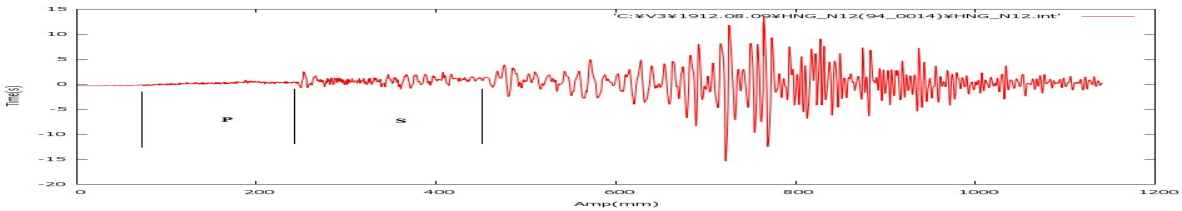

Figure B 9. P and S wave time interval chosen for the N-S component seismogram from HNG (Hongo, Japan) station for 09.08.1912, 01:29 Earthquake, recorded by Omori-1 seismometer

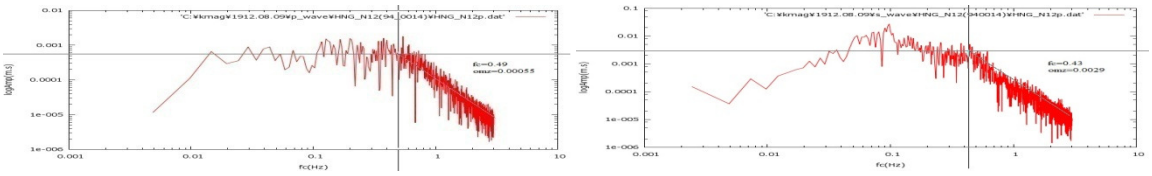

Figure B 10. P and S wave displacement spectra of N-S component seismogram of station for 09.08.1912, 01:29 Earthquake. Left figure shows P wave spectra (fc=0.49, Ω_o=0.00055). Right figure shows S wave spectra(fc=0.043, Ω_o=0.029)

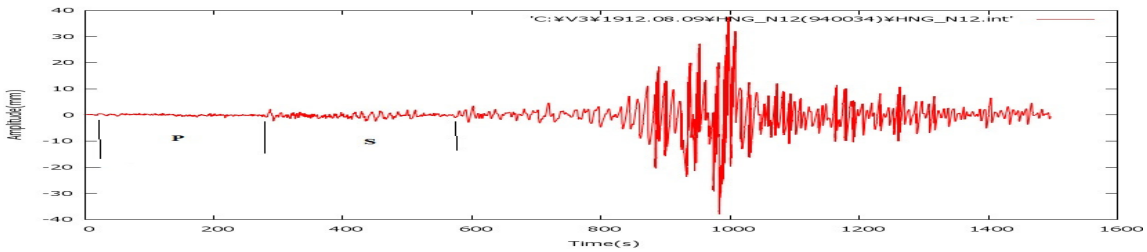

Figure B 11. P and S wave time interval chosen for the N-S component seismogram from HNG (Hongo, Japan) station for 09.08.1912, 01:29 Earthquake, recorded by Omori-2 seismometer

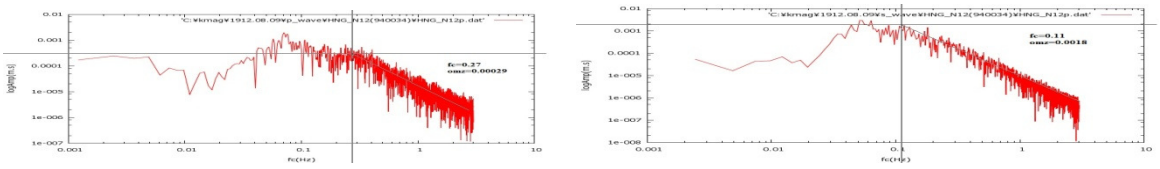

Figure B 12. P and S wave displacement spectra of N-S component seismogram of station for 09.08.1912, 01:29 Earthquake. Left figure shows P wave spectra (fc=0.27, Ω_o=0.00029). Right figure shows S wave spectra(fc=0.11, Ω_o=0.018)

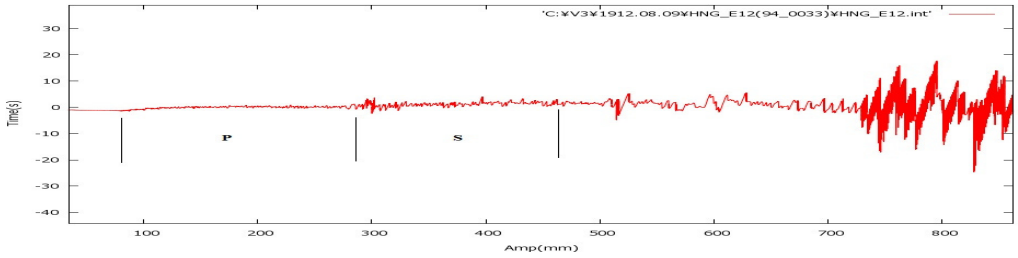

Figure B 13. P and S wave time interval chosen for the E-W component seismogram from HNG (Hongo, Japan) station for 09.08.1912, 01:29 Earthquake, recorded by Omori-1 seismometer

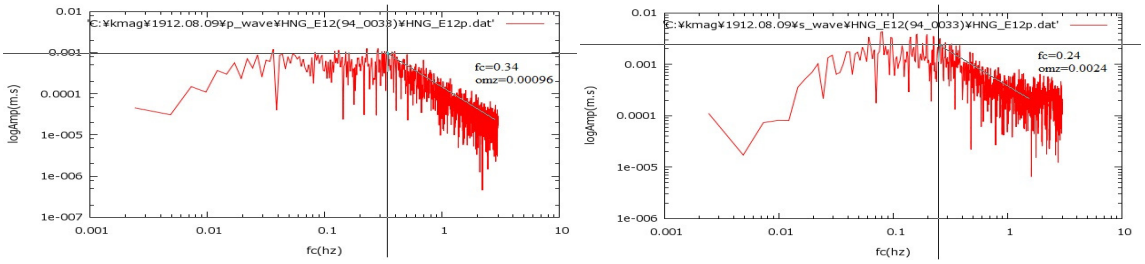

Figure B 14. P and S wave displacement spectra of E-W component seismogram of station for 09.08.1912, 01:29 Earthquake. Left figure shows P wave spectra (fc=0.34, Ω_o=0.00096). Right figure shows S wave spectra(fc=0.24, Ω_o=0.0024)

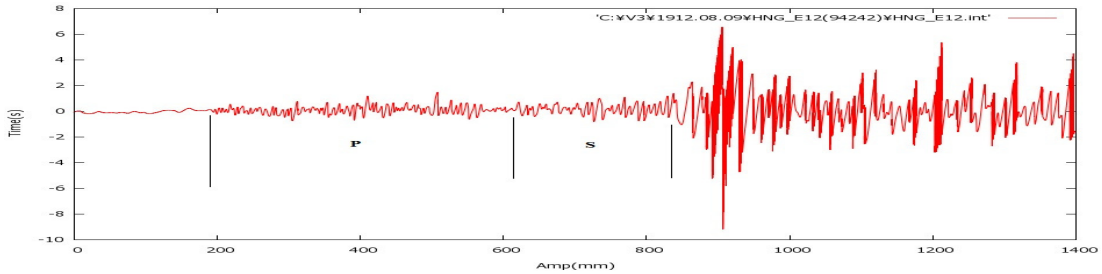

Figure B 15. P and S wave time interval chosen for the E-W component seismogram from HNG (Hongo, Japan) station for 09.08.1912, 01:29 Earthquake, recorded by Omori-2 seismometer

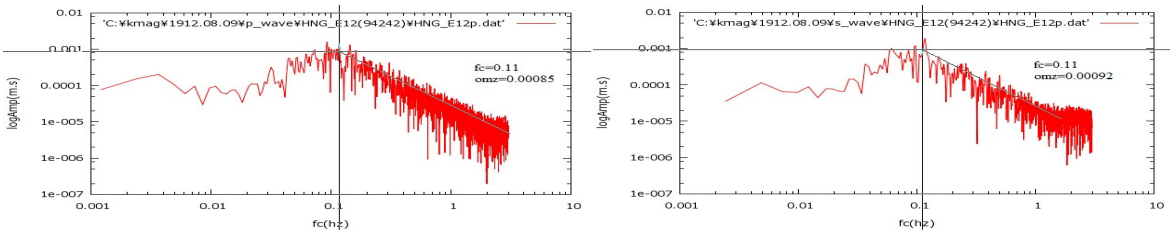

Figure B 16. P and S wave displacement spectra of E-W component seismogram of HNG station for 09.08.1912, 01:29 Earthquake. Left figure shows P wave spectra (fc=0.11, Ω_o=0.00085). Right figure shows S wave spectra(fc=0.11, Ω_o=0.00092)

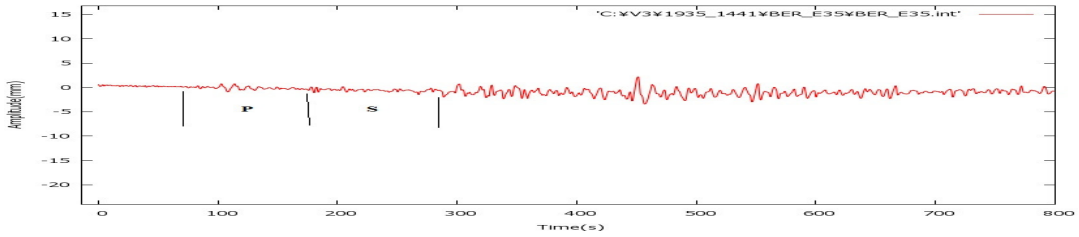

Figure B 17. P and S wave time interval chosen for the E-W component seismogram from BER (Bergen, Norwey) station for 04.01.1935, 14:41 Earthquake, recorded by Wiechert seismometer

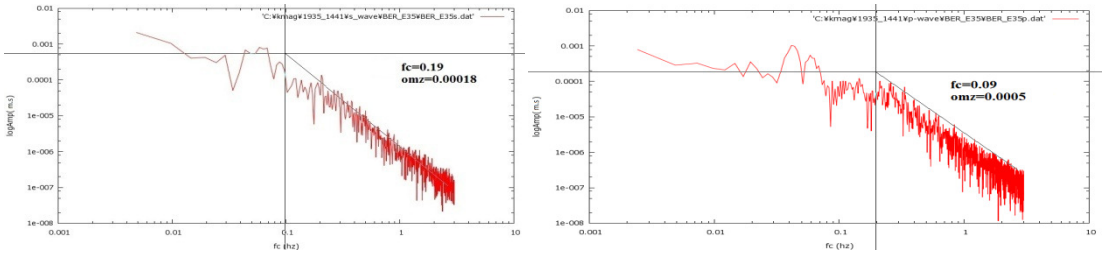

Figure B 18. P and S wave displacement spectra of E-W component seismogram of BER station for 04.01.1935, 14:41 Earthquake. Left figure shows P wave spectra (fc=0.19, Ω_o=0.00018). Right figure shows S wave spectra(fc=0.09, Ω_o=0.0005)

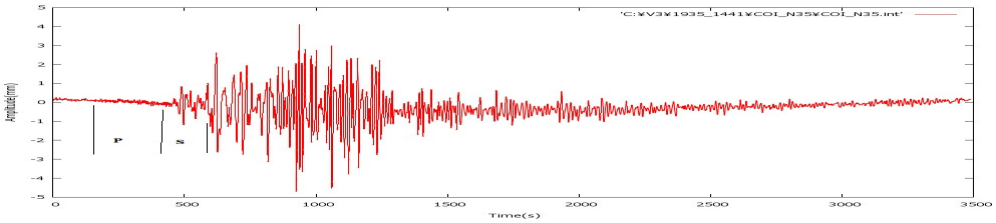

Figure B 19. P and S wave time interval chosen for the E-W component seismogram of COI (Coimbra, Portugal) station for 04.01.1935, 14:41 Earthquake, recorded by Wiechert seismometer

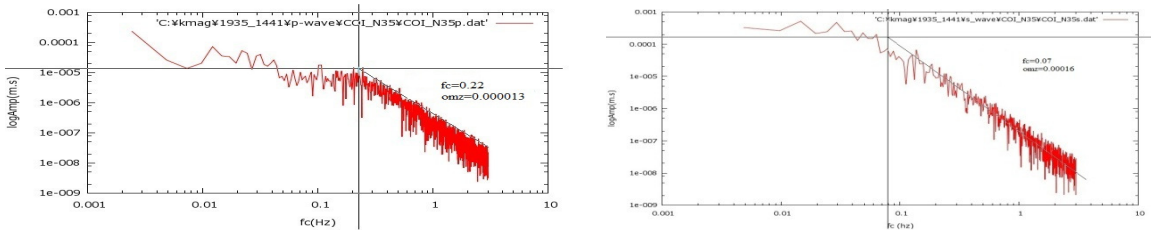

Figure B 20. P and S wave displacement spectra of N-S component seismogram of COI station for 04.01.1935, 14:41 Earthquake. Left figure shows P wave spectra (fc=0.22, Ω_o=0.00013). Right figure shows S wave spectra(fc=0.07, Ω_o=0.0004)

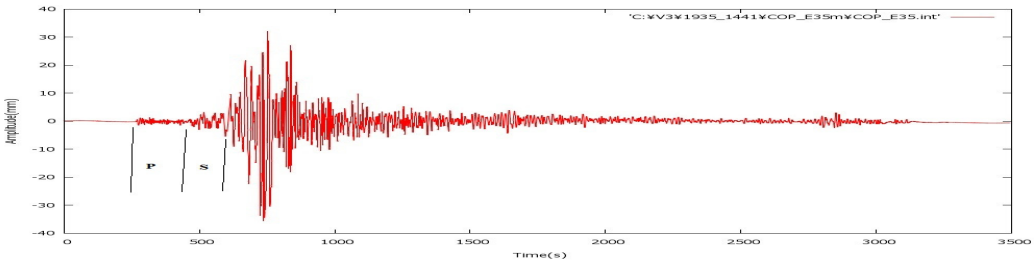

Figure B 21. P and S wave time interval chosen for the E-W component seismogram of COP (Copenhagenen, Denmark) station for 04.01.1935, 14:41 Earthquake, recorded by Milne-Shawn seismometer

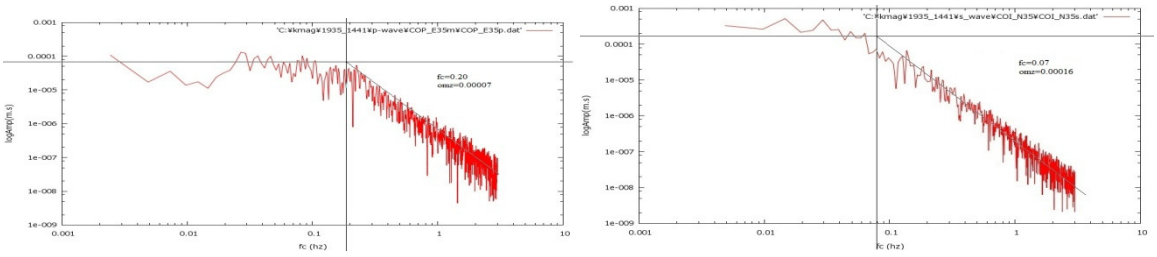

Figure B 22. P and S wave displacement spectra of N-S component seismogram of COP station for 04.01.1935, 14:41 Earthquake. Left figure shows P wave spectra (fc=0.20, Ω_o=0.00007). Right figure shows S wave spectra(fc=0.07, Ω_o=0.00016)

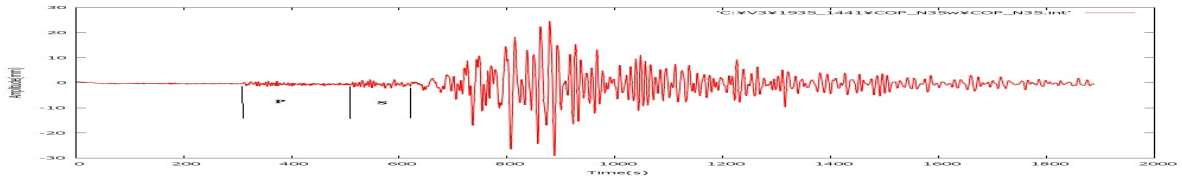

Figure B 23. P and S wave time interval chosen for the N-S component seismogram of COP (Copenhagenen, Denmark) station for 04.01.1935, 14:41 Earthquake, recorded by Wiechert seismometer

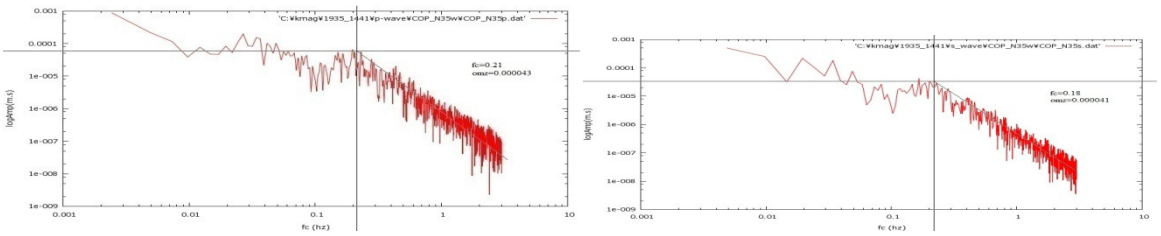

Figure B 24. P and S wave displacement spectra of N-S component seismogram of COP station for 04.01.1935, 14:41 Earthquake. Left figure shows P wave spectra (fc=0.21, Ω_o=0.000043). Right figure shows S wave spectra(fc=0.18, Ω_o=0.000041)

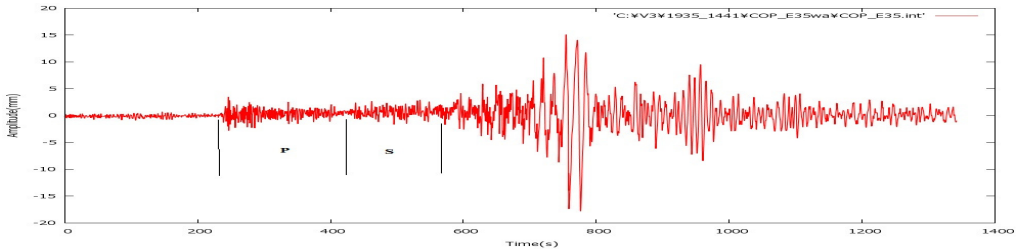

Figure B 25. P and S wave time interval chosen for the E-W component seismogram of COP (Copenhagenen, Denmark) station for 04.01.1935, 14:41 Earthquake, recorded by Wood-Anderson seismometer

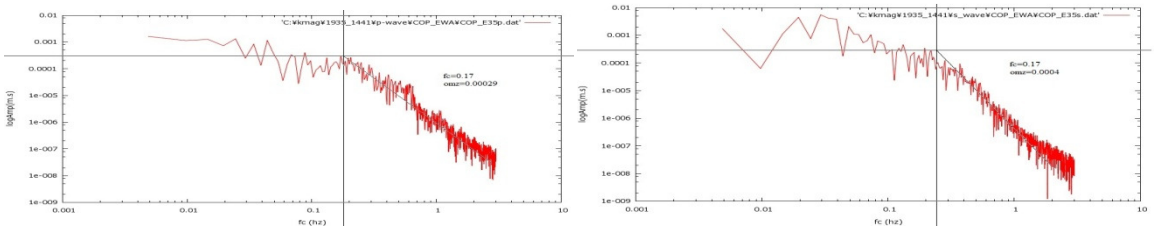

Figure B 26. P and S wave displacement spectra of E-W component seismogram of COP station for 04.01.1935, 14:41 Earthquake. Left figure shows P wave spectra (fc=0.17, Ω_o=0.00029). Right figure shows S wave spectra(fc=0.17, Ω_o=0.0004)

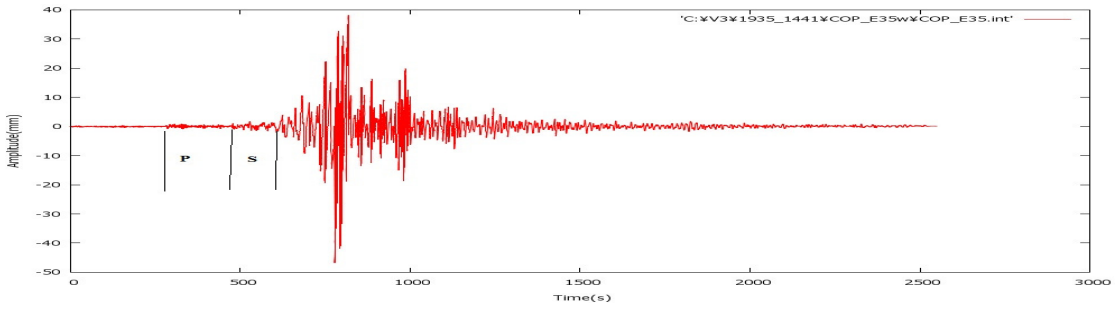

Figure B 27. P and S wave time interval chosen for the E-W component seismogram of COP (Copenhagenen, Denmark) station for 04.01.1935, 14:41 Earthquake, recorded by Wiechert seismometer

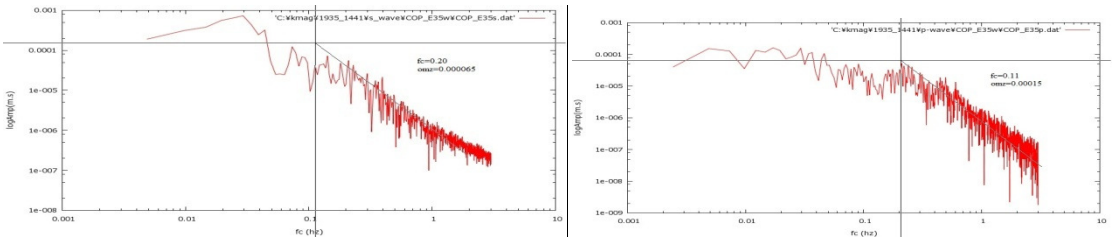

Figure B 28. P and S wave displacement spectra of E-W component seismogram of COP station for 04.01.1935, 14:41 Earthquake. Left figure shows P wave spectra (fc=0.20, Ω_o=0.000065). Right figure shows S wave spectra(fc=0.11, Ω_o=0.00015)

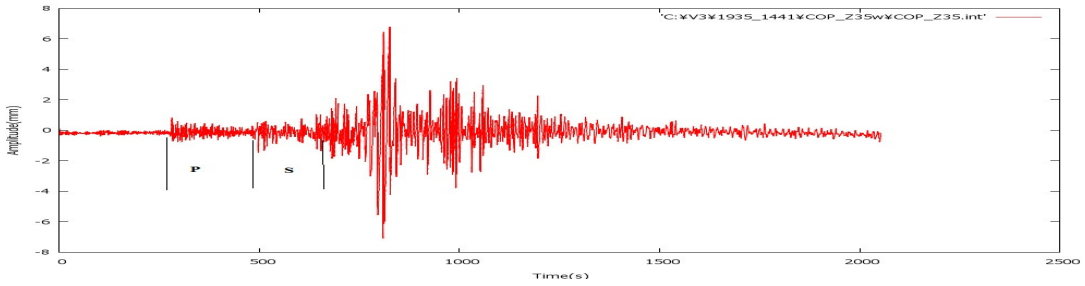

Figure B 29. P and S wave time interval chosen for the Z component seismogram of COP (Copenhagenen, Denmark) station for 04.01.1935, 14:41 Earthquake, recorded by Wiechert seismometer

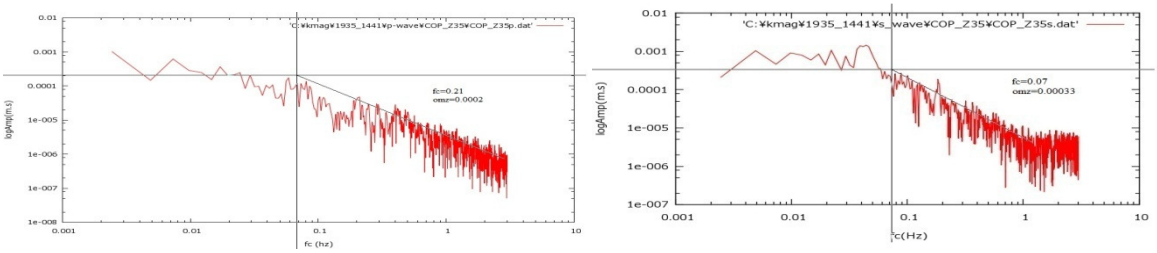

Figure B 30. P and S wave displacement spectra of Z component seismogram of COP station for 04.01.1935, 14:41 Earthquake. Left figure shows P wave spectra (fc=0.20, Ω_o=0.000065). Right figure shows S wave spectra(fc=0.11, Ω_o=0.00015)

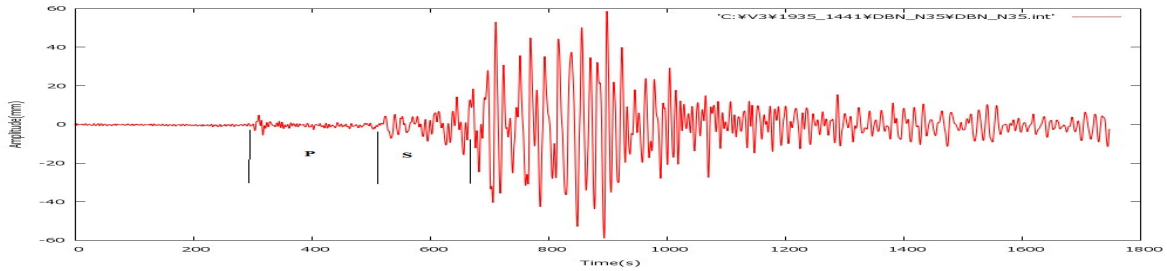

Figure B 31. P and S wave time interval chosen for the N-S component seismogram of DBN (DeBilt, The Netherlands) station for 04.01.1935, 14:41 Earthquake, recorded by Galitzin seismometer

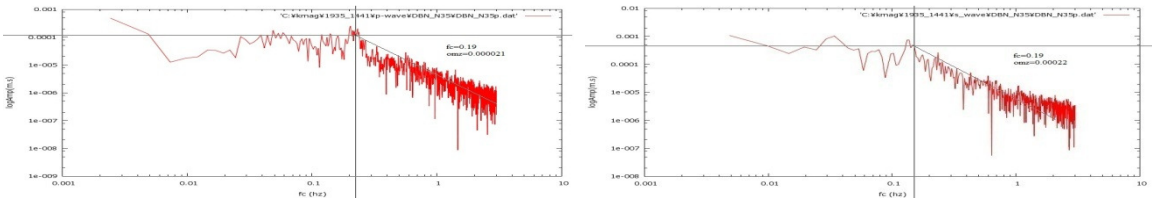

Figure B 32. P and S wave displacement spectra of N-S component seismogram of DBN station for 04.01.1935, 14:41 Earthquake. Left figure shows P wave spectra (fc=0.19, Ω_o=0.000021). Right figure shows S wave spectra(fc=0.19, Ω_o=0.00022)

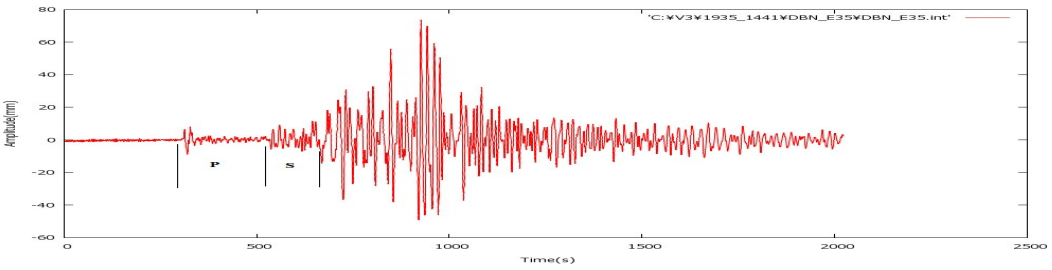

Figure B 33. P and S wave time interval chosen for the E-W component seismogram of DBN (De Bilt, The Netherlands) station for 04.01.1935, 14:41 Earthquake, recorded by Galitzin seismometer

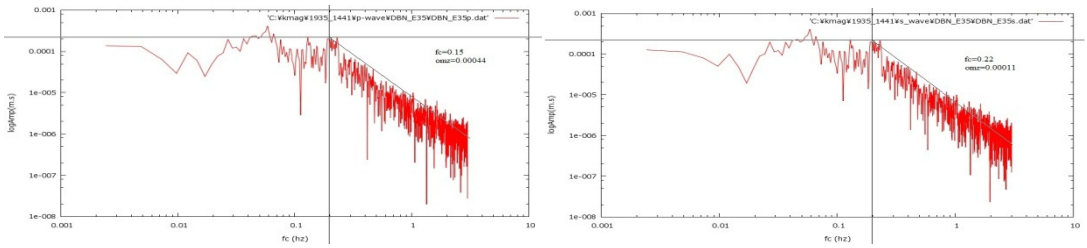

Figure B 34. P and S wave displacement spectra of E-W component seismogram of DBN station for 04.01.1935, 14:41 Earthquake. Left figure shows P wave spectra (fc=0.15, Ω_o=0.00044). Right figure shows S wave spectra(fc=0.22, Ω_o=0.00011)

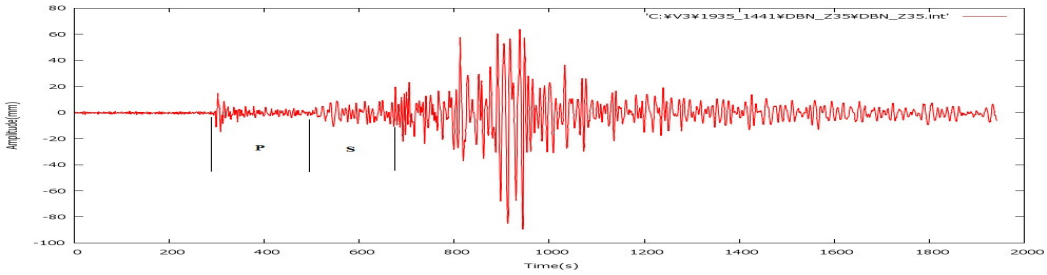

Figure B 35. P and S wave time interval chosen for the Z component seismogram of DBN (De Bilt, The Netherlands) station for 04.01.1935, 14:41 Earthquake, recorded by Galitzin seismometer

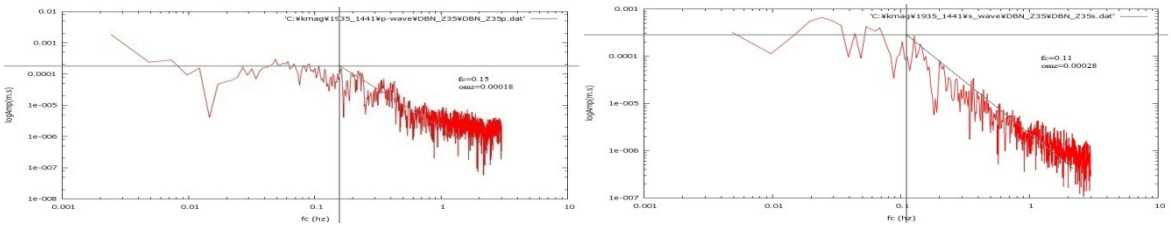

Figure B 36. P and S wave displacement spectra of Z component seismogram of DBN station for 04.01.1935, 14:41 Earthquake. Left figure shows P wave spectra (fc=0.15, Ω_o=0.00018). Right figure shows S wave spectra(fc=0.11, Ω_o=0.00028)

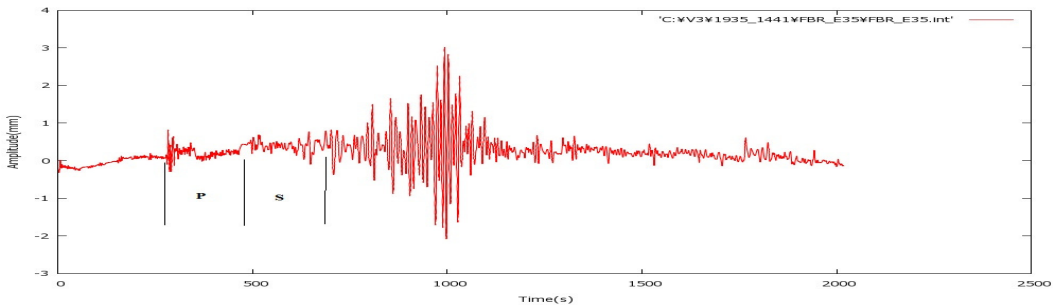

Figure B 37. P and S wave time interval chosen for the EW component seismogram of FBR (Fabra, Spain) station for 04.01.1935, 14:41 Earthquake, recorded by Mainka seismometer

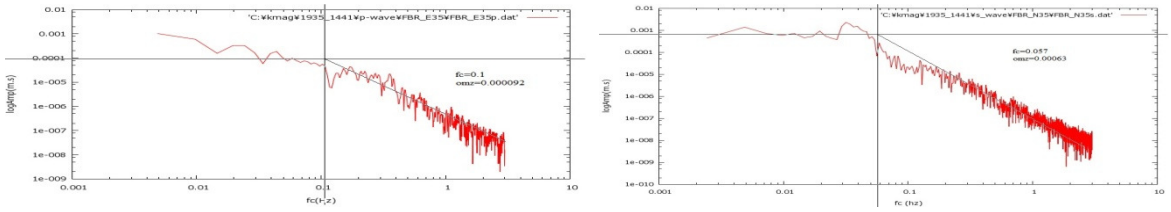

Figure B 38. P and S wave displacement spectra of EW component seismogram of FBR station for 04.01.1935, 14:41 Earthquake. Left figure shows P wave spectra (fc=0.11, Ω_o=0.000092). Right figure shows S wave spectra(fc=0.057, Ω_o=0.00063)

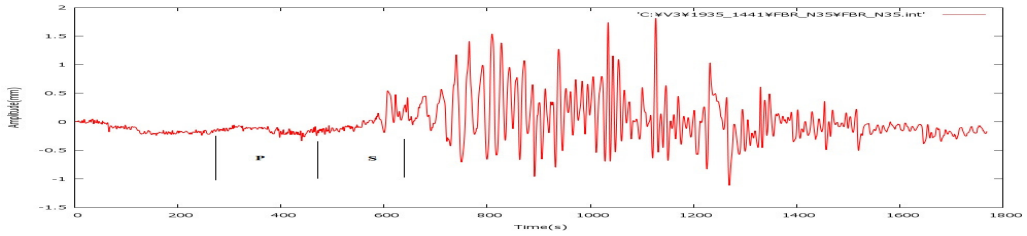

Figure B 39. P and S wave time interval chosen for the EW component seismogram of FBR (Fabra, Spain) station for 04.01.1935, 14:41 Earthquake, recorded by Mainka seismometer

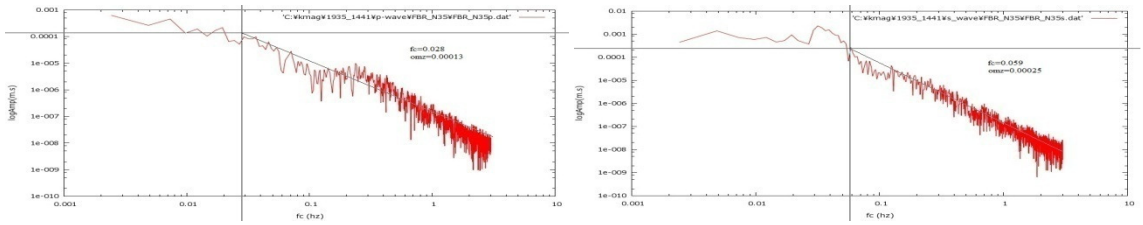

Figure B 40. P and S wave displacement spectra of E-W component seismogram of FBR station for 04.01.1935, 14:41 Earthquake. Left figure shows P wave spectra (fc=0.028, Ω_o=0.00013). Right figure shows S wave spectra(fc=0.059, Ω_o=0.00025)

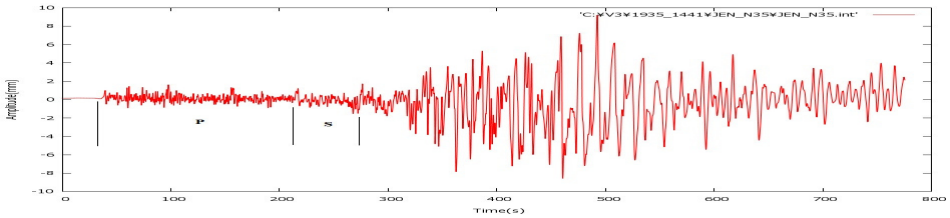

Figure B 41. P and S wave time interval chosen for the N-S component seismogram of JENA (Jena, Germany) station for 04.01.1935, 14:41 Earthquake, recorded by Wiechert(1200kg) seismometer

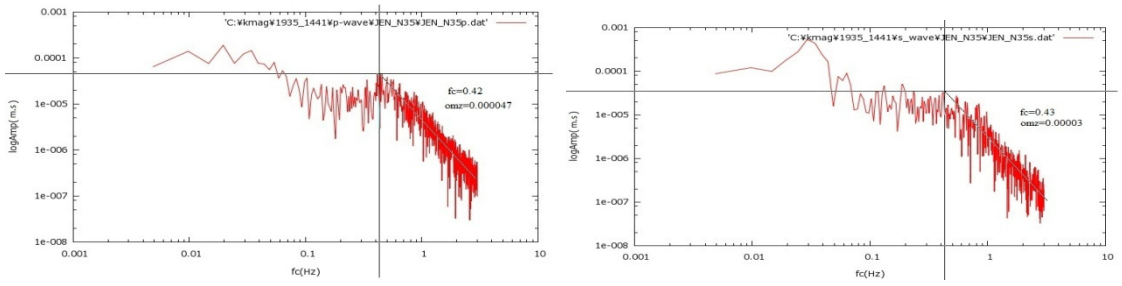

Figure B 42. P and S wave displacement spectra of N-S component seismogram of JEN station for 04.01.1935, 14:41 Earthquake. Left figure shows P wave spectra (fc=0.42, Ω_o=0.000047). Right figure shows S wave spectra(fc=0.43, Ω_o=0.00003)

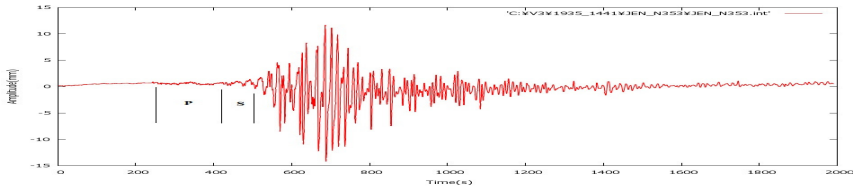

Figure B 43. P and S wave time interval chosen for the N-S component seismogram of JENA (Jena, Germany) station for 04.01.1935, 14:41 Earthquake, recorded by Wiechert(15000kg) seismometer

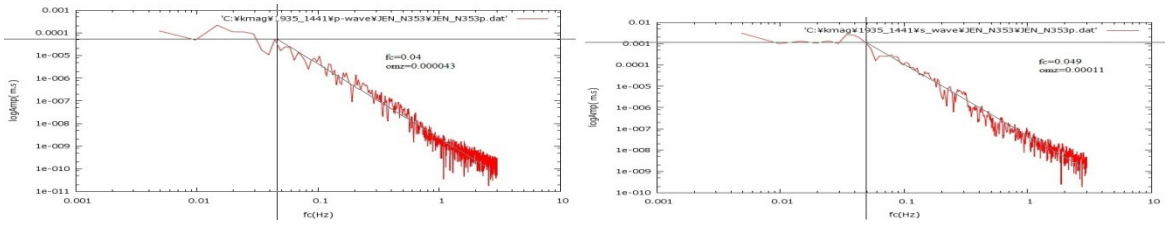

Figure B 44. P and S wave displacement spectra of N-S component seismogram of JEN station for 04.01.1935, 14:41 Earthquake. Left figure shows P wave spectra (fc=0.04, Ω_o=0.000043). Right figure shows S wave spectra(fc=0.049, Ω_o=0.00011).

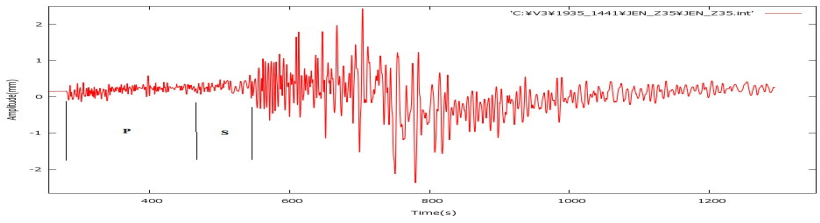

Figure B 45. P and S wave time interval chosen for the Z component seismogram of JENA (Jena, Germany) station for 04.01.1935, 14:41 Earthquake, recorded by Wiechert seismometer

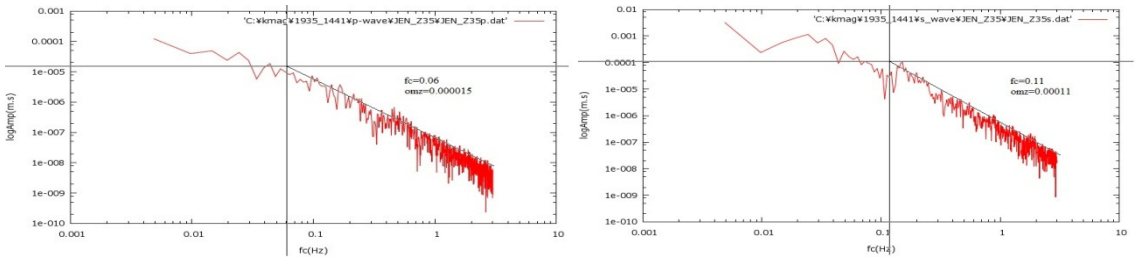

Figure B 46. P and S wave displacement spectra of Z component seismogram of JEN station for 04.01.1935, 14:41 Earthquake. Left figure shows P wave spectra (fc=0.06, Ω_o=0.000015). Right figure shows S wave spectra(fc=0.11, Ω_o=0.00011)

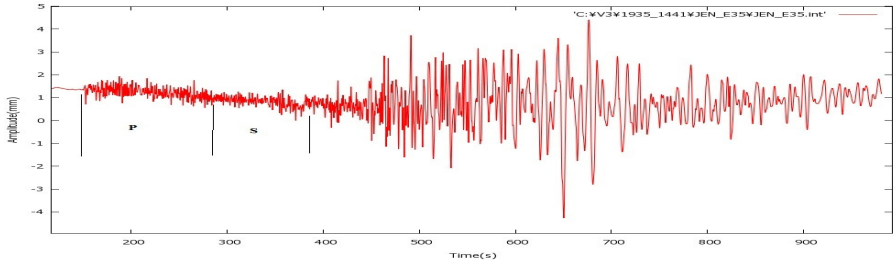

Figure B 47. P and S wave time interval chosen for the E-W component seismogram of JENA (Jena, Germany) station for 04.01.1935, 14:41 Earthquake, recorded by Wiechert(15000 kg) seismometer

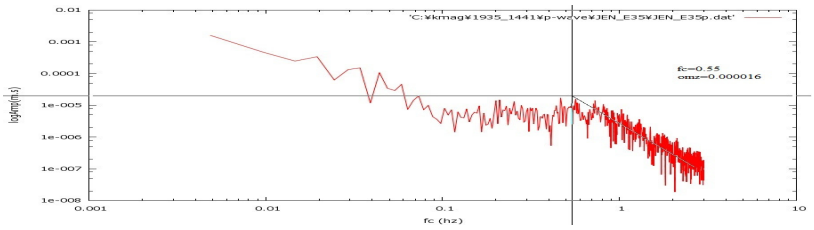

Figure B 48. P wave displacement spectra of E-W component seismogram of JEN station for 04.01.1935, 14:41 Earthquake. (fc=0.55, Ω_o=0.000016)

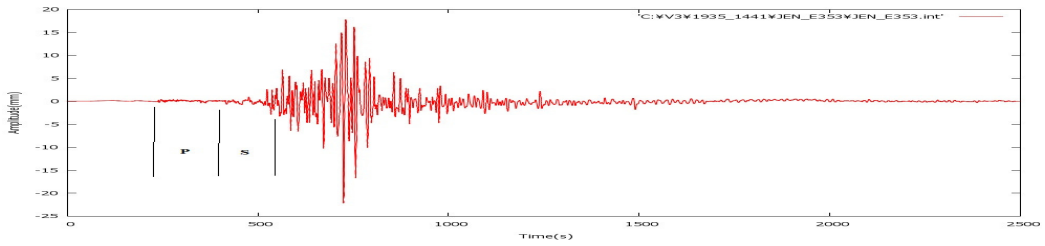

Figure B 49. P and S wave time interval chosen for the E-W component seismogram of JENA (Jena, Germany) station for 04.01.1935, 14:41 Earthquake, recorded by Wiechert(1200 kg) seismometer

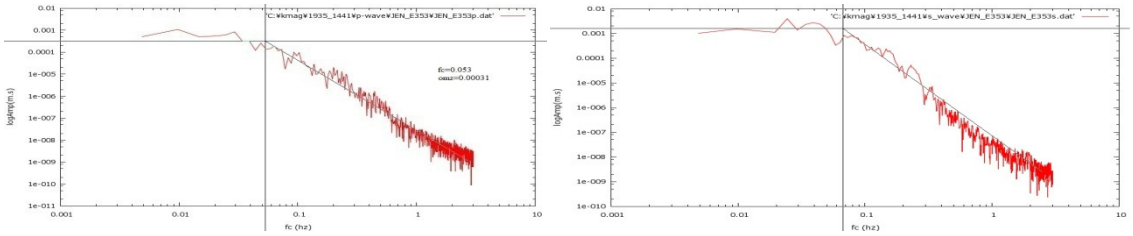

Figure B 50. P and S wave displacement spectra of E-W component seismogram of JEN station for 04.01.1935, 14:41 Earthquake. Left figure shows P wave spectra (fc=0.053, Ω_o=0.00031). Right figure shows S wave spectra(fc=0.08, Ω_o=0.0012)

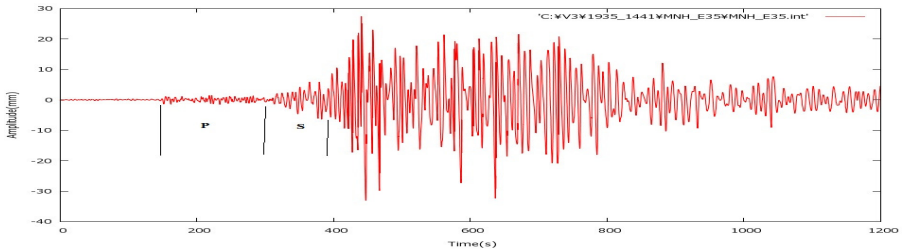

Figure B 51. P and S wave time interval chosen for the E-W component seismogram of MNH (Munich, Germany) station for 04.01.1935, 14:41 Earthquake, recorded by Wiechert seismometer

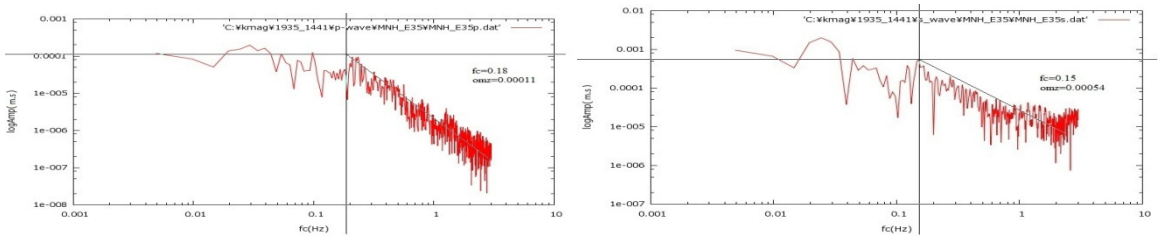

Figure B 52. P and S wave displacement spectra of E-W component seismogram of MNH station for 04.01.1935, 14:41 Earthquake. Left figure shows P wave spectra (fc=0.18, Ω_o=0.00011). Right figure shows S wave spectra(fc=0.15, Ω_o=0.00054)

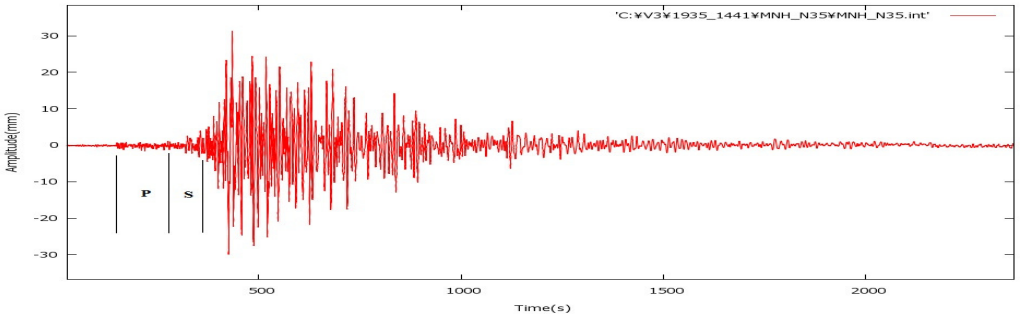

Figure B 53. P and S wave time interval chosen for the N-S component seismogram of MNH (Munich, Germany) station for 04.01.1935, 14:41 Earthquake, recorded by Wiechert seismometer

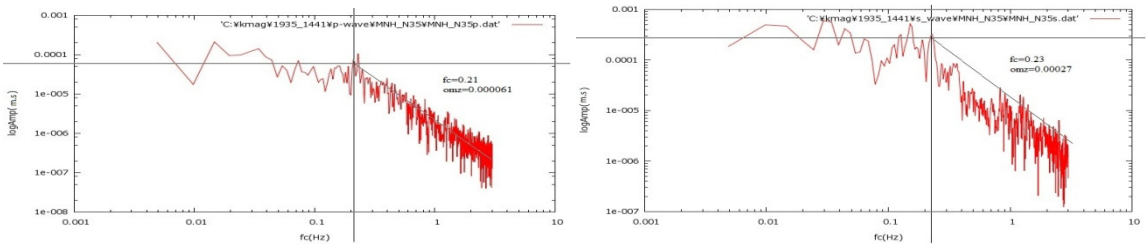

Figure B 54. P and S wave displacement spectra of N-S component seismogram of MNH station for 04.01.1935, 14:41 Earthquake. Left figure shows P wave spectra (fc=0.21, Ω_o=0.000062). Right figure shows S wave spectra(fc=0.21, Ω_o=0.000027

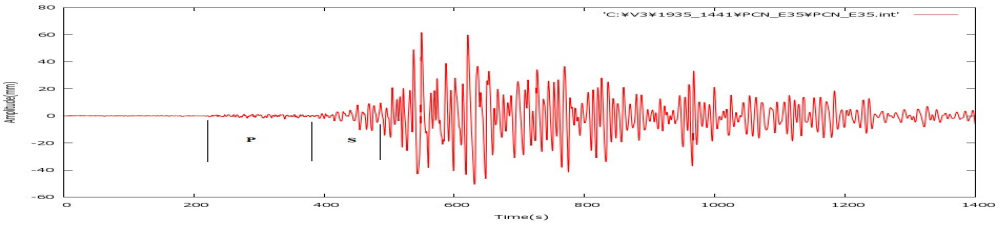

Figure B 55. P and S wave time interval chosen for the E-W component seismogram of PCN(Piacenza, Italy) station for 04.01.1935, 14:41 Earthquake, recorded by Wiechert seismometer

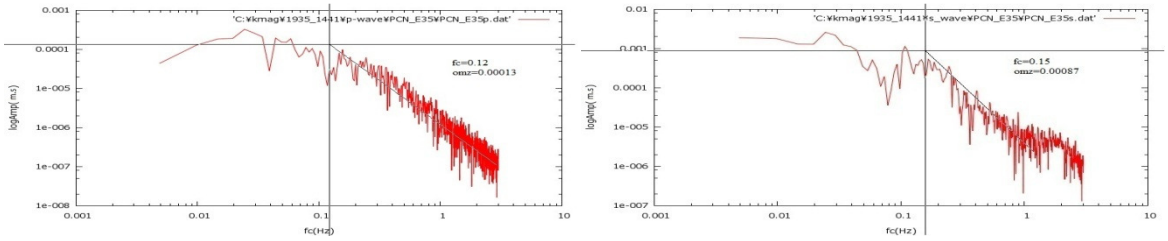

Figure B 56. P and S wave displacement spectra of E-W component seismogram of PCN station for 04.01.1935, 14:41 Earthquake. Left figure shows P wave spectra (fc=0.12, Ω_o=0.00013). Right figure shows S wave spectra(fc=0.15, Ω_o=0.00087)

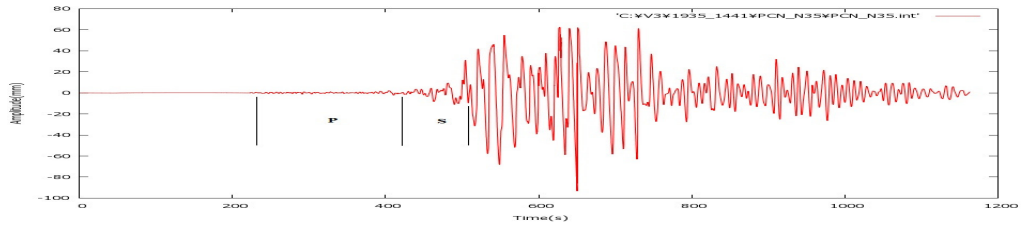

Figure B 57. P and S wave time interval chosen for the N-S component seismogram of PCN(Piacenza, Italy) station for 04.01.1935, 14:41 Earthquake, recorded by Wiechert seismometer

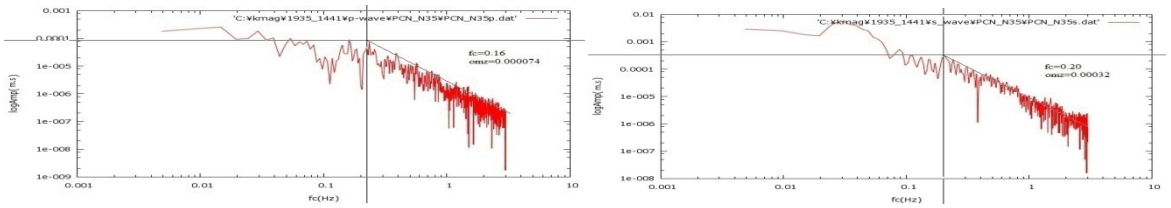

Figure B 58. P and S wave displacement spectra of N-S component seismogram of PCN station for 04.01.1935, 14:41 Earthquake. Left figure shows P wave spectra (fc=0.16, Ω_o=0.000074). Right figure shows S wave spectra(fc=0.20, Ω_o=0.00032)

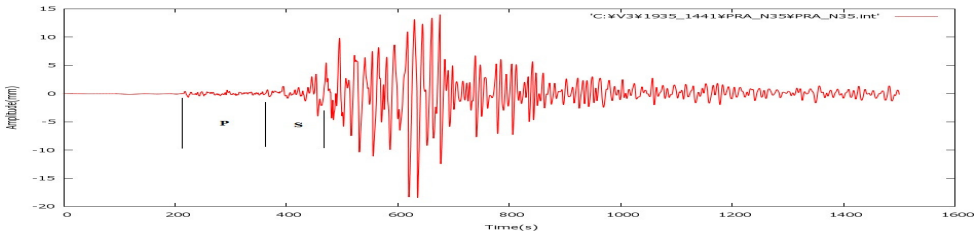

Figure B 59. P and S wave time interval chosen for the N-S component seismogram of PRA(Prague, Czech Republic) station for 04.01.1935, 14:41 Earthquake, recorded by Wiechert seismometer

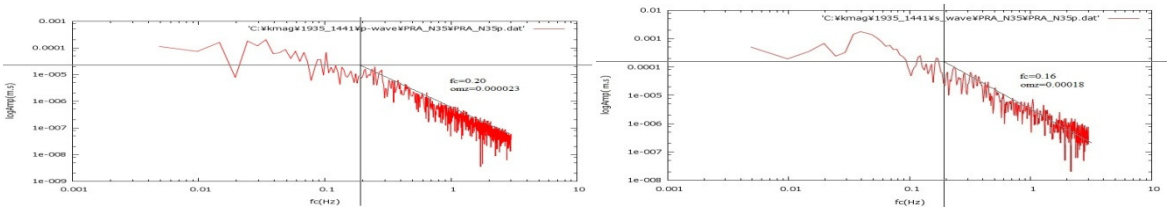

Figure B 60. P and S wave displacement spectra of N-S component seismogram of PRA station for 04.01.1935, 14:41 Earthquake. Left figure shows P wave spectra (fc=0.20, Ω_o=0.000023). Right figure shows S wave spectra(fc=0.16, Ω_o=0.00018)

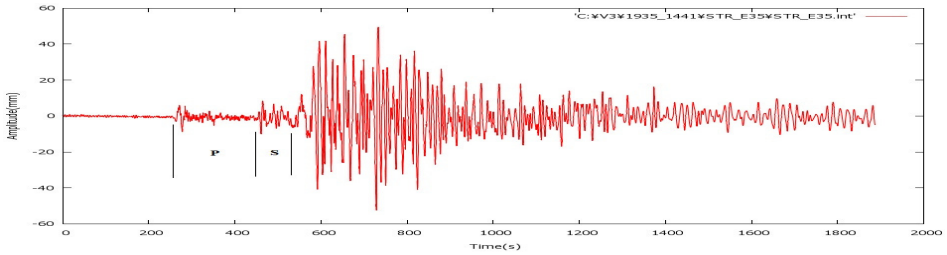

Figure B 61. P and S wave time interval chosen for the E-W component seismogram of STR(Strasbourg, France) station for 04.01.1935, 14:41 Earthquake, recorded by Galitzin seismometer

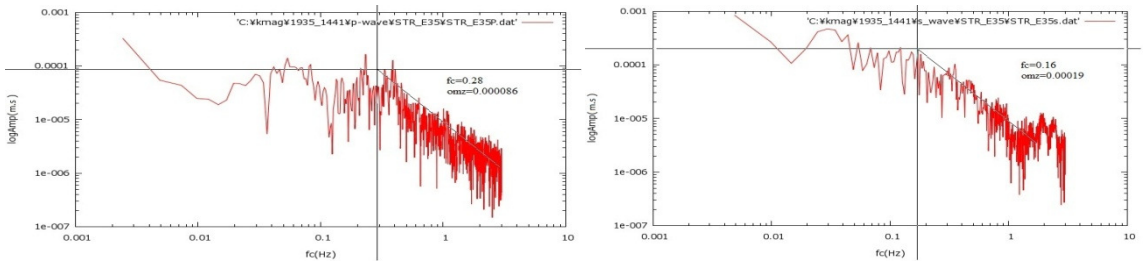

Figure B 62. P and S wave displacement spectra of N-S component seismogram of STR station for 04.01.1935, 14:41 Earthquake. Left figure shows P wave spectra (fc=0.28, Ω_o=0.000036). Right figure shows S wave spectra(fc=0.36, Ω_o=0.00019)

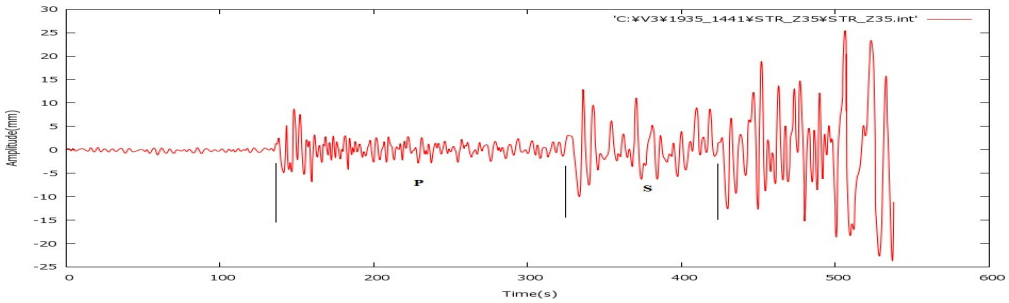

Figure B 63. P and S wave time interval chosen for the Z component seismogram of STR(Strasbourg, France) station for 04.01.1935, 14:41 Earthquake, recorded by Galitzin seismometer

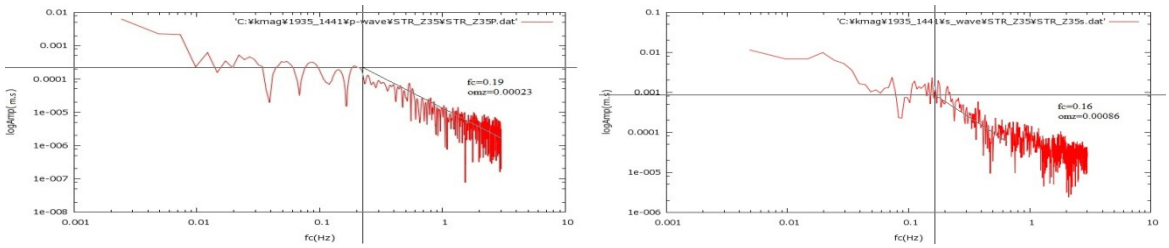

Figure B 64. P and S wave displacement spectra of Z component seismogram of STR station for 04.01.1935, 14:41 Earthquake. Left figure shows P wave spectra (fc=0.19, Ω_o=0.00023). Right figure shows S wave spectra(fc=0.16, Ω_o=0.00086)

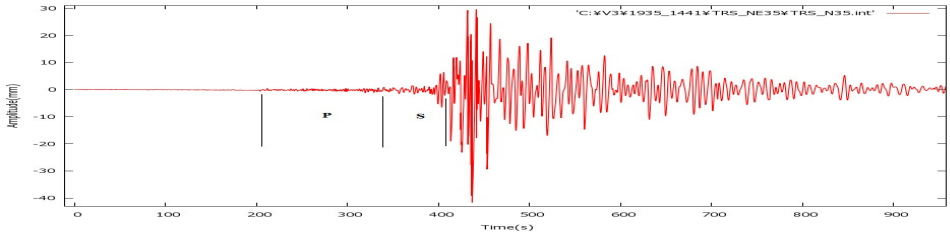

Figure B 65. P and S wave time interval chosen for the N-E component seismogram of TRS(Trieste, Italy) station for 04.01.1935, 14:41 Earthquake, recorded by Wiechert seismometer

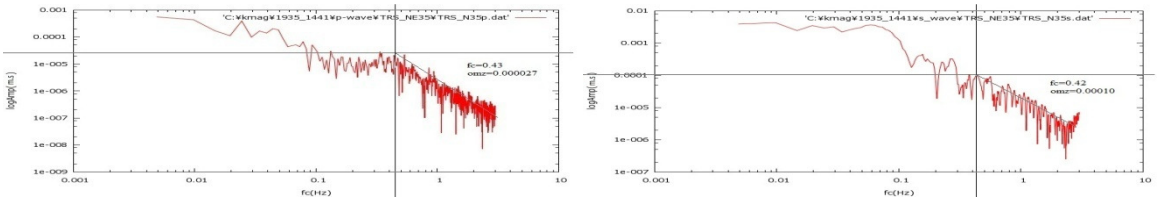

Figure B 66. P and S wave displacement spectra of N-E component seismogram of TRS station for 04.01.1935, 14:41 Earthquake. Left figure shows P wave spectra (fc=0.43, Ω_o=0.000027). Right figure shows S wave spectra(fc=0.42, Ω_o=0.00010)

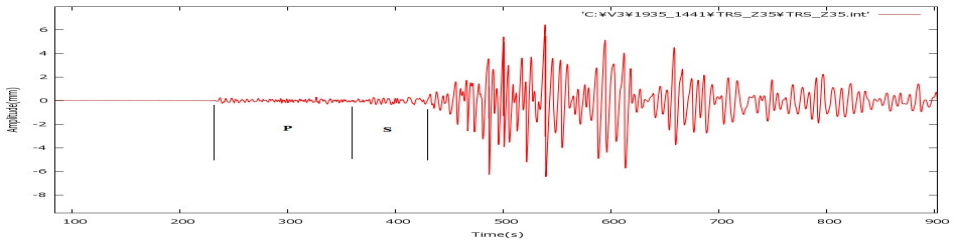

Figure B 67. P and S wave time interval chosen for the Z component seismogram of TRS(Trieste, Italy) station for 04.01.1935, 14:41 Earthquake, recorded by Wiechert seismometer

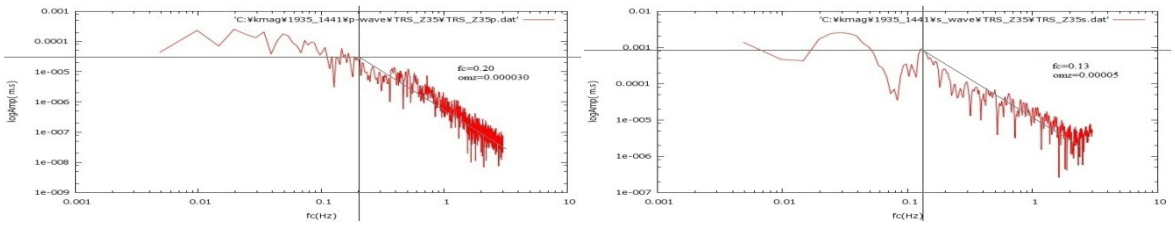

Figure B 68. P and S wave displacement spectra of Z component seismogram of TRS station for 04.01.1935, 14:41 Earthquake. Left figure shows P wave spectra (fc=0.20, Ω_o=0.000030). Right figure shows S wave spectra(fc=0.13, Ω_o=0.0005)

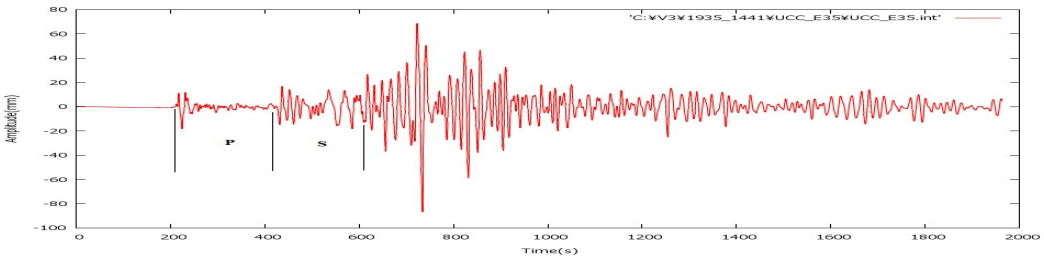

Figure B 69. P and S wave time interval chosen for the E-W component seismogram of UCC(Uccle, Belgium) station for 04.01.1935, 14:41 Earthquake, recorded by Galitzin seismometer

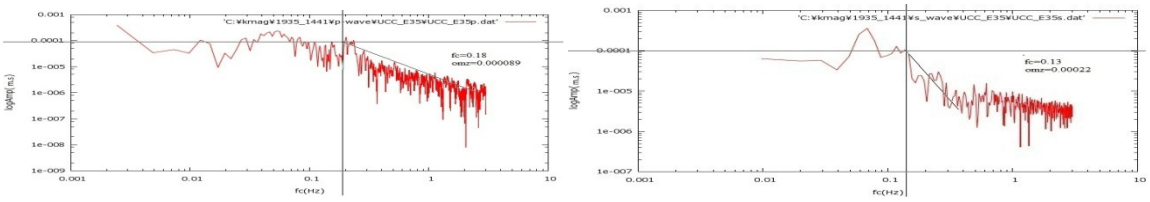

Figure B 70. P and S wave displacement spectra of E-W component seismogram of UCC station for 04.01.1935, 14:41 Earthquake. Left figure shows P wave spectra (fc=0.18, Ω_o=0.000089). Right figure shows S wave spectra(fc=0.13, Ω_o=0.00022)

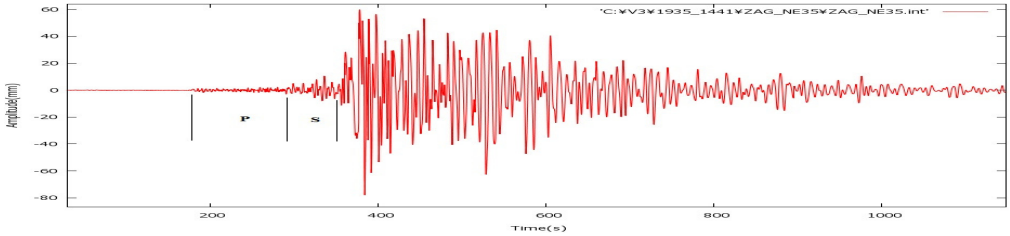

Figure B 71. P and S wave time interval chosen for the N-E component seismogram of ZAG(Zagreb, Croatia) station for 04.01.1935, 14:41 Earthquake, recorded by Wiechert seismometer

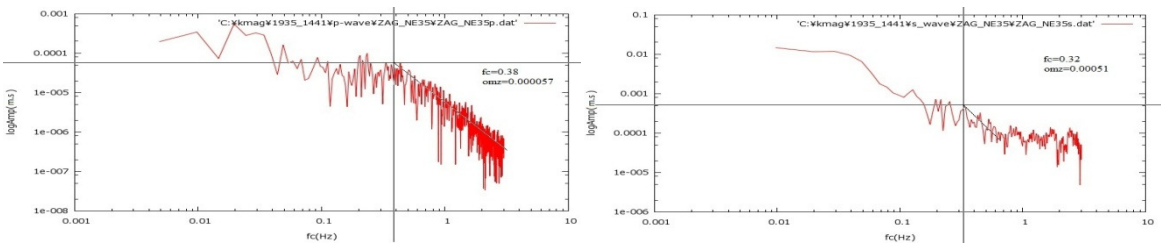

Figure B 72. P and S wave displacement spectra of E-W component seismogram of ZAG station for 04.01.1935, 14:41 Earthquake. Left figure shows P wave spectra (fc=0.38, Ω_o=0.000057). Right figure shows S wave spectra(fc=0.32, Ω_o=0.00051)

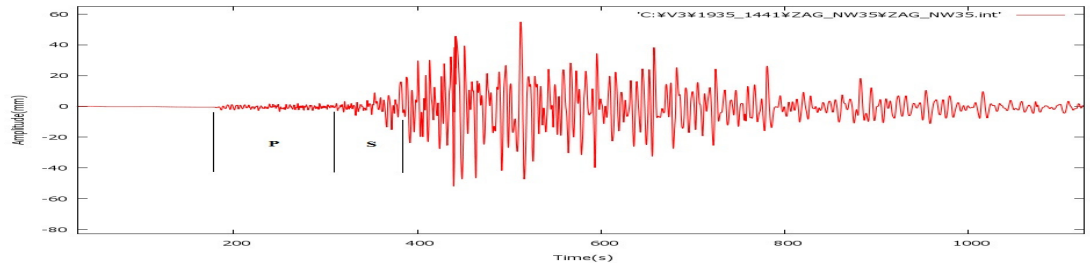

Figure B 73. P and S wave time interval chosen for the N-W component seismogram of ZAG(Zagreb, Croatia) station for 04.01.1935, 14:41 Earthquake, recorded by Wiechert seismometer

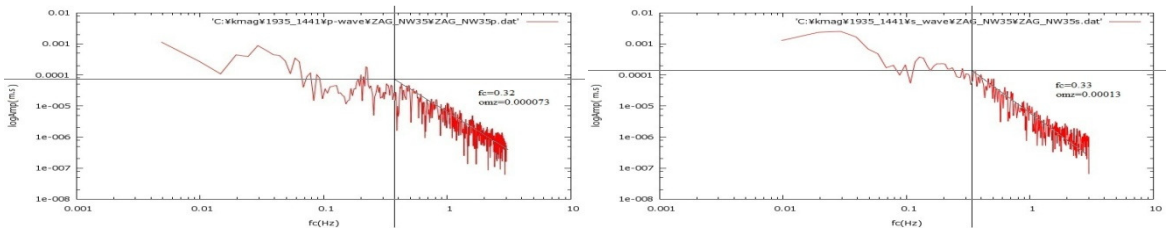

Figure B 74. P and S wave displacement spectra of N-W component seismogram of ZAG station for 04.01.1935, 14:41 Earthquake. Left figure shows P wave spectra (fc=0.32, Ω_o=0.000073). Right figure shows S wave spectra(fc=0.33, Ω_o=0.00013)

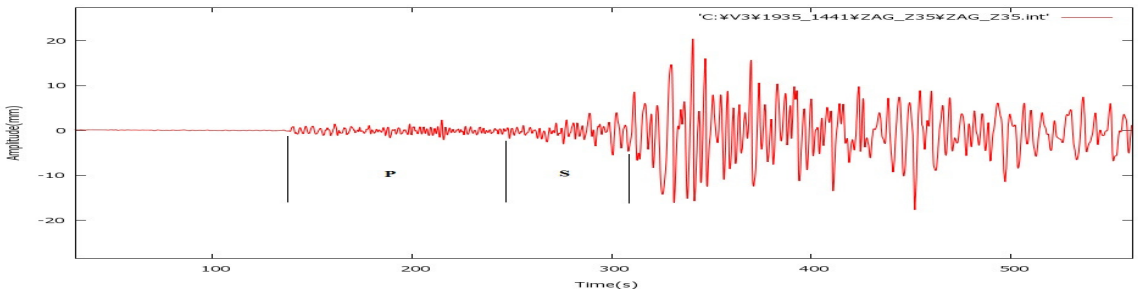

Figure B 75. P and S wave time interval chosen for the Z component seismogram of ZAG(Zagreb, Croatia) station for 04.01.1935, 14:41 Earthquake, recorded by Wiechert seismometer

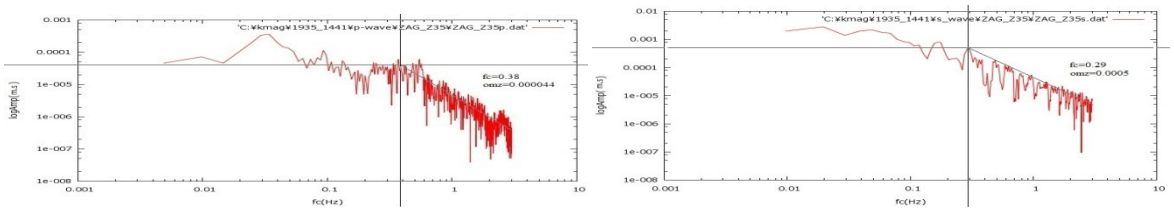

Figure B 76. P and S wave displacement spectra of Z component seismogram of ZAG station for 04.01.1935, 14:41 Earthquake. Left figure shows P wave spectra (fc=0.38, Ω_o=0.000044). Right figure shows S wave spectra(fc=0.29, Ω_o=0.0005)

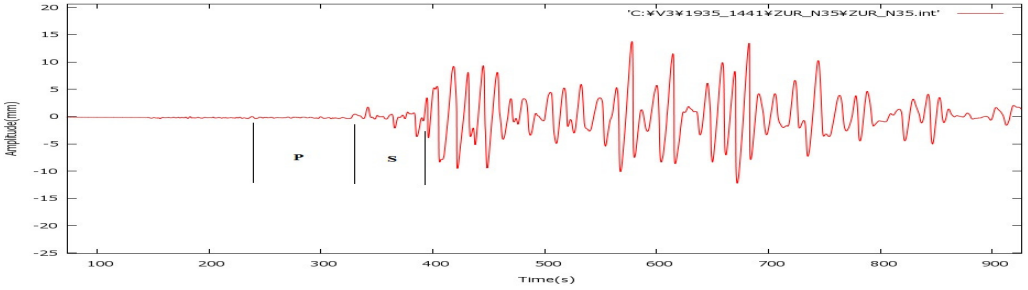

Figure B 77. P and S wave time interval chosen for the N-S component seismogram of ZUR(Zurich, Switzerland) station for 04.01.1935, 14:41 Earthquake, recorded by Mainka seismometer

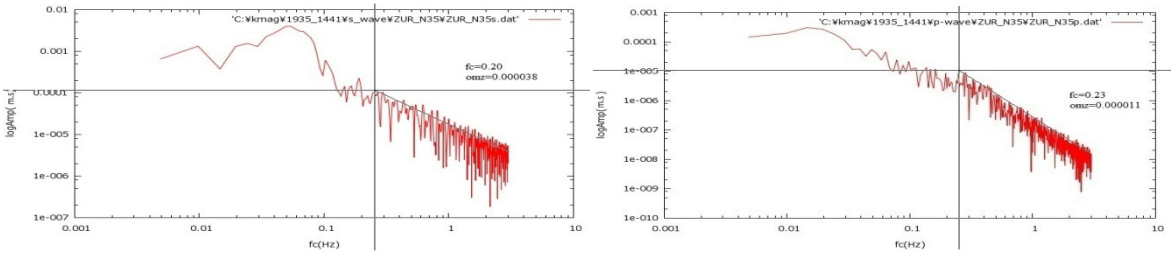

Figure B 78. P and S wave displacement spectra of N-S component seismogram of ZUR station for 04.01.1935, 14:41 Earthquake. Left figure shows P wave spectra (fc=0.20, Ω_o=0.000038). Right figure shows S wave spectra(fc=0.23, Ω_o=0.000011)

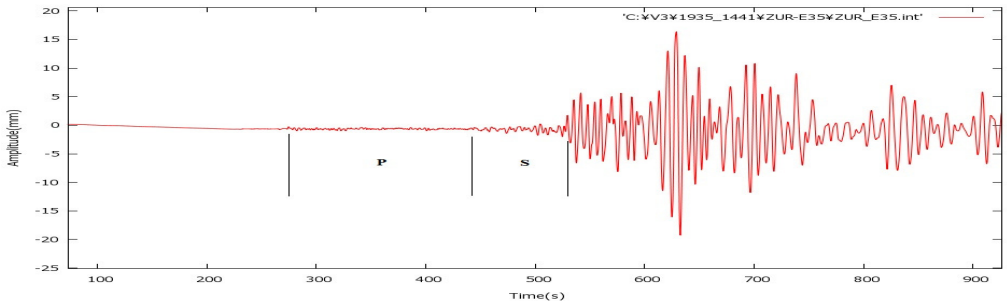

Figure B 79. P and S wave time interval chosen for the E-W component seismogram of ZUR(Zurich, Switzerland) station for 04.01.1935, 14:41 Earthquake, recorded by Mainka seismometer

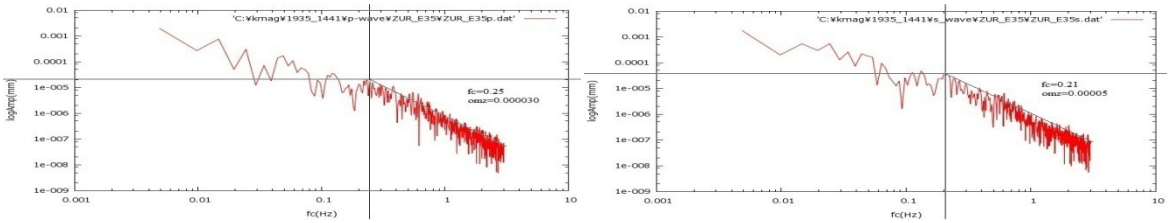

Figure B 80. P and S wave displacement spectra of E-W component seismogram of ZUR station for 04.01.1935, 14:41 Earthquake. Left figure shows P wave spectra (fc=0.25, Ω_o=0.000030). Right figure shows S wave spectra(fc=0.21, Ω_o=0.00005)

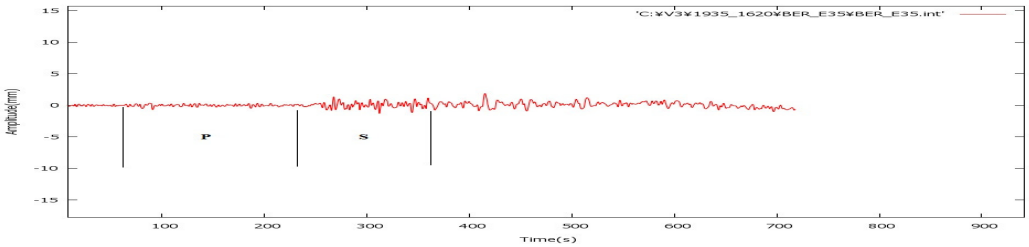

Figure B 81. P and S wave time interval chosen for the E-W component seismogram of BER(Bergen, Norwey) station for 04.01.1935, 16:20 Earthquake, recorded by Wiechert seismometer

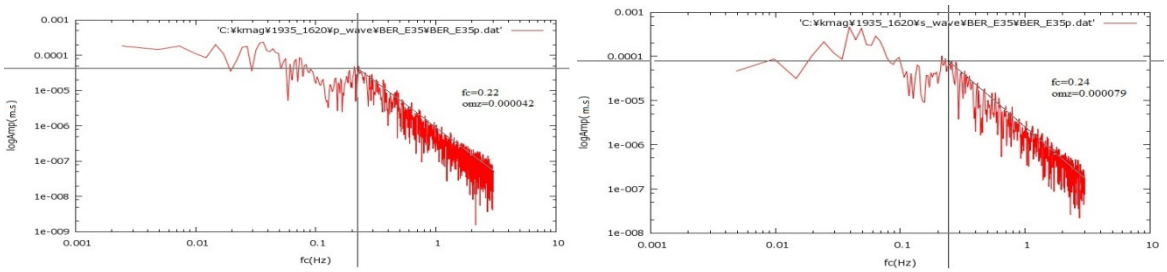

Figure B 82. P and S wave displacement spectra of E-W component seismogram of BER station for 04.01.1935, 16:20 Earthquake. Left figure shows P wave spectra (fc=0.22, Ω_o=0.000042). Right figure shows S wave spectra(fc=0.24, Ω_o=0.000079)

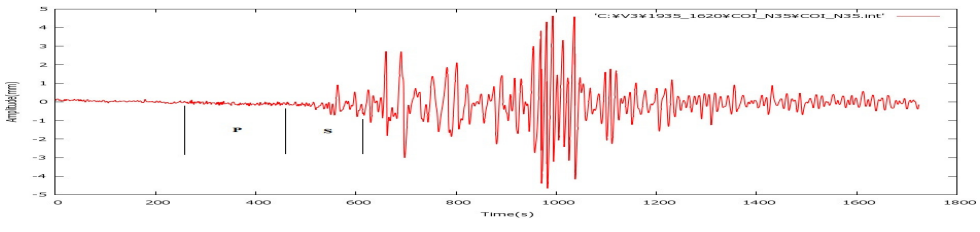

Figure B 83. P and S wave time interval chosen for the N-S component seismogram of COI(Coimbra, Portugal) station for 04.01.1935, 16:20 Earthquake, recorded by Wiechert seismometer

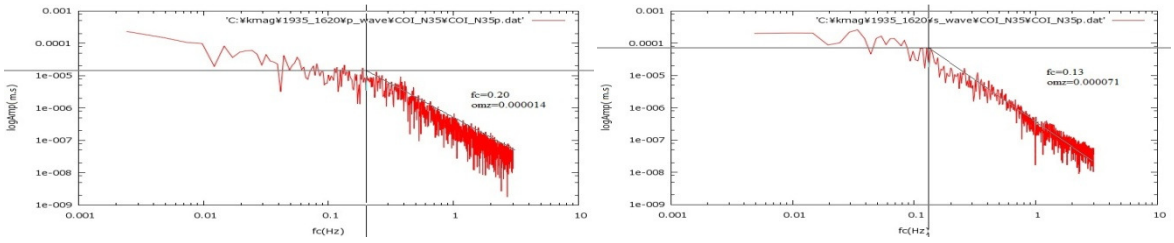

Figure B 84. P and S wave displacement spectra of N-S component seismogram of COI station for 04.01.1935, 16:20 Earthquake. Left figure shows P wave spectra (fc=0.20, Ω_o=0.000014). Right figure shows S wave spectra(fc=0.13, Ω_o=0.000071)

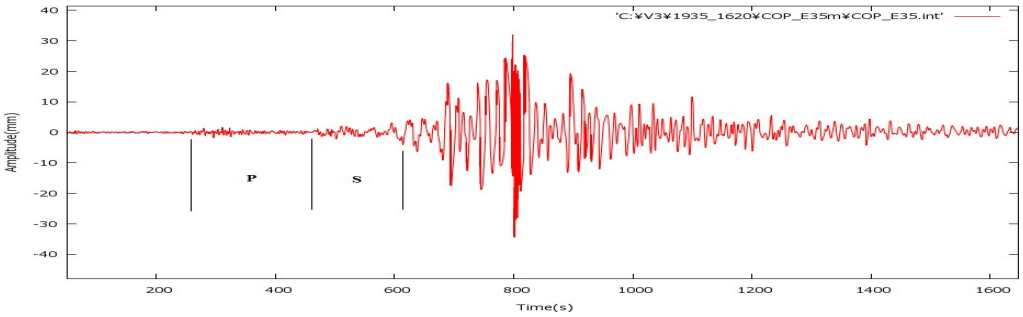

Figure B 85. P and S wave time interval chosen for the E-W component seismogram of COP(Copenhagenen, Denmark) station for 04.01.1935, 16:20 Earthquake, recorded by Milne-Shawn seismometer

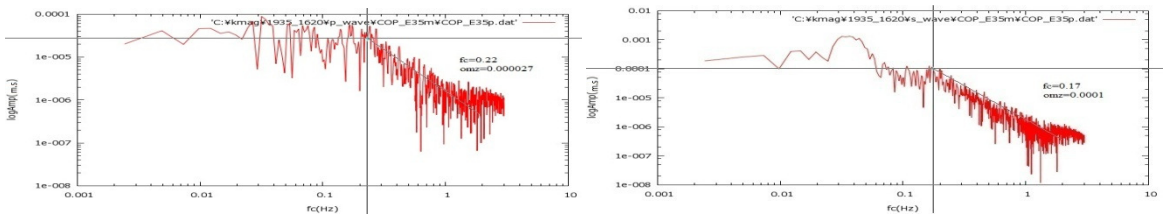

Figure B 86. P and S wave displacement spectra of E-W component seismogram of COP station for 04.01.1935, 16:20 Earthquake. Left figure shows P wave spectra (fc=0.22, Ω_o=0.000027). Right figure shows S wave spectra(fc=0.17, Ω_o=0.0001)

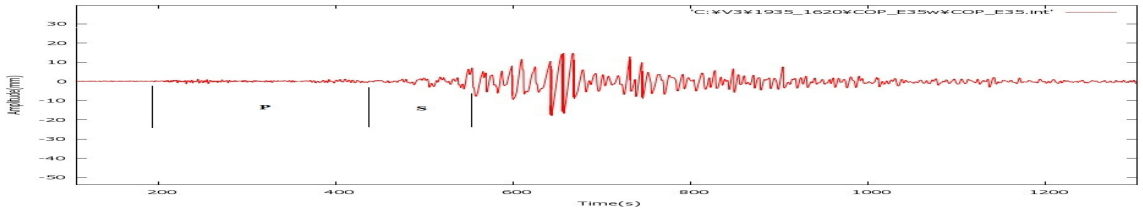

Figure B 87. P and S wave time interval chosen for the E-W component seismogram of COP(Copenhagenen, Denmark) station for 04.01.1935, 16:20 Earthquake, recorded by Wiechert seismometer

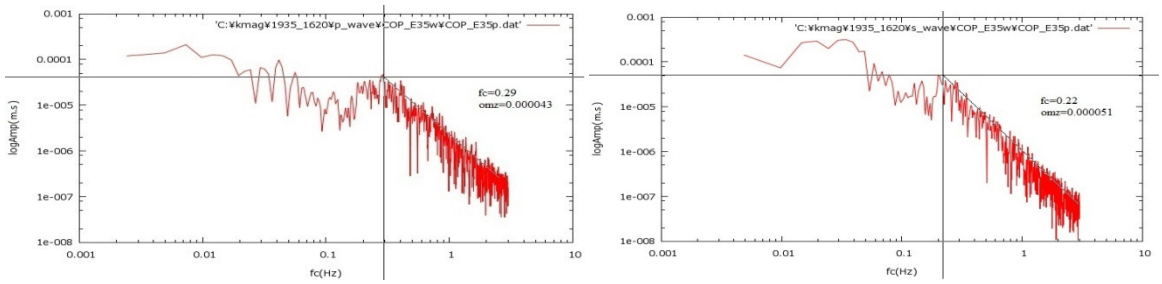

Figure B 88. P and S wave displacement spectra of E-W component seismogram of COP station for 04.01.1935, 16:20 Earthquake. Left figure shows P wave spectra (fc=0.29, Ω_o=0.000043). Right figure shows S wave spectra(fc=0.22, Ω_o=0.000051)

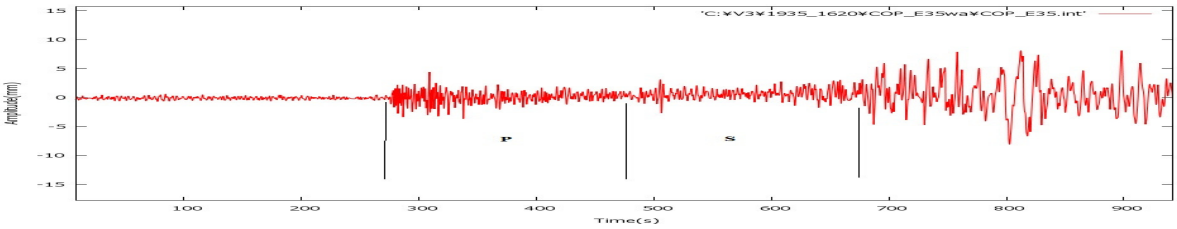

Figure B 89. P and S wave time interval chosen for the E-W component seismogram of COP(Copenhagenen, Denmark) station for 04.01.1935, 16:20 Earthquake, recorded by Wood-Anderson seismometer

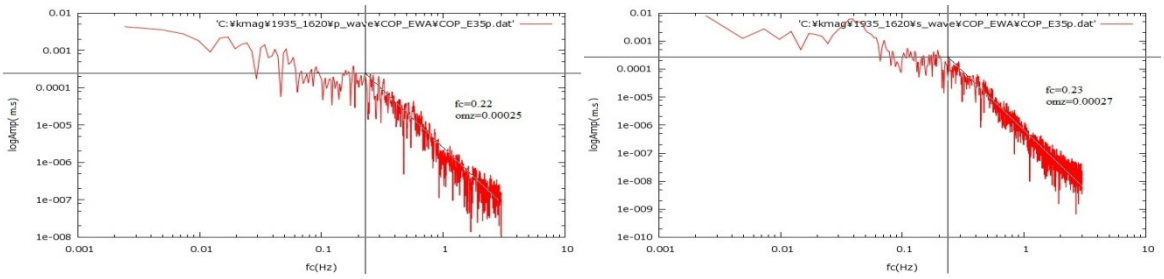

Figure B 90. P and S wave displacement spectra of E-W component seismogram of COP station for 04.01.1935, 16:20 Earthquake. Left figure shows P wave spectra (fc=0.22, Ω_o=0.00025). Right figure shows S wave spectra(fc=0.23, Ω_o=0.00027)

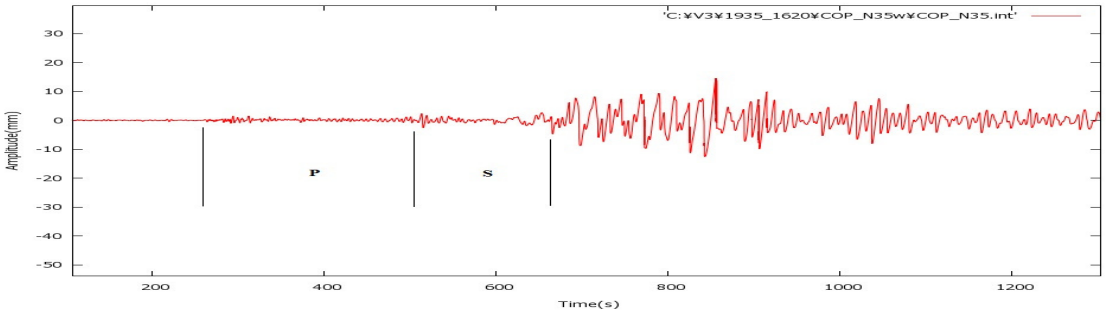

Figure B 91. P and S wave time interval chosen for the N-S component seismogram of COP(Copenhagenen, Denmark) station for 04.01.1935, 16:20 Earthquake, recorded by Wiechert seismometer

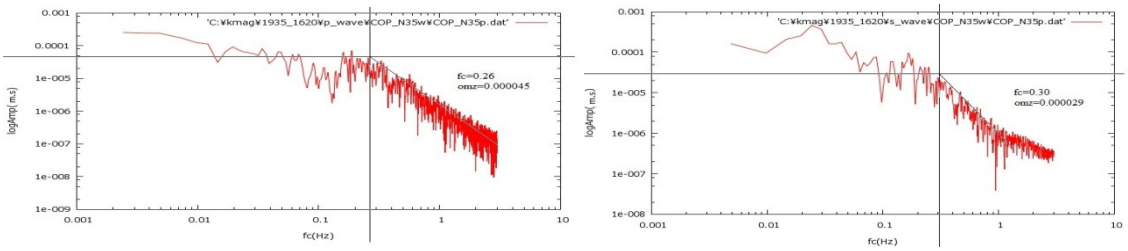

Figure B 92. P and S wave displacement spectra of E-W component seismogram of COP station for 04.01.1935, 16:20 Earthquake. Left figure shows P wave spectra (fc=0.26, Ω_o=0.00045). Right figure shows S wave spectra(fc=0.36, Ω_o=0.00029)

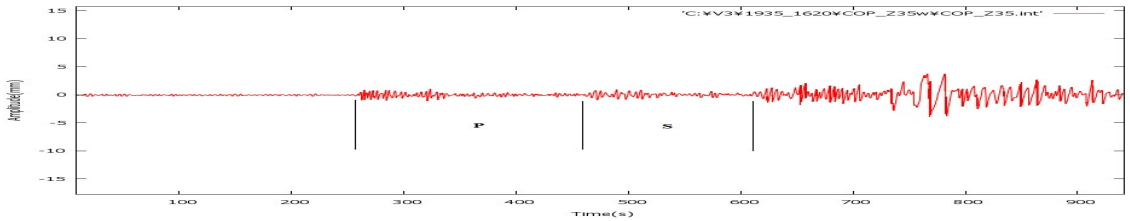

Figure B 93. P and S wave time interval chosen for the Z component seismogram of COP(Copenhagenen, Denmark) station for 04.01.1935, 16:20 Earthquake, recorded by Wiechert seismometer

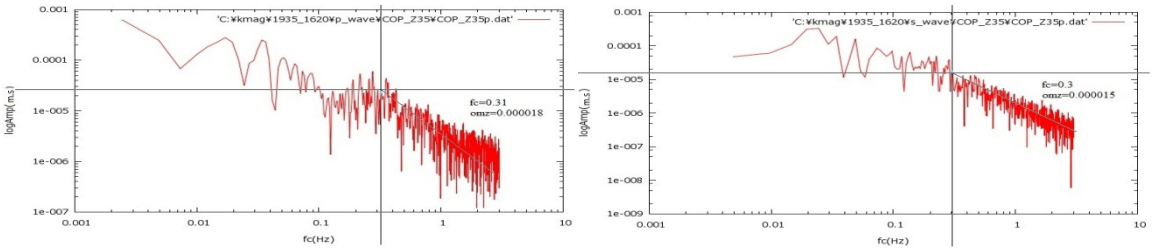

Figure B 94. P and S wave displacement spectra of Z component seismogram of COP station for 04.01.1935, 16:20 Earthquake. Left figure shows P wave spectra (fc=0,31 Ω_o=0.00018). Right figure shows S wave spectra(fc=0.3, Ω_o=0.00015)

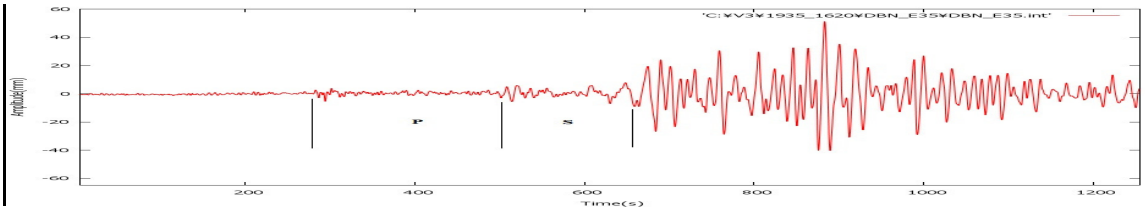

Figure B 95. P and S wave time interval chosen for the E-W component seismogram of DBN(DeBilt, The Netherlands) station for 04.01.1935, 16:20 Earthquake, recorded by Galitzin seismometer

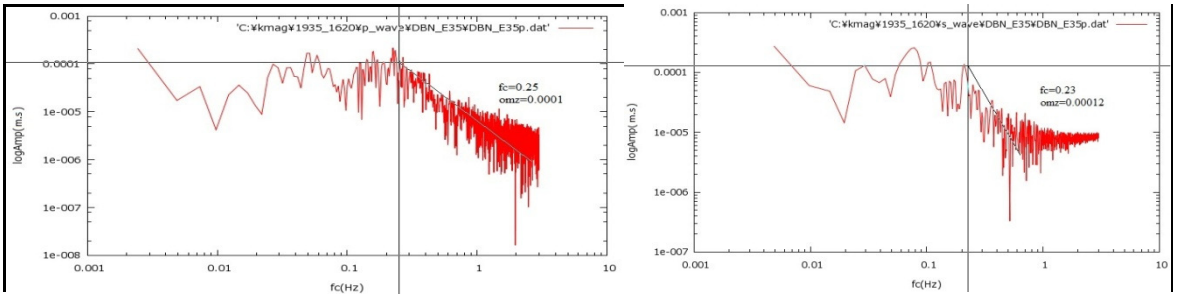

Figure B 96. P and S wave displacement spectra of E-W component seismogram of DBN station for 04.01.1935, 16:20 Earthquake. Left figure shows P wave spectra (fc=0,25 Ω_o=0.0001). Right figure shows S wave spectra(fc=0.23, Ω_o=0.00012)

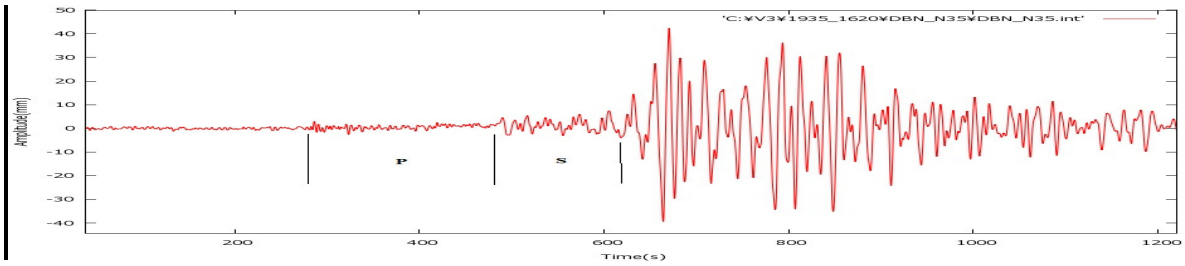

Figure B 97. P and S wave time interval chosen for the N-S component seismogram of DBN(DeBilt, The Netherlands) station for 04.01.1935, 16:20 Earthquake, recorded by Galitzin seismometer

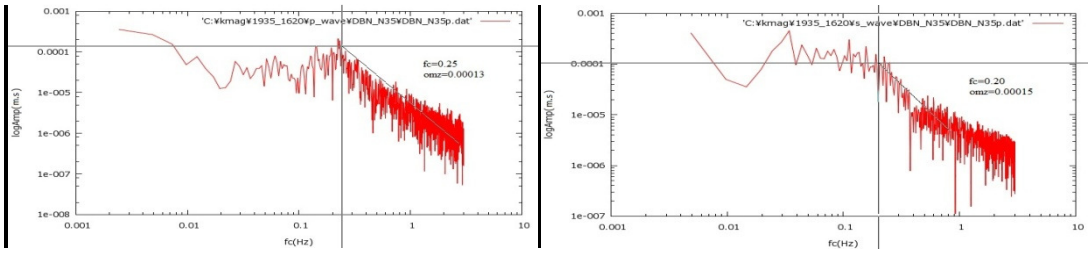

Figure B 98. P and S wave displacement spectra of N-S component seismogram of DBN station for 04.01.1935, 16:20 Earthquake. Left figure shows P wave spectra (fc=0,25 Ω_o=0.00013). Right figure shows S wave spectra(fc=0.20, Ω_o=0.00005)

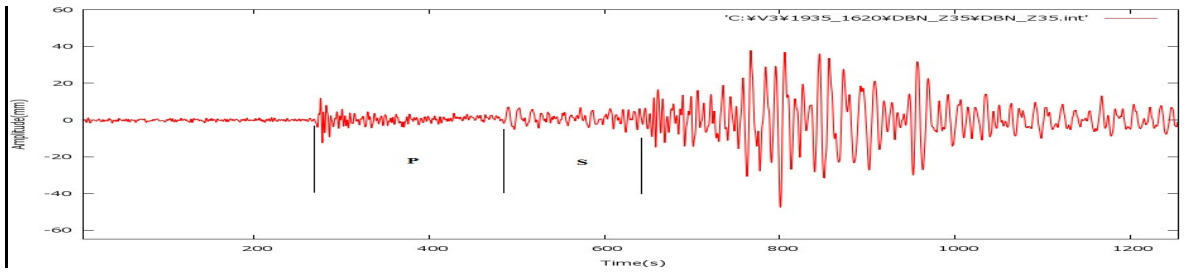

Figure B 99. P and S wave time interval chosen for the Z component seismogram of DBN(DeBilt, The Netherlands) station for 04.01.1935, 16:20 Earthquake, recorded by Galitzin seismometer

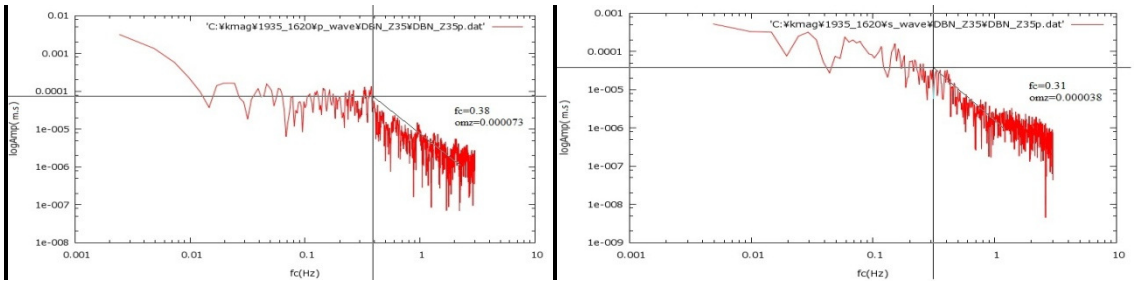

Figure B 100. P and S wave displacement spectra of N-S component seismogram of DBN station for 04.01.1935, 16:20 Earthquake. Left figure shows P wave spectra (fc=0.38, Ω_o=0.000073). Right figure shows S wave spectra(fc=0.31, Ω_o=0.000038)

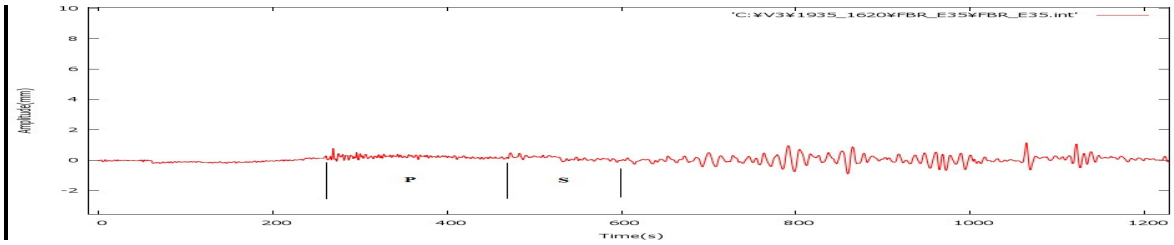

Figure B 101. P and S wave time interval chosen for the E-W component seismogram of FBR(Fabra, Spain) station for 04.01.1935, 16:20 Earthquake, recorded by Mainka seismometer

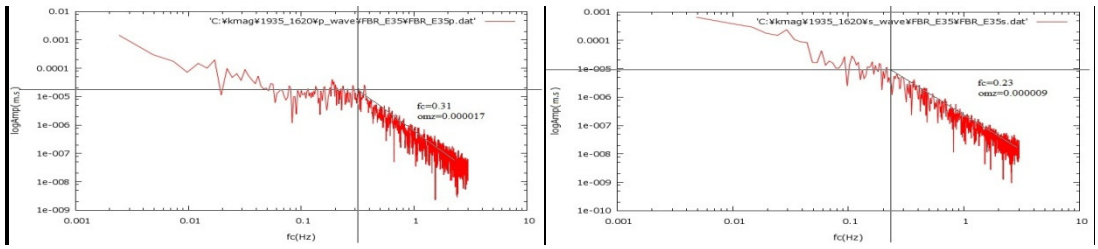

Figure B 102. P and S wave displacement spectra of E-W component seismogram of FBR station for 04.01.1935, 16:20 Earthquake. Left figure shows P wave spectra (fc=0.31, Ω_o=0.000017). Right figure shows S wave spectra(fc=0.23, Ω_o=0.000009)

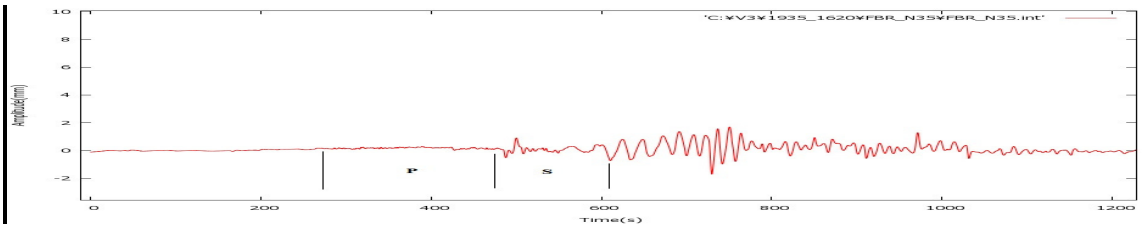

Figure B 103. P and S wave time interval chosen for the N-S component seismogram of FBR(Fabra, Spain) station for 04.01.1935, 16:20 Earthquake, recorded by Mainka seismometer

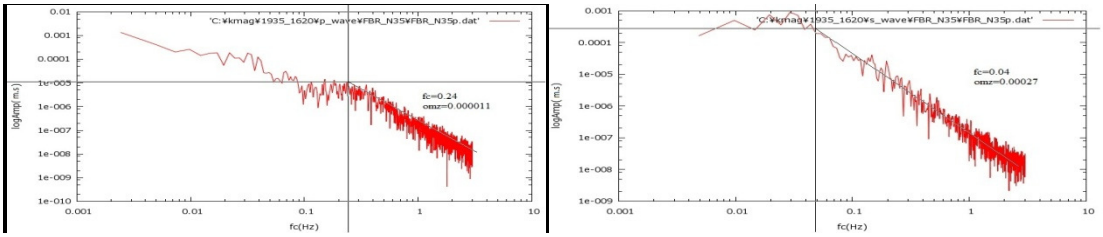

Figure B 104. P and S wave displacement spectra of N-S component seismogram of FBR station for 04.01.1935, 16:20 Earthquake. Left figure shows P wave spectra (fc=0.24, Ω_o=0.000011). Right figure shows S wave spectra(fc=0.04, Ω_o=0.00027)

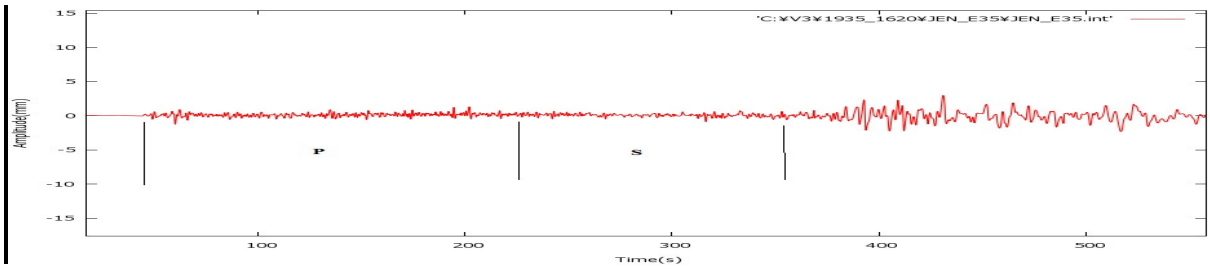

Figure B 105. P and S wave time interval chosen for the E-W component seismogram of JENA(Jena, Germany) station for 04.01.1935, 16:20 Earthquake, recorded by Wiechert(1200 kg) seismometer

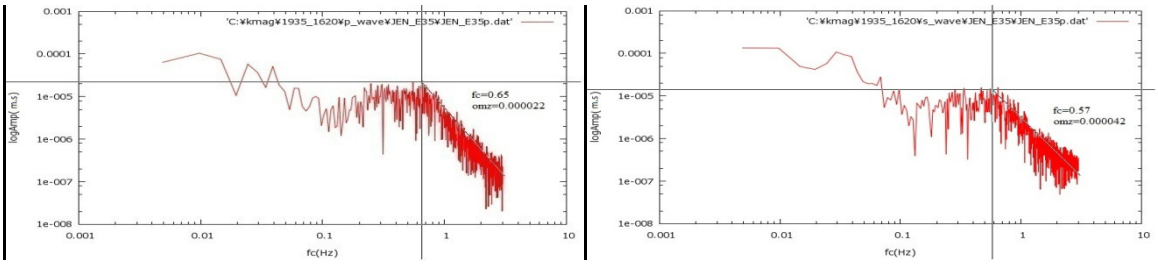

Figure B 106. P and S wave displacement spectra of E-W component seismogram of JENA station for 04.01.1935, 16:20 Earthquake. Left figure shows P wave spectra (fc=0.65, Ω_o=0.000022). Right figure shows S wave spectra(fc=0.57, Ω_o=0.000042)

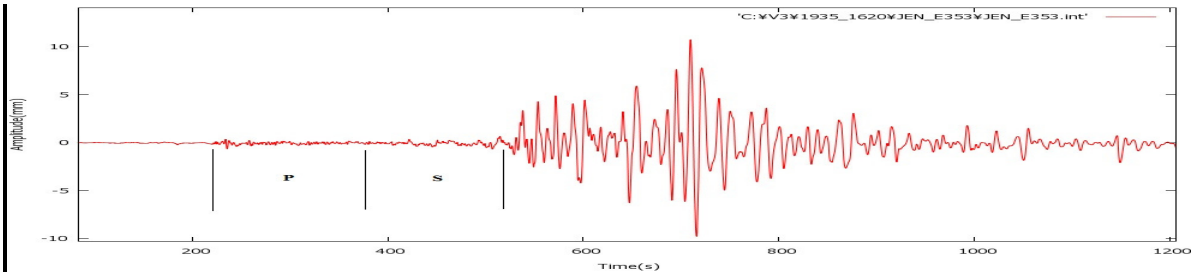

Figure B 107. P and S wave time interval chosen for the E-W component seismogram of JENA(Jena, Germany) station for 04.01.1935, 16:20 Earthquake, recorded by Wiechert(15000 kg) seismometer

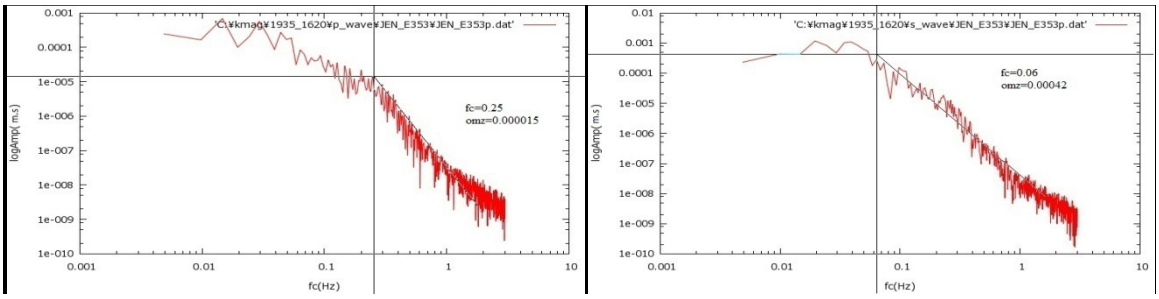

Figure B 108. P and S wave displacement spectra of E-W component seismogram of JENA station for 04.01.1935, 16:20 Earthquake. Left figure shows P wave spectra (fc=0.25, Ω_o=0.000015). Right figure shows S wave spectra(fc=0.06, Ω_o=0.00042)

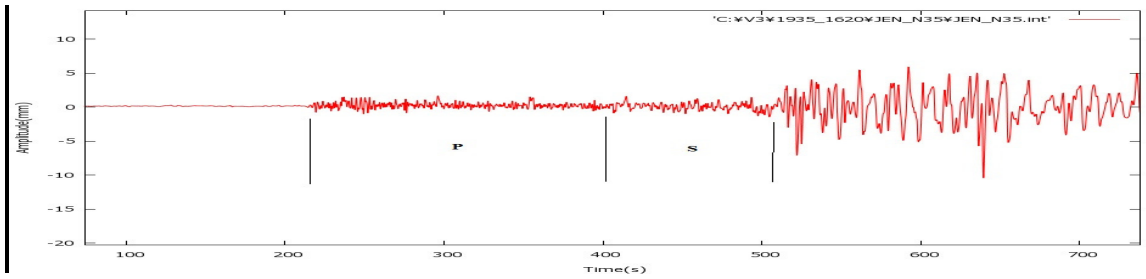

Figure B 109. P and S wave time interval chosen for the N-S component seismogram of JENA(Jena, Germany) station for 04.01.1935, 16:20 Earthquake, recorded by Wiechert(1200 kg) seismometer

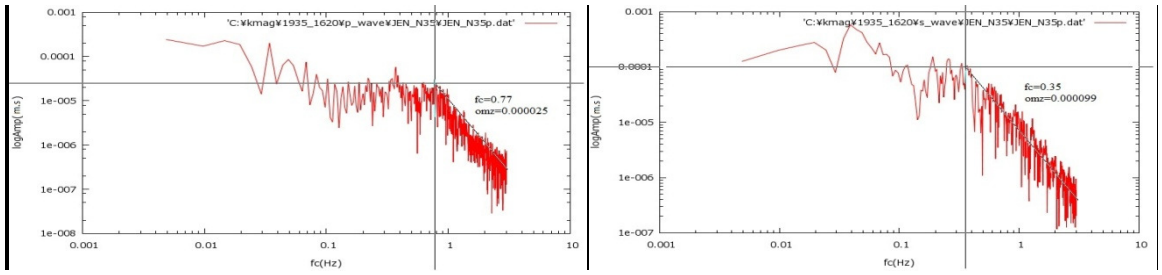

Figure B 110. P and S wave displacement spectra of N-S component seismogram of JENA station for 04.01.1935, 16:20 Earthquake. Left figure shows P wave spectra (fc=0.77, Ω_o=0.000025). Right figure shows S wave spectra(fc=0.35, Ω_o=0.000099)

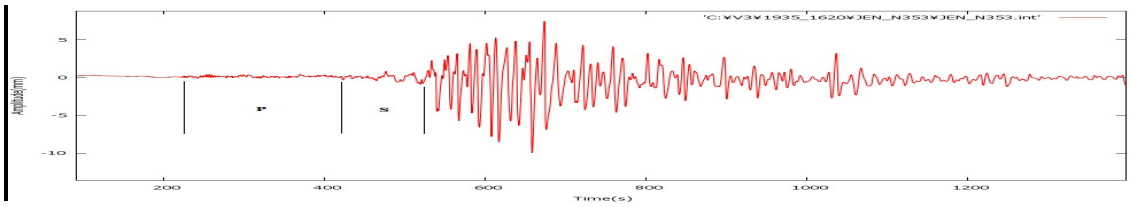

Figure B 111. P and S wave time interval chosen for the N-S component seismogram of JENA(Jena, Germany) station for 04.01.1935, 16:20 Earthquake, recorded by Wiechert(15000 kg) seismometer

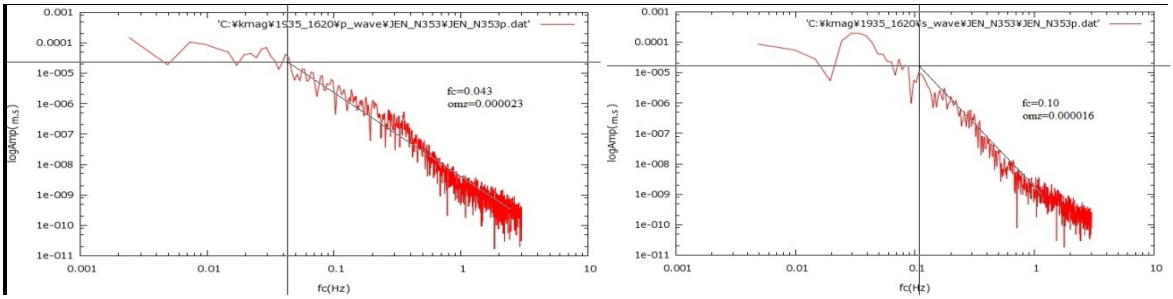

Figure B 112. P and S wave displacement spectra of N-S component seismogram of JENA station for 04.01.1935, 16:20 Earthquake. Left figure shows P wave spectra (fc=0.043, Ω_o=0.000023). Right figure shows S wave spectra(fc=0.10, Ω_o=0.000016)

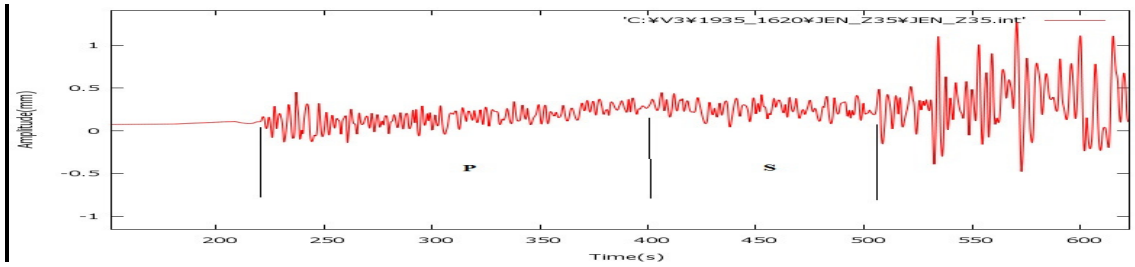

Figure B 113. P and S wave time interval chosen for the Z component seismogram of JENA(Jena, Germany) station for 04.01.1935, 16:20 Earthquake, recorded by Wiechert seismometer

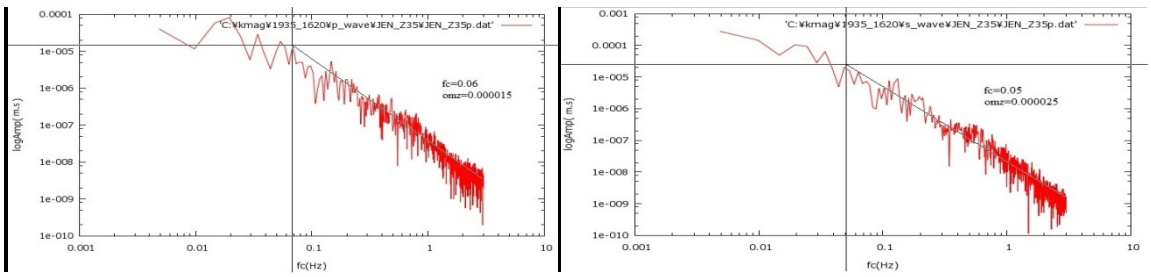

Figure B 114. P and S wave displacement spectra of Z component seismogram of JENA station for 04.01.1935, 16:20 Earthquake. Left figure shows P wave spectra (fc=0.06, Ω_o=0.000015). Right figure shows S wave spectra(fc=0.05, Ω_o=0.000025)

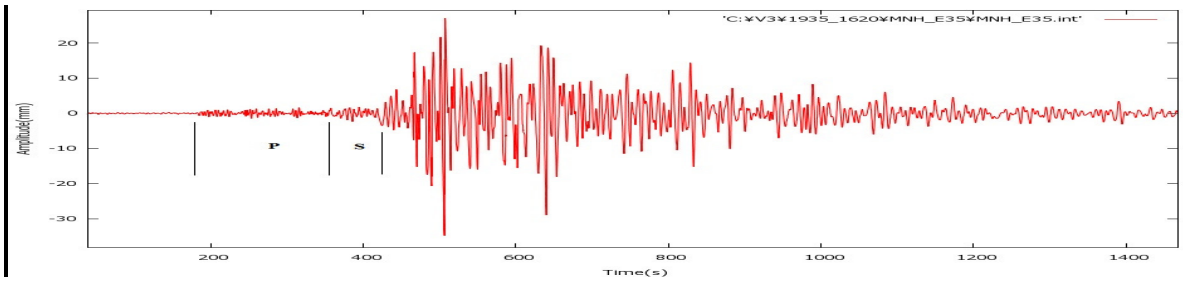

Figure B 115. P and S wave time interval chosen for the E-W component seismogram of MNH(Munich, Germany) station for 04.01.1935, 16:20 Earthquake, recorded by Wiechert seismometer

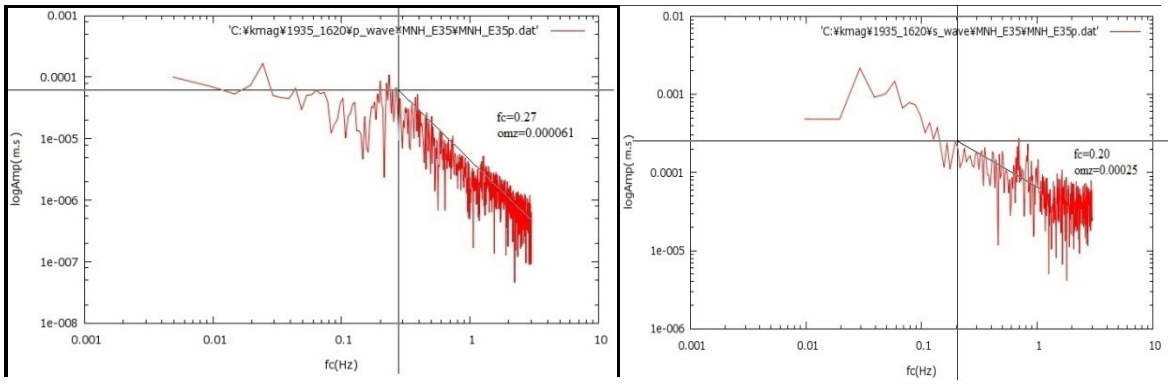

Figure B 116. P and S wave displacement spectra of E-W component seismogram of MNH station for 04.01.1935, 16:20 Earthquake. Left figure shows P wave spectra (fc=0.27, Ω_o=0.000061). Right figure shows S wave spectra(fc=0.20, Ω_o=0.00025)

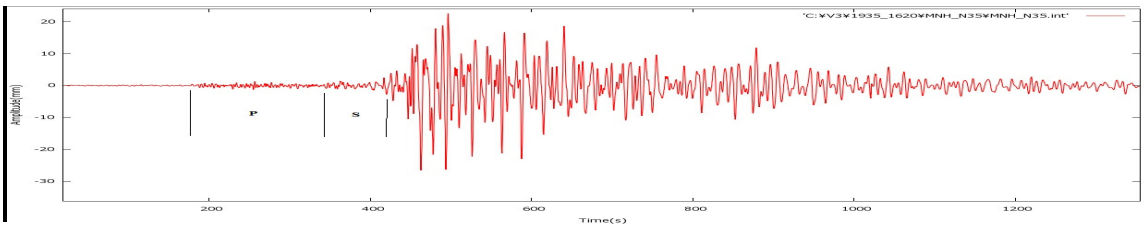

Figure B 117. P and S wave time interval chosen for the N-S component seismogram of MNH(Munich, Germany) station for 04.01.1935, 16:20 Earthquake, recorded by Wiechert seismometer

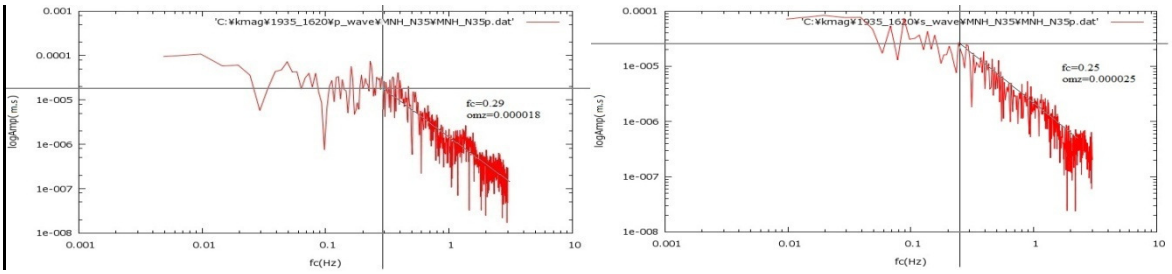

Figure B 118. P and S wave displacement spectra of N-S component seismogram of MNH station for 04.01.1935, 16:20 Earthquake. Left figure shows P wave spectra (fc=0.27, Ω_o=0.000061). Right figure shows S wave spectra(fc=0.20, Ω_o=0.00025)

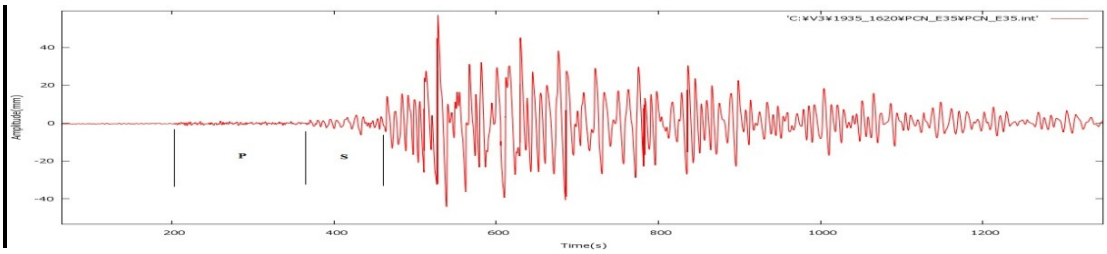

Figure B 119. P and S wave time interval chosen for the E-W component seismogram of PCN(Piacenza, Italy) station for 04.01.1935, 16:20 Earthquake, recorded by Wiechert seismometer

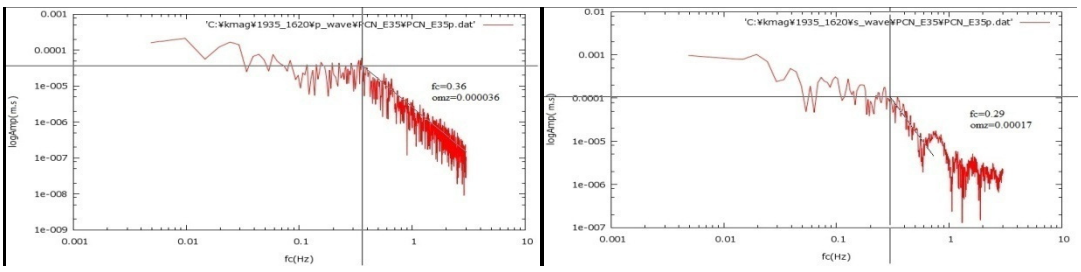

Figure B 120. P and S wave displacement spectra of E-W component seismogram of PCN station for 04.01.1935, 16:20 Earthquake. Left figure shows P wave spectra (fc=0.36, Ω_o=0.000036). Right figure shows S wave spectra(fc=0.29, Ω_o=0.00017)

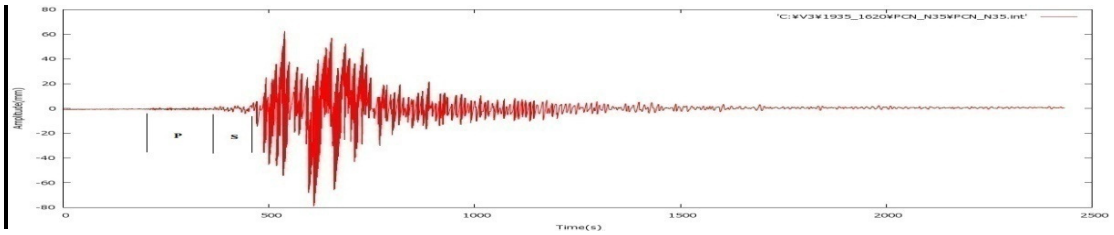

Figure B 121. P and S wave time interval chosen for the N-S component seismogram of PCN(Piacenza, Italy) station for 04.01.1935, 16:20 Earthquake, recorded by Wiechert seismometer

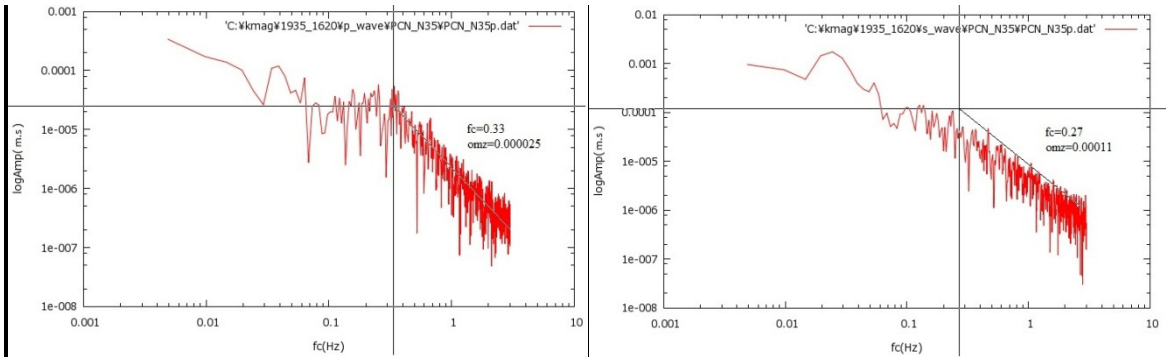

Figure B 122. P and S wave displacement spectra of N-S component seismogram of PCN station for 04.01.1935, 16:20 Earthquake. Left figure shows P wave spectra (fc=0.33, Ω_o=0.000025). Right figure shows S wave spectra(fc=0.27, Ω_o=0.00011)

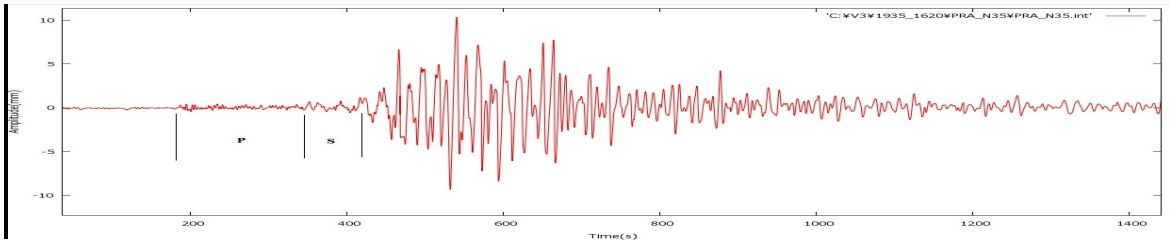

Figure B 123. P and S wave time interval chosen for the N-S component seismogram of PRA(Prague, Czech Republic) station for 04.01.1935, 16:20 Earthquake, recorded by Wiechert seismometer

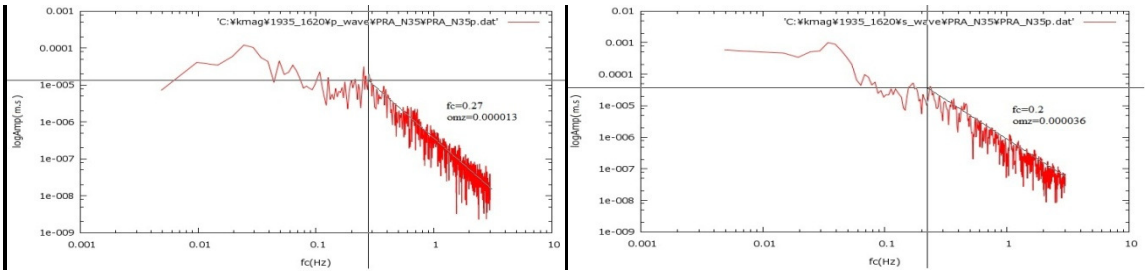

Figure B 124. P and S wave displacement spectra of N-S component seismogram of PRA station for 04.01.1935, 16:20 Earthquake. Left figure shows P wave spectra (fc=0.27, Ω_o=0.000033). Right figure shows S wave spectra(fc=0.2, Ω_o=0.000036)

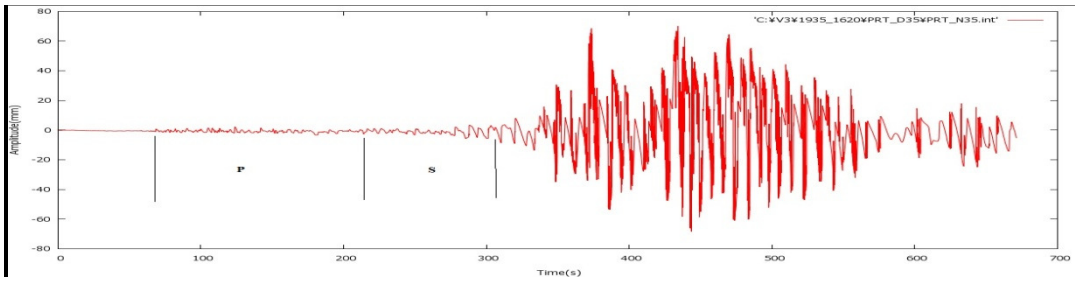

Figure B 125. P and S wave time interval chosen for the N-S component seismogram of PRT(Prato, Italy) station for 04.01.1935, 16:20 Earthquake, recorded by Omori seismometer

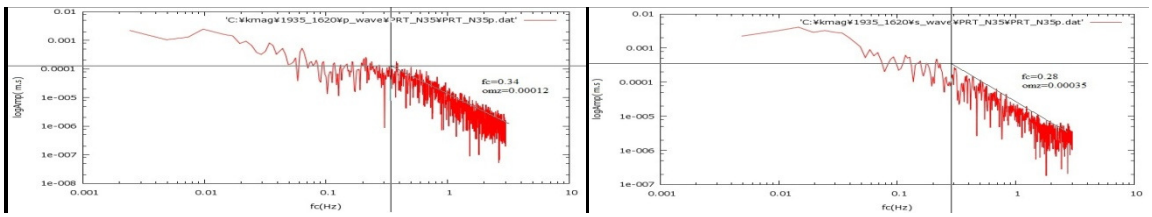

Figure B 126. P and S wave displacement spectra of N-S component seismogram of PRT station for 04.01.1935, 16:20 Earthquake. Left figure shows P wave spectra (fc=0.34, Ω_o=0.00012). Right figure shows S wave spectra(fc=0.28, Ω_o=0.00015)

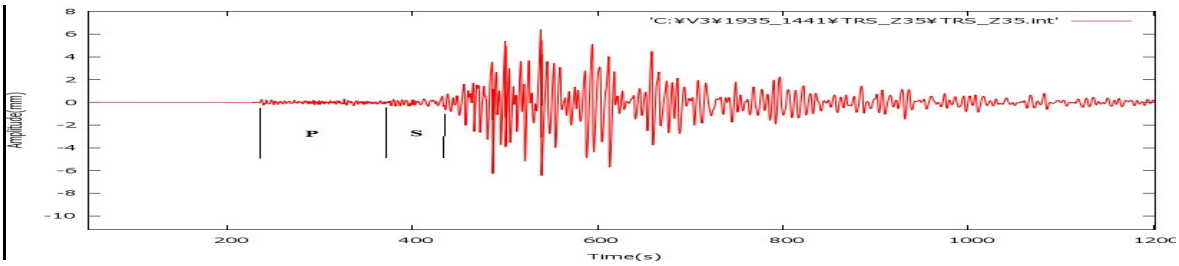

Figure B 127. P and S wave time interval chosen for the Z component seismogram of TRS(Trieste, Italy) station for 04.01.1935, 16:20 Earthquake, recorded by Wiechert seismometer

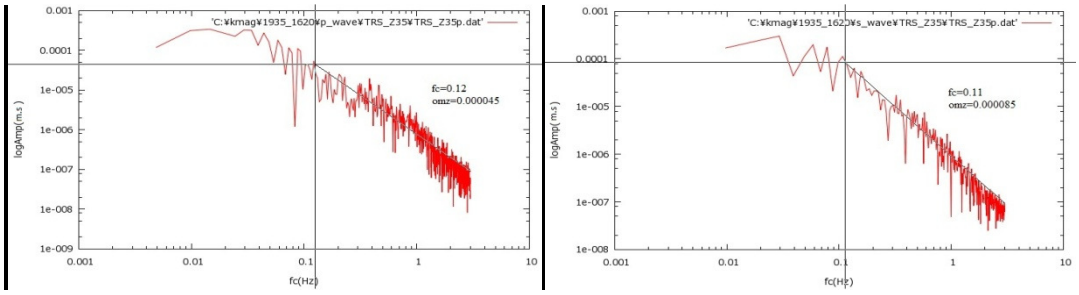

Figure B 128. P and S wave displacement spectra of Z component seismogram of TRS station for 04.01.1935, 16:20 Earthquake. Left figure shows P wave spectra (fc=0.12, Ω_o=0.000045). Right figure shows S wave spectra(fc=0.11, Ω_o=0.000085)

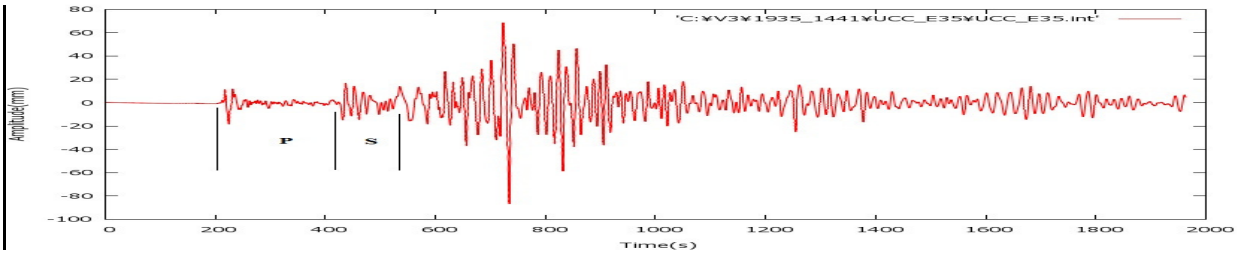

Figure B 129. P and S wave time interval chosen for the E-W component seismogram of UCC(Uccle, Belgium) station for 04.01.1935, 16:20 Earthquake, recorded by Galitzin seismometer

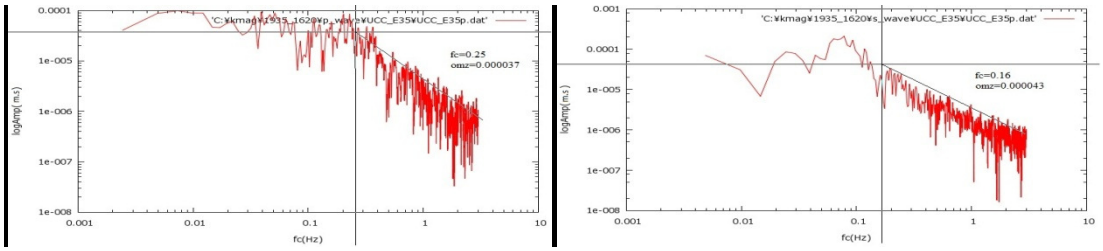

Figure B 130. P and S wave displacement spectra of E-W component seismogram of UCC station for 04.01.1935, 16:20 Earthquake. Left figure shows P wave spectra (fc=0.25, Ω_o=0.000037). Right figure shows S wave spectra(fc=0.16, Ω_o=0.000043)

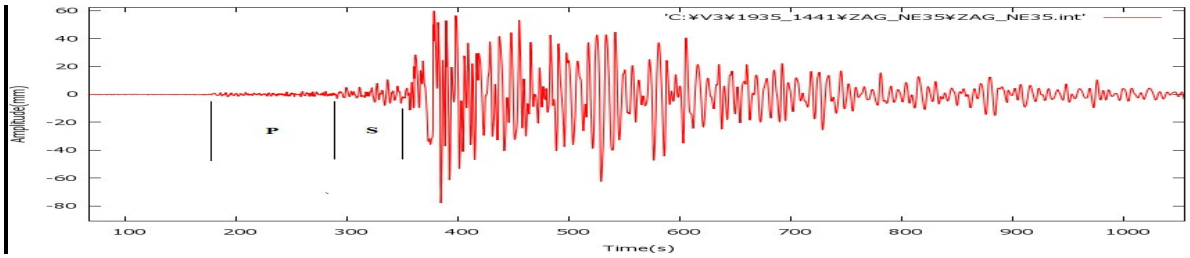

Figure B 131. P and S wave time interval chosen for the N-E component seismogram of ZAG(Zagreb, Croatia) station for 04.01.1935, 16:20 Earthquake, recorded by Wiechert seismometer

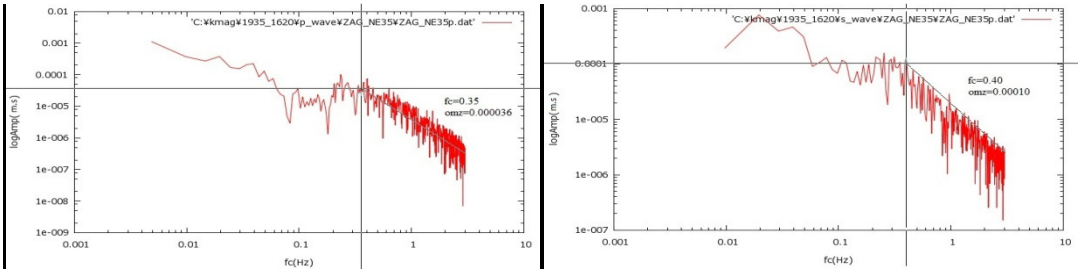

Figure B 132. P and S wave displacement spectra of N-E component seismogram of ZAG station for 04.01.1935, 16:20 Earthquake. Left figure shows P wave spectra (fc=0.35, Ω_o=0.000036). Right figure shows S wave spectra(fc=0.40, Ω_o=0.00010)

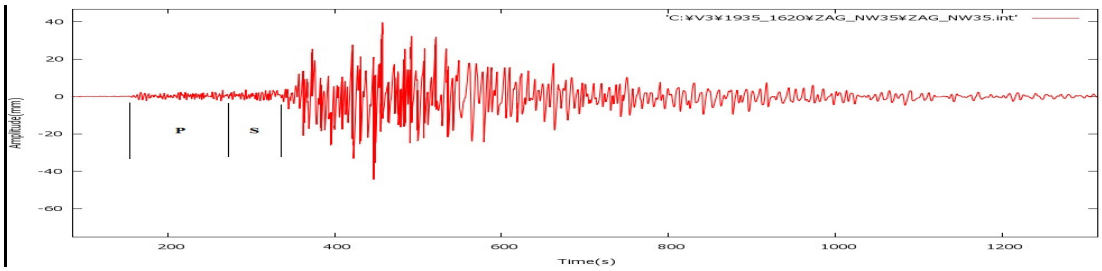

Figure B 133. P and S wave time interval chosen for the N-W component seismogram of ZAG(Zagreb, Croatia) station for 04.01.1935, 16:20 Earthquake, recorded by Wiechert seismometer

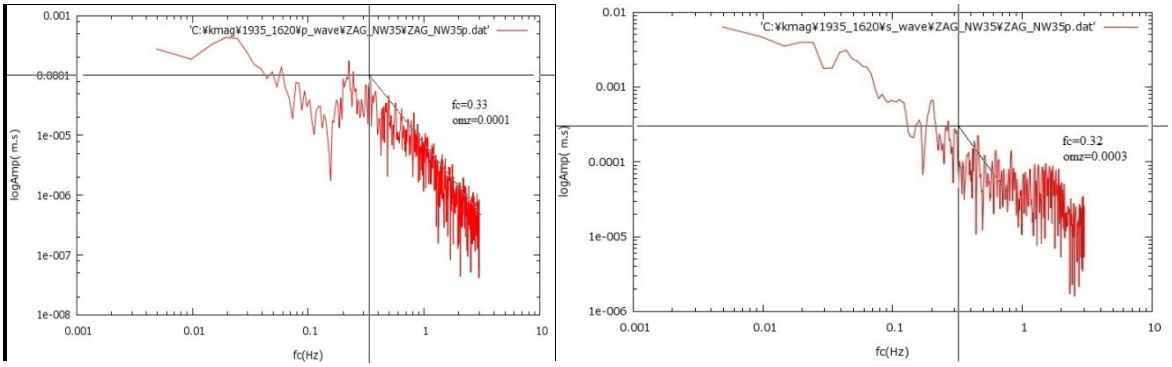

Figure B 134. P and S wave displacement spectra of N-W component seismogram of ZAG station for 04.01.1935, 16:20 Earthquake. Left figure shows P wave spectra (fc=0.33, Ω_o=0.0001). Right figure shows S wave spectra(fc=0.32, Ω_o=0.0003)

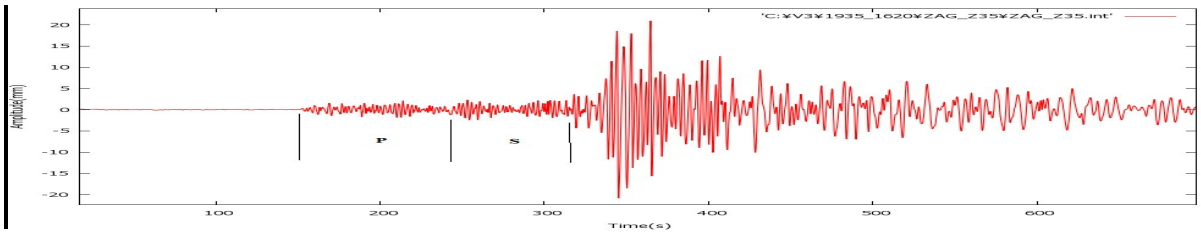

Figure B 135. P and S wave time interval chosen for the Z component seismogram of ZAG(Zagreb, Croatia) station for 04.01.1935, 16:20 Earthquake, recorded by Wiechert seismometer

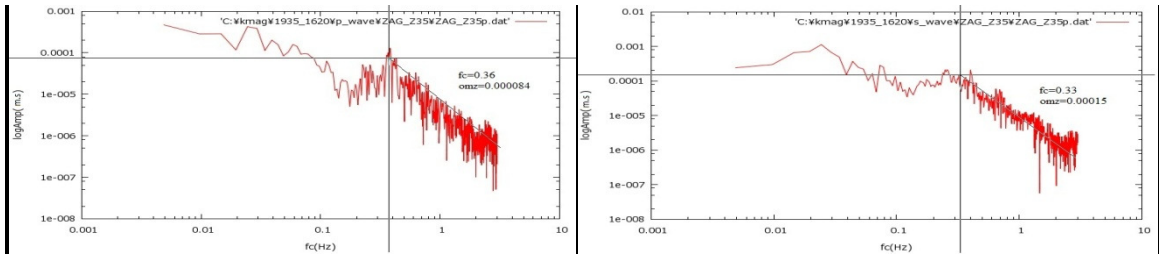

Figure B 136. P and S wave displacement spectra of Z component seismogram of ZAG station for 04.01.1935, 16:20 Earthquake. Left figure shows P wave spectra (fc=0.36, Ω_o=0.000084). Right figure shows S wave spectra(fc=0.33, Ω_o=0.00015)

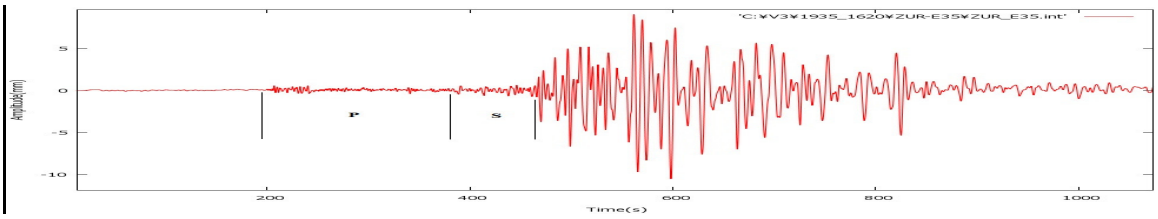

Figure B 137. P and S wave time interval chosen for the E-W component seismogram of ZUR(Zurich, Switzerland) station for 04.01.1935, 16:20 Earthquake, recorded by Mainka seismometer

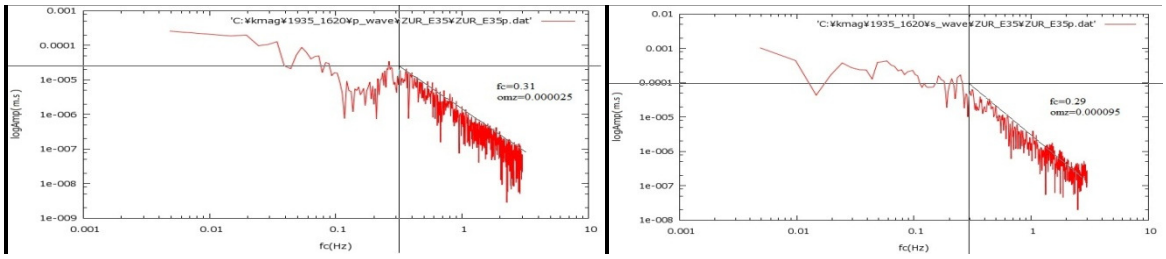

Figure B 138. P and S wave displacement spectra of E-W component seismogram of ZUR station for 04.01.1935, 16:20 Earthquake. Left figure shows P wave spectra (fc=0.31, Ω_o=0.000025). Right figure shows S wave spectra(fc=0.29, Ω_o=0.000095)

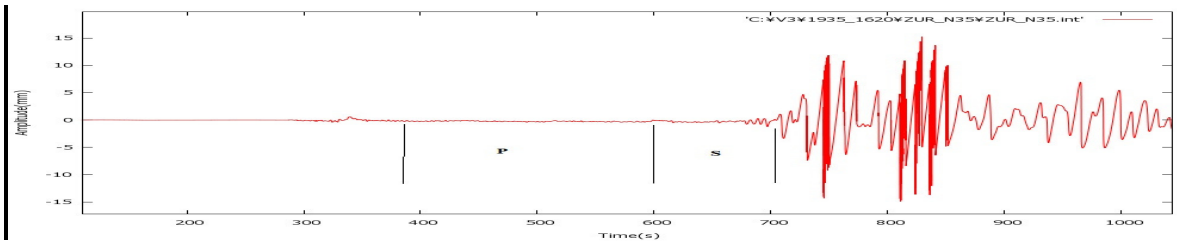

Figure B 139. P and S wave time interval chosen for the N-S component seismogram of ZUR(Zurich, Switzerland) station for 04.01.1935, 16:20 Earthquake, recorded by Mainka seismometer

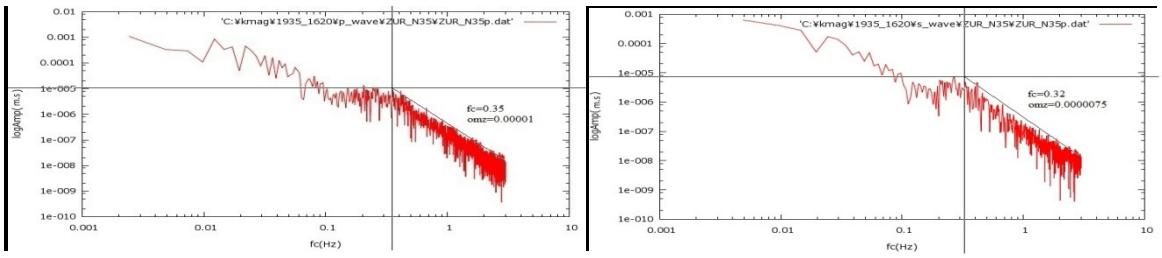

Figure B 140. P and S wave displacement spectra of N-S component seismogram of ZUR station for 04.01.1935, 16:20 Earthquake. Left figure shows P wave spectra (fc=0.35, Ω_o=0.00001). Right figure shows S wave spectra(fc=0.32, Ω_o=0.000075)

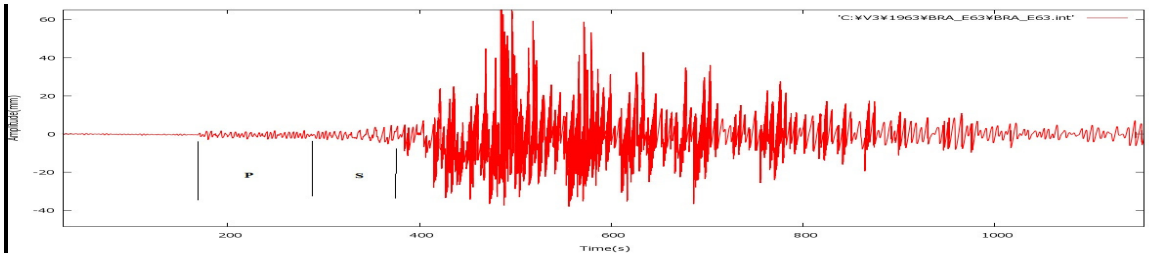

Figure B 141. P and S wave time interval chosen for the E-W component seismogram of BRA(Bratislava, Slovakia) station for 18.09.1963, 16:58 Earthquake, recorded by Wiechert seismometer

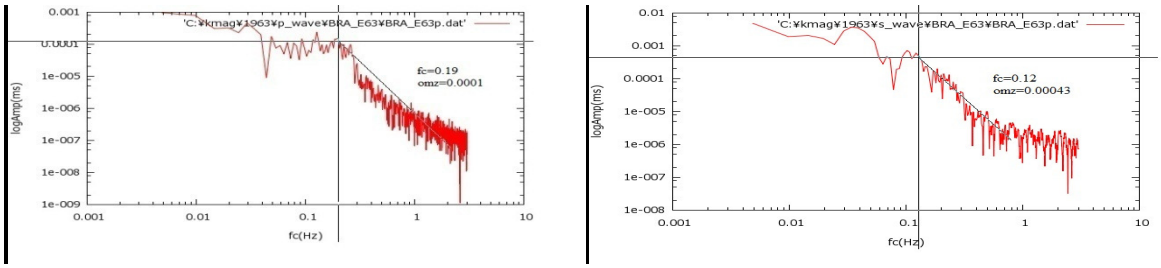

Figure B 142. P and S wave displacement spectra of E-W component seismogram of BRA station for 18.09.1963, 16:58 Earthquake. Left figure shows P wave spectra (fc=0.19, Ω_o=0.0001). Right figure shows S wave spectra(fc=012, Ω_o=0.000043)

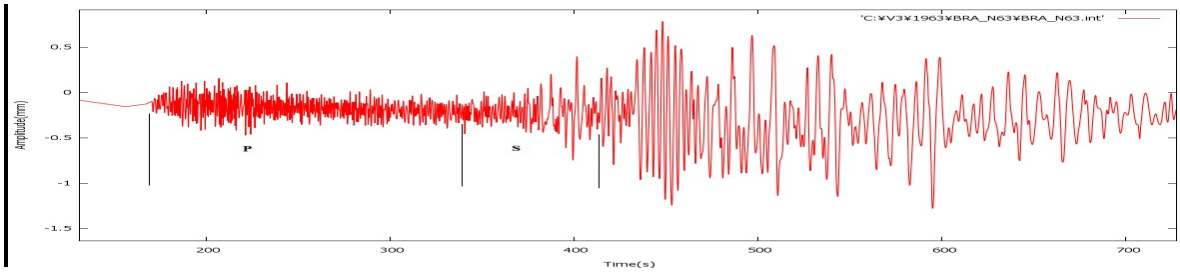

Figure B 143. P and S wave time interval chosen for the N-S component seismogram of BRA(Bratislava, Slovakia) station for 18.09.1963, 16:58 Earthquake, recorded by Wiechert seismometer

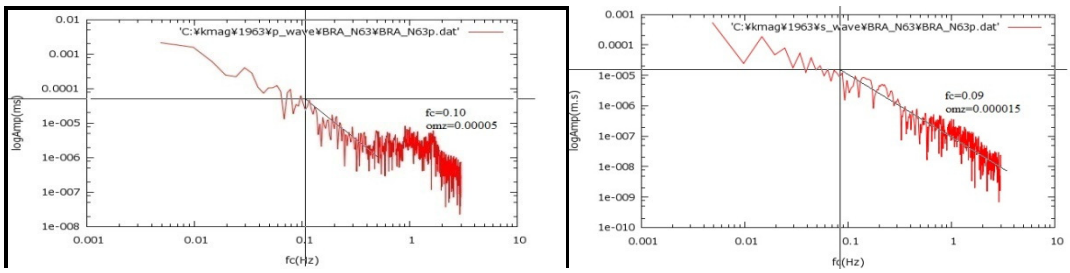

Figure B 144. P and S wave displacement spectra of N-S component seismogram of BRA station for 18.09.1963, 16:58 Earthquake. Left figure shows P wave spectra (fc=0.10, Ω_o=0.0005). Right figure shows S wave spectra(fc=0,09, Ω_o=0.000015)

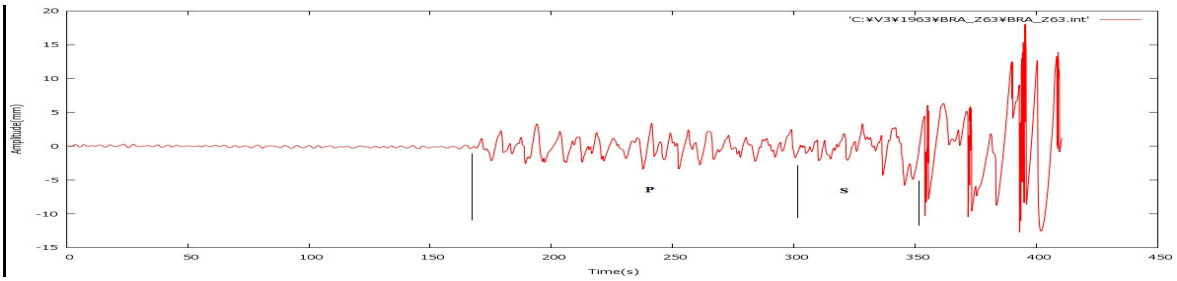

Figure B 145. P and S wave time interval chosen for the Z component seismogram of BRA(Bratislava, Slovakia) station for 18.09.1963, 16:58 Earthquake, recorded by Wiechert seismometer

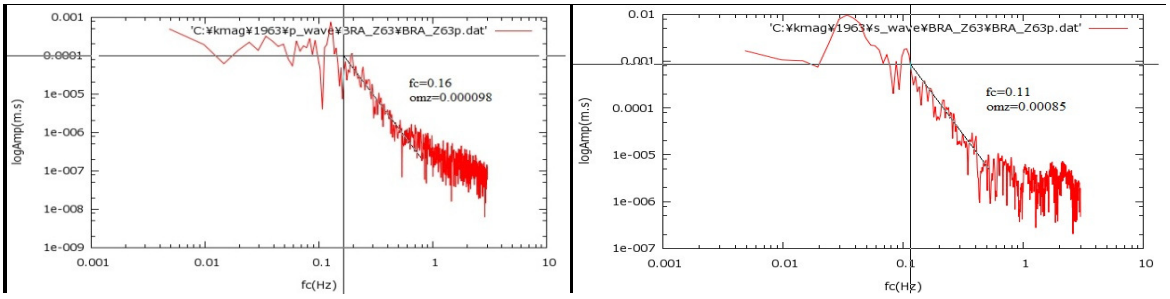

Figure B 146. P and S wave displacement spectra of Z component seismogram of BRA station for 18.09.1963, 16:58 Earthquake. Left figure shows P wave spectra (fc=0.16, Ω_o=0.000098). Right figure shows S wave spectra(fc=0,11, Ω_o=0.00085)

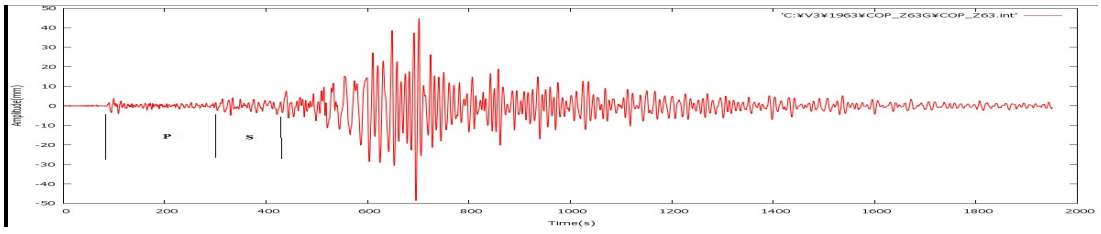

Figure B 147. P and S wave time interval chosen for the Z component seismogram of COP(Copenhagenen, Denmark) station for 18.09.1963, 16:58 Earthquake, recorded by Galitzin seismometer

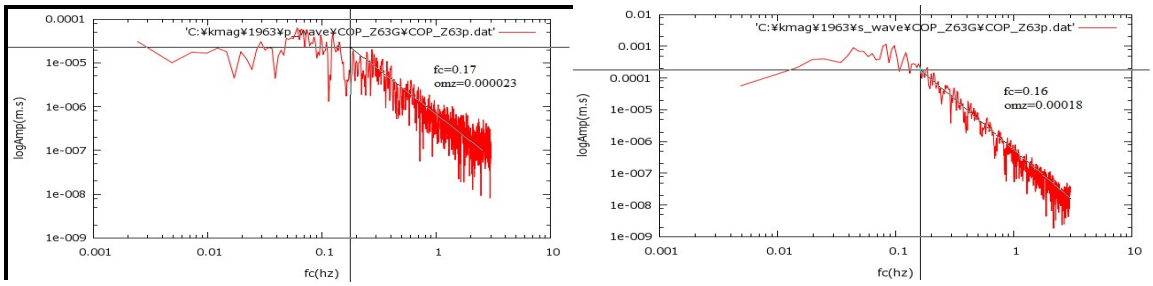

Figure B 148. P and S wave displacement spectra of Z component seismogram of COP station for 18.09.1963, 16:58 Earthquake. Left figure shows P wave spectra (fc=0.17, Ω_o=0.000023). Right figure shows S wave spectra(fc=0,16, Ω_o=0.00018)

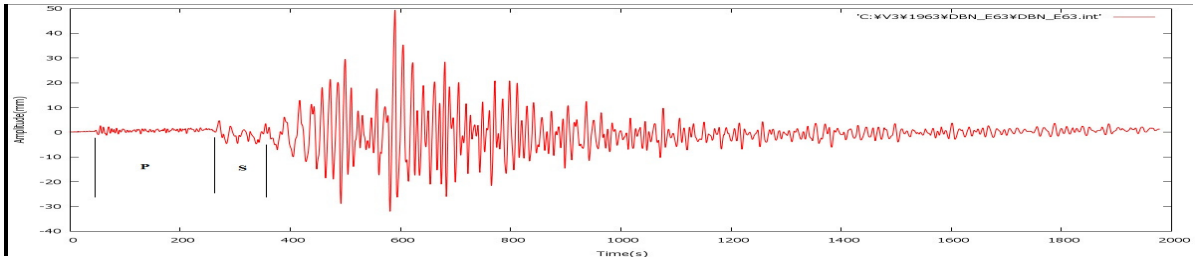

Figure B 149. P and S wave time interval chosen for the E-W component seismogram of DBN(Debilt, The Netherlands) station for 18.09.1963, 16:58 Earthquake, recorded by Galitzin seismometer

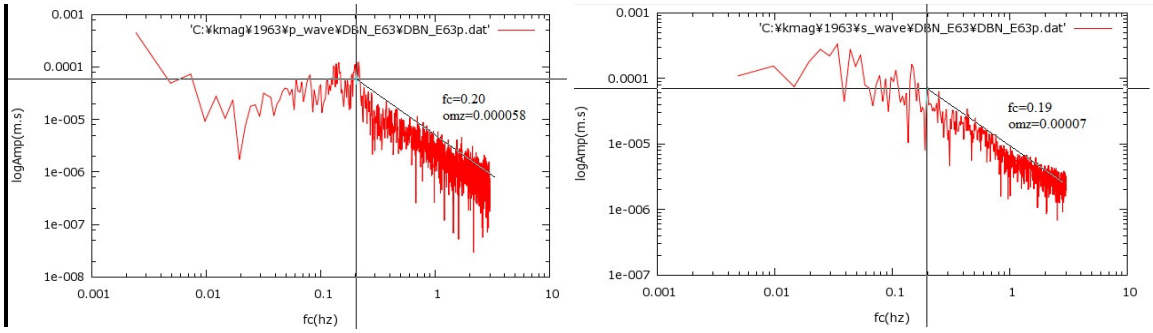

Figure B 150. P and S wave displacement spectra of E-W component seismogram of DBN station for 18.09.1963, 16:58 Earthquake. Left figure shows P wave spectra (fc=0.20, Ω_o=0.000058). Right figure shows S wave spectra(fc=0,19, Ω_o=0.00007)

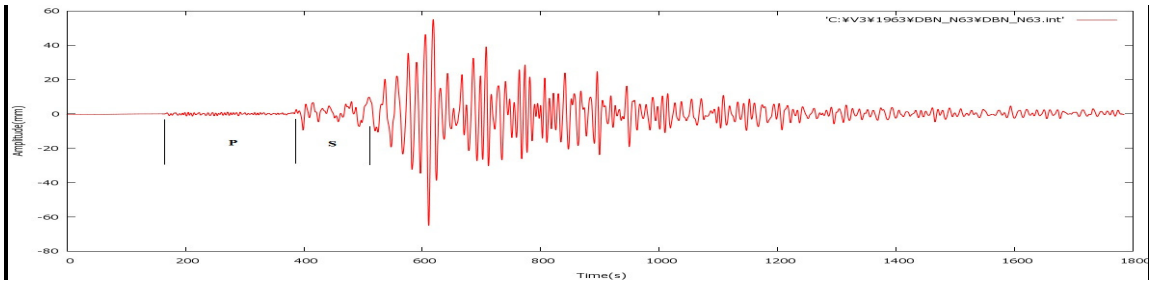

Figure B 151. P and S wave time interval chosen for the N-S component seismogram of DBN(Debilt, The Netherlands) station for 18.09.1963, 16:58 Earthquake, recorded by Galitzin seismometer

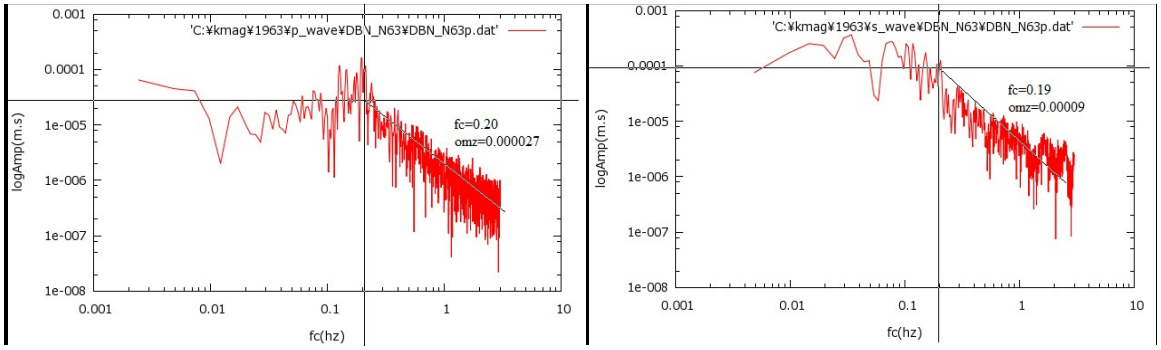

Figure B 152. P and S wave displacement spectra of E-W component seismogram of DBN station for 18.09.1963, 16:58 Earthquake. Left figure shows P wave spectra (fc=0.20, Ω_o=0.000027). Right figure shows S wave spectra(fc=0,19, Ω_o=0.00009)

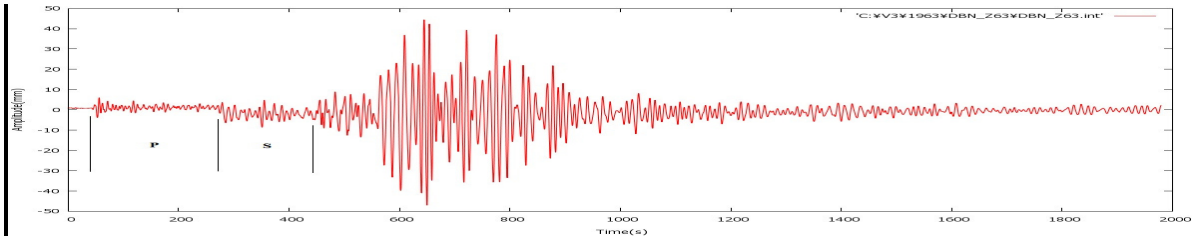

Figure B 153. P and S wave time interval chosen for the Z component seismogram of DBN(Debilt, The Netherlands) station for 18.09.1963, 16:58 Earthquake, recorded by Galitzin seismometer

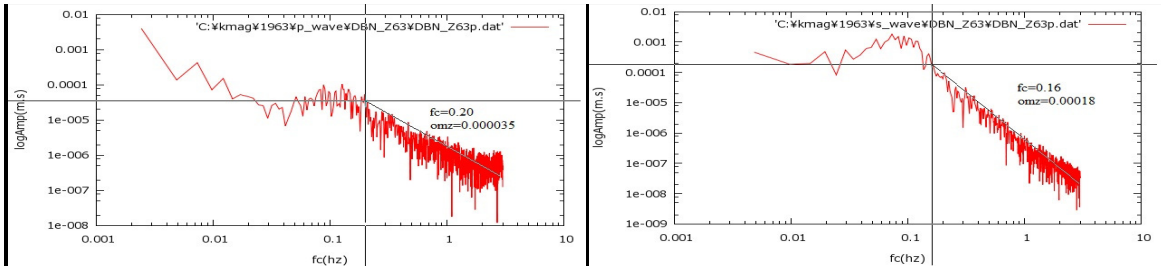

Figure B 154. P and S wave displacement spectra of Z component seismogram of DBN station for 18.09.1963, 16:58 Earthquake. Left figure shows P wave spectra (fc=0.20, Ω_o=0.000035). Right figure shows S wave spectra(fc=0,16, Ω_o=0.00018)

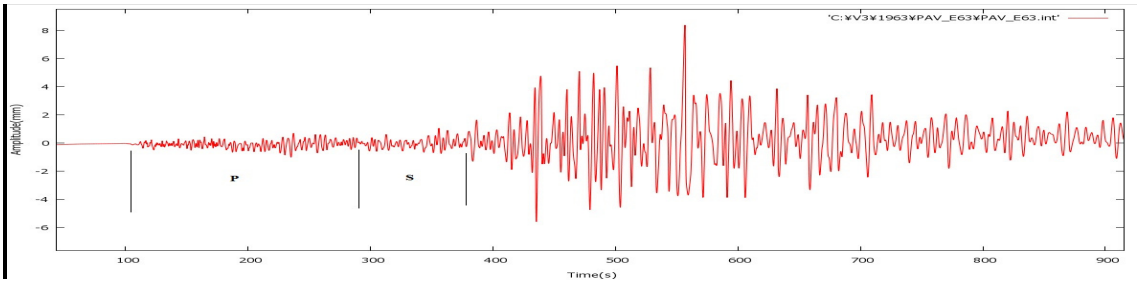

Figure B 155. P and S wave time interval chosen for the E-W component seismogram of PAV(Pavia, Italy) station for 18.09.1963, 16:58 Earthquake, recorded by Wiechert seismometer

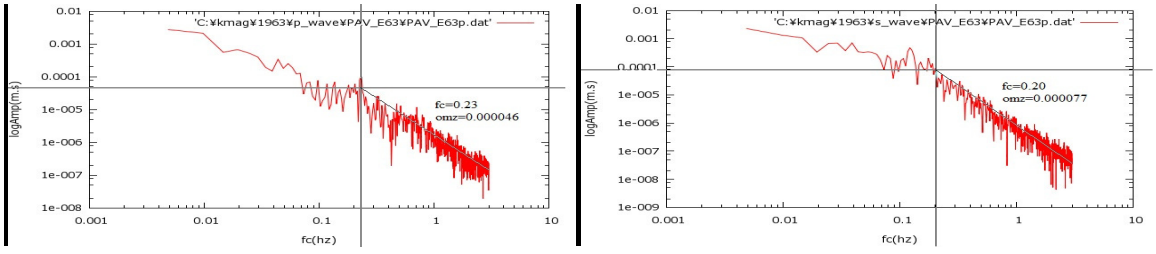

Figure B 156. P and S wave displacement spectra of E-W component seismogram of PAV station for 18.09.1963, 16:58 Earthquake. Left figure shows P wave spectra (fc=0.23, Ω_o=0.000046). Right figure shows S wave spectra(fc=0,20, Ω_o=0.00077)

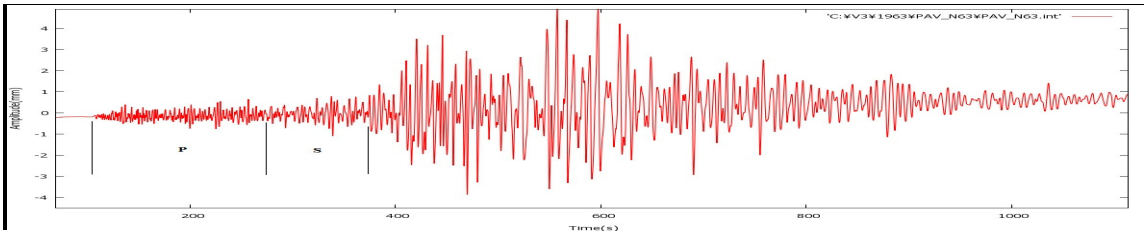

Figure B 157. P and S wave time interval chosen for the N-S component seismogram of PAV(Pavia, Italy) station for 18.09.1963, 16:58 Earthquake, recorded by Wiechert seismometer

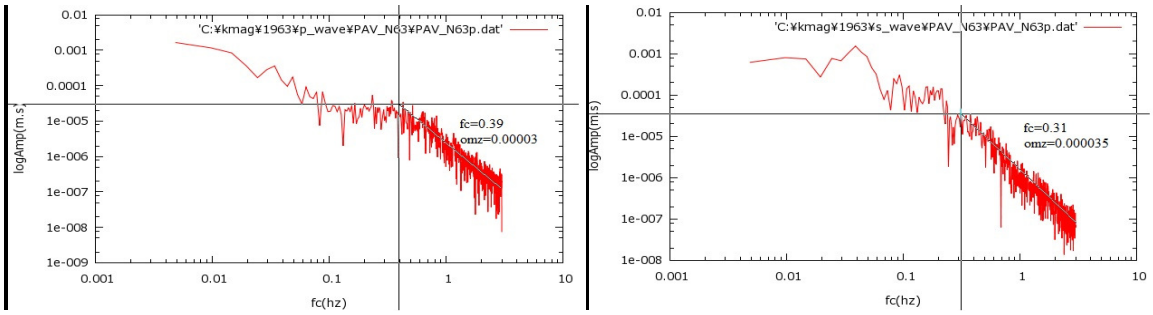

Figure B 158. P and S wave displacement spectra of N-S component seismogram of PAV station for 18.09.1963, 16:58 Earthquake. Left figure shows P wave spectra (fc=0.39, Ω_o=0.00003). Right figure shows S wave spectra(fc=0,31, Ω_o=0.000035)

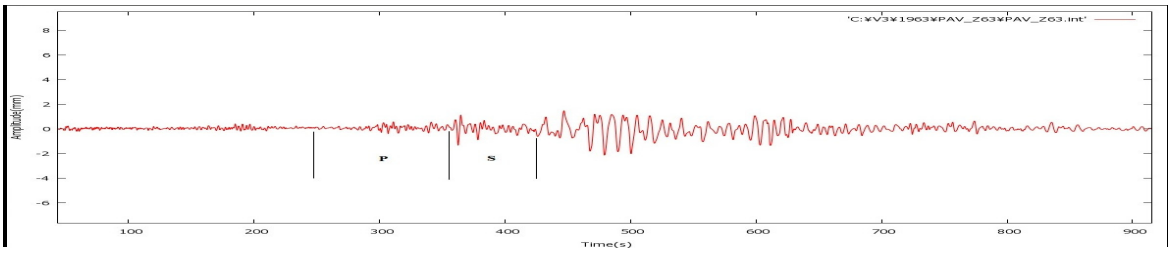

Figure B 159. P and S wave time interval chosen for the Z component seismogram of PAV(Pavia, Italy) station for 18.09.1963, 16:58 Earthquake, recorded by Wiechert seismometer

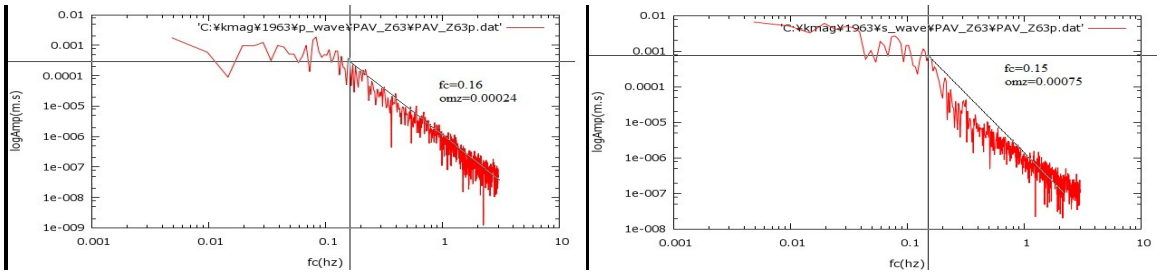

Figure B 160. P and S wave displacement spectra of Z component seismogram of PAV station for 18.09.1963, 16:58 Earthquake. Left figure shows P wave spectra (fc=0.16, Ω_o=0.000024). Right figure shows S wave spectra(fc=0,15, Ω_o=0.000075)

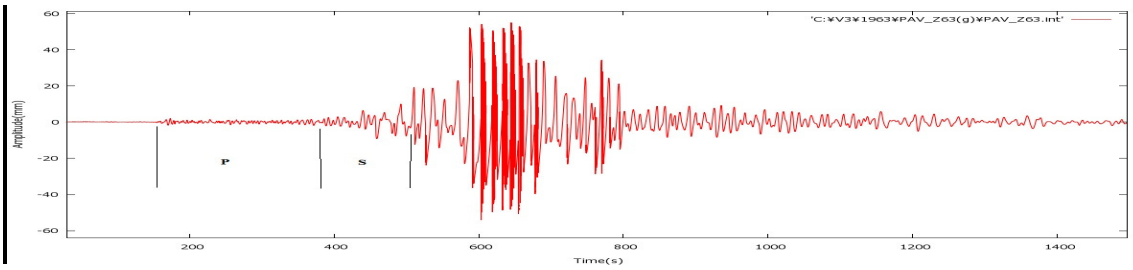

Figure B 161. P and S wave time interval chosen for the Z component seismogram of PAV(Pavia, Italy) station for 18.09.1963, 16:58 Earthquake, recorded by Galitzin seismometer

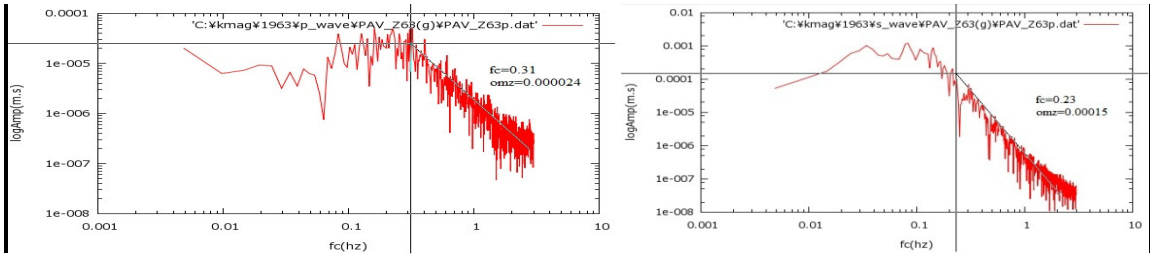

Figure B 162. P and S wave displacement spectra of Z component seismogram of PAV station for 18.09.1963, 16:58 Earthquake. Left figure shows P wave spectra (fc=0.31, Ω_o=0.000024). Right figure shows S wave spectra(fc=0,23, Ω_o=0.00015)

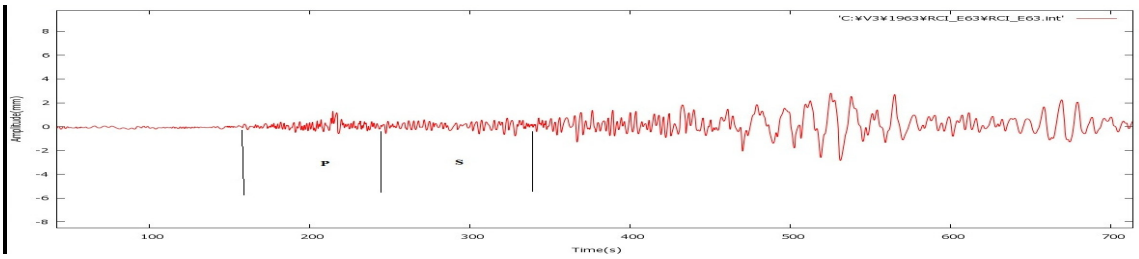

Figure B 163. P and S wave time interval chosen for the E-W component seismogram of RCI(Reggio Calabria, Italy) station for 18.09.1963, 16:58 Earthquake, recorded by Wiechert seismometer

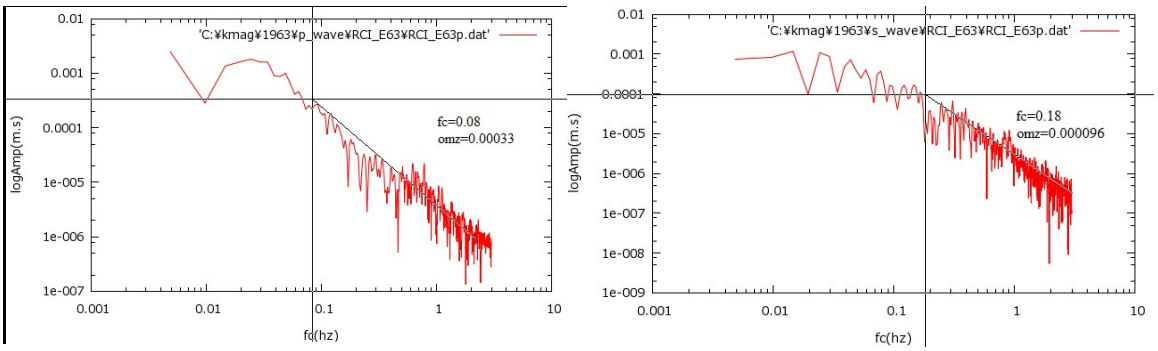

Figure B 164. P and S wave displacement spectra of E-W component seismogram of RCI station for 18.09.1963, 16:58 Earthquake. Left figure shows P wave spectra (fc=0.8, Ω_o=0.00033). Right figure shows S wave spectra(fc=0,18, Ω_o=0.000096)

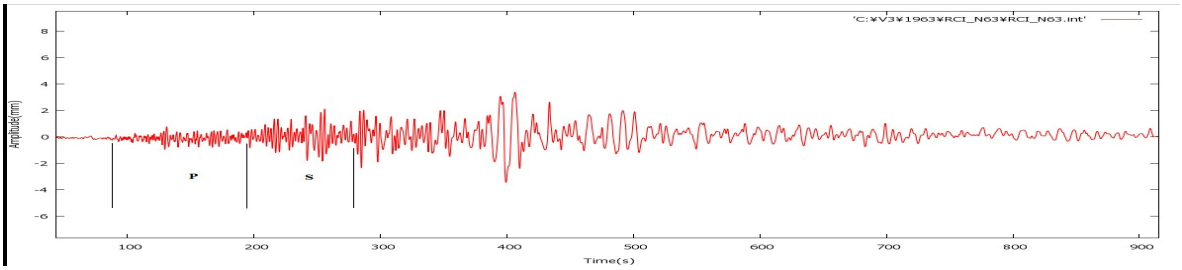

Figure B 165. P and S wave time interval chosen for the N-S component seismogram of RCI(Reggio Calabria, Italy) station for 18.09.1963, 16:58 Earthquake, recorded by Wiechert seismometer

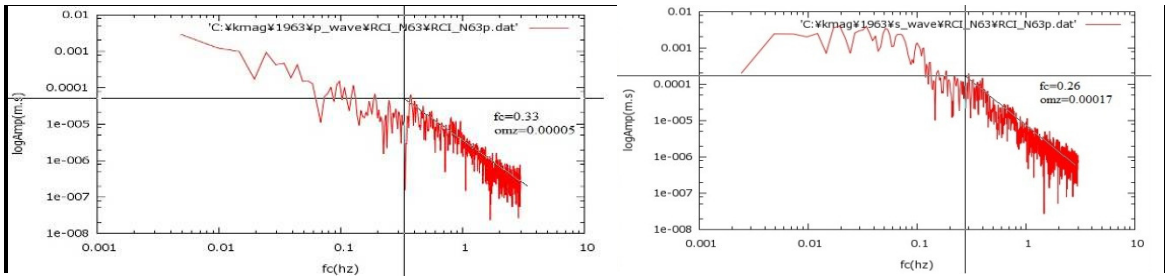

Figure B 166. P and S wave displacement spectra of N-S component seismogram of RCI station for 18.09.1963, 16:58 Earthquake. Left figure shows P wave spectra (fc=0.8, Ω_o=0.00033). Right figure shows S wave spectra(fc=0,18, Ω_o=0.000096)

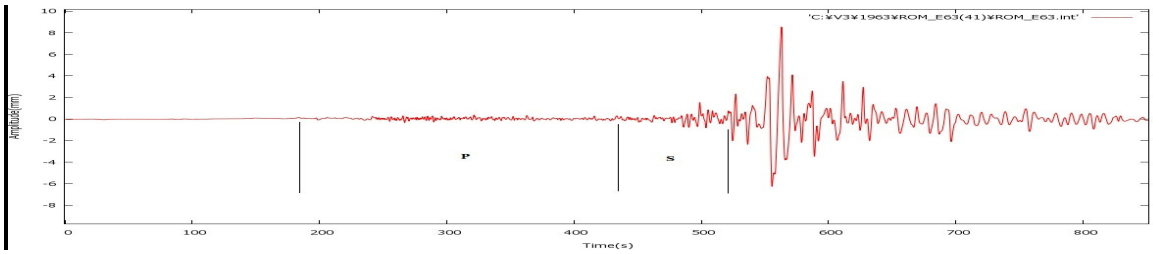

Figure B 167. P and S wave time interval chosen for the E-W component seismogram of ROM(Roma,Italy) station for 18.09.1963, 16:58 Earthquake, recorded by Wiechert (200kg) seismometer

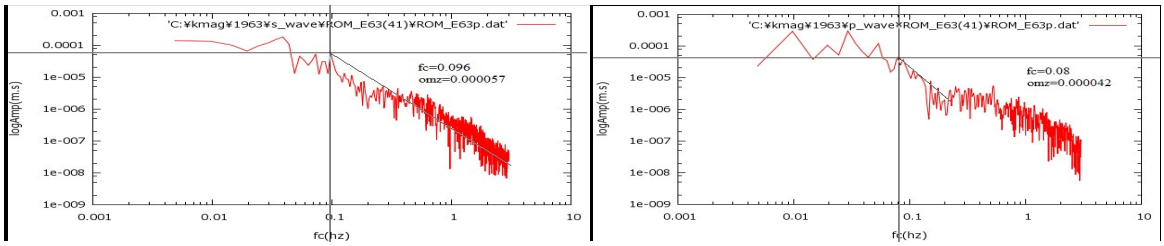

Figure B 168. P and S wave displacement spectra of E-W component seismogram of ROM station for 18.09.1963, 16:58 Earthquake. Left figure shows P wave spectra (fc=0.096, Ω_o=0.00057). Right figure shows S wave spectra(fc=0,08, Ω_o=0.000042)

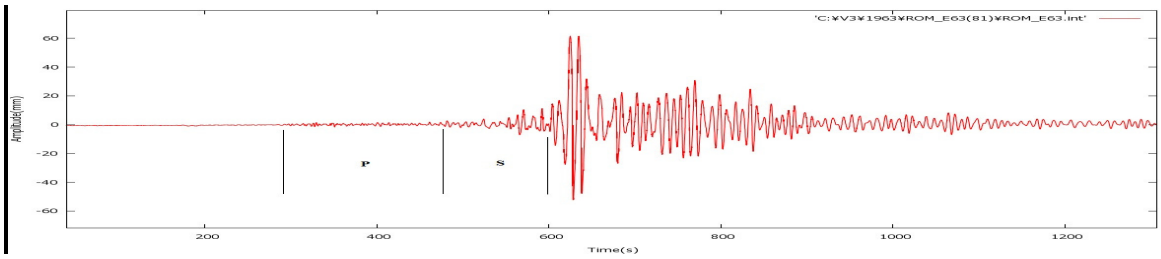

Figure B 169. P and S wave time interval chosen for the E-W component seismogram of ROM(Roma,Italy) station for 18.09.1963, 16:58 Earthquake, recorded by Wiechert(1000kg)seismometer

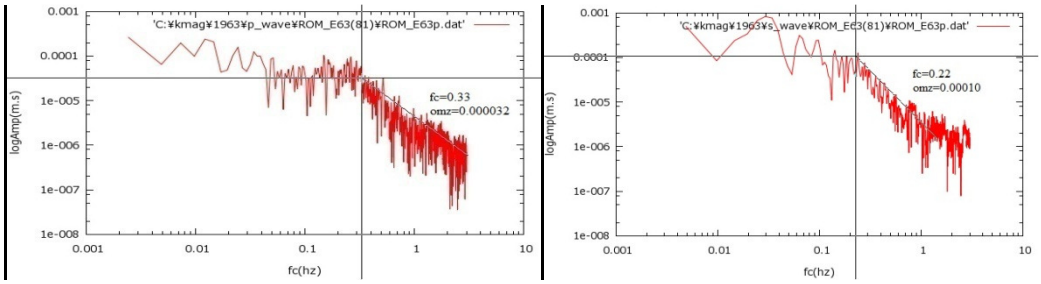

Figure B 170. P and S wave displacement spectra of E-W component seismogram of ROM station for 18.09.1963, 16:58 Earthquake. Left figure shows P wave spectra (fc=0.33, Ω_o=0.000032). Right figure shows S wave spectra(fc=0,22, Ω_o=0.00010)

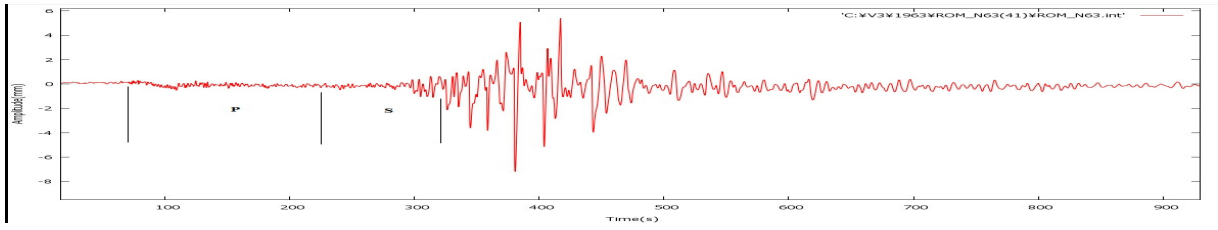

Figure B 171. P and S wave time interval chosen for the N-S component seismogram of ROM(Roma,Italy) station for 18.09.1963, 16:58 Earthquake, recorded by Wiechert(200kg)seismometer

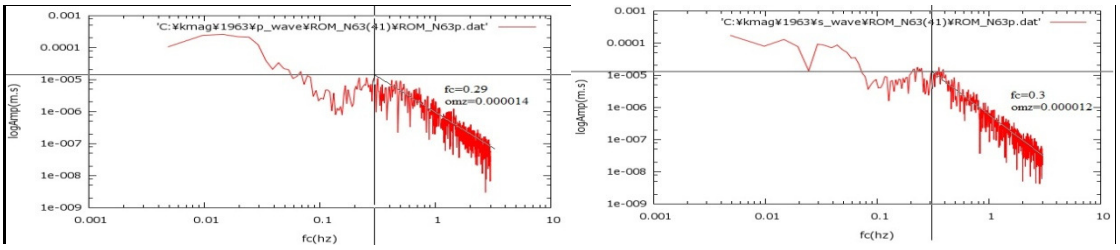

Figure B 172. P and S wave displacement spectra of N-S component seismogram of ROM station for 18.09.1963, 16:58 Earthquake. Left figure shows P wave spectra (fc=0.33, Ω_o=0.000014). Right figure shows S wave spectra(fc=0,3, Ω_o=0.000012)

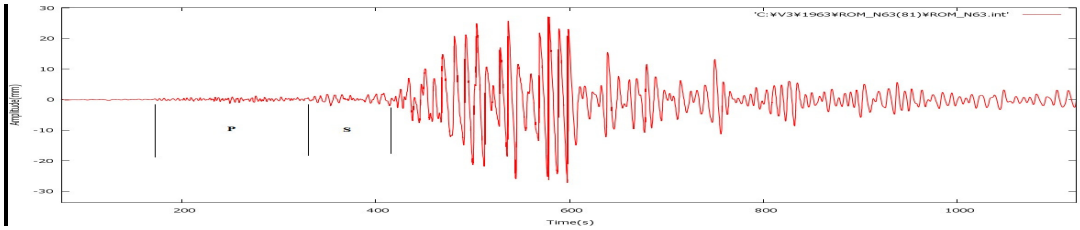

Figure B 173. P and S wave time interval chosen for the N-S component seismogram of ROM(Roma,Italy) station for 18.09.1963, 16:58 Earthquake, recorded by Wiechert(1000kg)seismometer

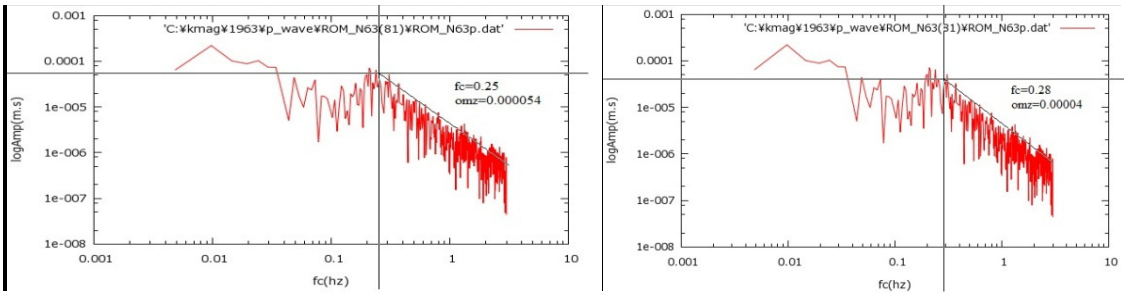

Figure B 174. P and S wave displacement spectra of N-S component seismogram of ROM station for 18.09.1963, 16:58 Earthquake. Left figure shows P wave spectra (fc=0.25, Ω_o=0.000054). Right figure shows S wave spectra(fc=0,28, Ω_o=0.00004)

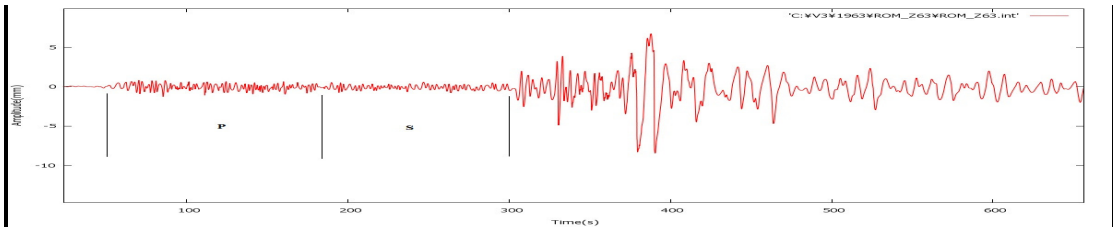

Figure B 175. P and S wave time interval chosen for the Z component seismogram of ROM(Roma,Italy) station for 18.09.1963, 16:58 Earthquake, recorded by Wiechert seismometer

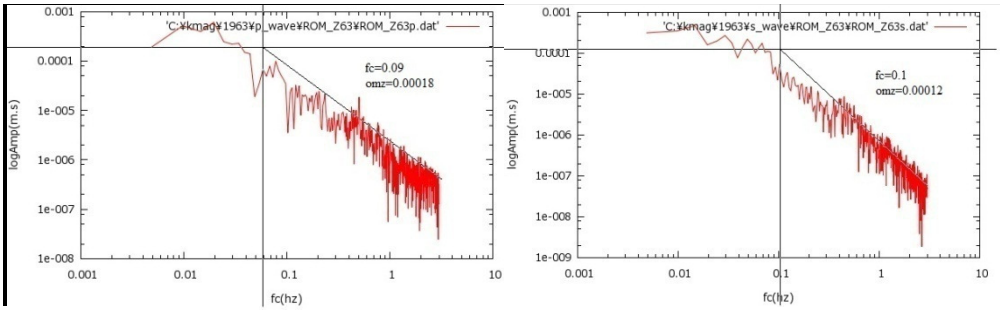

Figure B 176. P and S wave displacement spectra of Z component seismogram of ROM station for 18.09.1963, 16:58 Earthquake. Left figure shows P wave spectra (fc=0.09, Ω_o=0.00018). Right figure shows S wave spectra(fc=0,1, Ω_o=0.0001)

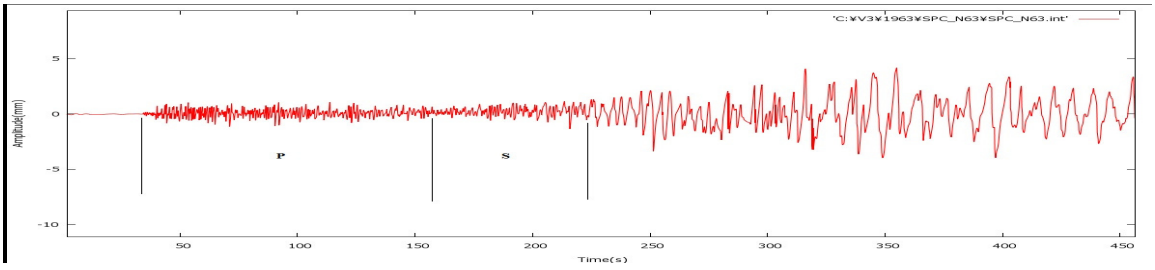

Figure B 177. P and S wave time interval chosen for the N-S component seismogram of SPC (Skalnaté-Pleso ,Slovakia) station for 18.09.1963, 16:58 Earthquake, recorded by Wiechert seismometer

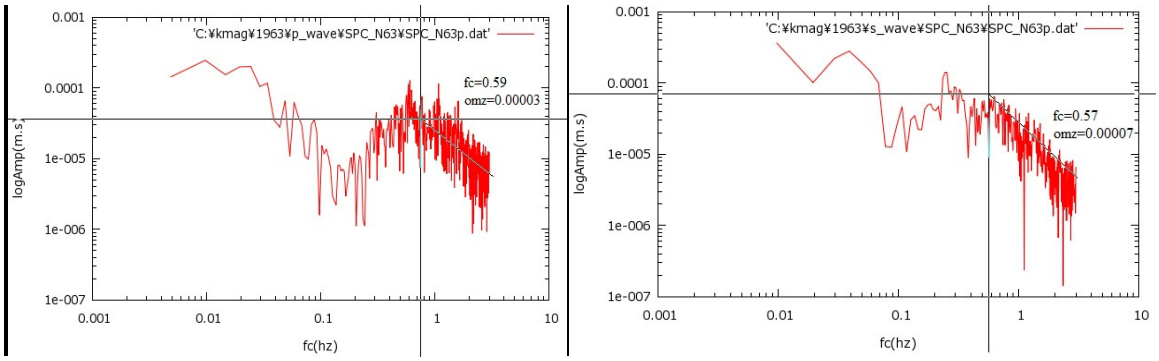

Figure B 178. P and S wave displacement spectra of N-S component seismogram of SPC station for 18.09.1963, 16:58 Earthquake. Left figure shows P wave spectra (fc=0.59, Ω_o=0.00033). Right figure shows S wave spectra(fc=0,57, Ω_o=0.00007)

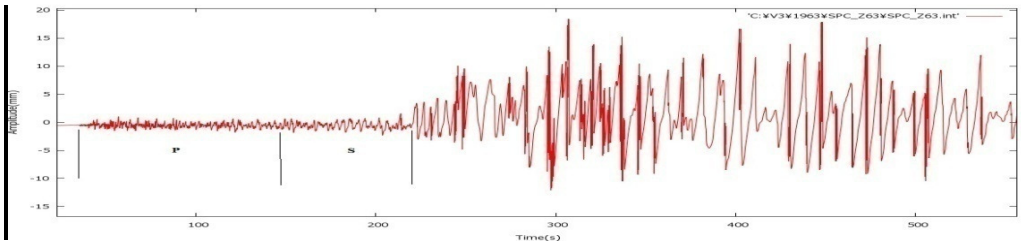

Figure B 179. P and S wave time interval chosen for the Z component seismogram of SPC (Skalnaté-Pleso ,Slovakia) station for 18.09.1963, 16:58 Earthquake, recorded by Wiechert seismometer

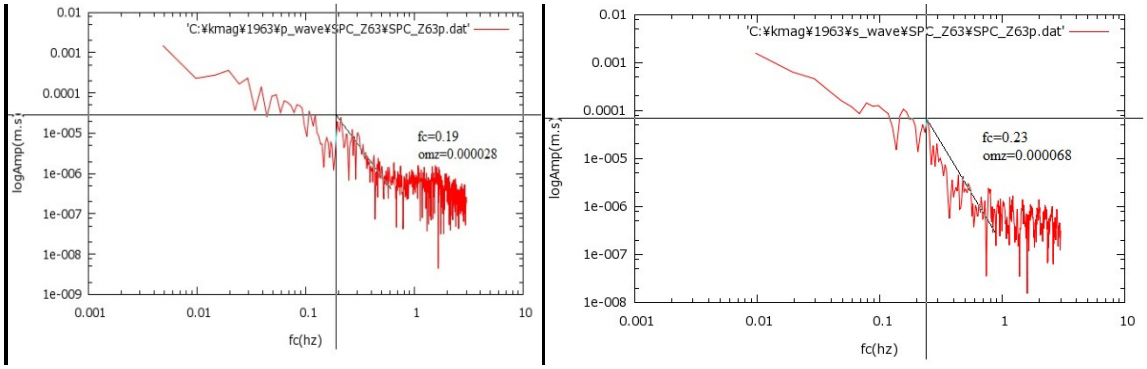

Figure B 180. P and S wave displacement spectra of N-S component seismogram of SPC station for 18.09.1963, 16:58 Earthquake. Left figure shows P wave spectra (fc=0.19, Ω_o=0.000028). Right figure shows S wave spectra(fc=0,23, Ω_o=0.000068)

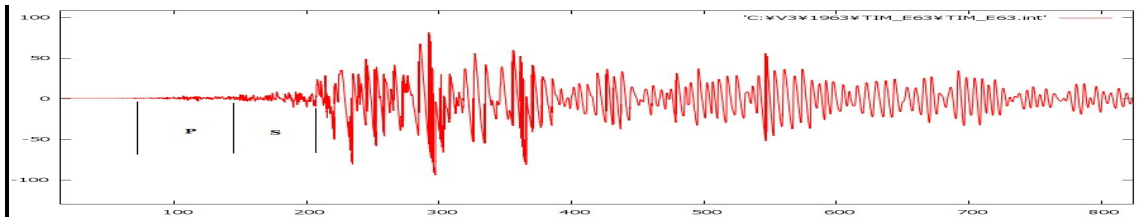

Figure B 181. P and S wave time interval chosen for the E-W component seismogram of TIM (Timisoara ,Romania) station for 18.09.1963, 16:58 Earthquake, recorded by Mainka seismometer

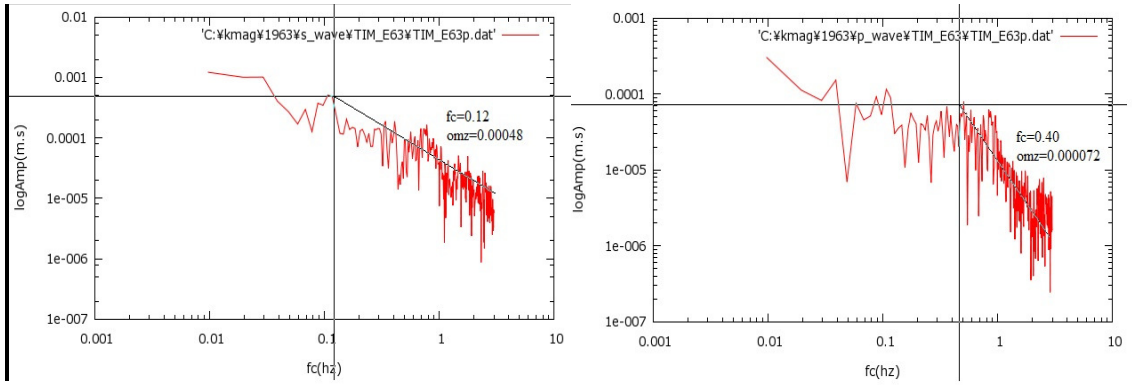

Figure B 182. P and S wave displacement spectra of E-W component seismogram of TIM station for 18.09.1963, 16:58 Earthquake. Left figure shows P wave spectra (fc=0.12, Ω_o=0.00048). Right figure shows S wave spectra(fc=0,40, Ω_o=0.000072)

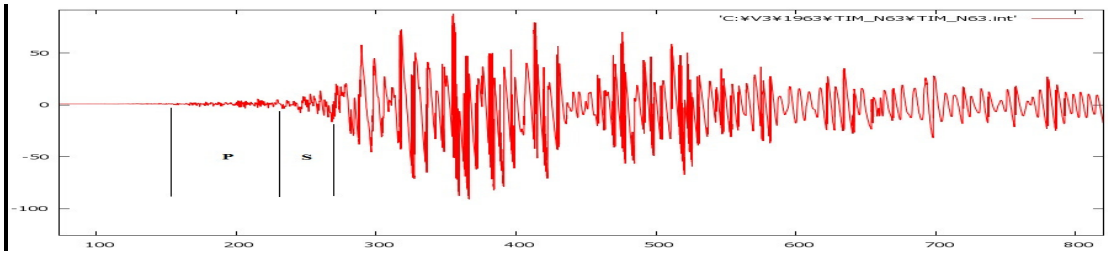

Figure B 183. P and S wave time interval chosen for the N-S component seismogram of TIM (Timisoara ,Romania) station for 18.09.1963, 16:58 Earthquake, recorded by Mainka seismometer

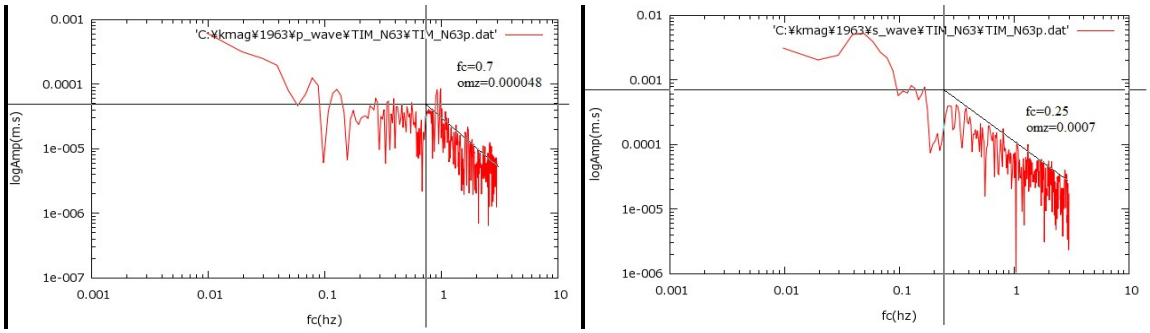

Figure B 184. P and S wave displacement spectra of N-S component seismogram of TIM station for 18.09.1963, 16:58 Earthquake. Left figure shows P wave spectra (fc=0.7, Ω_o=0.000048). Right figure shows S wave spectra(fc=0,25, Ω_o=0.00072)

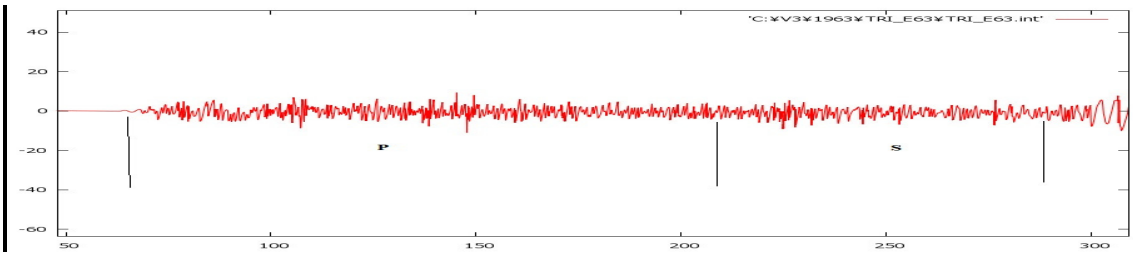

Figure B 185. P and S wave time interval chosen for the E-W component seismogram of TRI (Trieste ,Italy) station for 18.09.1963, 16:58 Earthquake, recorded by Benioff seismometer

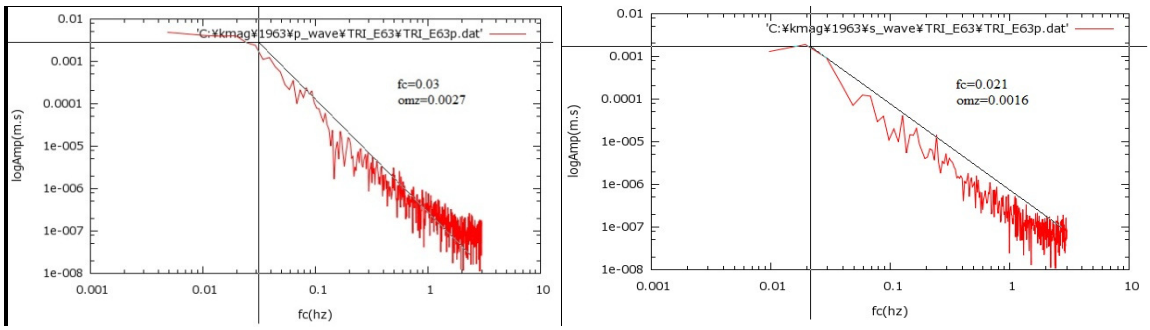

Figure B 186. P and S wave displacement spectra of E-W component seismogram of TRI station for 18.09.1963, 16:58 Earthquake. Left figure shows P wave spectra (fc=0.03, Ω_o=0.0027). Right figure shows S wave spectra(fc=0,021, Ω_o=0.0016)

APPENDIX C: P AND S ARRIVAL TIMES DATA USED FOR DETERMINING EPICENTRE LOCATION OF 04.01.1935, 14:41, 16:20 and 18.09.1963, 16:58 EARTHQUAKES

Table C1. P and S arrival times used for determining epicentral locations of 1935.01.04, 14:41 Erdek-Marmara Island Earthquake

No	Station	Code	Latitude	Longitude	P arrival	S arrival
1	Athens	ATH	37.9722	23.7167	14:42:10	14:43:00
2	Istanbul (Kandilli)	ISK	41.0656	29.0592	14:41:57	14.42:17
3	Sofia	SOF	42.6853	23.3342	14:42:26	14:43:16
4	Yalta	YAL	444.8750	341.5470	14:42:29	14:44:16
5	Ksara	KSA	338.2330	358.9000	14:43:29	14:45:29
6	Messina	MES	38.1989	15.5550	14:43:29	14:46:13
7	Budapest	BUD	47.4836	19.0239	14:43:29	14:45:29
8	Lemberg	LVV	49.8190	26.0310	14:43:29	14:46:29
9	Capodimonte	CAP	40.8667	14.2500	14:44:03	14:47:05
10	Zagreb	ZAG	45.8290	15.9940	14:43:29	14:45:29
11	Helwan	HLW	29.8583	31.3417	14:44:12	14:46:12
12	Laibach	LJU	46.0437	14.5274	14:44:08	14:46:29
13	Vienna	VIE	48.2483	16.3617	14:44:17	14:46:26
14	Triest	TRS	45.6428	13.7539	14:44:05	14:47:17
15	Venice	VEN	45.4333	12.3333	14:44:14	14:47:06
16	Florence	FIR	43.7778	11.2567	14:44:28	14:47:29
17	Padova	PAD	45.4086	11.8861	14:44:26	14:47:19
18	Prato	PRT	43.8800	11.0942	14:44:29	14:47:29
19	Erevan	ERE	40.1700	44.4700	14:44:29	14:48:29
20	Tiflis	TIF	41.7167	44.8000	14:44:29	14:47:06
21	Prague	PRA	50.0703	14.4331	14:44:29	14:47:09

22	Grozny	GRO	43.3200	45.7500	14:44:29	
23	Tunis	TUN	36.8000	10.1333	14:44:29	
24	Piacenza	PCN	45.0500	9.6667	14:44:29	14:47:29
25	Cheb	CHE	50.0794	12.3761	14:44:29	14:47:29
26	Ravensburg	RAV	47.7833	9.6139	14:44:29	14:48:00
27	Hof	HOF	50.3136	11.8775	14:45:00	14:48:00
28	Zurich	ZUR	47.3687	8.5804	14:45:06	14:48:02
29	Jena	JEN	50.9519	11.5833	14:45:00	14:48:00
30	Kösigsberg	KGN	54.8333	20.5000	14:45:01	14:48:00
31	Stuttgart	STU	48.7719	9.1950	14:45:00	14:48:11
32	Basle	BAS	47.5400	7.5829	14:45:11	
33	Karlsruche	KRL	49.0108	8.4122	14:45:19	14:48:18
34	Neuchatel	NEU	49.0063	6.9487	14:45:15	14:48:23
35	Strasbourg	STR	48.5794	7.7631	14:45:15	14:48:29
36	Grenoble	GRN	45.2425	5.7652	14:45:29	14:48:29
37	Marseilles	MAR	43.3053	5.3939	14:45:29	
38	Baku	BAK	40.3833	49.9000	14:45:29	14:48:29
39	Besancon	BES	47.2497	5.9875	14:45:24	14:48:29
40	Hamburg	HAM	53.4651	9.9248	14:45:29	14:48:29
41	Copenhagenen	COP	55.6853	12.4325	14:45:29	14:48:29
42	Barcelona	BARV	9.9839	-70.7456	14:45:29	14:49:29
43	Algiers	ALG	36.7717	3.0583	14:45:29	14:49:29
44	Uccle	UCC	50.7983	4.3594	14:45:29	14:49:27
45	De Bilt	DBN	52.1017	5.1767	14:45:29	14:49:29
46	Pulkovo	PUL	59.7667	30.3167	14:45:29	14:49:29
47	Paris	PAR	48.8094	2.4936	14:45:29	14:49:29
48	Göttingen	GTT	515,464	99,642	14:45:43	14:48:23
49	Bagneres	BDB	43.0650	0.1483	14:46:26	14:50:01
50	Alicante	ALI	38.3553	-0.4872	14:46:23	14:50:23
51	Kew	KEW	51.4683	-0.3131	14:46:25	14:50:21
52	Oxford	OXD	51.7667	-1.25	14:46:29	14:50:29
53	Toledo	TOL	39.8600	-4.0147	14:46:29	14:51:00

54	Durham	DUR	54.7684	-1.5855	14:46:29	14:51:00
55	Stonyhurst	STO	53.8500	-2.4667	14:46:29	14:50:29
56	Granada	NE14	37.1900	-3.5950	14:46:29	14:51:09
57	Bidston	BID	53.4000	-3.0667	14:46:29	14:51:05
58	Bergen	BER	60.3838	5.3339	14:46:29	14:50:29
59	Malaga	MAL	36.7275	-4.4111	14:46:29	14:51:18
60	Rathfarnham Castle	DUB	53.2986	-6.2825	14:47:29	14:52:09
61	San Fernando	SFS	36.4656	-6.2055	14:47:10	14:51:29
62	Sverdlovsk	SVE	56.8270	60.6370	14:47:08	14:51:29
63	Serro do Pilar	PTO	41.1386	-8.6022	14:47:21	14:52:28
64	Samarkand	SAM	39.6733	66.9900	14:47:29	
65	Tashkent	TAS	41.3250	69.2950	14:48:08	14:53:28
66	Semipalatinsk	SEM	50.4083	80.2500	14:48:29	
67	Dehra Dun	DDI	30.3225	78.0556	14:53:00	14:59:20
68	Agra	AGR	27.1333	78.0167	14:49:29	14:56:03
69	Bombay	BOM	18.8958	72.8127	14:49:29	14:56:15
70	Dakar	DAK	14.6667	-17.4333	14:50:00	14:56:29
71	Hyderabad	HYD	17.4169	78.5531	14:50:19	14:57:25
72	Kodaikanal	KOD	10.2333	77.4667	14:50:29	14:58:23
73	Calcutta	CAL	22.5392	88.3307	14:50:29	14:58:29
74	Colombo	COC	6.9000	79.8667	14:51:29	
75	Nanking	NAN	32.0633	118.7833	14:52:29	15:02:13
76	Medan	MED	3.5500	98.6833	14:53:26	15:02:28
77	Hong Kong	HKC	22.3036	114.1719	15:02:29	15:02:29
78	Toronto	TNT	43.6667	-79.4000	14:53:00	15:02:29
79	Cape Town	CTO	-33.9500	18.4500	14:51:29	15:02:29
80	Georgetown	GTD	38.7414	-75.4144	14:53:27	15:03:01
81	Saint Louis	SLM	38.6361	-90.2361	14:53:29	15:04:21
82	Manila	MAN	14.6600	121.0780	14:53:29	15:04:10
83	Batavia	DJA	-6.1833	106.8362	14:53:29	15:04:29
84	Little Rock	LRA	34.7783	-92.3517	14:54:15	15:04:29
85	Oak Ridge	ORT	45.9095	-84.3048	14:52:42	15:02:00

86	Pasadena	PAS	34.1484	-118.1711	14:55:13	
87	Sucre	SUC	-19.0467	-65.2644	15:00:29	
88	La Paz	LPZ	-16,4953	-68.1327	15:01:25	15:06:24
89	Melbourne	MEL	-37.8314	144.9733	15:04:13	
90	Coimbra	COI	40.2067	-8.4183	14:46:51	14:51:03
91	Munich	MNH	48.1500	11.6000	14:44:29	14:44:10
92	Fabra	FBR	41.4164	2.1250	14:45:46	14:49:30
93	Uppsala	UPP	59.8583	17.6267	14:41:29	14:46:01
94	Almeria	ALM	36.8525	-2.4595	14:47:29	14:50:29
95	Huancayo	HUA	-12.0384	-75.3228		15:06:27
96	Edinburgh	EDI	55.9233	-3.1861		14:51:22
97	ScoresbySund	SCO	70.4833	-21.9500		14:55:09
98	Tananarive	TAN	-18.9172	47.5517		15:00:17
99	Phu-Lien	PLV	20.8060	106.6290		15:01:29
100	Ottawa	OTT	45.3939	-75.7158		15:02:05
101	Zinsen	INC	37.4833	126.6333		15:15:29
102	Philadelphia	PHI	39.9589	-75.1750		15:02:29
103	Charlottesville	CVL	37.9814	-78.4608		15:03:10
104	Kobe	KBE	34.7345	135.1778		15:08:29
105	Sumoto	SUM	34.3350	134.9083		15:17:29
106	Victoria	VIC	48.5194	-123.4153		15:05:05

Table C 2. P and S arrival times used for determining epicentral locations of 1935.01.04, 16:20 Erdek-Marmara Island Earthquake

No	**Station**	**Code**	**Latitude**	**Longitude**	**P arrival**	**S arrival**
1	Athens	ATH	37.9722	23.7167	16:21:05	16:21:51
2	Istanbul (Kandilli)	ISK	41.0656	29.0592	16:20:30	16:20:49
3	Sofia	SOF	42.6853	23.3342	16:21:04	16:21:48
4	Yalta	YAL	444.8750	341.5470	16:21:37	16:22:43
5	Ksara	KSA	338.2330	358.9000	16:22:22	16:24:30
6	Messina	MES	38.1989	15.5550	16:22:16	16:24:37

7	Budapest	BUD	47.4836	19.0239	16:22:11	16:24:41
8	Lemberg	LVV	49.8190	26.0310	16:22:34	16:25:06
9	Capodimonte	CAP	40.8667	14.2500	16:22:35	16:25:50
10	Zagreb	ZAG	45.8290	15.9940	16:22:27	16:24:27
11	Helwan	HLW	29.8583	31.3417	16:22:43	16:24:54
12	Laibach	LJU	46.0437	14.5274	16:22:45	16:25:46
13	Vienna	VIE	48.2483	16.3617	16:22:41	16:24:58
14	Triest	TRS	45.6428	13.7539	16:22:44	
15	Venice	VEN	45.4333	12.3333	16:22:20	16:24:38
16	Florence	FIR	43.7778	11.2567	16:23:10	16:26:38
17	Padova	PAD	45.4086	11.8861	16:23:00	
18	Prato	PRT	43.8800	11.0942	16:23:04	16:26:19
19	Erevan	ERE	40.1700	44.4700	16:23:16	16:27:32
20	Tiflis	TIF	41.7167	44.8000	16:23:13	16:25:46
21	Prague	PRA	50.0703	14.4331	16:23:10	16:25:52
22	Grozny	GRO	43.3200	45.7500	16:23:38	16:27:56
23	Tunis	TUN	36.8000	10.1333	16:23:35	
24	Piacenza	PCN	45.0500	9.6667	16:23:25	16:26:12
25	Cheb	CHE	50.0794	12.3761	16:23:25	16:26:38
26	Ravensburg	RAV	47.7833	9.6139	16:23:33	
27	Hof	HOF	50.3136	11.8775	16:23:00	
28	Zurich	ZUR	47.3687	8.5804	16:23:40	16:26:49
29	Jena	JEN	50.9519	11.5833	16:23:36	16:26:54
30	Kösigsberg	KGN	54.8333	20.5000	16:23:36	16:26:28
31	Stuttgart	STU	48.7719	9.1950	16:23:37	16:26:43
32	Basle	BAS	47.5400	7.5829	16:23:48	
33	Karlsruche	KRL	49.0108	8.4122	16:24:00	16:26:51
34	Neuchatel	NEU	49.0063	6.9487	16:23:51	16:27:03
35	Strasbourg	STR	48.5794	7.7631	16:23:52	16:27:10
36	Grenoble	GRN	45.2425	5.7652	16:24:10	16:27:22
37	Marseilles	MAR	43.3053	5.3939	16:25:35	
38	Göttingen	GTT	515,464	99,642	16:23:54	16:27:05

39	Besancon	BES	47.2497	5.9875	16:24:04	16:27:30
40	Hamburg	HAM	53.4651	9.9248	16:24:07	16:27:14
41	Copenhagenen	COP	55.6853	12.4325	16:24:12	16:27:36
42	Barcelona	BARV	9.9839	-70.7456	16:24:26	16:28:05
43	Algiers	ALG	36.7717	3.0583	16:24:33	16:28:00
44	Uccle	UCC	50.7983	4.3594	16:24:28	16:28:06
45	De Bilt	DBN	52.1017	5.1767	16:24:29	16:28:12
46	Pulkovo	PUL	59.7667	30.3167	16:24:26	16:28:06
47	Paris	PAR	48.8094	2.4936	16:24:33	16:28:14
48	Uppsala	UPP	59.8583	17.6267	16:24:43	16:28:24
49	Alicante	ALI	38.3553	-0.4872	16:24:57	16:29:03
50	Kew	KEW	51.4683	-0.3131	16:24:59	16:29:04
51	Oxford	OXD	51.7667	-1.25	16:25:32	16:29:14
52	Toledo	TOL	39.8600	-4.0147	16:25:20	16:29:42
53	Durham	DUR	54.7684	-1.5850	16:25:20	16:29:41
54	Stonyhurst	STO	53.8500	-2.4667	16:25:17	16:29:39
55	Granada	NE14	37.1900	-3.5950	16:25:21	16:29:42
56	Bidston	BID	53.4000	-3.0667	16:25:20	16:29:45
57	Bergen	BER	60.3838	5.3339	16:25:20	16:29:40
58	Malaga	MAL	36.7275	-4.4111	16:25:31	16:29:57
59	Edinburgh	EDI	55.9233	-3.1861		16:30:10
60	Rathfarnham Castle	DUB	53.2986	-6.2825	16:26:12	16:30:51
61	San Fernando	SFS	36.4656	-6.2055	16:25:50	16:30:36
62	Sverdlovsk	SVE	56.8270	60.6370	16:25:47	16:30:32
63	Serro do Pilar	PTO	41.1386	-8.6022	16:25:52	16:30:49
64	Samarkand	SAM	39.6733	66.9900	16:27:30	
65	Tashkent	TAS	41.3250	69.2950	16:25:26	
66	Semipalatinsk	SEM	50.4083	80.2500	16:27:22	
67	ScoresbySund	SCO	70.4833	-21.9500	16:27:36	16:33:48
68	Dehra Dun	DDI	30.3225	78.0556	16:28:50	16:34:50
69	Agra	AGR	27.1333	78.0167	16:28:08	16:34:37
70	Bombay	BOM	18.8958	72.8127	16:28:14	16:34:49

71	Dakar	DAK	14.6667	-17.4333	16:28:37	16:35:27
72	Hyderabad	HYD	17.4333	78.4500	16:29:02	16:35:38
73	Kodaikanal	KOD	10.2333	77.4667	16:29:24	16:37:11
74	Calcutta	CAL	22.5392	88.3307	16:29:38	16:37:10
75	Colombo	COC	6.9000	79.8667	16:33:30	
76	Tananarive	TAN	-18.9172	47.5517	16:38:58	
77	Oak Ridge	ORT	35.9095	-84.3048	16:31:15	
78	Ottawa	OTT	45.3939	-75.7158	16:40:26	
79	Nanking	NAN	32.0633	118.7833	16:31:28	16:41:11
80	Medan	MED	3.5500	98.6833	16:32:10	16:41:00
81	Hong Kong	HKC	22.3036	114.1719	16:41:09	16:41:09
82	Philadelphia	PHI	39.9589	-75.1750		16:41:54
83	Toronto	TNT	43.6667	-79.4000	16:31:26	16:41:11
84	Cape Town	CTO	-33.9500	18.4500	16:41:24	
85	Georgetown	GTD	38.7414	-75.4144	16:31:50	16:41:18
86	Saint Louis	SLM	38.6361	-90.2361	16:32:28	
87	Manila	MAN	14.6600	121.0780	16:32:38	16:43:00
88	Batavia	DJA	-6.1833	106.8362	16:29:26	
89	Little Rock	LRA	34.7783	-92.3517	16:32:49	16:43:44
90	Pasadena	PAS	34.1484	-118.1711		16:58:02
91	Coimbra	COI	40.2067	-8.4183	16:26:31	16:30:36
92	Munich	MNH	48.1500	11.6000	16:23:10	16:26:08
93	Fabra	FBR	41.4164	2.1250	16:24:24	16:28:11

Table C 3. P and S arrival times used for determining epicentral locations of 1963.09.18, 16:58, Çınarcık Earthquake

No	**Station**	**Code**	**Latitude**	**Longitude**	**P arrival**	**S arrival**
1	Istanbul un.	IST	41.0456	28.9958	16:58:18	
2	Bucharest	BUC	44.4136	26.0967	16:59:19	17:00:10
3	Sofia	SOF	42.6853	23.3342	16:59:23	17:00:14
4	Athens	ATH	37.9722	23.7167	16:59:26	17:00:21

5	Campulung	CMP	45.2683	25.0383	16:59:34	
6	Simferopol	SIM	44.9490	34.1160	16:59:34	17:00:36
7	Skopje	SKO	41.9721	21.4396	16:59:41	17:00:53
8	Bacau	BAC	46.5667	26.9000	16:59:42	17:00:59
9	Patras	PAT	38.2364	21.7467	16:59:48	17:00:58
10	Iasi	IAS	47.1933	27.5617	16:59:49	
11	Belgrade	BEO	44.8214	20.4553	16:59:59	17:01:31
12	Titograd	TTG	42.4297	19.2608	16:59:59	17:01:37
13	Timisoara	TIM	45.7366	21.2208	17:00:00	17:01:21
14	Ksara	KSA	33.8233	35.8900	17:00:18	17:02:11
15	Taranto	TAR	40.4750	17.2583	17:00:40	
16	Jerusalem	JER	31.7719	35.1972	17:00:38	17:02:52
17	Skalnate pl.	SPC	49.1889	20.2450	17:00:32	17:02:15
18	Hurbanovo	HRB	47.8736	18.1928	17:00:48	17:04:25
19	Niedzıka	NIE	49.4189	20.3131	17:00:46	
20	Reggio cala.	RCI	38.1056	15.6433	17:00:43	17:02:43
21	Messina	MES	38.1989	15.5550	17:00:45	17:02:47
22	Zagreb	ZAG	45.8290	15.9940	17:00:47	17:02:51
23	Krakow	KRA	50.0561	19.9397	17:00:53	17:04:11
24	Bratislava	BRA	48.1683	17.1050	17:00:56	17:02:31
25	Vienna-h.	VIE	48.2483	16.3617	17:01:00	17:04:19
26	Tiflis	TIF	41.7167	44.8000	17:01:03	
27	Ljubljana	LJU	46.0437	14.5274	17:00:59	17:03:05
28	Chorzow	CHZ	50.2925	18.9917	17:01:06	
29	Aquila	AQU	42.3539	13.4019	17:01:00	
30	Raciborz	RAC	50.0833	18.1942	17:01:08	
31	Trieste	TRI	45.7089	13.7642	17:01:05	17:04:13
32	Rome	ROM	41.9033	12.5133	17:01:10	17:04:44
33	Warsaw	WAR	52.2417	21.0236	17:01:15	17:04:48
34	Goris	GRS	39.5000	46.3333	17:01:24	
35	Padova	PAD	45.4086	11.8861	17:01:25	17:04:47
36	Bologna	BOL	44.4867	11.3290	17:01:28	17:05:04

37	Prato	PRT	43.8800	11.0942	17:01:38	17:04:26
38	Pruhonice	PRU	49.9883	14.5417	17:01:25	17:04:55
39	Kasperske	KHC	49.1309	13.5782	17:01:26	
40	Prague	PRA	50.0703	14.4331	17:01:29	17:04:08
41	Pavia	PAV	45.1833	9.1736	17:01:46	
42	Chur	CHU	46.8499	9.5367	17:01:48	17:05:01
43	Ravensburg	RAV	47.7833	9.6139	17:01:49	
44	Cuglieri	CUG	40.1869	8.5698	17:01:50	17:05:00
45	Jena	JEN	50.9519	11.5833	17:01:54	17:05:00
46	Moscow	MOS	55.7383	37.6250	17:01:52	17:04:49
47	Halle	HLE	51.4979	11.9569	17:01:52	
48	Stuttgart	STU	48.7719	9.1950	17:04:56	17:01:57
49	Tubingen	TUB	48.5269	9.0611	17:02:00	
50	Monaco	MON	43.7306	7.4258	17:02:07	
51	Isola	ISO	44.1833	7.0500	17:02:06	17:05:29
52	Heidelberg	HEI	49.3986	8.7264	17:02:04	
53	Karlsruhe	KRL	49.0108	8.4122	17:02:06	17:05:26
54	Strasbourg	STR	48.5794	7.7631	17:02:08	17:05:23
55	Karlskrona	KLS	56.1650	15.5917	17:02:20	
56	Besancon	BES	47.2497	5.9875	17:02:18	
57	Welschbruch	WLS	48.4128	7.3536	17:02:10	
58	Tehran	TEH	35.7367	51.3817	17:02:24	17:06:09
59	Bensberg	BNS	50.9639	7.1756	17:02:25	17:05:55
60	Copenhagenen	COP	55.6853	12.4325	17:02:26	17:05:48
61	Pulkovo	PUL	59.7667	30.3167	17:02:30	17:06:05
62	Wıtteveen	WIT	52.8133	6.6683	17:02:39	
63	Dourbes	DOU	50.0960	4.5942	17:02:38	
64	Clermont-fd.	CFF	45.7630	3.1112	17:02:40	17:06:27
65	Helsinki	HEL	60.1756	24.9570	17:02:37	
66	Garchy	GRC	47.2956	3.0736	17:02:41	
67	Uccle	UCC	50.7983	4.3594	17:02:44	17:06:27
68	De bılt	DBN	52.1017	5.1767	17:02:45	17:06:28

69	Nurmıjarvı	NUR	60.5090	24.6490	17:02:41	17:06:12
70	Goteborg	GOT	57.6983	11.9783	17:02:46	
71	Barcelona	FBR	41.4164	2.1250	17:02:50	17:06:59
72	Uppsala	UPP	9.8583	17.6267	17:02:47	17:06:28
73	Parıs	PAR	48.8094	2.4936	17:02:46	17:06:39
74	Bagneres	BDB	43.0650	0.1483	17:03:05	
75	Shıraz	SHI	29.6418	52.5133	17:03:05	17:07:08
76	Folınıere	FLN	48.7625	-0.4819	17:02:40	
77	Kongsberg	KON	59.6491	9.5982	17:04:09	17:07:39
78	Ashkhabad	ASH	37.9500	58.3500	17:04:12	17:07:23
79	Kew	KEW	51.4683	-0.3131	17:04:13	17:07:21
80	Alicante	ALI	38.3553	-0.4872	17:04:15	17:07:22
81	Kajaani	KJN	64.0853	27.7119	17:04:20	17:07:46
82	Jersey	JRS	49.1924	-2.0917	17:04:18	17:07:32
83	Umea	UME	63.8150	20.2367	17:04:22	17:07:33
84	Bergen	BER	60.3838	5.3339	17:04:33	
85	Durham	DUR	54.7684	-1.5850	17:04:33	17:07:55
86	Almerıa	ALM	36.8525	-2.4598	17:04:33	17:08:01
87	Skalstugan	SKA	63.5800	12.2800	17:04:33	
88	Toledo	TOL	39.8814	-4.0486	17:04:36	17:08:00
89	Granada	CRT	37.1900	-3.5979	17:04:47	17:08:34
90	Sverdlovsk	SVE	56.8270	60.6370	17:04:42	
91	Aberdeen	ABE	57.1667	-2.1000	17:04:47	17:08:28
92	Malaga	MAL	36.7275	-4.4111	17:04:50	17:08:08
93	Sodankyla	SDF	67.4203	26.3936	17:04:50	
94	Apatıty	APA	67.5689	33.4050	17:04:52	17:08:24
95	Kıruna	KIR	67.8400	20.4167	17:04:57	17:08:36
96	Valentia	VAL	51.9394	-10.2442	17:04:12	17:09:32
97	Kevo	KEV	69.7553	27.0067	17:04:11	17:09:06
98	Tromsoe	TRO	69.6325	18.9281	17:04:14	
99	Averroes	AVE	33.2981	-7.4133	17:04:20	17:09:16
100	Tashkent	TAS	41.3250	69.2950	17:04:20	17:09:56

101	Quetta	QUE	30.1883	66.9500	17:04:39	17:10:12
102	Frunze	FRU	42.8333	74.6167	17:04:53	
103	Warsak dam	WRS	35.1500	71.4167	17:04:55	
104	Semipalatnsk	SEM	50.4083	80.2500	17:05:19	17:10:56
105	Lahore	LAH	31.5500	74.3333	17:05:22	
106	Bangui	BNG	4.4350	18.5467	17:05:22	17:11:02
107	Scoresby sd.	SCO	70.4833	-21.9500	17:05:47	17:11:58
108	New Delhi	NDI	28.6833	77.2167	17:05:56	17:12:10
109	Lwiro	LWI	-2.2393	28.8025	17:06:09	
110	Bombay	BOM	18.8958	72.8127	17:06:11	17:12:36
111	Poona	POO	18.5295	73.8492	17:06:20	17:12:55
112	Esen bulak	EBM	46.3900	96.2600	17:06:48	17:13:48
113	M.bour	MBO	14.3908	-16.9547	17:06:49	17:13:54
114	Hyderabad	HYD	17.4333	78.4500	17:06:57	17:14:09
115	Chatra	CHA	26.8333	87.1667	17:07:01	17:14:21
116	Bokaro	BOK	23.7948	85.8858	17:07:05	17:14:23
117	Alert	ALE	82.5033	-62.3500	17:07:06	
118	Irkutsk	IRK	52.2431	104.2711	17:07:10	17:14:30
119	Luanda	LUA	-8.5000	13.2333	17:07:19	
120	Madras	MDR	13.0000	80.1833	17:07:25	17:14:38
121	Shillong	SHL	25.5667	91.8833	17:07:31	17:15:03
122	Tiksi	TIK	71.6333	128.8667	17:07:41	17:15:25
123	Broken hill	BHA	-14.4467	28.4683	17:07:42	
124	Chıleka	CLK	-15.6800	34.9767	17:07:53	
125	Bandeira	SDB	-14.9258	13.5719	17:07:58	
126	Resolute	RES	74.6867	-94.9000	17:08:11	
127	Yakutsk	YAK	62.0311	129.6811	17:08:12	
128	Bulawayo	BUL	-20.1433	28.6133	17:08:22	
129	Scheffervlle	SCH	54.8167	-66.7833	17:08:24	
130	Mould bay	MBC	76.2417	-119.3600	17:08:28	
131	Tananarıve	TAN	-18.9172	47.5517	17:08:31	
132	Port blaır	PBA	11.6559	92.7428	17:08:34	

133	Halifax	HAL	44.6377	-63.5920	17:08:48	
134	Changalane	CNG	-26.2917	32.1883	17:09:03	17:17:56
135	Phu-lien	PLV	20.8060	106.6290	17:09:07	
136	Shawinigan	SHF	46.5517	-72.7633	17:09:14	
137	Kimberley	KIM	-28.7517	24.7800	17:09:18	
138	Pietermzburg	PIE	-29.6200	30.3967	17:09:30	
139	Hong kong	HKC	22.3036	114.1719	17:09:40	
140	Palisades	PAL	41.0055	-73.9079	17:09:39	17:19:13
141	Fordham	FOR	40.8631	-73.8856	17:09:40	17:19:12
142	Grahams town	GRH	-33.3100	26.5750	17:09:46	
143	Y.-sakhlınsk	YSS	46.9539	142.7550	17:09:50	
144	College	COL	64.9000	-147.7933	17:09:50	
145	Pennsylvania	PAGS	40.2278	-76.7221	17:09:54	
146	Hermanus	HER	-34.4250	19.2250		17:19:45
147	London ont.	LDN	43.0400	-81.1833	17:09:55	
148	Georgetown	GEO	38.9000	-77.0667	17:10:04	17:19:20
149	Washington	WAS	38.8925	-77.0331	17:09:55	
150	Cleveland	CLE	41.4888	-81.5321	17:10:02	17:19:59
151	Abuyama	ABU	34.8603	135.5739	17:10:14	
152	Blacksburg	BLA	37.2113	-80.4210	17:10:15	17:20:20
153	Chappel hill	CEH	35.8908	-79.0928	17:10:17	
154	Matusiro	MAT	36.5417	138.2089	17:10:16	17:20:18
155	Baguıo cıty	BAG	16.4108	120.5797	17:10:23	
156	Tukubasan	MTJ	36.2108	140.1100	17:10:28	17:20:28
157	Columbıa	CSC	34.0000	-81.0333	17:10:29	17:20:53
158	Manila	MAN	14.6600	121.0780	17:10:39	
159	Cumberland	CPO	35.5948	-85.5704	17:10:36	17:20:58
160	Trinidad	TDJ	37.2536	-104.3347	17:10:39	
161	Tangerang	TNG	-6.1717	106.6462	17:09:46	
162	Rapid city	RCD	44.0750	-103.2083	17:10:47	
163	Hungry horse	HHM	48.3494	-114.0275	17:10:49	
164	Butte	BUT	46.0133	-112.5633	17:10:56	

165	Caracas	CAR	10.5067	-66.9276	17:11:00	17:21:24
166	Victoria	VIC	48.5194	-123.4153	17:10:58	
167	Seattle	SEA	47.6550	-122.3083	17:11:12	
168	Tulsa	TSO	36.1482	-95.8979	17:11:02	17:21:35
169	Blue mts.	BML	43.8680	-74.4020	17:11:07	17:21:49
170	Golden	GLD	39.7492	-105.2201	17:11:08	
171	Flaming gorge	FGU	40.9264	-109.3862	17:11:12	
172	Wichita mts.	WMO	34.7379	-98.7810	17:11:13	17:22:10
173	Uinta basin	UBO	40.3217	-109.5687	17:11:14	17:22:17
174	Price	PCU	39.6067	-110.8050	17:11:18	
175	Dug way	DUG	40.1950	-112.8133	17:11:20	
176	Eureka	EUR	39.4833	-115.9700	17:11:29	
177	Albuquerque	ALQ	34.9425	-106.4575	17:11:30	
178	Shasta	SHS	40.6950	-122.3883	17:11:35	
179	Mineral	MIN	40.3460	-121.6066	17:11:36	
180	Boulder city	BCN	35.9808	-144.8339	17:11:42	
181	Calistoga	CLS	38.6367	-122.5850	17:11:45	
182	Tonto forest	TFO	34.2678	-111.2703	17:11:42	
183	Bogota	RSNC				17:22:19
184	Berkeley	BRK	37.8735	-122.2610	17:11:41	17:23:18
185	Lick	MHC	37.3416	-121.6426	17:11:45	
186	Chinchina	CHN	4.9667	-75.6167		17:22:23
187	Priest	PRI	36.1417	-120.6650	17:11:39	
188	Pasadena	PAS	34.1484	-118.1711	17:12:01	17:23:42
189	La paz	LPZ	-16.495	-63.1327	17:17:07	
199	Antofagasta	ANT	-23.7050	-70.4153		
200	Port Moresby	PMG	9.4062	147.1589		
201	Charters ts.	CTA	-20.0883	146.2544		
202	Adelaide	ADE	-34.9669	138.7089	17:17:11	
203	Honiara	HNR	-9.4322	159.9471		
204	South pole	SPA	-89.9954	115.0000	17:17:29	
205	Toolangi	TOO	-37.5714	145.4906	17:17:24	

206	Brisbane	BRS	-27.3917	152.7750	17:17:25	
207	Canberra	CAN	-35.3208	148.9986	17:17:27	
208	Riverview	RIV	-33.8294	151.1583	17:17:42	
209	Byrd station	BYR	-80.0167	-119.5167	17:17:32	
210	Cape hallett					
211	Afiamalu	AFI	-13.9094	-171.7772	17:17:57	
212	Karapiro	KRP	-37.9250	175.5375	17:18:09	
213	Wellington	WEL	-41.2861	174.7683	17:18:09	